

Utah State University

DigitalCommons@USU

---

All Graduate Theses and Dissertations

Graduate Studies

---

5-2017

## Mechanism of Substrate Reduction by Nitrogenase

Nimesh Khadka  
*Utah State University*

Follow this and additional works at: <https://digitalcommons.usu.edu/etd>

 Part of the [Biochemistry Commons](#)

---

### Recommended Citation

Khadka, Nimesh, "Mechanism of Substrate Reduction by Nitrogenase" (2017). *All Graduate Theses and Dissertations*. 5614.

<https://digitalcommons.usu.edu/etd/5614>

This Dissertation is brought to you for free and open access by the Graduate Studies at DigitalCommons@USU. It has been accepted for inclusion in All Graduate Theses and Dissertations by an authorized administrator of DigitalCommons@USU. For more information, please contact [digitalcommons@usu.edu](mailto:digitalcommons@usu.edu).



MECHANISM OF SUBSTRATE REDUCTION BY NITROGENASE

by

Nimesh Khadka

A dissertation submitted in partial fulfillment  
of the requirements for the degree

of

DOCTOR OF PHILOSOPHY

in

Biochemistry

Approved:

---

Lance C. Seefeldt, Ph.D.  
Major Professor

---

Scott A. Ensign, Ph.D.  
Committee Member

---

Sean Johnson, Ph.D.  
Committee Member

---

Edwin Antony, Ph.D.  
Committee Member

---

Korry Hintze, Ph.D.  
Committee Member

---

Mark McLellan, Ph.D.  
Vice President for Research and  
Dean of the School of Graduate Studies

UTAH STATE UNIVERSITY  
Logan, Utah

2017

Copyright © Nimesh Khadka 2017  
All Rights Reserved

## ABSTRACT

Mechanism of Substrate Reduction by Nitrogenase

by

Nimesh Khadka, Doctor of Philosophy

Utah State University, 2017

Major Professor: Dr. Lance C. Seefeldt  
Department: Chemistry and Biochemistry

Nitrogen (N) is a chemical constituent for almost all biological molecules including proteins, DNA, RNA, lipids and is therefore vital for life. The ultimate source of nitrogen is the atmospheric dinitrogen ( $N_2$ ) but that only becomes bioavailable through a process of nitrogen fixation, the process that converts  $N_2$  to ammonia ( $NH_3$ ). The industrial Haber-Bosch process and biological nitrogen fixation account for the majority of nitrogen fixed every year. However, due to its high temperature, pressure and fossil fuel requirements, Haber-Bosch is an expensive process. Every year, approximately 3% of the global energy demand is used to manufacture ammonia through Haber-Bosch process. On the other hand, biological systems produce ammonia by reducing dinitrogen at ambient temperature and pressure using an anaerobic enzyme called nitrogenase. Research in understanding the mechanism of nitrogenase could eventually allow researchers to mimic the enzyme and fix nitrogen efficiently at standard temperature and pressure.

In this research, nitrogenase of *Azotobacter vinelandii* was studied to understand the mechanism of delivery of electrons/protons to the active site and how these accumulated reducing equivalents are used for substrates reduction. Through a series of studies, it has been demonstrated that the electrons and protons are added to the active site in a concerted manner which are then stored as bridging hydrides. The accumulated hydrides are used in four different mechanisms, namely reductive elimination, hydride protonolysis, migratory insertion and proton coupled electron transfer, to catalyze the reduction of varieties of unsaturated molecules. This fundamental understanding of molecular detail of nitrogenase catalysis could eventually help in development of more efficient, robust and selective catalysts.

(291 pages)

## PUBLIC ABSTRACT

## Mechanism of Substrate Reduction by Nitrogenase

Nimesh Khadka

Nitrogen (N) is a vital element of life and the main component of chemical fertilizer. The industrial Haber-Bosch process fulfills the demands of today's nitrogen need and is therefore considered as one of the major scientific breakthroughs of the last century. However, the Haber-Bosch process operates at very high temperature and pressure, and requires fossil fuels to drive the reaction, making it an energy expensive process. The energy demand for this process accounts for almost 3% of the total global energy consumption. In addition, the rapid population growth, economic development and depletion of limited non-renewable fossil fuels have already created an energy crisis. Therefore, along with many other processes, a method for sustainable ammonia production is a must for the future of humanity. One of the strategies would be to understand the functioning of nitrogenase, a molecular catalyst of nature that makes ammonia from atmosphere at optimum temperature and pressure, and mimic it to create a robust and efficient artificial catalyst. With this inspiration, the present research is focused in elucidation the fundamental details on working of nitrogenase. A key chemical state of nitrogenase that allows it to efficiently reduce and make ammonia has been characterized in this research that would possibly be a cornerstone in our thrust for the ultimate catalyst. In addition, employing nitrogenase to convert greenhouse gas,

carbon dioxide, into value added product is also revisited in this research.

## ACKNOWLEDGMENTS

I would like to thank first and foremost my loved ones. Special thanks to my Mom and Dad who gave me all those opportunities that they could afford to pursue my dream. They have been always supportive to me and also a constant source of inspiration through every aspect of my life. Also I would like to acknowledge my wife, Rajani, who constantly loved and supported me throughout my graduate studies. And not to mention, my daughter Radhyaa who brought a real meaning to my life. My family have taught me the virtue of life and shaped my inspiration to become a better scientist.

There are people at work who have been amazing over the past seven years. First and foremost, my professor Dr. Seefeldt, who allowed an immature undergraduate student to enroll in his lab, tolerated all my inefficiencies and finally trained me to think and act scientifically. Besides academic mentoring, he is always there with his direct support and guidance to nurture us to become successful and productive in an ethical manner. I will always be thankful to you and hope to maintain this relationship for the rest of my life. I would also like to thank all my supervisory committee members for all your help and guidance and encouragement for all these years.

I would also like to thank my colleague Sudipta, Rhesa, Derek, Danyal, Simon, Yang, AJ, Alex and the numerous others who were always there with their with their open hearted help and support. I would also like to thank all my collaborators Dmitriy, Roman, Simone, Nakul, Ziliang, Noopur and Ross.



Finally, I would like to thank the departmental and university administration Maury, Geri and Margaret (past member) for setting up a great scientific research environment here at Utah State University.

Nimesh Khadka

## CONTENTS

	Page
ABSTRACT.....	iii
PUBLIC ABSTRACT .....	v
ACKNOWLEDGMENTS .....	vii
LIST OF TABLES.....	xii
LIST OF FIGURES .....	xiii
ABBREVIATIONS .....	xx
CHAPTER	
1. INTRODUCTION .....	1
Nitrogen Fixation.....	1
Mo-dependent Nitrogenase.....	3
Iron Protein .....	4
MoFe Protein .....	5
Mechanism of Electron Transfer .....	8
Mechanism of Substrate Reduction on FeMo-co.....	9
References.....	21
2. EXPLORING ELECTRON/PROTON TRANSFER AND CONFORMATIONAL CHANGE IN THE NITROGENASE MoFe PROTEIN THROUGH CRYOREDUCTION/EPR MEASUREMENT .....	27
Abstract.....	27
Introduction.....	28
Materials and Methods.....	32
Results.....	35
Discussion.....	47
References.....	55
Appendix: Supporting Information.....	59
3. CO <sub>2</sub> REDUCTION CATALYZED BY NITROGENASE: PATHWAYS TO FORMATE, CARBON MONOXIDE AND METHANE .....	70

Abstract.....	70
Introduction.....	71
Materials and Methods.....	75
Results.....	79
Discussion.....	89
References.....	96
Appendix: Supporting Information.....	100
4. PATHWAY OF CO <sub>2</sub> REDUCTION TO CH <sub>4</sub> AND C-C BOND FORMATION CATALYZED BY NITROGENASE .....	119
Abstract.....	119
Introduction.....	120
Materials and Methods.....	123
Results.....	126
Discussion.....	139
Conclusion .....	150
References.....	151
Appendix: Supporting Information.....	155
5. REVERSIBLE PHOTOINDUCED REDUCTIVE ELIMINATION OF H <sub>2</sub> FROM THE NITROGENASE DIHYDRIDE STATE: THE E <sub>4</sub> (4H) JANUS INTERMEDIATE .....	165
Abstract.....	165
Introduction.....	166
Materials and Methods.....	171
Results and Discussion .....	174
Summary and Prospect .....	186
References.....	188
Appendix: Supporting Information.....	194
6. REDUCTIVE ELIMINATION OF H <sub>2</sub> ACTIVATES NITROGENASE TO REDUCE N≡N TRIPLE BOND: CHARACTERIZATION OF THE E <sub>4</sub> (4H) JANUS INTERMEDIATE IN WILD TYPE ENZYME.....	200
Abstract.....	200
Introduction.....	201
Materials and Methods.....	208
Results and Discussion .....	209
Conclusion/Summary.....	226
References.....	228
7. SUMMARY AND FUTURE DIRECTIONS .....	232

Probing the Reactivity of Metal Hydride.....	234
Mechanism of CO <sub>2</sub> Reduction .....	237
Mechanism of N <sub>2</sub> Reduction.....	241
References.....	242
Appendix: Experimental Methods .....	244
APPENDIX.....	256
CURRICULUM VITAE.....	266

## LIST OF TABLES

Table		Page
3-1	Product accumulation and electron distribution for wild type MoFe protein .....	80
3-S1	Coefficients ( $c_A$ and $c_B$ ) and occupation of selected Natural Bond Orbitals, $\phi$ (A-B).....	104
3-S2	Magnitude of the charge qCT transferred from the NBOs $\phi_1$ and to the NBO $\phi_2$ , $\phi_1(A-B) \rightarrow \phi_2(C-D)$ , for selected species, where $\phi_{2=1,2} = \sigma$ (sigma bonding), $\sigma^*$ (antibonding), $\pi^*$ (pi antibonding), and n (lone pair).....	105
3-S3	NBO point charges ( $e$ ) on the FeMoco cluster in catalytic intermediates .....	106
3-S4	Natural valence electron configuration for the Fe ( $n = 4$ ) and H ( $n = 1$ ) atoms in $E_0$ , $E_2(2H)$ , $E_2(2H)-CO_2$ and $E_4(4H)$ .....	108
3-S5	Product accumulation and electron distribution for MoFe protein variants .....	109
4-S1	Formation of propylene with various substrate .....	164
5-S1	Specific Activities for MoFe proteins at pH 7.0 .....	198
5-S2	Stretched Exponential parameters describing the photoinduced <i>re</i> of $E_4(4H)$ .....	199

## LIST OF FIGURES

Figure		Page
1-1	Bio-geochemical Nitrogen cycle .....	2
1-2	Molybdenum dependent nitrogenase.....	3
1-3	FeMo-cofactor of nitrogenase .....	7
1-4	EPR spectrum of wild type (WT) and $\alpha$ -70 <sup>IIc</sup> MoFe proteins in resting and turnover states.....	10
1-5	Simplified Lowe-Thorneley (LT) kinetic scheme for nitrogen fixation .....	11
1-6	Schematic representation of proton coupled electron transfer (PCET).....	12
1-7	Showing the two fates of Janus state.....	14
1-8	Schematic of <i>re/oa</i> equilibrium.....	16
1-9	X-band EPR spectra of Wild type (WT) nitrogenase.....	17
1-10	Showing the mechanism of HD formation.....	18
2-1	First two steps of the LT MoFe protein cycle showing the accumulation of electrons/protons as well as the possible loss of H <sub>2</sub> by relaxation .....	28
2-2	X-band EPR spectra of nitrogenase MoFe protein oxidized to the (primarily) Mox state with loss of 90% of M <sup>N</sup> signal (upper) and then cryoreduced at 77 K and annealed at progressively higher temperatures for 2 minutes each.....	36
2-3	X-band EPR spectra of nitrogenase in resting state and freeze-quenched during TO under low electron flux and high electron flux under Ar .....	38
2-4A	Low-field EPR spectra of nitrogenase freeze-trapped under low-flux/Ar TO, cryoreduced (3 Mrad) and annealed at indicated temperatures .....	40

2-4B	High field EPR spectra of cryoreduced low flux Ar turnover nitrogenase annealed at indicated temperatures.....	42
2-5	Kinetics of formation of $E_2(2H)$ $S = 3/2$ 1b state in $H_2O$ (red) and $D_2O$ (blue) and the decay of $S = 1/2$ $E_2^*$ species ( $g_1 = 2.21$ ) (green) during annealing cryoreduced low-flux/Ar TO nitrogenase at 216 K.....	43
2-6	Effect of $H_2O$ and $D_2O$ on kinetics of $S = 3/2$ 1b state formation during annealing cryoreduced high flux Ar and $N_2$ TO nitrogenase at 216 K.....	44
2-7	Kinetics of formation of $E_2(2H)$ , $S = 3/2$ (1b) species during annealing cryoreduced low flux (green) and high flux (red) nitrogenase Ar TO at 216 K.....	45
2-8	High-field EPR spectra of resting-state nitrogenase after radiolytic cryoreduction (3 Mrad), and annealed at indicated temperatures; g-values label features associated with oxidized P-cluster (see text). ....	46
2-9	Scheme for electron/proton delivery and conformational changes during early-stage $[e^-/H^+]$ accumulation by the MoFe protein ( $MF$ ) through reduction by the Fe protein ( $F$ ).....	49
2-S1a	X-band EPR spectra of resting state nitrogenase before (red) and after radiolytic cryoreduction (3 Mrad , black) and subsequent it's annealing at 235K for 1 min (blue dashed).....	60
2-S1b	2 K 35 GHz EPR spectra of resting state nitrogenase before (red) and after radiolytic cryoreduction (3 Mrad , black). ....	61
2-S2	X-band EPR spectra of cryogenerated oxidized P cluster in $\gamma$ -irradiated resting state nitrogenase prepared without and in the presence of 10% glycerol. ....	62
2-S3	Effect of temperature on EPR spectra of the cryogenerated $S = 1/2$ intermediate of cryoreduced low-flux Ar turnover nitrogenase. ....	63
2-S4	High field EPR spectra of cryoreduced nitrogenase in resting state and prepared at low flux under Ar turnover annealed at 160 K for 1 min.....	64
2-S5	2K 35GHz EPR spectra of cryoreduced resting state and low flux TO nitrogenase annealed at 160 K for 1 min. ....	65

2-S6	Time course of growth of S=3/2 1b EPR signal (difference spectrum, see Figure 2-4A) during annealing cryoreduced low-flux Ar turnover nitrogenase at 216 K.....	66
2-S7	EPR spectra of the cryoreduced high flux Ar turnover nitrogenase annealed at indicated temperatures .....	67
2-S8	Low field EPR spectra of the cryoreduced E <sub>1</sub> state (B) generated by cryoreduction of nitrogenase in resting state (A) and followed subsequent annealing at 235 K (C) EPR spectrum of (B) after annealing at 235 K for 1 min .....	68
2-S9	EPR spectra of cryogenerated oxidized P cluster in resting state nitrogenase exposed to $\gamma$ -irradiation at 77 K with dose 9 Mrad after annealing at 160 -235 K for 1 min .....	69
3-1	FeMo-co of nitrogenase .....	71
3-2	Pathways for N <sub>2</sub> and nitrite reduction .....	73
3-3	Effect of H <sub>2</sub> on N <sub>2</sub> and CO <sub>2</sub> reduction .....	82
3-4	Possible pathways for CO <sub>2</sub> reduction .....	84
3-5	Computed free energy diagram for CO <sub>2</sub> reduction and H <sub>2</sub> formation occurring at the E <sub>2</sub> state of FeMo-cofactor .....	87
3-6	Product distribution under CO <sub>2</sub> for different MoFe proteins.....	89
3-S1	HCOO <sup>-</sup> via <sup>13</sup> C NMR.....	111
3-S2	Colorimetric assay for formate .....	112
3-S3	Structures of the models used for the DFT calculations .....	113
3-S4	Computed free energy diagram for CO <sub>2</sub> reduction and H <sub>2</sub> formation occurring at the E <sub>2</sub> state of FeMo-cofactor .....	114
3-S5	Structure and relative free energy of various E <sub>2</sub> states examined computationally.....	115
3-S6	Structure of the transition state for the direct hydride transfer to CO <sub>2</sub> as computed from model 2.....	116



3-S7	Selected structures of species leading to the formation of formate (associative pathway) and CO as computed from model 1 and model 2.....	117
3-S8	Key catalytic residue around FeMo-cofactor that modulate catalytic selectivity.....	118
4-1	Crystal structure of FeMo-co .....	120
4-2	Simplified Lowe-Thorneley (LT) kinetic scheme for nitrogen fixation .....	121
4-3	Time dependent CO <sub>2</sub> reduction to CH <sub>4</sub> .....	127
4-4	CO <sub>2</sub> reduction to CH <sub>4</sub> likely follows CO pathway .....	128
4-5	Predicted pathway for activation of CO <sub>2</sub> toward CO formation.....	129
4-6	Solvent Isotope effect on $\alpha$ -70 <sup>Ala</sup> / $\alpha$ -195 <sup>Gln</sup> MoFe protein catalyzed steady state formation of CO with changing electron flux [Fe protein]:[MoFe protein] .....	130
4-7	Formamide and formic hydrazide reduction to CH <sub>4</sub> by $\alpha$ -70 <sup>Ala</sup> / $\alpha$ -195 <sup>Gln</sup> MoFe protein.....	132
4-8	Effect of electron flux on the formation of CO and CH <sub>4</sub> during formic hydrazide turnover using $\alpha$ -70 <sup>Ala</sup> / $\alpha$ -195 <sup>Gln</sup> MoFe protein .....	133
4-9	EPR / Photolysis of freeze quench sample of formic hydrazide turnover with $\alpha$ -70 <sup>Ala</sup> / $\alpha$ -195 <sup>Gln</sup> MoFe protein .....	134
4-10	Activity of different MoFe protein for reducing CO <sub>2</sub> to CH <sub>4</sub> and CO <sub>2</sub> to CO .....	136
4-11	Reduction of CO to CH <sub>4</sub> using different MoFe proteins .....	137
4-12	Reduction of formic hydrazide to CH <sub>4</sub> using different MoFe proteins .....	138
4-13	Formation of C-C bond during co-reduction of CO <sub>2</sub> , CO, HCONHNH <sub>2</sub> , and HCN with C <sub>2</sub> H <sub>2</sub> .....	139
4-14	Simplified mechanism of Ni-Fe CO dehydrogenase .....	140

4-15	Mechanism of N <sub>2</sub> reduction and convergence of different reduction pathways by nitrogenase .....	146
4-16	Proposed mechanism for the reduction of CO <sub>2</sub> to CH <sub>4</sub> and the formation of the C-C bond .....	148
4-S1	$\alpha$ -70 <sup>Ala</sup> / $\alpha$ -195 <sup>Gln</sup> MoFe protein catalyzed time dependent CO <sub>2</sub> reduction to CO formation and CO to CH <sub>4</sub> .....	156
4-S2	Test if metal formate (M-(OCOH)) isomerizes to yield CO.....	157
4-S3	Ratio of steady state of CO formation in H <sub>2</sub> O and D <sub>2</sub> O during CO <sub>2</sub> reduction by $\alpha$ -70 <sup>Ala</sup> / $\alpha$ -195 <sup>Gln</sup> MoFe protein.....	158
4-S4	Test of solvent isotope effect for the rate of CO binding and change of molar extinction coefficient of CO-Hb complex.....	159
4-S5	Showing CH <sub>4</sub> formation during formic hydrazide turnover using $\alpha$ -70 <sup>Ala</sup> / $\alpha$ -195 <sup>Gln</sup> MoFe protein .....	160
4-S6	Catalytic reduction of formic hydrazide (HCONHNH <sub>2</sub> ) to CH <sub>4</sub> by $\alpha$ -70 <sup>Ala</sup> / $\alpha$ -195 <sup>Gln</sup> MoFe protein .....	161
4-S7	Concentration dependence formic hydrazide reduction to CH <sub>4</sub> by $\alpha$ -70 <sup>Ala</sup> / $\alpha$ -195 <sup>Gln</sup> MoFe protein.....	162
4-S8	Formation of CO during formic hydrazide turnover with $\alpha$ -70 <sup>Ala</sup> / $\alpha$ -195 <sup>Gln</sup> MoFe protein.....	163
5-1	Crystal structure of FeMo-co .....	166
5-2	Schematic of <i>re/oa</i> Equilibrium.....	168
5-3	Schematic of alternative limiting mechanisms for <i>re/oa</i> equilibrium .....	170
5-4	X-band EPR spectra of MoFe protein ( $\alpha$ -70 <sup>Ile</sup> ) freeze-trapped during Ar turnover in H <sub>2</sub> O before ( <i>black</i> ) and during irradiation with 450 nm diode laser at 12 K ( <i>blue</i> (2.5 min) and <i>red</i> (20 min) traces); <i>Red</i> arrows highlight the conversion of E <sub>4</sub> (4H) to the photoinduced <i>S</i> state .....	175
5-5	Q-band stochastic <sup>1</sup> H CW ENDOR spectra showing loss of signals from hydrides, H1 and H2, through photolysis. ( <i>Black</i> )	

	Before and ( <i>red</i> ) after 450 nm photolysis of MoFe protein ( $\alpha$ -70 <sup>lle</sup> / $\alpha$ -195 <sup>Gln</sup> ) trapped during Ar turnover in H <sub>2</sub> O buffer.....	176
5-6	Alternative mechanisms for the E <sub>4</sub> (4H) $\Rightarrow$ S photo-conversion through loss of both hydrides and release of H <sub>2</sub> and thermal reverse.....	178
5-7	Decay during 193 K annealing of E <sub>4</sub> (2H)* photoinduced in MoFe ( $\alpha$ -70 <sup>lle</sup> ) freeze-trapped during turnover in H <sub>2</sub> O (red) and D <sub>2</sub> O (blue), along with the parallel recoveries of E <sub>4</sub> (4H) .....	180
5-8	Time course of <i>in situ</i> 450 nm photoinduced conversion of E <sub>4</sub> (4H) intermediate trapped during MoFe protein ( $\alpha$ -70 <sup>lle</sup> ) turnover in H <sub>2</sub> O (lower) and D <sub>2</sub> O (upper) .....	182
5-9	Idealized energy surfaces for photoinduced <i>re/oa</i> of the Janus intermediate, E <sub>4</sub> (4H) .....	184
5-10	Cartoon showing nodal properties of an excited MO for an M(H) <sub>2</sub> complex that is bonding between the two hydrides and antibonding between each one and the metal dz <sup>2</sup> orbital .....	185
5-11	Cartoon showing nodal properties of the excited MO's for bridging hydrides (parallel arrangement), each antibonding between the hydride and the two dz <sup>2</sup> orbitals on the Fe ions it bridges .....	186
5-S1	Temperature dependence of X-band EPR spectra of irradiated MoFe protein ( $\alpha$ -70 <sup>lle</sup> ) trapped during Ar turnover in H <sub>2</sub> O buffer.....	195
5-S2	Photoinduced changes in Q-band CW EPR (upper) and <sup>1</sup> H field- modulated Q-band CW ENDOR (lower) spectra of MoFe protein ( $\alpha$ -70 <sup>lle</sup> ) trapped during Ar turnover in H <sub>2</sub> O buffer .....	196
6-1	Simplified Lowe-Thorneley (LT) kinetic scheme for nitrogen reduction that focus on the electron-accumulation and FeMo-co activation (boxed) stages.....	201
6-2	Crystal structure of FeMo-co .....	202
6-3	Schematic of <i>re/oa</i> Equilibrium.....	204
6-4	X-band EPR spectra of WT nitrogenase turnover samples trapped under different conditions .....	210

6-5	EPR and ENDOR spectrum for WT and $\alpha$ -70 <sup>Val→Ile</sup> MoFe protein under Ar turnover.....	211
6-6	Photoinduced changes in EPR spectra of WT and $\alpha$ -70 <sup>Val→Ile</sup> freeze-trapped during enzymatic turnover in H <sub>2</sub> O during 24.5 minutes of 450 nm diode laser irradiation at 12 K.....	215
6-7	Kinetic isotope effect on photolysis of E <sub>4</sub> (4H) state in WT MoFe protein .....	217
6-8	Showing kinetic reversibility of the <i>re/oa</i> mechanism in Wild (WT) MoFe protein .....	218
6-9	Timecourses of four EPR detected states during -50 °C cryoannealing of WT low P(N <sub>2</sub> ) ~ 0.05 atm turnover in H <sub>2</sub> O .....	224
7-1	Cyclic voltammetry (CV) for WT MoFe protein.....	234
7-2	Proton Inventory for WT (Red), $\beta$ -98 <sup>His</sup> (Magenta), $\alpha$ -70 <sup>Ile</sup> (Green), $\alpha$ -70 <sup>Ala</sup> / $\alpha$ -195 <sup>Gln</sup> (Blue) MoFe protein and <i>nifX</i> -FeMo-co (Black) .....	235
7-3	Inhibition of CO <sub>2</sub> reduction to HCOO <sup>-</sup> in presence of CO .....	239
7-4	Showing electron distribution during CO <sub>2</sub> reduction by different variants of MoFe protein.....	240

## ABBREVIATIONS

ADP	Adenosine diphosphate
AMPPCP	$\beta\gamma$ -methylene Adenosine Triphosphate
ATP	Adenosine Triphosphate
Apo-MoFe protein	FeMo-cofactor deficient MoFe protein
Cobaltocene	Bis(cyclopentadienyl) cobalt (II)
CO <sub>2</sub>	Carbon dioxide
CO	Carbon monoxide
DTPA	Diethylene triamine pentaacetic acid
EDTA	Ethylenediaminetetraacetic acid
EGTA	Ethylene glycol tetraacetic acid
E <sub>m</sub>	Midpoint potential
E <sub>n</sub>	MoFe protein reduced by n electrons (n=1-8)
ENDOR	Electron nuclear double resonance
EPR	Electron paramagnetic resonance
ET	Electron transfer
F cluster	[4Fe-4S] cluster of the iron protein
Fe Protein	Iron protein
FeMo-cofactor	Iron-molybdenum cofactor
H <sub>2</sub>	Hydrogen
Hb	Hemoglobin
HCOO <sup>-</sup>	Formate

HEPES	4-[2-hydroxyethyl]-1-piperazineethanesulfonic acid
IR	Infrared
$K_m$	Michaelis constant
$k_{Pi}$	Rate of phosphate release
$k_{ET}$	Rate of electron transfer
$k_{Diss}$	Rate of dissociation
$k_{ATP}$	Rate of ATP hydrolysis
M cluster	Iron-molybdenum cofactor (FeMo-cofactor)
$M^N$	FeMo-cofactor in the dithionite reduced state
MOPS	3-(N-morpholino) propanesulfonic acid
MoFe protein	Molybdenum iron protein
$M^{OX}$	Oxidized FeMo-cofactor
$M^R$	FeMo-cofactor reduced beyond $M^N$
$N_2$	Dinitrogen
NHE	Normal hydrogen electrode
NMR	Nuclear magnetic resonance
NRVS	Nuclear resonance vibrational spectroscopy
P cluster	[8Fe-8S] cluster of MoFe protein
$P^{1+}$	P cluster in the one electron oxidized state
$P^{2+}$	P cluster in the two electron oxidized state
$P^{3+}$	P cluster in the three electron oxidized state
Pi	Inorganic phosphate

$P^N$	P cluster in the dithionite reduced state
$P^{ox}$	Oxidized P cluster
SDS-PAGE	Sodium dodecyl sulfate polyacrylamide gel electrophoresis
SCE	Saturated calomel electrode
sKIE	Secondary kinetic isotope effect
sIIE	Solvent inverse isotope effect
SF	Stopped-flow
UV-Vis	Ultra violet-visible

## CHAPTER 1

### INTRODUCTION

#### **Nitrogen Fixation**

Nitrogen (N) is one of the fundamental elements of life and ranks behind carbon, hydrogen, and oxygen in its contribution to the total mass of living organisms. Most of the nitrogen in a living system is bound up in amino acids and nucleotides while a small portion is used in the synthesis of small crucial molecules such as adenosine triphosphate (ATP), dopamine, and others. In addition, nitrogen is also an important element for industrial products like fertilizers (urea, nitrate, nitrites, etc.), and drugs (morphine, quinolones etc.).<sup>1</sup>

Dinitrogen (N<sub>2</sub>) is the major constituent (79%) of the earth's atmosphere and represents the largest global pool of nitrogen. However, only the reduced form of dinitrogen is bioavailable and usable for various life processes. This is largely a consequence of the high bond dissociation energy associated with the breaking of the N-N triple bond of N<sub>2</sub> (~ 941 kJ/mole).<sup>2</sup> Three different ways are known that converts N<sub>2</sub> to NH<sub>3</sub>, a process known as nitrogen fixation and requires a significant input of energy. Approximately 1% of the total fixed nitrogen ( $3 \times 10^{11}$  gallons / annum) comes from the lightning strikes in the atmosphere.<sup>3</sup> An other 49 % of the total fixed nitrogen is produced through an industrial process known as Haber-Bosh process.<sup>4</sup> In this process, N<sub>2</sub> is reacted with H<sub>2</sub> at very high temperatures (~ 450 °C) and pressures (> 200 atm) in the presence of an iron catalyst. The extreme energy demand in this process is responsible for nearly 3% of the total fossil fuel used globally.<sup>5-8</sup> The remaining 50 % of total nitrogen



fixed each year comes through a biological process occurring in specific type of microorganisms called diazotrophs.<sup>9,10</sup> Diazotrophs include certain families of bacteria and archaea that encode the genes (*Nif*, *Vnf*, or *Anf*) required for the synthesis of an active but O<sub>2</sub> sensitive metalloenzyme called nitrogenase that reduces N<sub>2</sub> to NH<sub>3</sub> at ambient temperature and pressure. In biogeochemical nitrogen (N) cycle, ammonia is the most reduced form of nitrogen and it enters to the N cycle as a source of electron. Thus, by catalyzing the most difficult reaction of N cycle, nitrogenase plays a key role in maintaining the homeostasis in biogeochemical N cycle (**Figure 1-1**).<sup>11</sup>

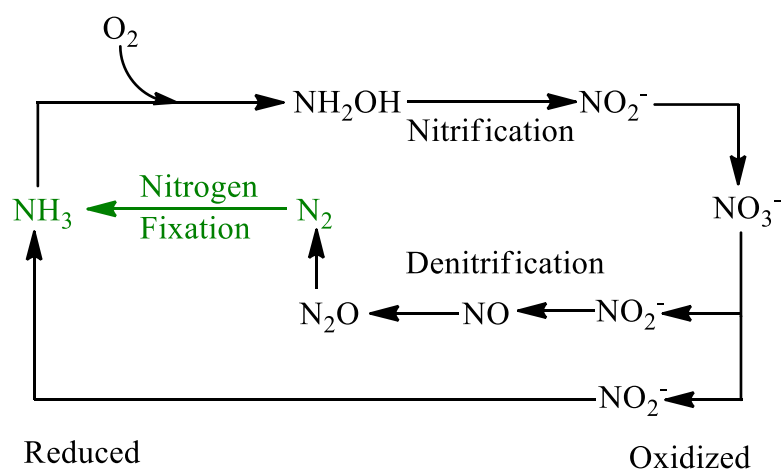


**Figure 1-1: Bio-geochemical nitrogen cycle.** Green highlight represents nitrogen fixation by nitrogenase.

Three major classes of nitrogenase have been reported a) Molybdenum-Iron (MoFe) nitrogenase, b) Vanadium-Iron (VFe) nitrogenase and c) Iron-Iron (FeFe) nitrogenase.<sup>12</sup> These nitrogenase differ in the identity of the hetero-metal contained in the metal cluster of their active site. The MoFe nitrogenase is widely distributed, most active toward N<sub>2</sub> reduction, and well-studied nitrogenase.<sup>13</sup> This dissertation focuses on further

understanding the mechanism of substrate reduction by MoFe nitrogenase isolated from *Azotobacter vinlandii*.

### Mo-dependent Nitrogenase

Mo-dependent nitrogenase contains two different components, the iron (Fe) protein (or dinitrogenase reductase) and the molybdenum-iron (MoFe) protein (or dinitrogenase) (**Figure 1-2**). Fe protein is the physiological reductant for the MoFe protein. It delivers the electrons to the active site of MoFe protein where the reduction of  $N_2$  occurs with following stoichiometry (**eqn. 1-1**).<sup>14,15</sup>

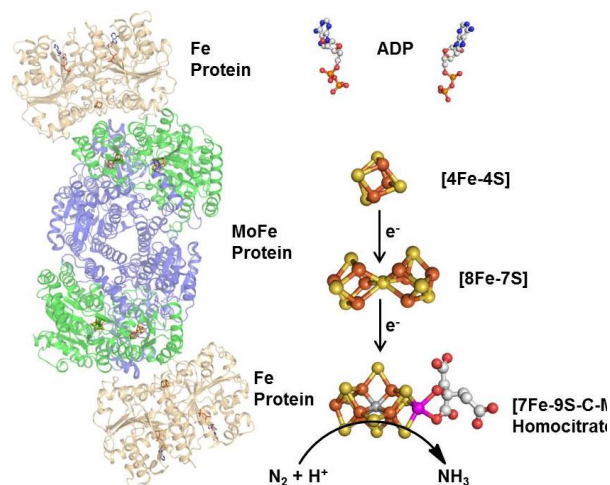
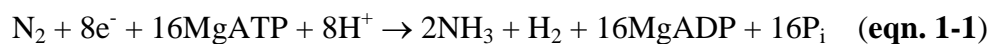
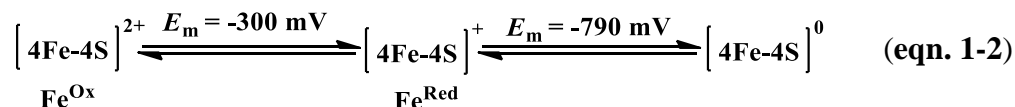


**Figure 1-2: Molybdenum dependent nitrogenase.** Shown is the structure of nitrogenase MoFe protein (blue and green) and Fe protein (light brown). The MoFe protein is  $\alpha_2\beta_2$  tetramer and each  $\alpha$   $\beta$  unit has a P cluster [8Fe-7S] in between  $\alpha$  and  $\beta$  subunits and a FeMo-cofactor [7Fe-9S-1C-Mo-Homocitrate] solely embedded within  $\alpha$  subunit of MoFe protein. The Fe protein is a dimeric protein with one [4Fe-4S] redox center. Shown on right are the metal clusters and ADP, with Fe in rust, S in yellow, C in gray, O in red, N in blue, and Mo in magenta. Coordinates from PDB 2AFI.

## Iron Protein

The iron (Fe) protein, encoded by the *nifH* gene, is a homodimer with a molecular mass of approximately 64 kDa. Each monomer has one nucleotide (MgATP or MgADP) binding sites. A single [4Fe-4S] cluster is covalently linked with cysteine from each of the two monomers. Thus, [4Fe-4S] cluster provides a structural support and also plays redox active role in electron transfer.<sup>16</sup> The [4Fe-4S] cluster of nucleotide unbound Fe protein is known to exist in three redox states at pH=7.0 (eqn. 1-2).<sup>14,17</sup>



Binding of MgATP or MgADP to Fe protein lowers the mid-point redox potential ( $E_m$  vs. NHE) values for  $[4\text{Fe-4S}]^{2+/1+}$  redox couple from -300 mV to -430 mV or -420 mV respectively.<sup>18</sup> This shift of approximately -120 mV is achieved by translating the nucleotide binding energy to the chemical potential through conformational changes in the Fe protein which is revealed in small angle X-ray scattering (SAXS) and X-ray crystallography.<sup>16,19</sup> Isolation, purification and *in-vitro* assay are usually performed in the presence of the non-physiological reductant, dithionite ( $\text{S}_2\text{O}_4^{2-}$ ), that has  $E_m$  of about -660 mV at neutral pH.<sup>20</sup> Hence, under dithionite reduced condition, only  $[4\text{Fe-4S}]^{2+/1+}$  couple is thermodynamically favorable to achieve and is likely the functioning redox couple for both *in-vitro* and *in-vivo* nitrogenase catalysis.

The electronic properties of [4Fe-4S] cluster of Fe protein is modulated by pH, conformational change and most influentially by the redox state. The oxidized  $[4\text{Fe-4S}]^{2+}$

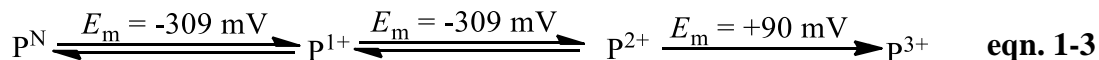
cluster is diamagnetic in nature and do not show any signal in electron paramagnetic resonance (EPR) spectroscopy, therefore deemed as EPR silent.  $[4\text{Fe-4S}]^+$  state is paramagnetic and exhibits mixed spin ( $S$ ) state with  $S = 1/2$  and  $S = 3/2$ . This results in EPR spectrum in two different  $g$  regions. The EPR spectrum at  $g = 2$  region corresponds to  $S = 1/2$  and is rhombic in line shape with  $g$  values of 2.04, 1.94 and 1.84 while at  $g \sim 5$  the EPR signal is a broad inflection due to spin state of  $S = 3/2$ .<sup>21</sup>  $[4\text{Fe-4S}]^0$  state is achieved only in presence of strong reductant like Eu (II)-DTPA or titanium (III) citrate.<sup>22</sup> It is paramagnetic in nature with  $S = 4$  and shows an inflection at  $g = 16.4$  in parallel mode EPR.

### **MoFe Protein**

The two catalytic halves containing MoFe protein is a  $\alpha_2\beta_2$  heterotetramer ( $M_r \sim 240\text{kDa}$ ) with the  $\alpha$  and  $\beta$  subunits encoded by the *nifD* and *nifK* genes, respectively. Each catalytic half comprises of one  $\alpha$  and one  $\beta$  subunit and contains two distinct metalloclusters: a P-cluster ( $[8\text{Fe-7S}]$ ) and a FeMo-cofactor ( $[7\text{Fe-9S-Mo-1C-(R-homocitrate)]$ ; Figure 1-3). P-cluster resides at the interface between the  $\alpha$  and  $\beta$  subunits while the FeMo-cofactor is embedded in the peptide matrix of  $\alpha$ -subunit.<sup>15,23</sup>

Structurally, the P-cluster can be considered as two cubic  $[4\text{Fe-4S}]$  clusters sharing a common sulfide ligand at one vertex. The thiol functional group (-SH) of cysteine residues of the  $\alpha$  and  $\beta$  subunit covalently coordinate with Fe atoms of P cluster and thus hold the cluster at the interface. The physiological role of the P cluster is to mediate the electron transfer between  $[4\text{Fe-4S}]$  cluster of Fe protein to FeMo-cofactor.

The redox behaviors of the P cluster has been studied using various oxidants. The dithionite reduced state, also known as resting state P cluster ( $P^N$ ), can be oxidized sequentially to  $P^{1+}$ ,  $P^{2+}$  redox couple and irreversibly to  $P^{3+}$  states (**eqn. 1-3**).<sup>24-26</sup>



Using mediated redox titration, the  $E_m$  for  $P^{N/+1}$  and  $P^{+1/+2}$  redox couple at pH = 7.0 was estimated to be -309 mV vs. NHE. The oxidation of  $P^{2+}$  to  $P^{3+}$  occurs at +90 mV but unlike  $P^{N/+1}$  and  $P^{+1/+2}$  redox couple this process is irreversible.<sup>27-29</sup> In presence of dithionite as reductant, P cluster is reduced from  $P^{2+}$  to  $P^{3+}$  to  $P^N$  state. There is no evidence of reduction of P cluster beyond  $P^N$  even in presence of solvated electrons that has redox potential < -2.87 V vs. NHE.<sup>30,31</sup> This has led researchers to suggest the model, known as “deficient spending model”, to explain the mechanism of electron transfer from Fe protein to MoFe protein.<sup>30,32</sup> According to this model, the electron is first transferred from P cluster to FeMo-cofactor that creates an electronic deficiency at the P cluster which is then backfilled by the electron transfer from the reduced Fe protein. Like the dithionite reduced [4Fe-4S] cluster of Fe protein,  $P^N$  state is also diamagnetic and therefore EPR silent.  $P^{1+}$  state is paramagnetic with the spin of  $S = 1/2$  and  $5/2$  and shows EPR spectrum at  $g = 2.06, 1.95, \text{ and } 1.82$  and  $g = 6.67$  and  $5.3$ .  $P^{2+}$  state has a non-Kramer integer spin ( $S \geq 3$ ) and therefore observable only in parallel mode EPR at  $g = 11.8$ .  $P^{3+}$  state also exist in two spin state ( $S = 1/2$  and  $7/2$ ) and shows an EPR spectrum at  $g = 10.4, 7.4$  and  $g = 2$  respectively.<sup>26</sup>

The FeMo-cofactor, also called the M-cluster, is the active site of nitrogenase where substrate binding and reduction take place. An early X-ray structure revealed FeMo-cofactor as a hetero-metallocluster [7Fe-9S-Mo-X-(*R*)-homocitrate] with the interstitial X atom being unassigned.<sup>15</sup> Recently, through a 1.0 Å-resolution X-ray structure, ESEEM spectroscopy, X-ray emission spectroscopy (XES), and biochemical analysis using <sup>14</sup>C labelled *S*-adenosyl methionine (SAM), X atom is conclusively established as a carbon atom with the oxidation state of -4 (C<sup>4-</sup>; carbide).<sup>33-35</sup> The FeMo-cofactor is ligated to the peptide matrix through two covalent linkage between cysteine ( $\alpha$ -275<sup>Cys</sup>) and histidine ( $\alpha$ -442<sup>His</sup>) to Fe and Mo atom respectively.<sup>15</sup>

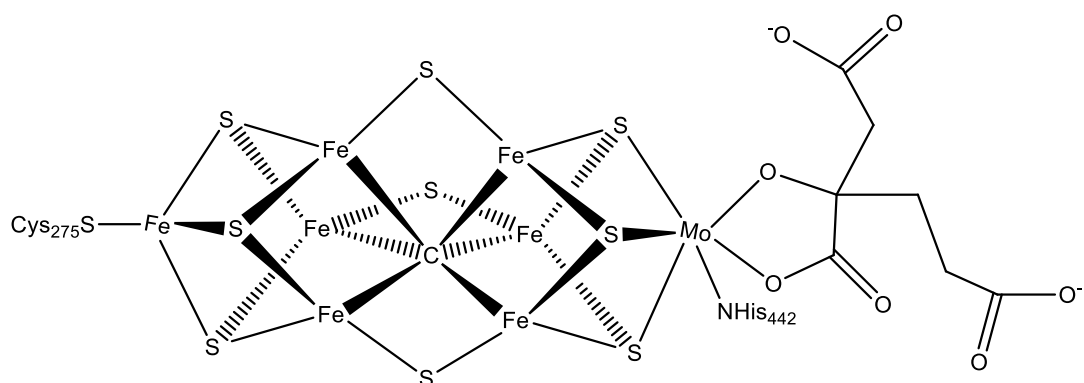


**Figure 1-3: FeMo-cofactor of nitrogenase.** Showing three dimensional orientations of atoms in FeMo-cofactor with associated  $\alpha$ -275<sup>Cys</sup>,  $\alpha$ -442<sup>His</sup>, and *R*-homocitrate as ligand.

The resting state of FeMo-cofactor ( $M^N$ ), defined as FeMo-cofactor in dithionite reduced state, is paramagnetic with  $S = 3/2$  spin and shows a rhombic EPR signal at  $g = 2$ , 3.64, and 4.32.<sup>36</sup> The Mössbauer study of the  $M^N$  suggest that the atoms on the FeMo-cofactor have an oxidation state of  $Mo^{4+}$ ,  $3Fe^{3+}$ ,  $4Fe^{2+}$ , and  $9S^{2-}$ .<sup>37</sup> A reversible one electron oxidation of  $M^N$  to the diamagnetic  $M^{Ox}$  state ( $S = 0$ ) is achieved by redox

titrating with oxidants and  $E_m$  for the  $M^{Ox/N}$  redox couple was previously reported to be about -40 mV.<sup>21,25,38</sup> Similarly,  $M^N$  is one electron reduced to an EPR silent ( $S \geq 1$ )  $M^R$  state by using either Fe protein as a reductant or through solvated electrons generated at cryo-temperature when exposed to  $\gamma$ -radiation.<sup>30,39</sup> During catalytic turnover, FeMo-cofactor can exist in multiple electronic states depending on the number of electrons/protons added but the oxidation state of FeMo-cofactor recycles only through one redox couple.<sup>40</sup>

### **Mechanism of electron transfer**

ATP bound reduced Fe protein docks on the MoFe protein on the surface just above the P cluster.<sup>15,23</sup> The binding energy due to the association of Fe protein to the MoFe protein induces conformation change on the MoFe protein that triggers the electron transfer. Biophysical studies suggest that a change in surface area of about 800 Å occurs during the primary electron transfer event.<sup>41</sup> Thus, electron transfer is gated by conformational change. The opening of the gate allows the intramolecular electron transfer from P cluster to FeMo-cofactor at the estimated rate of  $\sim 160 \text{ s}^{-1}$ . Only one electron is transferred from P cluster causing the oxidation of it by one electron. The deficiency of an electron on P cluster is back filled through the electron transfer from docked reduced Fe protein at the rate constant of  $\sim 1600 \text{ s}^{-1}$ .<sup>32</sup> This mechanism of electron transfer is named as “deficient spending”. The oxidation of Fe protein triggers the hydrolysis of two bound ATP and releases two molecules of phosphate in a rate ( $\sim 6 \text{ s}^{-1}$ ) that controls the overall catalysis.<sup>42</sup> Subsequently, Fe protein dissociates from MoFe protein through a series of conformation changes that involves the rolling of Fe protein

over the 2000 Å surface area of MoFe protein.<sup>43</sup> The dissociated oxidized Fe protein accepts an electron from the reductant and exchange 2 ADP for 2 ATP. The refurbished reduced Fe protein with bound 2 ATP is then ready for the second cycle of electron transfer. Recent findings demonstrate that even though the two Fe protein binding sites on the MoFe protein are completely occupied, only one of the Fe proteins is catalytically active to transfer the electron at a given time.<sup>44</sup>

### **Mechanism of substrate reduction on FeMo-cofactor**

Nitrogenase catalyzes multi electron/proton reduction of various unsaturated substrates. The first glimpse into the mechanism of substrate reduction was revealed when the freeze quench argon (Ar) turnover samples trapped an EPR active species ( $S = 1/2$ ) during the reduction of proton to  $H_2$ .<sup>45</sup> This  $S = 1/2$  Ar turnover signal was trapped both in wild type (WT) and  $\alpha$ -70<sup>lle</sup> MoFe protein however the signal intensity was significantly larger in the latter and hence was used for further analysis (**Figure 1-4**). <sup>1,2</sup>H Electron Nuclear Double Resonance (ENDOR) measurement on this trapped intermediate disclosed two solvent nonexchangeable “H” atoms having a strong hyperfine coupling  $A_{iso} \approx 23$  MHz which strongly suggest they are bound to the FeMo-cofactor. Analysis of the two dimension field-frequency <sup>1</sup>H ENDOR plots for both H gave a similar principal value indicating that both H have identical chemical environment. Based on these evidences, the two H were assigned as two bridging hydrides bound to the FeMo-cofactor. Also for charge balance, the two solvent exchangeable protons were assumed to protonate two sulfurs of the FeMo-cofactor.<sup>45</sup> Each hydride is formed by accumulation of 2 electrons and protons; therefore, the trapped state with two bridging hydrides must have



accumulated 4 electrons and protons and hence designated as  $E_4(4H)$  state in Lowe-Thorneley kinetic scheme for nitrogenase catalysis (**Figure 1-5**).

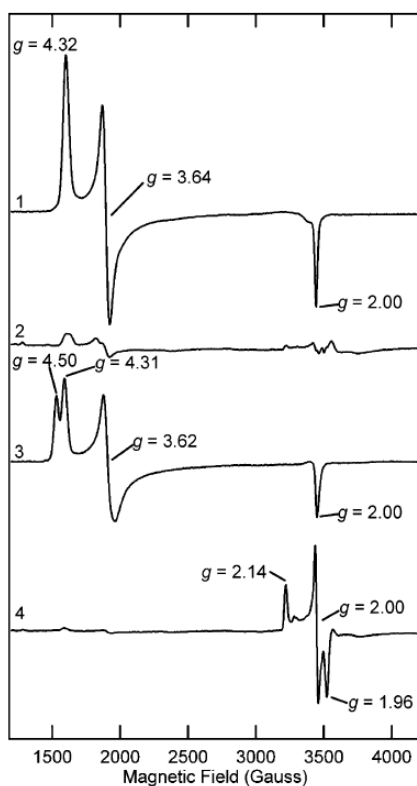


**Figure 1-4: EPR spectra of wild-type (WT) and  $\alpha$ -70<sup>Ile</sup> MoFe proteins in the resting and turnover states.** Resting state EPR spectra are shown for the wild-type (trace 1) and  $\alpha$ -70<sup>Ile</sup> (trace 3) MoFe proteins. Both have FeMo-co at  $S = 3/2$  spin in the resting state but an inflection at  $g = 4.3$  is observed in  $\alpha$ -70<sup>Ile</sup> variant. Turnover trapped states during  $H_2$  evolution for the wild-type (trace 2) and  $\alpha$ -70<sup>Ile</sup> (trace 4) MoFe proteins are also shown. A strong signal at  $g = 2$  ( $S = 1/2$ ) is trapped in  $\alpha$ -70<sup>Ile</sup> MoFe protein.<sup>45</sup>

<sup>95</sup>Mo ENDOR on the trapped  $E_4(4H)$  in <sup>95</sup>Mo enriched  $\alpha$ -70<sup>Ile</sup> MoFe protein demonstrate that the two bridging hydride are associated not with molybdenum atom but only with four Fe atoms.<sup>46</sup> <sup>57</sup>Fe ENDOR obtained on  $E_4(4H)$  state showed that the redox states of FeMo-cofactor at  $E_4(4H)$  and  $E_0$  are identical; which means that the electron

density is concentrated in iron hydride (Fe-H) bond rather than on metal center.<sup>40</sup> The further evidence of dihydride intermediate in  $E_4(4H)$  came through EPR/cryoannealing experiment in the frozen state at  $-20\text{ }^\circ\text{C}$  which prevents further delivery of electrons from Fe protein but allows the relaxation of reactive intermediates by forming stable products. In the cryoannealing experiment,  $E_4(4H)$  relaxed to  $E_0$  with the release of two successive dihydrogen molecules ( $H_2$ ) and both steps showed a strong kinetic isotope effect (KIE,  $k_H/k_D$ ) of 3-4.<sup>47</sup> Formation of two molecules of dihydrogen is consistent with  $E_4(4H)$

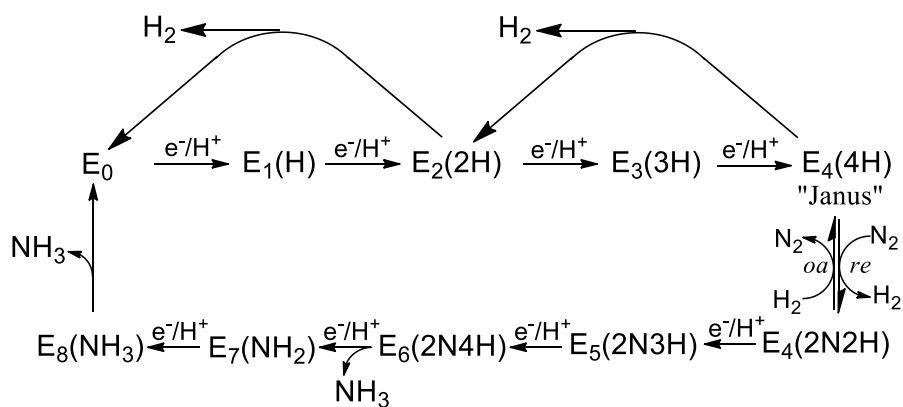


**Figure 1-5: Simplified Lowe-Thorneley (LT) kinetic scheme for nitrogen fixation.** In the  $E_n$  notation,  $n$  = number of  $[e^-/H^+]$  added to FeMo-co; parenthesis denotes the stoichiometry of H/N bound to FeMo-cofactor. Also, shown is the relaxation of  $E_4(4H)$  to  $E_2(2H)$  and  $E_2(2H)$  to  $E_0$  through the release of  $H_2$  by hydride protonation mechanism.

being 4 electrons and protons accumulated state while a strong KIE on both steps confirms 4 electrons and protons on  $E_4(4H)$  are stored as iron hydride bond. Although a significant amount of information is reported on  $E_4(4H)$  but no information on how electrons and protons are delivered to FeMo-cofactor has been reported in the literature. In chapter 2 of this dissertation, the fundamental understanding of the delivery of

electrons and protons to FeMo-cofactor is presented. Theoretically, the electron-proton transfer can occur by three different mechanisms (i) electron transfer followed by proton transfer, (ii) proton transfer followed by electron transfer, and (iii) concerted proton coupled electron transfer (**Figure 1-6**).

As detailed in chapter 2, we demonstrate that the transfer of each electron to FeMo-cofactor is associated with concerted proton transfer. As a consequence, addition

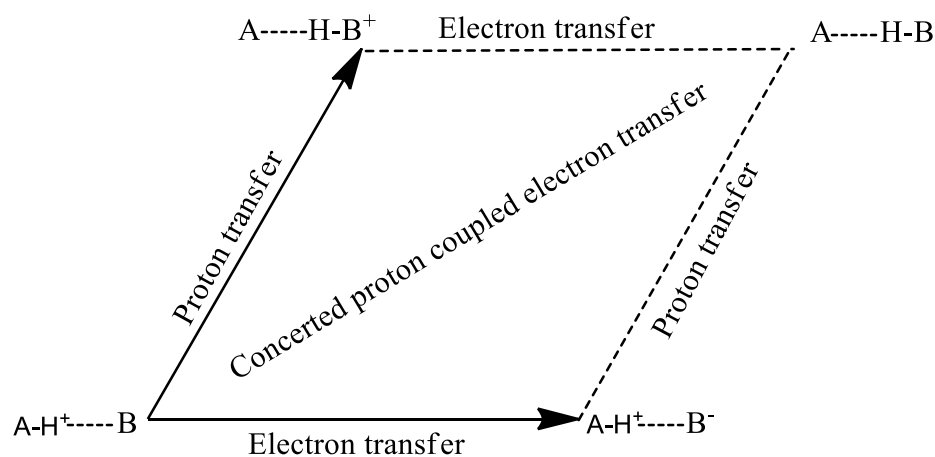


**Figure 1-6: Schematic representation of proton coupled electron transfer (PCET).** Shown are the three possible pathways for the transfer of electron/proton from A (donor) to B (acceptor).

of an electron to the resting state of FeMo-cofactor ( $E_0$ ) is accompanied by a rapid concerted proton transfer to form 1 electron reduced  $E_1(1H)$  state. A previous study using cryoannealing protocol has established that there is no hydride in  $E_1(1H)$  state and therefore the electron must be stored as reduced metal.<sup>39</sup>

As demonstrated in chapter 2, the addition of second electron to  $E_1(1H)$  promptly protonates the Fe center of the FeMo-cofactor to make iron hydride (Fe-H) even at 77 K.

Hence, at  $E_1(1H)$  state reduced Fe atom of FeMo-cofactor can act as nucleophile to catalyze the reduction chemistry through proton coupled electron transfer (PCET) mechanism while at  $E_2(2H)$  state hydride act as nucleophile and catalyze the reduction through hydride transfer (HT) mechanism. This unique ability of nitrogenase to catalyze either PCET or HT allows it to overcome the kinetic and thermodynamic barrier associated with multi electron and proton reduction of various unsaturated molecules. One of such alternative substrates is carbon dioxide ( $CO_2$ ).<sup>48</sup>  $CO_2$  is a greenhouse gas and there is a considerable interest in understanding the fundamental mechanism of transforming  $CO_2$  to value added products.<sup>49</sup> Early studies have established that WT MoFe reduces  $CO_2$  to CO and  $\alpha$ -70<sup>Ala</sup>/ $\alpha$ -195<sup>Gln</sup> MoFe protein further reduce  $CO_2$  by 6 more electrons and protons to yield  $CH_4$  as final product.<sup>48,50</sup> The molecular details on activation of  $CO_2$ , which usually involves a huge kinetic and thermodynamic barrier, have not been explored for nitrogenase. In chapter 3, experimental evidences coupled with quantum mechanical calculation are presented to elucidate the molecular mechanism of  $CO_2$  reduction by nitrogenase. We demonstrate that formate ( $HCOO^-$ ) is the major product of  $CO_2$  reduction by nitrogenase and the quantum mechanical calculations suggest that a direct hydride transfer from Fe-H bond to C atom of  $CO_2$  is the most favorable pathway for the formation of formate. In addition, an unfavorable associative pathway where  $CO_2$  binds to FeMo-cofactor through C atom followed by the deprotonation of metal hydride is proposed as the possible pathway for CO/ $CH_4$  formation. Finally, the alteration of product profile ( $HCOO^-$  vs. CO/ $CH_4$ ) is shown to be the function of substitution of amino acids around the FeMo-cofactor. Further evidences

to support the proposed mechanism for CO<sub>2</sub> reduction to CH<sub>4</sub> and the C-C bond formation are presented in chapter 4. In this study, we show that CO<sub>2</sub> reduction follows CO pathway and the thermodynamic barrier associated with the reversibility of CO and formyl (-CHO) likely governs the feasibility of CO<sub>2</sub> reduction to CH<sub>4</sub> by various MoFe proteins. Similarly, as observed for “N” containing substrates, a convergence of different reduction pathways for C substrate is also demonstrated.

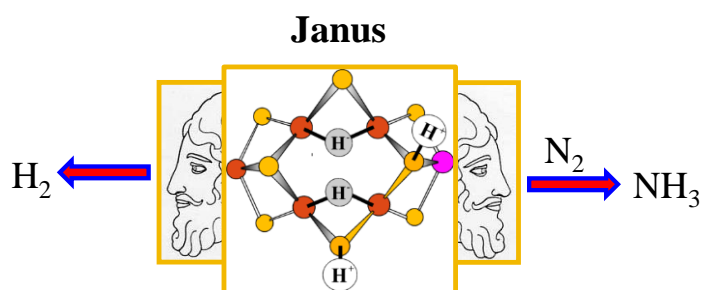


**Figure 1-7: Showing the two fates of Janus state.** It can relax back to resting state by releasing two H<sub>2</sub> or commit for N<sub>2</sub> reduction.

The trapping and spectroscopic characterization of E<sub>4</sub>(4H) intermediate was a fundamental breakthrough in advancing our understanding of nitrogenase catalysis especially N<sub>2</sub> reduction to NH<sub>3</sub>. Early kinetics studies have shown that the binding and reduction of N<sub>2</sub> occurs at E<sub>4</sub>(4H) state. E<sub>4</sub>(4H) state, therefore, sits in the transition in the N<sub>2</sub> reduction pathway that is equally posed either relax back to E<sub>0</sub> by releasing two molecule of H<sub>2</sub> or binds N<sub>2</sub> and commits it toward reduction pathway for NH<sub>3</sub> formation. Hence, E<sub>4</sub>(4H) state is denoted as “Janus”, referring to the Roman God of transition having two faces, one looking to the past and other looking to the future (**Figure 1-7**).<sup>51</sup>

Several intriguing kinetic data on N<sub>2</sub> reduction exists in the literature. First, an obligatory release of one molecule of H<sub>2</sub> per molecule of N<sub>2</sub> reduced is observed.<sup>14</sup> This

leads to the stoichiometry for the reduction of N<sub>2</sub> by nitrogenase as shown in **eqn 1-1**. Nitrogenase requires 8 electrons and protons rather than 6 electrons and protons needed for chemical reduction of N<sub>2</sub> to NH<sub>3</sub>. The stoichiometry holds true even when the turnover is carried under 50 atmospheric pressure of N<sub>2</sub>.<sup>52</sup> Second, H<sub>2</sub> inhibits N<sub>2</sub> reduction in a competitive fashion.<sup>53</sup> Third, substituting H<sub>2</sub> by D<sub>2</sub> furnished HD as product with the stoichiometry of 1 electron used per HD formed.<sup>54</sup> Fourth, when T<sub>2</sub> is used as inhibitor for N<sub>2</sub> reduction, HT is formed in the gas phase. However, no T<sup>+</sup> was observed in H<sub>2</sub>O solvent phase.<sup>55</sup> Fifth, H<sub>2</sub>, D<sub>2</sub> or T<sub>2</sub> only reacts with the diazene level reduced intermediate.<sup>56</sup> All these observation allowed researchers to formulate mechanistic constrain for nitrogenase catalysis as represented below:

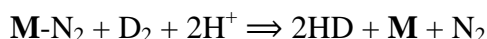
***Key Constraints on Nitrogenase Mechanism***

(i) *State when N<sub>2</sub> is Reduced:*

N<sub>2</sub> is reduced at the E<sub>4</sub>(4H) state

(ii) *D<sub>2</sub> or T<sub>2</sub> only react during N<sub>2</sub> Turnover, during which:*

(a) *2HD form stoichiometrically:*



(b) *Reduction Level of this reaction:*

D<sub>2</sub>/T<sub>2</sub> reacts at E<sub>4</sub>(2N2H) level

(c) *No Scrambling with solvent:*

‘No’ T<sup>+</sup> released to solvent under T<sub>2</sub>

Recently, reductive elimination/oxidative addition (*re/oa*) mechanism is proposed for N<sub>2</sub> reduction that satisfies all the mechanistic constrains.<sup>51,57</sup> The fundamental basis of

*re/oa* lies on the fact that the reducing equivalent in  $E_4(4H)$  state are stored as two bridging hydrides. According to *re/oa* mechanism, the binding of  $N_2$  to  $E_4(4H)$  triggers the release of two dihydride as  $H_2$  causing reduction of FeMo-cofactor by 2 electrons and hence the process being designated as *re*. The 2 electrons reduced FeMo-cofactor promptly transfer 2 electrons back to  $\pi^*$  orbital of  $N_2$ . Accumulation of electron density on  $\pi^*$  orbital of  $N_2$  allows the transfer of proton from the adjacent protonated sulfide ( $-SH^+$ ) of FeMo-cofactor that ultimately hydrogenate  $N_2$  to diazene level intermediate,  $E_4(2N_2H)$  (**Figure 1-8**). In the latter process, FeMo-cofactor is oxidized and hence the process called *oa*. *re/oa* mechanism thus accounts for the obligatory release of one molecule of dihydrogen per molecule of dinitrogen reduced and explains the need of 8 rather than 6 electrons and protons for reduction of  $N_2$ .

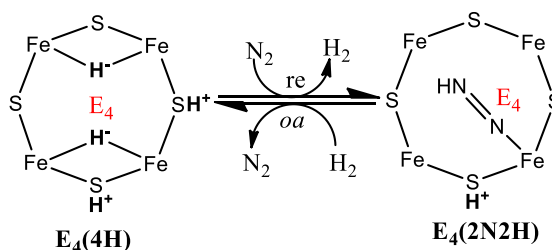


**Figure 1-8: Schematic of *re/oa* equilibrium.** The cartoon represents the Fe 2,3,6,7 face of FeMo-co, and the ‘2N2H’ implies a species at the diazene reduction level of unknown structure and coordination geometry. In the indicated equilibrium the binding and activation of  $N_2$  is mechanistically coupled to the *re* of  $H_2$ , as described in the text.

The *re/oa* model also predicts that the reaction is reversible which means under the sufficient concentration of  $H_2$ ,  $E_4(2N_2H)$  state should reverse to  $E_4(4H)$  through an *oa* of  $H_2$ . The first experimental evidence on  $E_4(2N_2H) \rightleftharpoons E_4(4H)$  reversibility was recently

established through temperature dependent EPR/cryoannealing experiment. WT MoFe protein was previously known to trap  $N_2$  intermediates ( $E_4(2N_2H)$ ) (**Figure 1-9**)<sup>58</sup> and further analysis with  $^{15}N$  and  $^1H$  ENDOR on the trapped state revealed that NN bond is still intact and therefore it represents the early state intermediate of the reduction pathway.<sup>59</sup>

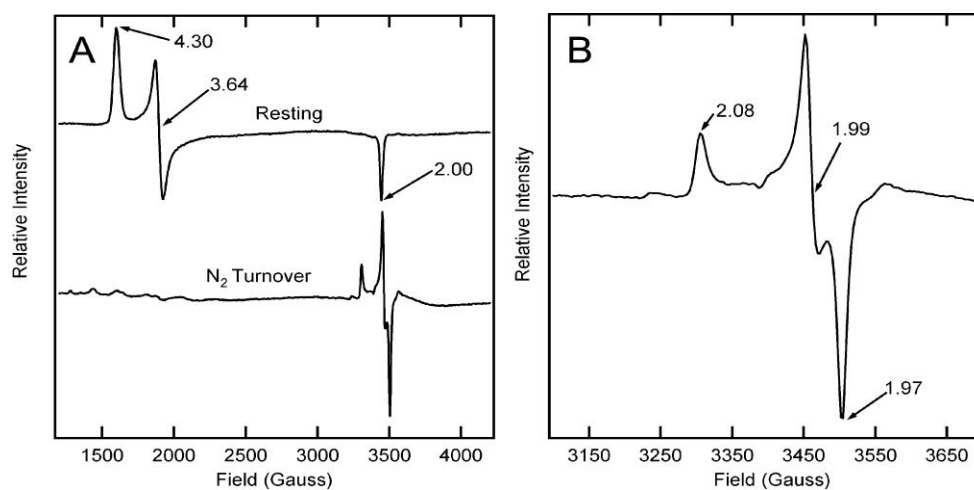


**Figure 1-9: X-Band EPR spectra of wild type (WT) nitrogenase.** (A) X-Band EPR spectrum for the resting state of the WT MoFe protein (Resting) and of the WT MoFe protein trapped by being frozen to 77 K during turnover under 1 atm of  $N_2$  ( $N_2$  turnover). (B) Expansion of  $g \sim 2$  region of the  $N_2$  turnover-trapped state,  $E_4(2N_2H)$ , showing the rhombic signal with  $S = \frac{1}{2}$  spin and the respective  $g$  values of 2.08, 1.99, and 1.97.<sup>58</sup>

The trapped  $E_4(2N_2H)$  state undergoes thermal decay to  $E_4(4H)$  state at temperature above  $-50$  °C and this decay kinetics was found to be directly proportional to the concentration of  $H_2$  and inversely proportional to the concentration of  $N_2$  in the solution. Also, the rate of decay of  $E_4(2N_2H)$  is identical to the rate of formation of  $E_4(4H)$  indicating no kinetic barrier during this transition. Hence, this confirmed that  $E_4(2N_2H) \rightleftharpoons E_4(4H)$  process as kinetically and thermodynamically reversible.<sup>60</sup> Thus



*re/oa* mechanism gives a mechanistic explanation for why  $H_2$  is a competitive inhibitor of  $N_2$  reduction.

The *re/oa* mechanism also delineates the process of formation of HD during  $D_2$  inhibition of  $N_2$  reduction in  $H_2O$  buffer as shown below (**Figure 1-10**).<sup>51</sup> The *oa* of  $D_2$  to  $E_4(2N_2H)$  intermediate breaks D-D bond and incorporates two D's on FeMo-cofactor as two iron deuteride (Fe-D) with a concerted release of one molecule of  $N_2$ . The protonolysis of these two deuteride, through a mechanism termed as hydride protonation, forms two molecule of HD. In this process, the two electrons stored in  $E_4(2N_2H)$  state are diverted toward formation of two molecules of HD. Thus, *re/oa* mechanism provides a mechanistic explanation of why  $D_2$  ( $H_2$  or  $T_2$ ) reacts only at diazene level intermediate and why 1 electron is consumed per HD formation. The *oa* of  $D_2$  to  $E_4(2N_2H)$  intermediate is verified in an elegant  $N_2/D_2/C_2H_2$  mixture experiment.<sup>61</sup> During nitrogenase turnover,  $D_2$  hydrogenate  $C_2H_2$  only in presence of  $N_2$  yielding both mono-deuterated and di-deuterated ethylene as predicted by *re/oa* mechanism.

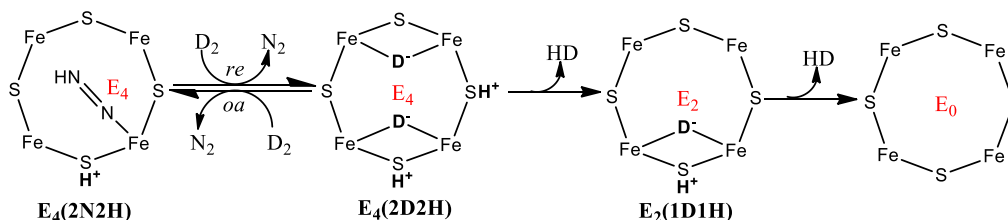


**Figure 1-10: Showing the mechanism of HD formation.** Oxidative addition of  $D_2$  on FeMo-cofactor is stored as two Fe-D bonds that are protonated by the transfer of solvent proton ( $H^+$ ) to make two molecules of HD.

The *re/oa* mechanism is also consistent with the final key constrain and mechanistic test that was revealed by Burgess and co-worker. When nitrogenase is turned

over under the atmosphere of  $N_2$  and  $T_2$ , HT is formed but only a negligible tritium ( $T^+$ ) is released to solvent (~2%). According to *re/oa* mechanism, the *oa* of  $T_2$  to FeMo-cofactor incorporates two T's in the form of two bridging tritride (Fe-T). <sup>1,2</sup>ENDOR measurement on the trapped  $E_4(4H)$  and  $E_4(4D)$  intermediate have demonstrated that the hydrides (Fe-H) or deuterides (Fe-D) are solvent non-exchangeable and therefore the only possibility to release these hydride or deuteride from FeMo-cofactor is through hydride protonation or reductive elimination. None of these mechanisms would cause the release of  $T^+$  in the solvent.<sup>45</sup>

The accumulated date on *re/oa* mechanism provided a broad mechanistic overview on the activation of  $N_2$  by nitrogenase. However, the atomic level detail of this process is still unanswered. In chapter 4, a direct evidence of reductive elimination is presented along with the identification of key electronic state of FeMo-cofactor that possibly can bind and activate  $N_2$ . One of the predictions of *re/oa* mechanism is the formation of reduced FeMo-cofactor after the reductive elimination of dihydride. Studies on mono-nuclear model complexes have shown that *cis*-dihydride are photolabile and undergo ligand electronic excitation to release  $H_2$  through *re* mechanism.<sup>62</sup> A similar approach is employed in this study to photolyze the dihydride of  $E_4(4H)$  and create a new state of FeMo-cofactor represented as *S* state ( $E_4(2H)^*$ ) that is predicted to bind and activate  $N_2$ . Most interestingly, in this study we show the *S* state is even in wild type nitrogenase that undoubtable solidifies the proposed mechanism. Identification of the *S* state of FeMo-cofactor has led to better understanding of nitrogenase catalysis as explained in the chapter.

Besides mechanistic studies, recently using either europium diethylenetriaminepentaacetic acid (Eu-DTPA) or cobaltocene as electron mediator, nitrogenase is demonstrated to electrocatalytically reduce proton, acetylene, nitrite, and azide.<sup>63,64</sup> However, the mechanism of substrate reduction under mediated electrocatalysis are unknown. As a preliminary study, we show the use of kinetic isotope effect to elucidate the mechanism of proton reduction by nitrogenase. Previous studies have shown that the dissociation of Fe protein from the MoFe protein after transfer of electron requires the release of phosphate and kinetically this release of phosphate is the rate limiting step for overall nitrogenase catalysis.<sup>42</sup> However, under mediated electrocatalysis a normal kinetic isotope effect for the formation of H<sub>2</sub> is observed which strongly supports substrate reduction being the rate limiting step. In addition, proton inventory for formation of H<sub>2</sub> demonstrate one proton being involved in the transition state of the rate limiting step which is consistent with the hydride protonolysis mechanism suggested by the quantum mechanical study. Finally, we also show that substitution of amino acids around FeMo-cofactor alters the hydricity of Fe-H formed on FeMo-cofactor that insights into why certain variants of MoFe protein is capable of performing certain reduction chemistry and other do not.

In summary, this dissertation focus on how the electrons and protons are accumulated on FeMo-cofactor and how these accumulated reducing equivalents are used for substrates reduction especially N<sub>2</sub> and CO<sub>2</sub>.

## References

- (1) Lehninger, A. L.; Nelson, D. L.; Cox, M. M. *Lehninger principles of biochemistry*, 4th ed.; W.H. Freeman: New York, 2005.
- (2) Ferguson, S. J. *Curr. Opin. Chem. Biol.* **1998**, 2 (2), 182–193.
- (3) Igarashi, R. Y.; Seefeldt, L. C. *Crit. Rev. Biochem. Mol. Biol.* **2003**, 38 (4), 351–384.
- (4) Smil, V. *Enriching the Earth: Fritz Haber, Carl Bosch, and the Transformation of World Food Production*; MIT Press, 2004.
- (5) Ertl, G. *Angew. Chem. Int. Ed.* **2008**, 47 (19), 3524–3535.
- (6) Kim, D.; Sakimoto, K. K.; Hong, D.; Yang, P. *Angew. Chem. Int. Ed.* **2015**, 54 (11), 3259–3266.
- (7) Lan, R.; Irvine, J. T. S.; Tao, S. *Sci. Rep.* **2013**, 3.
- (8) Appl, M. In *Ullmann's Encyclopedia of Industrial Chemistry*; Wiley-VCH Verlag GmbH & Co. KGaA, 2000.
- (9) Gruber, N.; Galloway, J. N. *Nature* **2008**, 451 (7176), 293–296.
- (10) Burris, R. H.; Roberts, G.P. *Annu. Rev. Nutr.* **1993**, 13 (1), 317–335.
- (11) Ribbe, M. W. *Nitrogen fixation: methods and protocols*; Methods in molecular biology; Humana ; Springer: New York, 2011.
- (12) Eady, R. R. *Chem. Rev.* **1996**, 96 (7), 3013–3030.
- (13) Seefeldt, L. C.; Hoffman, B. M.; Dean, D. R. *Annu. Rev. Biochem.* **2009**, 78, 701–722.
- (14) Burgess, B. K.; Lowe, D. J. *Chem. Rev.* **1996**, 96 (7), 2983–3012.

- (15) Kim, J.; Rees, D. C. *Science* **1992**, *257* (5077), 1677–1682.
- (16) Georgiadis, M. M.; Komiya, H.; Chakrabarti, P.; Woo, D.; Kornuc, J. J.; Rees, D. C. *Science* **1992**, *257* (5077), 1653–1659.
- (17) Mitra, D.; George, S. J.; Guo, Y.; Kamali, S.; Keable, S.; Peters, J. W.; Pelmeshnikov, V.; Case, D. A.; Cramer, S. P. *J. Am. Chem. Soc.* **2013**, *135* (7), 2530–2543.
- (18) Watt, G. D.; Wang, Z. C.; Knotts, R. R. *Biochemistry* **1986**, *25* (25), 8156–8162.
- (19) Sarma, R.; Mulder, D. W.; Brecht, E.; Szilagyi, R. K.; Seefeldt, L. C.; Tsuruta, H.; Peters, J. W. *Biochemistry* **2007**, *46* (49), 14058–14066.
- (20) Mayhew, S. G. *Eur. J. Biochem.* **1978**, *85* (2), 535–547.
- (21) Lindahl, P. A.; Day, E. P.; Kent, T. A.; Orme-Johnson, W. H.; Münck, E. *J. Biol. Chem.* **1985**, *260* (20), 11160–11173.
- (22) Angove, H. C.; Yoo, S. J.; Münck, E.; Burgess, B. K. *J. Biol. Chem.* **1998**, *273* (41), 26330–26337.
- (23) Kim, J.; Rees, D. C. *Nature* **1992**, *360* (6404), 553–560.
- (24) Surerus, K. K.; Hendrich, M. P.; Christie, P. D.; Rottgardt, D.; Orme-Johnson, W. H.; Münck, E. *J. Am. Chem. Soc.* **1992**, *114* (22), 8579–8590.
- (25) Zimmermann, R.; Münck, E.; Brill, W. J.; Shah, V. K.; Henzl, M. T.; Rawlings, J.; Orme-Johnson, W. H. *Biochim. Biophys. Acta* **1978**, *537* (2), 185–207.
- (26) Tittsworth, R. C.; Hales, B. J. *J. Am. Chem. Soc.* **1993**, *115* (21), 9763–9767.
- (27) Lanzilotta, W. N.; Christiansen, J.; Dean, D. R.; Seefeldt, L. C. *Biochemistry* **1998**, *37* (32), 11376–11384.

- (28) Morgan, T. V.; Mortenson, L. E.; McDonald, J. W.; Watt, G. D. *J. Inorg. Biochem.* **1988**, *33* (2), 111–120.
- (29) Pierik, A. J.; Wassink, H.; Haaker, H.; Hagen, W. R. *Eur. J. Biochem.* **1993**, *212* (1), 51–61.
- (30) Davydov, R.; Khadka, N.; Yang, Z.-Y.; Fielding, A. J.; Lukoyanov, D.; Dean, D. R.; Seefeldt, L. C.; Hoffman, B. M. *Isr. J. Chem.* **2016**, *56* (9-10), 841–851.
- (31) Abedini, A.; Daud, A. R.; Abdul Hamid, M. A.; Kamil Othman, N.; Saion, E. *Nanoscale Res Lett* **2013**, *8* (1), 474.
- (32) Danyal, K.; Dean, D. R.; Hoffman, B. M.; Seefeldt, L. C. *Biochemistry* **2011**, *50* (43), 9255–9263.
- (33) Spatzal, T.; Aksoyoglu, M.; Zhang, L.; Andrade, S. L. A.; Schleicher, E.; Weber, S.; Rees, D. C.; Einsle, O. *Science* **2011**, *334* (6058), 940–940.
- (34) Lancaster, K. M.; Roemelt, M.; Ettenhuber, P.; Hu, Y.; Ribbe, M. W.; Neese, F.; Bergmann, U.; DeBeer, S. *Science* **2011**, *334* (6058), 974–977.
- (35) Wiig, J. A.; Hu, Y.; Lee, C. C.; Ribbe, M. W. *Science* **2012**, *337* (6102), 1672–1675.
- (36) Orme-Johnson, W. H.; Hamilton, W. D.; Jones, T. L.; Tso, M. Y.; Burriss, R. H.; Shah, V. K.; Brill, W. J. *Proc. Natl. Acad. Sci. U.S.A.* **1972**, *69* (11), 3142–3145.
- (37) Yoo, S. J.; Angove, H. C.; Papaefthymiou, V.; Burgess, B. K.; Münck, E. *J. Am. Chem. Soc.* **2000**, *122* (20), 4926–4936.
- (38) Schultz, F. A.; Gheller, S. F.; Newton, W. E. *Biochim. Biophys. Acta* **1988**, *152* (2), 629–635.

- (39) Lukoyanov, D.; Yang, Z.-Y.; Duval, S.; Danyal, K.; Dean, D. R.; Seefeldt, L. C.; Hoffman, B. M. *Inorg. Chem.* **2014**, *53* (7), 3688–3693.
- (40) Doan, P. E.; Telser, J.; Barney, B. M.; Igarashi, R. Y.; Dean, D. R.; Seefeldt, L. C.; Hoffman, B. M. *J. Am. Chem. Soc.* **2011**, *133* (43), 17329–17340.
- (41) Danyal, K.; Mayweather, D.; Dean, D. R.; Seefeldt, L. C.; Hoffman, B. M. *J. Am. Chem. Soc.* **2010**, *132* (20), 6894–6895.
- (42) Yang, Z.-Y.; Ledbetter, R.; Shaw, S.; Pence, N.; Tokmina-Lukaszewska, M.; Eilers, B.; Guo, Q.; Pokhrel, N.; Cash, V. L.; Dean, D. R.; Antony, E.; Bothner, B.; Peters, J. W.; Seefeldt, L. C. *Biochemistry* **2016**, *55* (26), 3625–3635.
- (43) Tezcan, F. A.; Kaiser, J. T.; Mustafi, D.; Walton, M. Y.; Howard, J. B.; Rees, D. C. *Science* **2005**, *309* (5739), 1377–1380.
- (44) Danyal, K.; Shaw, S.; Page, T. R.; Duval, S.; Horitani, M.; Marts, A. R.; Lukoyanov, D.; Dean, D. R.; Raugei, S.; Hoffman, B. M.; Seefeldt, L. C.; Antony, E. *Proc. Natl. Acad. Sci. U.S.A* **2016**, *113* (40), E5783–E5791.
- (45) Igarashi, R. Y.; Laryukhin, M.; Dos Santos, P. C.; Lee, H.-I.; Dean, D. R.; Seefeldt, L. C.; Hoffman, B. M. *J. Am. Chem. Soc.* **2005**, *127* (17), 6231–6241.
- (46) Lukoyanov, D.; Yang, Z.-Y.; Dean, D. R.; Seefeldt, L. C.; Hoffman, B. M. *J. Am. Chem. Soc.* **2010**, *132* (8), 2526–2527.
- (47) Lukoyanov, D.; Barney, B. M.; Dean, D. R.; Seefeldt, L. C.; Hoffman, B. M. *Proc. Natl. Acad. Sci. U.S.A* **2007**, *104* (5), 1451–1455.
- (48) Yang, Z.-Y.; Moure, V. R.; Dean, D. R.; Seefeldt, L. C. *PNAS* **2012**, *109* (48), 19644–19648.

- (49) Appel, A. M.; Bercaw, J. E.; Bocarsly, A. B.; Dobbek, H.; DuBois, D. L.; Dupuis, M.; Ferry, J. G.; Fujita, E.; Hille, R.; Kenis, P. J. A.; Kerfeld, C. A.; Morris, R. H.; Peden, C. H. F.; Portis, A. R.; Ragsdale, S. W.; Rauchfuss, T. B.; Reek, J. N. H.; Seefeldt, L. C.; Thauer, R. K.; Waldrop, G. L. *Chem. Rev.* **2013**, *113* (8), 6621–6658.
- (50) Seefeldt, L. C.; Rasche, M. E.; Ensign, S. A. *Biochemistry* **1995**, *34* (16), 5382–5389.
- (51) Hoffman, B. M.; Lukoyanov, D.; Yang, Z.-Y.; Dean, D. R.; Seefeldt, L. C. *Chem. Rev.* **2014**, *114* (8), 4041–4062.
- (52) Simpson, F. B.; Burris, R. H. *Science* **1984**, *224* (4653), 1095–1097.
- (53) Guth, J. H.; Burris, R. H. *Biochemistry* **1983**, *22* (22), 5111–5122.
- (54) Li, J. L.; Burris, R. H. *Biochemistry* **1983**, *22* (19), 4472–4480.
- (55) Burgess, B. K.; Wherland, S.; Newton, W. E.; Stiefel, E. I. *Biochemistry* **1981**, *20* (18), 5140–5146.
- (56) Dilworth, M. J.; Fisher, K.; Kim, C. H.; Newton, W. E. *Biochemistry* **1998**, *37* (50), 17495–17505.
- (57) Hoffman, B. M.; Lukoyanov, D.; Dean, D. R.; Seefeldt, L. C. *Acc. Chem. Res.* **2013**, *46* (2), 587–595.
- (58) Barney, B. M.; Lukoyanov, D.; Igarashi, R. Y.; Laryukhin, M.; Yang, T.-C.; Dean, D. R.; Hoffman, B. M.; Seefeldt, L. C. *Biochemistry* **2009**, *48* (38), 9094–9102.



- (59) Barney, B. M.; Yang, T.-C.; Igarashi, R. Y.; Dos Santos, P. C.; Laryukhin, M.; Lee, H.-I.; Hoffman, B. M.; Dean, D. R.; Seefeldt, L. C. *J. Am. Chem. Soc.* **2005**, *127* (43), 14960–14961.
- (60) Lukoyanov, D.; Yang, Z.-Y.; Khadka, N.; Dean, D. R.; Seefeldt, L. C.; Hoffman, B. M. *J. Am. Chem. Soc.* **2015**, *137* (10), 3610–3615.
- (61) Yang, Z.-Y.; Khadka, N.; Lukoyanov, D.; Hoffman, B. M.; Dean, D. R.; Seefeldt, L. C. *Proc. Natl. Acad. Sci. U.S.A* **2013**, *110* (41), 16327–16332.
- (62) Perutz, R. N.; Procacci, B. *Chem. Rev.* **2016**, *116* (15), 8506–8544.
- (63) Milton, R. D.; Abdellaoui, S.; Khadka, N.; Dean, D. R.; Leech, D.; Seefeldt, L. C.; Minteer, S. D. *Energy Environ. Sci.* **2016**, *9* (8), 2550–2554.
- (64) Paengnakorn, P.; Ash, P. A.; Shaw, S.; Danyal, K.; Chen, T.; Dean, D. R.; Seefeldt, L. C.; Vincent, K. A. *Chem. Sci.* **2016**.

## CHAPTER 2

EXPLORING ELECTRON/PROTON TRANSFER AND CONFORMATIONAL  
CHANGES IN THE NITROGENASE MOFE PROTEIN AND FEMO-COFACTOR  
THROUGH CRYOREDUCTION/EPR MEASUREMENTS**Abstract**

We combine cryoreduction/annealing/EPR measurements of nitrogenase MoFe protein with results of earlier investigations to provide a detailed view of the electron/proton transfer events and conformational changes that occur during early stages of  $[e^-/H^+]$  accumulation by the MoFe protein. This includes reduction of the non-catalytic  $M^{ox}$  state formed by chemical oxidation of the iron-molybdenum cofactor (FeMo-co) active site to its resting state ( $M^N$ ,  $S = 3/2$ ) within resting MoFe ( $E_0$ ), through the states that have accumulated,  $n = 1, 2$ ,  $[e^-/H^+]$ , denoted  $E_1(H)$  ( $S \geq 1$ ) and  $E_2(2H)$  ( $S = 3/2$ ) in the Lowe-Thorneley kinetic scheme. FeMo-co does not undergo a major change of conformation during reduction of  $M^{ox}$ , thus acting merely as a ‘simple’ electron-transfer cluster. In contrast, FeMo-co undergoes substantial conformational changes during the reduction of  $E_0$  to  $E_1(1H)$ , and of  $E_1(1H)$  to  $E_2(2H)$ . The experimental results further suggest that the  $E_1(1H) \rightarrow E_2(2H)$  step involves coupled delivery of a proton and electron (PCET) to FeMo-co of  $E_1(H)$  to generate a non-equilibrium  $S = 1/2$  form  $E_2(2H)^*$ . This subsequently undergoes conformational relaxation and attendant change in FeMo-co spin state, to generate the equilibrium  $E_2(2H)$  ( $S = 3/2$ ) state. Unexpectedly, these experiments

---

\*Coauthored by Roman Davydov, Nimesh Khadka, Zhi-Yong Yang, Andrew J. Fielding, Dmitriy Lukoyanov, Dennis R. Dean, Lance C. Seefeldt, and Brian M. Hoffman (2016) *Israel Journal of Chemistry* **56**, 841-851]. Copyright © [2016] John Wiley & Sons, Inc. Reprinted with permission.

also reveal conformational coupling between FeMo-co and P-cluster, and between Fe protein binding and FeMo-co, which might play a role in gated ET from reduced Fe protein to FeMo-co.

## Introduction

Nitrogenase catalyzes the reduction of dinitrogen ( $N_2$ ) to two ammonia ( $NH_3$ ) molecules, and is the dominant contributor of fixed nitrogen in the biogeochemical nitrogen cycle.<sup>[1]</sup> The reduction of  $N_2$  by Mo-dependent nitrogenase occurs at the FeMo-cofactor (7Fe-9S-1Mo-1C-1homocitrate) contained within the nitrogenase MoFe protein.<sup>[2-3]</sup> Substrate reduction involves the transfer of electrons, one-at-a-time, from the [4Fe-4S] cluster of the reduced nitrogenase Fe protein ( $Fe^{red}$ ) to FeMo-co, each transfer being associated with the hydrolysis of two ATP.<sup>[2]</sup> The catalytic cycle has been described by the Lowe-Thorneley (LT) kinetic scheme<sup>[2, 4-5]</sup> in which each electron-transfer (ET) step involves the coupled transfer of a proton to FeMo-co from an adjacent proton-delivery network.

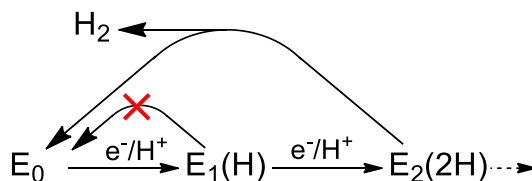
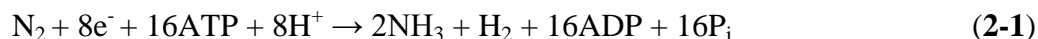


**Figure 2-1: First two steps of the LT MoFe protein cycle showing the accumulation of electrons/protons as well as the possible loss of  $H_2$  by relaxation.**

The LT catalytic cycle involves multiple steps of electron transfer from  $Fe^{red}$  to the MoFe protein, in which the stages are denoted as  $E_n$ , and posits that the  $n^{th}$  stage

MoFe protein has accumulated  $n$  protons as well as  $n$  electrons. Hence the more complete notation of  $E_n(nH)$ , which is incorporated in a representation of the first two steps, **Figure 2-1**.

We recently established<sup>[3, 6-9]</sup> that nitrogen fixation by nitrogenase is driven by the *obligatory* reductive elimination (*re*) of  $H_2$  in order to activate FeMo-co for  $N_2$  binding and reduction.<sup>[10] [11]</sup> This finding implies an optimal (limiting) stoichiometry for nitrogen fixation by nitrogenase (**eqn. 2-1**),



with the accumulation of  $n$  equals eight electrons and protons, rather than the six required for chemical reduction of  $N_2$ .

Four steps of electron/proton accumulation are required prior to  $N_2$  reduction, which begins at  $E_4$ , and the understanding of these processes is incomplete. We have shown<sup>[12-16]</sup> that the  $E_0 \rightarrow E_1(H)$  reduction through ET from reduced Fe protein ( $Fe^{red}$ ) to MoFe protein involves a ‘deficit-spending’ process in which the first step is the transfer of an electron from the MoFe protein auxiliary P cluster (8Fe7S) to FeMo-co. This process is kinetically gated by a rate-limiting conformational change, likely at the Fe/MoFe interface that does not involve correlated proton transfer (no KIE), with follow-up ‘reimbursement’ of the oxidized P cluster through rapid ET from  $Fe^{red}$ .<sup>[12-16]</sup> The LT kinetic scheme incorporates the same electron-transfer ‘Fe-protein cycle’ at each step of electron/proton delivery, and thus would incorporate this process at each stage of the

catalytic cycle.

Regarding changes at FeMo-co itself, it has been shown that one-electron oxidized MoFe protein contains a diamagnetic ( $S = 0$ ) form of FeMo-co, denoted  $M^{\text{ox}}$ ,<sup>[17]</sup> and reduction to the resting state,  $E_0$ , with its EPR-active ( $S = 3/2$ ) FeMo-co, denoted  $M^{\text{N}}$ , involves a form of proton-coupled electron transfer (PCET<sup>[18-19]</sup>). There is indeed a thermodynamically coupled uptake of a proton in this reduction, as incorporated in the LT scheme for steps in the catalytic cycle (e.g., **Figure 2-1**),<sup>[20]</sup> but early ENDOR spectroscopic studies long ago showed that this proton must bind at a site remote from the paramagnetic metal ions of FeMo-co<sup>[21]</sup> Later Mossbauer studies showed that the equilibrium  $E_1(1\text{H})$  state generated by electron transfer from  $\text{Fe}^{\text{red}}$  to the resting state,  $E_0$ , generates an integer-spin reduced FeMo-co ( $S \geq 1$ , denoted  $M^{\text{R}}$ ) without a major change in spin coupling among the Fe ions.<sup>[17]</sup> FeMo-co of  $E_1(\text{H})$  appears to accept the electron at Mo to generate an integer-spin cluster,  $S \geq 1$ .<sup>[17]</sup> FeMo-co of  $E_2(2\text{H})$  has spin,  $S = 3/2$ ,<sup>[2]</sup> but nothing is known directly about FeMo-co of  $E_3(3\text{H})$ . In contrast  $E_4(4\text{H})$ , which has an  $S = 1/2$  FeMo-co has been trapped and extensive study by ENDOR spectroscopy has shown it contains two [Fe-H-Fe] bridging hydrides. Perhaps surprisingly, of the four steps of electron/proton accumulation in the catalytic cycle prior to  $\text{N}_2$  reduction,  $E_n$ ,  $n \leq 4$ , direct experiment has only verified the delivery of a total of  $n \text{ H}^+$  to FeMo-co for  $n = 2$ , which state can decay to  $E_0$  in the frozen solution by loss of its two protons/electrons in the form of  $\text{H}_2$ , and for  $n = 4$ , which state can decay to  $E_0$  by loss of two  $\text{H}_2$ .<sup>[2, 4-5]</sup> The impediment to the study of FeMo-co in electron-accumulation intermediates (as well as the others) is that reduction of MoFe protein is rate-limited by the off-rate of the oxidized

Fe protein subsequent to electron delivery.<sup>[22]</sup> As a result solution-kinetic measurements provide little insight into the nature of the coupling between proton and electron delivery to the MoFe protein, and of electron/proton delivery to FeMo-co itself, while the difficulty of trapping intermediates has precluded study of conformational changes that might be undergone by FeMo-co during electron and/or proton delivery.

It appeared to us that radiolytic cryoreduction/annealing/EPR<sup>[23]</sup> studies of nitrogenase offered a possible means of decoupling and revealing the details of proton and electron delivery to FeMo-co itself, and of disclosing possible attendant conformational changes that occur at this multimetallic cluster. Cryoreduction of a metal center such as FeMo-co in 77 K frozen solution involves the direct injection of a radiolytically generated mobile electron into the center, and thus decouples electron and proton transfer. The cryoreduced FeMo-co is trapped in the conformation of its precursor state, and step-annealing to higher temperature typically allows it to structurally relax, revealing any conformational changes between FeMo-co in the reduced state, and in the precursor MoFe protein state; the occurrence of a KIE during relaxation signals that the rate-limiting step in the process involves a proton transfer.<sup>[23-24]</sup> However, in some cases, when the protein environment is well-poised for proton delivery, such proton transfer is 'hidden' during 77 K reduction/annealing, because it can accompany electron injection even at 77 K or below; in one case it was found that 6 K cryoreduction was coupled to proton tunneling.<sup>[25]</sup> To explore proton delivery to FeMo-co and conformational changes at FeMo-co that accompany reduction of the MoFe protein, we begin by examining cryoreduction/annealing of preparations in which most of the resting-state

FeMo-co,  $M^N$  has been chemically oxidized to  $M^{ox}$ , using EPR to monitor the  $M^{ox} \rightarrow M^N$  cryoreduction/annealing. However, the main focus is the cryoreduction/annealing conversion of  $E_1(H)$  to  $E_2(2H)$ . We have carried out cryoreduction/annealing/EPR measurements on MoFe protein containing high populations of  $E_1(H)$  generated in multiple ways. In each case the state formed by 77 K cryoreduction of  $E_1(1H)$  is first examined by EPR, then cryoannealed at higher temperatures in the frozen state while its relaxation to the equilibrium  $E_2(2H)$  form is monitored.

By combining the results from the present study with those of an earlier cryoreduction/Mossbauer investigation<sup>[17]</sup> and studies of ET during turnover,<sup>[12-16]</sup> we arrive at a provisional view of the electron/proton transfer events and conformational changes that occur during accumulation of  $[e^-/H^+]$  by the MoFe protein, starting from the non-catalytic  $M^{ox}$  state and proceeding through the  $E_2(2H)$  stage of the LT scheme, a view that likely extends at least through the  $E_4(4H)$  state. This study further reveals allosteric coupling between FeMo-co and P-cluster, and between FeMo-co and the binding of Fe protein, which might well play a role in the gated ET from reduced Fe protein to FeMo-co.

## Materials and Methods

**Materials and Protein purification:** All reagents were obtained from SigmaAldrich (St. Louis, MO) or Fisher Scientific (Fair Lawn, NJ) and were used without further purification. Argon and dinitrogen gases were purchased from Air Liquide America Specialty Gases LLC (Plumsteadville, PA) and were passed through an activated copper catalyst to remove any traces of dioxygen before use. *Azotobacter*

*vinelandii* strain DJ995 (wild-type MoFe protein with a His tag) was grown, and the corresponding nitrogenase MoFe protein, having a seven-His tag addition near the carboxyl-terminal end of the  $\alpha$ -subunit, was expressed and purified as described.<sup>[26]</sup> Protein concentrations were determined by the Biuret assay. The purities of these proteins were >95% based on SDS/PAGE analysis with Coomassie staining. Handling of proteins and buffers was done in septum-sealed serum vials under an argon atmosphere or on a Schlenk vacuum line. All liquid were transferred using gas-tight syringes.

**Preparation of cryoreduction samples:**  $M^{ox}/P^{ox}$  samples were made using methylene blue (MB) as oxidant ( $E_m = +11$  mV). Wild type MoFe protein was passed through a column packed with Dowex/G25 resin to remove residual dithionite. The protein was eluted with 200 mM MOPS pH=7.4 containing 150 mM NaCl and the concentration was determined using Biuret assay. 800  $\mu$ M MB (10 mM MB stock made in 100 mM MOPS pH=7.4) was added to 400  $\mu$ L of 200 mM MOPS buffer pH=7.4 containing 110  $\mu$ M MoFe, 150 mM NaCl and 11% glycerol. The mixture was kept at room temperature for 30 min and 350  $\mu$ L of samples was transferred to an 18.5 cm long and 4 mm diameter calibrated quartz EPR tube and rapidly frozen in liquid nitrogen.

The resting state samples, used for  $E_0 \square E_1$  study, were made at room temperature in 200 mM MOPS buffer at pH 7.3 with 50 mM dithionite. MoFe protein was at a final concentration of  $\sim$ 100  $\mu$ M. About 300  $\mu$ L of samples (out of a total volume  $\sim$ 400  $\mu$ L) was transferred to a calibrated quartz EPR tube and rapidly frozen in liquid nitrogen. All turnover samples were prepared in a dioxygen free buffer (total volume  $\sim$ 400  $\mu$ L)



containing a MgATP regeneration system with final concentrations of 13 mM ATP, 15 mM MgCl<sub>2</sub>, 20 mM phosphocreatine, 2.0 mg/mL bovine serum albumin, and 0.3 mg/mL phosphocreatine kinase in a 200 mM MOPS buffer at pH 7.3 (or pD = 7.3 with a pH meter reading of 6.9 in D<sub>2</sub>O buffer<sup>[27]</sup>) with 50 mM dithionite. Glycerol (10% glycerol (v/v)) was added in the buffer where noted. Low-flux samples were made by adding MoFe protein at ~100 μM final concentration and initiating the reaction by adding Fe protein at ~2 μM concentration. The reaction was allowed to run for 10 min at room temperature at which point ~300 μL of sample was transferred to the EPR tubes and frozen as described above. High-flux samples were made with ~100 μM MoFe proteins and ~150 μM Fe protein. After the addition of the Fe protein, the reaction was allowed to run at room temperature under Ar or N<sub>2</sub> atmosphere for 20-25 s before freezing the samples.

**Cryoreduction:**  $\gamma$ -irradiation of the nitrogenase samples at 77 K typically was performed for ~ six hours (dose rate of 0.5 Mrad/h, total dose 3 Mrad) using a Gamma cell 220 <sup>60</sup>Co source. Annealing at temperatures over the range 77 K-270 K was performed by placing the EPR samples in the appropriate bath (n-pentane or methanol cooled with liquid N<sub>2</sub>) and then refreezing in liquid nitrogen. As discussed, cryoreduction of the E<sub>1</sub> state produces an  $S = 1/2$  intermediate that converts to the equilibrium  $S=3/2$  E<sub>2</sub> state during cryoannealing. The kinetic progress curves for these processes are measured as the amplitudes of these species' EPR spectra at their maximum g-value:  $S = 3/2$ ,  $g_{\max} = 4.23$ ;  $S = 1/2$ ,  $g_{\max} = 2.23$ .

**EPR:** EPR spectra were recorded on an X-band Bruker ESP 300 spectrometer equipped with an Oxford Instruments ESR 900 continuous He flow cryostat. 2 K 35 GHz EPR spectra were measured on an instrument described elsewhere.<sup>[28-29]</sup>

## Results

### Cryoreduction/Annealing of $M^{\text{ox}}$

To extend the earlier studies of  $M^{\text{ox}}$ , and for comparison with the present results for cryoreduction/annealing of the  $E_0$  and  $E_1$  stages of the catalytic cycle, we chemically oxidized resting-state  $E_0$  MoFe protein to a state that contains the EPR-silent, singly oxidized FeMo-co, denoted  $M^{\text{ox}}$ , cryoreduced it, and examined the transformation to  $E_0$  ( $M^{\text{N}}$ ). As usual, the  $E_0$  MoFe protein shows the  $S = 3/2$  EPR signal,  $g = [4.35, 3.65, 2.0]$ , associated with resting-state FeMo-co,  $M^{\text{N}}$ , plus variable small amounts of a conformer(s) with somewhat higher rhombicity e.g., ( $g \sim [4.5, 3.5, 2.0]$ ).<sup>[2, 30-31]</sup> The chemical oxidation converts roughly 90% of  $M^{\text{N}}$  to  $M^{\text{ox}}$ , as shown by the loss of the  $S = 3/2$   $M^{\text{N}}$  signal, **Figure 2-1**. Cryoradiolysis at 77 K directly reduces roughly one-half of the  $M^{\text{ox}}$  back to  $M^{\text{N}}$ , as seen by the reappearance of the  $S = 3/2$   $M^{\text{N}}$  EPR signal, **Figure 2-1**, although with a somewhat increased population of the more rhombic conformers of  $M^{\text{N}}$ .

During stepwise annealing of the cryoreduced sample for 2 min at each of several temperatures up to 260 K, these  $M^{\text{N}}$  conformers relax to the majority resting  $M^{\text{N}}$  form of

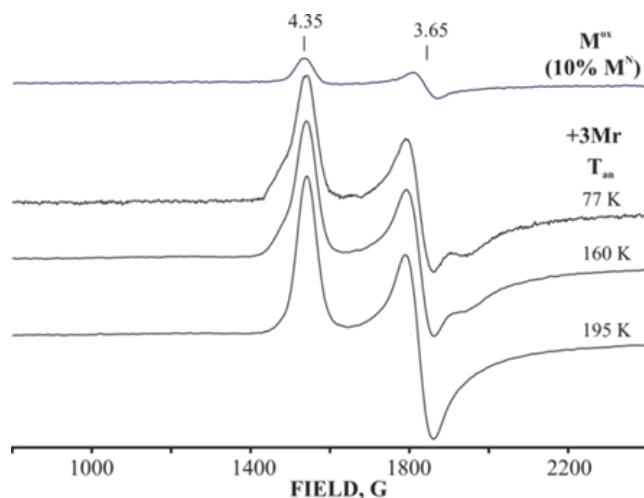


**Figure 2-2: X-band EPR spectra of nitrogenase MoFe protein oxidized to the (primarily)  $M^{ox}$  state with loss of 90% of  $M^N$  signal (upper) and then cryoreduced at 77 K and annealed at progressively higher temperatures for 2 minutes each.** Conditions: Microwave power 5 mW, modulation amplitude 10 G, microwave frequency 9.375 GHz,  $T=10$  K.

the cluster by  $T_{an} \sim 180$  K without loss of net signal; upon further annealing at  $T > 180$  K the  $S = 3/2$  signal does not change at all, and no new high-spin (**Figure 2-2**) or low-spin (not shown) signal appears. These observations imply that the structure of  $M^{ox}$  (epr-silent) differs little from that of  $M^N$  ( $S = 3/2$ ) and that  $M^{ox}$  undergoes direct 77 K cryoreduction to the  $M^N$  resting state of the cofactor.

### **Generation of high populations of $E_1(H)$ :**

We have employed three procedures to generate high populations of the  $E_1(H)$  state for subsequent cryoreduction: turnover under low electron flux (MoFe protein:Fe protein = 50:1); turnover under high flux (MoFe protein:Fe protein = 1:1.5); cryoreduction of resting ( $E_0$ ) state MoFe protein (not undergoing TO), followed by cryoannealing at 235 K. **Figure 2-3** presents the EPR spectra of resting ( $E_0$ ) state MoFe protein as well as of samples prepared during TO under Ar with concentrations of Fe

protein that generate conditions of either low or high electron flux. As reported,<sup>[30]</sup> reduction of MoFe protein during turnover under Ar can convert a high percentage of the  $S = 3/2$   $E_0$  state to the EPR-silent  $E_1(H)$  state. This is seen in **Figure 2-3**, where turnover at low flux causes the intensity of the  $E_0$  signal to decrease to ~20% of the resting-state value through conversion to  $E_1$ , and where turnover at high flux decreases the  $E_0$  signal to less than 10% of resting. The high-flux Ar TO sample in addition shows a weak  $S = 3/2$  signal from FeMo-co with  $g = [4.23, 3.76, \sim 2.0]$ , denoted 1b, which overlaps that of  $E_0$  and is assigned to  $E_2(2H)$ .<sup>[31]</sup> The low-field region of the spectra obtained for samples of high-flux TO under  $N_2$  are similar to those from high-flux TO under Ar.

At fields around  $g \sim 2$ , **Figure 2-3**, the spectrum of the low-flux samples exhibits only a weak signal from the low concentration of reduced Fe protein ( $g = 1.935$  and  $1.86$ ) and the  $g_3 \sim 2$  feature of the  $S=3/2$   $E_0$  signal, whereas high flux samples show well-resolved features from the high concentrations of reduced Fe protein. In addition, high-flux Ar TO shows a well-resolved signal at  $g_1 = 2.15$  from an intermediate that may be  $E_4(4H)$ , whereas high-flux  $N_2$  TO shows the signal from the  $E_4(2N2H)$  intermediate (not shown). Interference by the strong signals in the  $g=2$  region that appear in high-flux samples, lead us to focus on low-flux samples.

Neither high nor low-flux TO creates a new signal at fields lower than  $g_1 = 4.34$  of  $E_0$ , fields where non-Kramer's signals from an integer-spin reduced FeMo-co state are sometimes seen.<sup>[9]</sup> This is consistent with the earlier Mössbauer study, which showed that the  $E_1(H)$  state produced by TO contains an EPR-silent (integer-spin;  $S \geq 1$ ) reduced form of FeMo-co that was denoted  $M^R$ .<sup>[17]</sup>

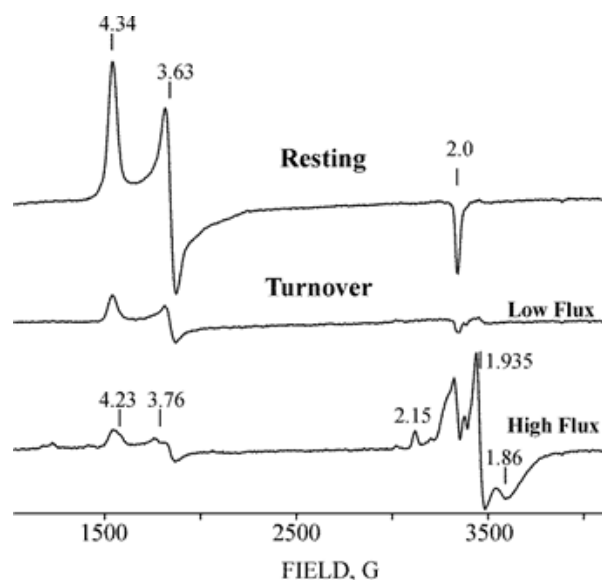


**Figure 2-3: X-band EPR spectra of nitrogenase in resting state and freeze-quenched during TO under low electron flux and high electron flux under Ar (see Materials and Methods).** Instrument conditions: Microwave power 5 mW, modulation amplitude 10 G, microwave frequency, 9.375 GHz, T=10 K.

In addition to making high populations of  $E_1(H)$  through TO, we have also reduced resting state MoFe protein (not under turnover with Fe protein) through radiolytic cryoreduction. Cryoradiolysis of resting-state MoFe protein in 10% glycerol/buffer at 77 K with a dose of 3 megarad (Mrad) causes ~50% decrease in the intensity of the  $S = 3/2 E_0 (M^N)$  signal without appearance of other high-spin signals or non-Kramers signals (**Figure 2-S1a**) in agreement with the previous report.<sup>[17]</sup> In the earlier report, Mössbauer spectroscopy showed that cryoreduction produces an alternative, non-Kramers (integer-spin) form of FeMo-co, which was denoted as  $M^I$ ; we here also denote the MoFe protein that contains this cluster with the LT notation, as  $E_1^I$ .<sup>[17]</sup>

As cryogenic radiolysis of an odd-electron Kramers center such as FeMo-co of

the  $E_0$  resting state can generate an even-electron non-Kramers state not only by cryoreduction, but less commonly by cryooxidation, we carried out measurements to confirm we are indeed cryoreducing the  $M^N$  FeMo-co of  $E_0$ . These two processes can be distinguished experimentally: cryoreduction is greatly enhanced, and cryooxidation is suppressed, in samples containing glycerol, the reverse being true in the absence of glycerol.<sup>[32]</sup> To determine whether the radiation-induced loss of  $E_0$  signal represents cryoreduction or cryooxidation of FeMo-co, we cryo-irradiated a frozen aqueous buffer solution of resting-state MoFe protein without added glycerol. We observed no noticeable decrease in the intensity of the  $E_0 S = 3/2$  signal (not shown), confirming that the loss of  $S = 3/2$  intensity in **Figure 2-S1a** occurs through one-electron cryoreduction of  $M^N$  to  $M^1$ .<sup>[17]</sup> Careful examination of the low-field region of the 2 K 35 GHz EPR spectrum of the cryoreduced enzyme again fails to show a new EPR signal for the irradiated MoFe protein in glycerol buffer, **Figure 2-S1b**, as expected from the Mössbauer study.<sup>[17]</sup>

We have demonstrated<sup>[30]</sup> the  $E_1(H)$  state of MoFe protein produced during TO does not relax to the resting state  $E_0$  during extended cryoannealing in the frozen state at temperatures as high as 253 K (**Figure 2-S1a**) Stepwise annealing of the cryoreduced resting-state nitrogenase at temperatures up to 235 K (**Figure S1a**) or higher (not shown) likewise does not cause recovery of the  $E_0$  signal through relaxation of  $E_1'$  to  $E_0$ , as expected.

### **Cryoreduction /annealing of $E_1(H)$ :**

The above results show that high populations of the  $E_1(H)$  state can be generated in multiple ways: by reduction of  $E_0$  during TO with Fe protein in the presence of ATP

under conditions of low and high electron flux (MoFe/Fe protein 50/1 and 1/1.5 respectively) under either Ar or N<sub>2</sub>, or by cryoreduction/annealing of the E<sub>0</sub> MoFe protein. All three types of E<sub>1</sub>(H), samples were cryoirradiated (3 Mrad) and annealed as a means of examining electron injection and proton transfer into the E<sub>1</sub>(H) state. It will now be shown that the results of cryoreduction/annealing of E<sub>1</sub>(H) are independent of the way E<sub>1</sub>(H) was generated.

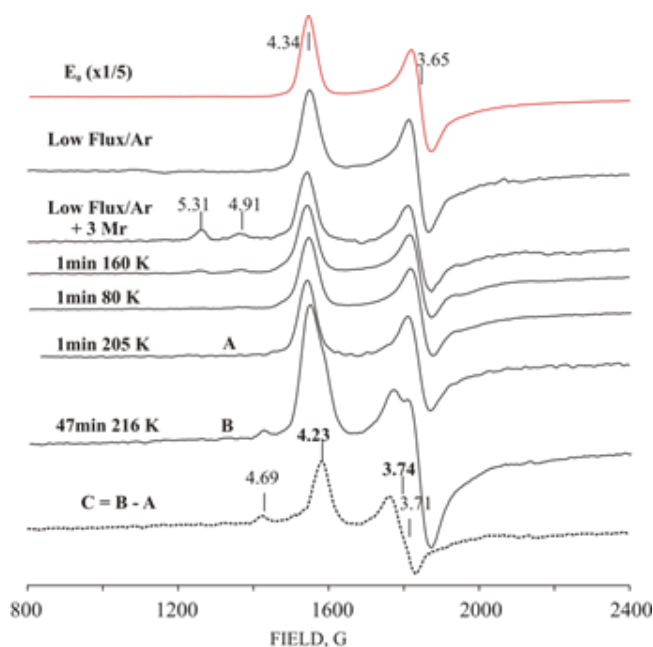


**Figure 2-4A: Low-field EPR spectra of nitrogenase freeze-trapped under low-flux/Ar TO, cryoreduced (3 Mrad) and annealed at indicated temperatures.** Upper two spectra - resting state and low flux/Ar TO before radiolytic cryoreduction; C – difference spectrum between cryoreduced nitrogenase annealed at 216 K for 47 min (B) and 205 K for 1 min (A). Instrument conditions as in **Figure 2-2**.

*Cryoreduction/annealing of low-flux TO samples:* **Figure 2-4A** shows the EPR spectrum of resting-state nitrogenase (E<sub>0</sub>) and nitrogenase that had been cryoreduced subsequent to generation of E<sub>1</sub>(H) by turnover under low electron flux/Ar conditions with

glycerol-containing buffer. The intensity of the  $S = 3/2$   $E_0$  EPR signal is decreased five-fold relative to resting state by TO, and undergoes a small additional decrease in intensity from the irradiation.<sup>[33]</sup> We had anticipated that irradiation of  $E_1(H)$ -containing samples would generate the  $S = 3/2$  EPR signal characteristic of the equilibrium two-electron reduced state  $E_2(2H)$ , denoted 1b, with  $g = [4.23, 3.76, \sim 2.0]$ .<sup>[30-31]</sup> This expectation was strengthened by the observation of direct radiolytic conversion of Mox to MN, described above.

To our surprise this did not occur, **Figure 2-4B**. Instead, irradiation produces a new, relatively broad low-spin EPR signal, which overlaps with the signals from radiolytically generated radicals. The signal resolves better when the radical signal has partly annealed away at  $T > 160$  K, revealing it can be characterized by,  $g = [2.21, 2.08, \text{nd}]$ , **Figure 2-4B** (additional features at  $g = 1.815$  and  $1.772$  in this figure belong to cryogenerated  $P^{\text{ox}}$ , and are discussed below). The  $g = 2.21$  signal arises from a MoFe intermediate trapped during 77 K cryoreduction. This  $g = 2.21$  signal is not created when resting state MoFe protein is cryoreduced by irradiation with a dose of 3 Mrad (**Figure 2-S4, 2-S5**), which confirms that it is indeed generated by the cryoreduction of  $E_1(H)$ , not of  $E_0$ , and that the signal arises from a previously unobserved form of  $E_2$  which we denote,  $E_2^*$ . The signal is only visible at temperatures below 30 K (**Figure 2-S3**), its shape only varies slightly with temperature (Fig.S3), and the shape does not change noticeably on annealing at  $T > 180$ K or during its decay at 216 K (Fig.3B). The presence of the radical signals precludes a detailed analysis of this new  $S = 1/2$  signal, but these characteristics indicate that this spectrum represents a single state, while the breadth of



the features in the spectrum is suggestive of some conformational heterogeneity of the  $E_1$  precursor. We also observe the appearance of the  $E_2^*$  signal upon 77 K cryoreduction of the low-flux turnover sample prepared under 1 atm  $N_2$  (not shown).

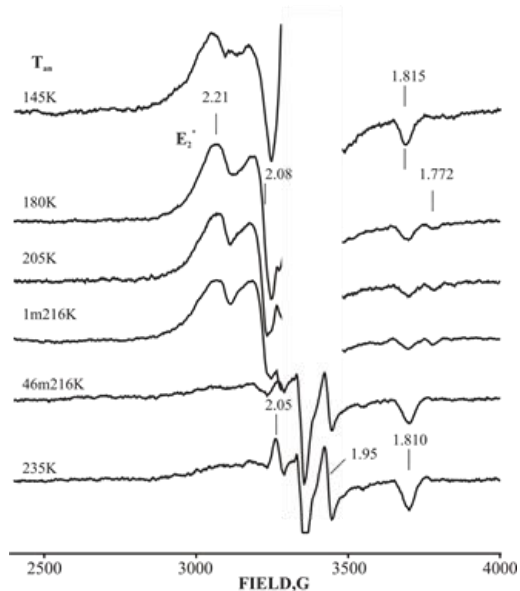


**Figure 2-4B: High field EPR spectra of cryoreduced low flux Ar turnover nitrogenase annealed at indicated temperatures.**  $E_2^*$  signal and  $g$ -values, bold; other  $g$ -values for  $P^{ox}$  (see text). (The radical signal was cut off for clarity). Instrument conditions as in Fig 3.

During progressive annealing of the cryoreduced low-flux/Ar sample at 216 K, the  $g_1 = 2.21$   $E_2^*$  signal decays (**Figure 2-4B**) with the parallel appearance of the  $1b/E_2(2H)$  signal (**Figure 2-4A, 2-S6**).<sup>[34]</sup> Measurements of the annealing kinetics show that within the accuracy of measurement ( $\sim 15\%$ ), the two signals evolve with the same half-time,  $\sim 4.8$  min, **Figure 2-5**, which suggests that annealing involves direct  $E_2^* \rightarrow E_2$  relaxation. The same behavior is seen during cryoreduction/annealing of low-flux TO samples prepared under 1 atm.  $N_2$  (not shown). In both cases, during subsequent annealing at temperatures of 260 K and above,  $E_2(2H)$  then relaxes to  $E_0$  through loss of

H<sub>2</sub> (Figure 2-S7), as seen previously.<sup>[35]</sup>

To test whether the rate-limiting step of the E<sub>2</sub>\* → E<sub>2</sub> relaxation process involves the transfer of a proton to cryoreduced FeMo-co, we looked for kinetic isotope effects (KIE) in the annealing process. Annealing would exhibit a KIE if 77 K cryoreduction decoupled PCET, such that radiolytic electron injection into E<sub>1</sub>(H) at 77 K forms E<sub>2</sub>\*, and that E<sub>2</sub>\* → E<sub>2</sub>(2H) relaxation is rate-limited proton transfer. However Figure 2-5 shows that E<sub>2</sub>\* → E<sub>2</sub>(2H) relaxation is rate-limited proton transfer. However Figure 2-5 shows that E<sub>2</sub>\* generated by cryoreduction of samples trapped under low flux/Ar TO relaxes with the same ‘1/e’ decay time ( $\tau = 5$  min) in both H<sub>2</sub>O and D<sub>2</sub>O buffer, namely *without* a KIE. This establishes that proton transfer is not involved in the rate-limiting E<sub>2</sub>\* → E<sub>2</sub>(2H) step of the relaxation. As discussed below, we suggest that E<sub>2</sub>\* has been formed from E<sub>1</sub>(H) by coupled electron injection *and* proton transfer during cryoreduction at 77 K.

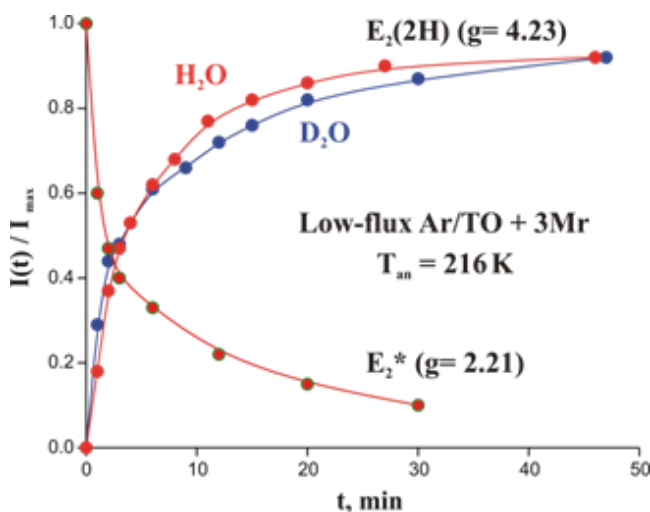


**Figure 2-5: Kinetics of formation of E<sub>2</sub>(2H) S = 3/2 1b state in H<sub>2</sub>O (red) and D<sub>2</sub>O (blue) and the decay of S = 1/2 E<sub>2</sub>\* species (g<sub>1</sub> = 2.21) (green) during annealing cryoreduced low-flux/Ar TO nitrogenase at 216 K. (Curves are to guide the eye).**

*Cryoreduction/annealing of high-flux TO samples:* In parallel experiments on

samples that contain  $E_1(\text{H})$  generated during high-flux TO under either Ar or  $\text{N}_2$  (**Figure 2-S7**), irradiation again produced  $E_2^*$  through cryoreduction of  $E_1(\text{H})$ . Overlap of the  $E_2^*$  signal with other signals in the  $g \sim 2$  region (see **Figure 2-3**) made it impossible to accurately measure its changing intensity during cryoannealing, but it was straightforward to measure the appearance of  $E_2(2\text{H})$   $S = 3/2$  formed during  $E_2^* \rightarrow E_2(2\text{H})$  relaxation. **Figure 2-6** shows that in both Ar and  $\text{N}_2$  high-flux TO the  $E_2^* \rightarrow E_2(2\text{H})$  relaxation during 216 K annealing occurs with the same time constant, namely *without* a KIE.

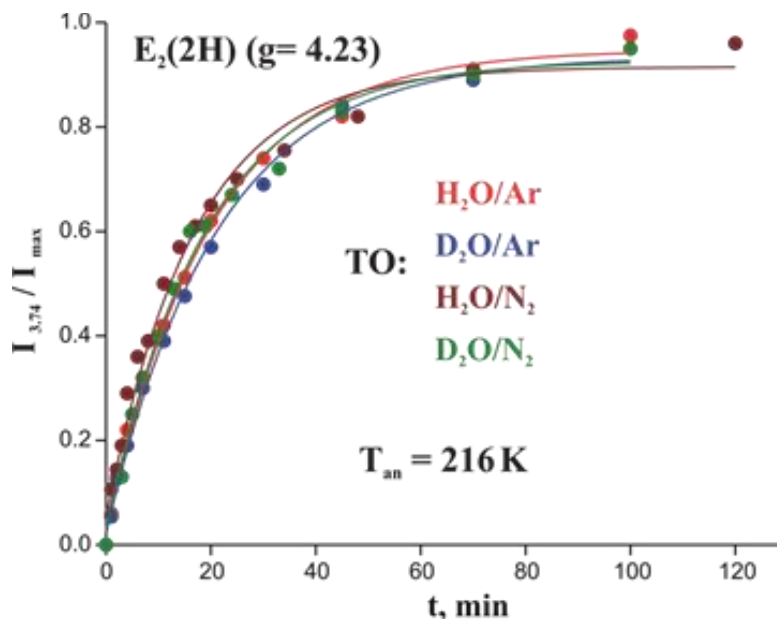


**Figure 2-6: Effect of  $\text{H}_2\text{O}$  and  $\text{D}_2\text{O}$  on kinetics of  $S = 3/2$  1b state formation during annealing cryoreduced high flux Ar and  $\text{N}_2$  TO nitrogenase at 216 K.** (Solid line, fit exponential rise with median time-constant,  $\tau = 19$  min, for the four traces).

Surprisingly, however, comparison of **Figures 2-5** and **2-6** shows that the  $E_2(2\text{H})^* \rightarrow E_2(2\text{H})$  relaxation at 216 K, seen in low-flux/Ar TO samples slows in the

presence of the high concentration of Fe protein in high-flux TO. The direct comparison of the formation of the  $E_2(2H)$  during cryoannealing, **Figure 2-7**, shows that at 216 K, the time constant for formation is  $\sim 20$  min in high flux vs from  $\sim 4.8$  min at low flux. In low-flux TO, the MoFe protein/Fe protein ratio is 50/1, so almost none of the MoFe protein exhibiting the  $E_2^*$  signal has a bound Fe protein. In high flux, the ratio is 1/1.5. As there are 2 FeMo-co per MoFe protein, this means that roughly  $\frac{3}{4}$  of the Fe protein binding sites on MoFe protein are occupied. The effects of electron flux on the relaxation is thus interpreted to mean that binding Fe protein to MoFe protein allosterically modulates the rate of  $E_2^* \rightarrow E_2(2H)$  relaxation of FeMo-co.

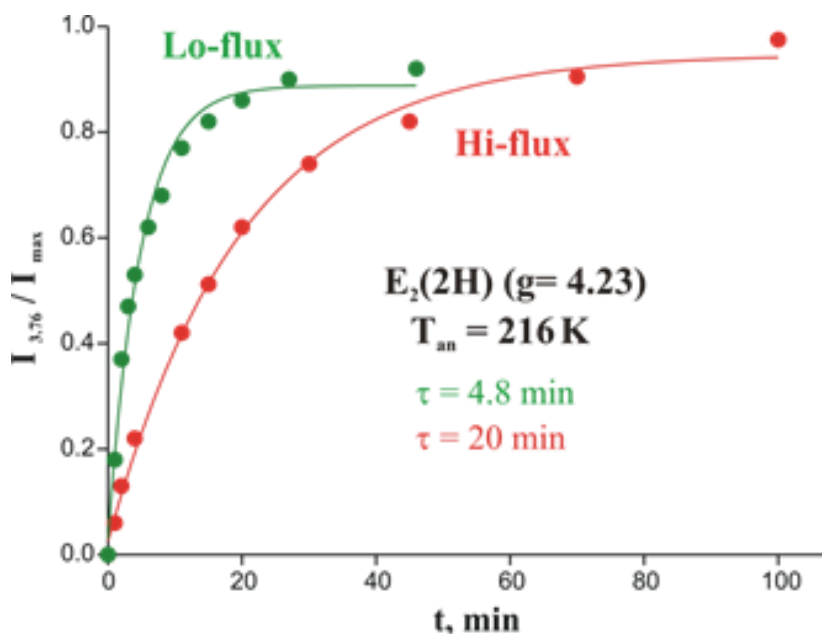


**Figure 2-7: Kinetics of formation of  $E_2(2H)$ ,  $S = 3/2$  (1b) species during annealing cryoreduced low flux (green) and high flux (red) nitrogenase Ar TO at 216 K. Solid lines: fit to exponential with time-constant,  $\tau = 5$  min (low flux) and  $\tau = 20$  min (high flux).**

*Cryoreduction/annealing of  $E_1(H)$  state generated by cryoreduction of  $E_0$ : For*

completeness, we note that if the  $E_1(H)$  state initially produced by 3 Mrad cryoreduction of  $E_0$  is annealed at 235 K, then cryoreduced again with a second 3 Mrad dose, this likewise generates the  $E_2(2H)$  state (1b signal) after annealing at  $T > 216$  K (**Figure 2-S8**). This result, combined with those presented above, show that the  $E_2(2H)$  state is the same, regardless of how it is formed.

*Effects of  $E_0$  cryoirradiation on P cluster:* The  $g \sim 2$  region of the EPR spectrum of a glycerol-containing  $E_0$  resting-state sample irradiated at 77 K with a dose of 3 Mrad shows a new feature at  $g = [1.814]$  whose entire spectrum can be seen in full after annealing up to 235 K, **Figure 2-8**.

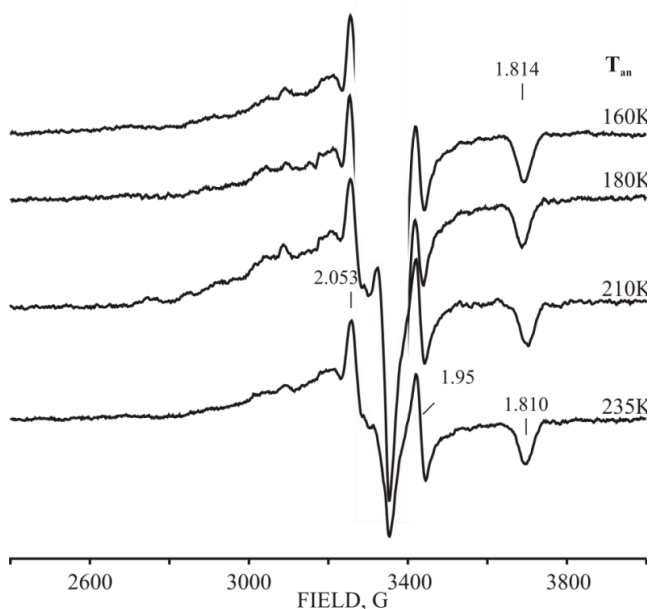


**Figure 2-8: High-field EPR spectra of resting-state nitrogenase after radiolytic cryoreduction (3 Mrad), and annealed at indicated temperatures; g-values label features associated with oxidized P-cluster (see text). Instrument conditions as in Figure 2-2. (The radiolytically generated radical signal was cut off for clarity)**

This signal is characterized by  $g = [2.05, 1.95, 1.814]$  and arises from  $P^{ox}$ ,

generated by cryooxidation of the P cluster.<sup>[2]</sup> This assignment is confirmed by the finding that this signal is ~ 2-fold stronger when a sample without added glycerol is irradiated (**Figure 2-S2**); the absence of glycerol enhances cryooxidation relative to cryoreduction,<sup>[36]</sup> Apparently, the all-ferrous state of the P cluster ( $P^N$ ) cannot be radiolytically cryoreduced to a state containing an Fe(I), but can only be radiolytically cryooxidized, and this even occurs to a degree in samples that contain glycerol. As discussed below, this observation is supportive of our proposed ‘deficit spending’ model for ET from reduced Fe protein to MoFe protein.<sup>[15]</sup> During annealing up to 235 K the  $g_3$  feature of the  $P^{OX}$  signal shifts only very slightly, to  $g_3 = 1.81$  (**Figure 2-8**).

The properties of the P cluster cryooxidized in the presence of high populations of FeMo-co in the reduced state(s) differ from those in irradiated resting-state MoFe protein (**Figure 2-4B**). Roughly  $\frac{3}{4}$  of the  $E_0$  state of FeMo-co can be converted to  $E_1(H)$  by either a high radiation dose (6 Mrad) applied to resting state MoFe or by the standard 3 Mrad dose applied to a sample freeze-quenched during low-flux TO under Ar (**Figure 2-3B, 2-S9**) or high-flux TO (not shown). During annealing of such samples at temperatures above 160-180 K intensity of  $g_3 = 1.81$  feature decreases and a new  $P^{OX}$  intermediate with  $g_{min} = 1.772$  appears. The latter relaxes to the equilibrium  $P^{OX}$   $g_{min} = 1.81$  state at higher temperatures (**Figure 2-4B, 2-S9**). The observation of the intervening, second  $P^{OX}$  conformer, which appears only in a sample with a high population of reduced FeMo-co, suggests an allosteric influence of the redox state of FeMo-co on the relaxation of cryogenerated  $P^{OX}$  cluster.

## Discussion

By combining the results from the present study with those of earlier investigations we arrive at a proposed view of the electron/proton transfer events and conformational changes that occur during accumulation of  $[e^-/H^+]$  by the MoFe protein, beginning with the  $M^{ox}$  state and going through the  $E_2(2H)$  stage of the LT scheme, **Figure 2-9**. In this figure, equilibrium states of the MoFe protein, and of FeMo-co when it had been labeled historically, are presented ‘in-line’. The characteristics of the Fe protein ( $F$ )  $\rightarrow$  MoFe protein ( $MF$ ) electron transfer, including conformational gating and  $H^+$  delivery are indicated ‘above-line’. Those processes as experienced by FeMo-co, and revealed by cryoreduction/annealing studies in the frozen state, are indicated ‘below-line’.

Considering the ‘above-line’,  $[e^-/H^+]$  delivery to MoFe protein, the  $E_0 \rightarrow E_1(1H)$  conversion associated with ET from  $Fe^{red}$  to MoFe protein is kinetically gated by a rate-limiting conformational change that does not involve a coupled proton transfer (no KIE), and uses a ‘deficit-spending’ process in which the first step is the gated transfer of an electron from the P cluster to FeMo-co, with follow-up ‘reimbursement’ of the oxidized P cluster through rapid ET from  $Fe^{red}$ .<sup>[16]</sup> The conformational gate during MoFe reduction by  $Fe^{red}$  is believed to involve motion at the Fe<sup>-</sup>protein/MoFe-protein interface.<sup>[16]</sup> ATP hydrolysis then follows ET, rather than preceding it or proceeding synchronously.<sup>[12]</sup> The LT kinetic scheme incorporates the same ‘Fe-protein cycle’ at each step of electron delivery,<sup>[2, 37]</sup> and thus each step in **Figure 2-9** shows the same ‘above-line’ gated activation/deficit-spending steps observed for the  $E_0 \rightarrow E_1(1H)$  step.

Considering the ‘below-line’ changes in FeMo-co during  $[e^-/H^+]$  delivery to the MoFe

protein, we begin on the left of **Figure 2-9**, with the  $M^{\text{ox}}$  ( $S = 0$ ) state of enzyme-bound FeMo-co prepared by oxidation of the resting state cofactor,  $M^{\text{N}}$ . The pH dependence for the midpoint potential of the reduction of  $M^{\text{ox}}$  ( $S = 0$ ) to  $M^{\text{N}}$  ( $S = 3/2$ ) in solution shows that this process is coupled with the delivery of a proton to MoFe protein.<sup>[20]</sup> However,

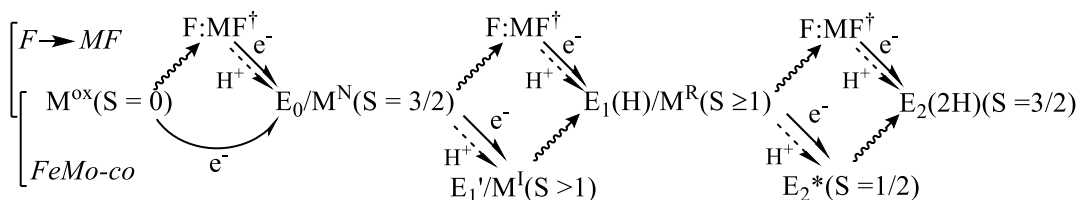


**Figure 2-9: Scheme for electron/proton delivery and conformational changes during early-stage [e-/H+] accumulation by the MoFe protein (MF) through reduction by the Fe protein (F).** *Above-line:* the ‘Fe-protein cycle’ for ET. The LT kinetic scheme incorporates the same ‘Fe-protein cycle’ at each step of electron delivery; details of the  $E_0 \rightarrow E_1(H)$  conversion process were characterized previously;<sup>[12-16]</sup> *In-line:* states of MoFe and FeMo-co (see text): solid arrow,  $e^-$  transfer; dashed arrow, proposed  $H^+$  transfer; undulating arrow, conformational change. *Below-line:* Changes in MoFe as revealed by cryoreduction/annealing, with  $M^{\text{ox}} \rightarrow E_0$  and  $E_1(H) \rightarrow E_2(2H)$  characterized in this study, and with  $E_0 \rightarrow E_1(H)$  inferred through joint consideration of present work and prior Mossbauer investigation.<sup>[17]</sup> TO conversions are in-line or below, with  $E_1(1H) \rightarrow E_2(2H)$  determined in this study.

ENDOR spectroscopy long ago showed that there is no bound proton in the vicinity of the spin-bearing metal ions of  $M^{\text{N}}$ ,<sup>[21]</sup> so the proton must be taken up by an amino acid residue, or possibly by the homocitrate bound to Mo, which has almost no local contribution from the cluster spin.<sup>[38]</sup> Despite the conversion to a high-spin state upon reduction of  $M^{\text{ox}}$ , which implies a major change in the spin-coupling scheme, the present finding that cryoreduction directly converts  $M^{\text{ox}}$  to  $M^{\text{N}}$  at 77K indicates that these two FeMo-co states exhibit at most minimal structural differences, probably only the



‘breathing’ caused by changes in metal-metal distances as seen by EXAFS spectroscopy.<sup>[39]</sup> Thus, during the  $M^{ox} \rightleftharpoons M^N$  redox process FeMo-co behaves like a ‘simple’ electron-transfer cluster.

The behavior of the cofactor during electron/proton accumulation steps that form part of the catalytic cycle is quite different. The Mossbauer/cryoreduction studies imply that FeMo-co itself undergoes a substantial conformational change upon the cofactor  $M^N \rightarrow M^R$  reduction. Thus, the Mossbauer study showed that TO generates an equilibrium  $E_1(H)$  state that contains an equilibrium form of reduced FeMo-co,  $M^R$ ,<sup>[17]</sup> ( $S \geq 0$ ) without a major change in spin coupling among the Fe ions,<sup>[17]</sup> whereas 77 K cryoreduction produces an alternative FeMo-co state,  $M^I$ , with a major change in spin coupling. We conclude that the non-equilibrium  $M^I$  cofactor exhibits structural differences from  $M^R$ , FeMo-co in the  $E_1(H)$  state, and that cryoannealing  $E_1'$  would allow it to undergo conformational relaxation to the equilibrium  $E_1(1H)$ , with an accompanying  $M^I \rightarrow M^R$  conformational change, **Figure 2-9**.

Consider next the  $E_1(1H) \rightarrow E_2(2H)$  step of electron/proton delivery, **Figure 1-1**. As there was no direct evidence regarding electron/proton coupling or conformational rearrangements at FeMo-co itself during this TO process, we here turned to the cryoreduction/annealing/EPR protocol. The suite of these experiments reported here imply that 77 K radiolytic reduction of the  $E_1(H)$  state produces a low-spin ( $S = 1/2$ ,  $g = [2.21, 2.08, nd]$ ), doubly-reduced FeMo-co, denoted  $E_2^*$ , trapped in a non-equilibrium conformation characteristic of the  $E_1(H)$  precursor.  $E_2^*$  relaxes to the equilibrium  $E_2(2H)$  conformation (1b,  $S=3/2$  signal) upon annealing at relatively high temperature,  $T \gtrsim$

210K, **Figure 2-4A**. This process occurs without a KIE, which establishes that protonation of the cryoreduced FeMo-co  $E_2^*$  is not the rate-limiting step of the relaxation. This low-spin ( $S = 1/2$ ) to high-spin ( $S = 3/2$ ) process must therefore involve as its rate-limiting step a conformational relaxation at FeMo-co that leads to a change in the cluster spin-coupling scheme.

The equilibrium  $E_2(2H)$  state must have received two protons at or on a residue adjacent to FeMo-co, given that this state relaxes directly to  $E_0$  with loss of  $H_2$ . Given that protonation of FeMo-co is not the rate-limiting step in the observed  $E_2^* \rightarrow E_2(2H)$  relaxation, in principle cryoreduction/annealing of  $E_1(H)$  could be following one of two pathways. (i) It might be that cryoradiolysis induces PCET to FeMo-co, with proton transfer coupled to the radiolytic reduction process at 77 K, in which case, the ( $S = 1/2$ ) cofactor of  $E_2^*$  is the product of PCET (and the state thus may be denoted,  $E_2^*(2H)$ ) that is trapped in a conformation appropriate to  $E_1(H)$ . Then, during cryoannealing  $E_2^*(2H)$  undergoes conformational relaxation to the equilibrium  $E_2(2H)$  ( $S = 3/2$ ) state seen when nitrogenase is freeze-trapped under TO. (ii) Alternatively, cryoreduction/annealing could decouple electron and proton transfer to FeMo-co, such that the  $E_2^*$  state is produced by electron injection into FeMo-co without proton delivery (and the MoFe state thus might be denoted  $E_2^*(H)$ ). In this case, the present results would indicate that during 216 K cryoannealing  $E_2^*(H)$  undergoes rate-limiting conformational relaxation followed by rapid, non-rate limiting, proton delivery to form the equilibrium  $E_2(2H)$  state. Possible structure-modulation of FeMo-co during the catalytic cycle has been considered many times in the past, one example being as a possible role for the interstitial carbide of

FeMo-co.<sup>[40-42]</sup>

Analogy to our studies of cryoreduction of oxy-ferroheme complexes<sup>[23]</sup> support pathway (i): cryoreduction of E<sub>1</sub>(H) at 77 K generates E<sub>2</sub>\* (2H) through PCET, namely the delivery of *both* an electron and proton to FeMo-co. During radiolysis of an oxy-ferrous hemoprotein<sup>[23]</sup> at low temperature, the initial (primary) product of electron injection is the non-protonated ferric-peroxo intermediate. However, when the parent oxy hemoprotein complex has a proton-delivery network tied to the peroxo ligand through H-bonding to a water molecule, the peroxo intermediate is promptly protonated upon cryoreduction at 77 K or below.<sup>[23]</sup> Indeed, with oxy heme oxygenase we saw such PCET through prompt protonation by proton tunneling at 6 K!<sup>[25]</sup> Detailed analyses of the MoFe protein crystal structure<sup>[43-44]</sup> in fact have identified three proton-delivery networks tied to FeMo-co: a water-filled channel running from the protein exterior to the homocitrate ligand of FeMo-co and two hydrogen-bonded chains to sulfur atoms of FeMo-co.<sup>[43-44]</sup> The presence of these networks supports the proposal that E<sub>2</sub>\* is the product of 77 K PCET to E<sub>1</sub>(H), but is trapped in a non-equilibrium  $S = 1/2$  conformation, E<sub>2</sub>\* (2H), which relaxes to the equilibrium E<sub>2</sub>(2H) ( $S = 3/2$ ) conformer during cryoannealing. This proposal is even more strongly supported by our cryoannealing studies of E<sub>4</sub>(4H). These experiments show that E<sub>2</sub>(2H) and E<sub>4</sub>(4H) indeed have their full complement of  $n$  protons ‘stored’ at FeMo-co, for  $n = 4$ , as two bridging hydrides and two protons: these two states respectively relax to the resting state by the stoichiometric release of ‘protons’ in the form of one and by two H<sub>2</sub>,<sup>[3, 35]</sup>

This proposal implies that the proton delivery network that supplies FeMo-co

with the proton during PCET must likewise be well-poised for proton delivery in fluid-solution at ambient temperatures, and can deliver the proton essentially in synchrony with electron delivery. As is well understood,<sup>[18-19]</sup> this behavior would seem mandatory in order to minimize the driving force needed to reduce FeMo-co, because it obviates the energetically costly buildup of charge associated with ET in the absence of proton transfer. It would also seem mandatory in reducing the driving force needed to reduce N<sub>2</sub>: the electron delivery by the Fe protein in effect would correspond to transfer of the net-neutral components of an H atom, not electron delivery first, followed by delivery of a proton. The LT kinetic scheme incorporates the same ‘Fe-protein cycle’, at each of the  $n = 1-8$  steps of electron/proton delivery, and thus would at least incorporate the same TO processes described here at each step. The alternative interpretation of our data, that proton delivery occurs only after a conformation/spin change that occurs after electron delivery cannot be ruled out, but would seem to carry all the disadvantages implied directly above.

*Summary:* **Figure 2-9** summarizes our view of the electron/proton transfer events and conformational changes that occur during accumulation of [e-/H+] by the MoFe protein, starting with the non-catalytic M<sup>ox</sup> state, through the E<sub>2</sub>(2H) stage of the LT scheme (**Figure 2-1**). In keeping with this scheme, the same reduction process is taken to occur at each stage: the gated/deficit-spending electron delivery shown to occur in E<sub>1</sub>(1H) → E<sub>2</sub>(2H) reduction.<sup>[12-16]</sup>

Reduction of the M<sup>ox</sup> state of the MoFe protein to E<sub>0</sub> was previously shown to occur through [e-/H+] PCET to MoFe protein,<sup>[20]</sup> but with the proton delivered to a site

remote from the paramagnetic metal ions of FeMo-co.<sup>[21]</sup> The present cryoreduction/annealing study shows FeMo-co does not undergo a major change of conformation during this process, thus acting merely as a ‘simple’ electron-transfer cluster. In contrast, cryoreduction/Mossbauer studies have shown that FeMo-co undergoes substantial conformational changes during the reduction of E<sub>0</sub> to E<sub>1</sub>(1H), the first step in catalysis.

Likewise, the present cryoreduction/annealing/EPR studies show that FeMo-co in the E<sub>1</sub>(1H) and E<sub>2</sub>(2H) states of the nitrogenase catalytic cycle exhibit significant conformational differences. The experimental results further suggest that the E<sub>1</sub>(1H) → E<sub>2</sub>(2H) step involves coupled delivery of a proton and electron (PCET) to FeMo-co of E<sub>1</sub>(H) subsequent to the gating step associated with electron delivery from reduced Fe protein, with the proton-delivery likely involving the proton network(s) seen crystallographically.<sup>[43-44]</sup> This PCET generates a non-equilibrium  $S = 1/2$  form E<sub>2</sub>(2H)\*, which subsequently undergoes conformational relaxation and attendant change in FeMo-co spin state, to generate the equilibrium E<sub>2</sub>(2H) ( $S = 3/2$ ) state.

These experiments have additional implications. Turning to the P cluster, we note the observation that the strongly reducing electrons generated by cryoradiolysis do not reduce P cluster. Rather, the observed oxidation of the P cluster under these reducing conditions supports the idea that electron delivery from reduced Fe protein to MoFe protein *cannot* occur via the stepwise process that begins with reduction of P cluster by reduced Fe protein with follow-up reduction of FeMo-co by reduced P cluster. Rather, this result supports our ‘deficit spending’ model for electron delivery, in which the first

step is reduction of FeMo-co by P<sup>N</sup> cluster, followed by rapid reduction of the resulting P<sup>ox</sup> by reduced Fe protein.<sup>[12-16]</sup>

Finally, as remarkable and unexpected findings, the reduction of FeMo-co allosterically influences the P-cluster conformation, while the binding of Fe protein allosterically modulates the relaxation of FeMo-co during the E<sub>2</sub>\*→E<sub>2</sub> relaxation. Such conformational coupling between FeMo-co and P-cluster, and between Fe protein binding and FeMo-co, could play a role in the gated ET from reduced Fe protein to FeMo-co revealed in our earlier work.<sup>[16]</sup>

#### References:

- [1] V. Smil, *Enriching the Earth: Fritz Haber, Carl Bosch, and the Transformation of World Food Production*, MIT Press, Cambridge, MA, **2001**.
- [2] B. K. Burgess, D. J. Lowe, *Chem. Rev.* **1996**, *96*, 2983-3012.
- [3] B. M. Hoffman, D. Lukoyanov, Z. Y. Yang, D. R. Dean, L. C. Seefeldt, *Chem. Rev.* **2014**, *114*, 4041-4062.
- [4] R. N. F. Thorneley, D. J. Lowe, *Metal Ions in Biology* **1985**, *7*, 221-284.
- [5] R. Thorneley, D. Lowe, *Biochem. J.* **1984**, *224*, 887.
- [6] D. Lukoyanov, Z. Y. Yang, N. Khadka, D. R. Dean, L. C. Seefeldt, B. M. Hoffman, *J. Am. Chem. Soc.* **2015**, *137*, 3610-3615.
- [7] Z.-Y. Yang, N. Khadka, D. Lukoyanov, B. M. Hoffman, D. R. Dean, L. C. Seefeldt, *Proc. Natl. Acad. Sci. U.S.A.* **2013**, *110*, 16327-16332.

- [8] B. M. Hoffman, D. Lukoyanov, D. R. Dean, L. C. Seefeldt, *Acc. Chem. Res.* **2013**, *46*, 587-595.
- [9] D. Lukoyanov, Z.-Y. Yang, B. M. Barney, D. R. Dean, L. C. Seefeldt, B. M. Hoffman, *Proc. Natl. Acad. Sci. U.S.A.* **2012**, *109*, 5583-5587.
- [10] In contrast, for example to the suggestion that roughly stoichiometric production of H<sub>2</sub> occurs at the P cluster in a mechanistically uncoupled fashion, see ref [11].
- [11] F. B. Simpson, R. H. Burris, *Science* **1984**, *224*, 1095–1097.
- [12] S. Duval, K. Danyal, S. Shaw, A. K. Lytle, D. R. Dean, B. M. Hoffman, E. Antony, L. C. Seefeldt, *Proc. Natl. Acad. Sci. U.S.A.* **2013**, *110*, 16414-16419.
- [13] L. C. Seefeldt, B. M. Hoffman, D. R. Dean, *Curr. Opin. Chem. Biol.* **2012**, *16*, 19-25.
- [14] D. Mayweather, K. Danyal, D. R. Dean, L. C. Seefeldt, B. M. Hoffman, *Biochemistry* **2012**, *51*, 8391-8398.
- [15] K. Danyal, D. R. Dean, B. M. Hoffman, L. C. Seefeldt, *Biochemistry* **2011**, *50*, 9255-9263.
- [16] K. Danyal, D. Mayweather, D. R. Dean, L. C. Seefeldt, B. M. Hoffman, *J. Am. Chem. Soc.* **2010**, *132*, 6894-6895.
- [17] S. J. Yoo, H. C. Angove, V. Papaefthymiou, B. K. Burgess, E. Münck, *J. Am. Chem. Soc.* **2000**, *122*, 4926-4936.
- [18] D. R. Weinberg, C. J. Gagliardi, J. F. Hull, C. F. Murphy, C. A. Kent, B. C. Westlake, A. Paul, D. H. Ess, D. G. McCafferty, T. J. Meyer, *Chem. Rev.* **2012**, *112*, 4016-4093.

- [19] A. Migliore, N. F. Polizzi, M. J. Therien, D. N. Beratan, *Chem. Rev.* **2014**, *114*, 3381-3465.
- [20] M. J. O'Donnell, B. E. Smith, *Biochem. J.* **1978**, *173*, 831-838.
- [21] B. M. Hoffman, J. E. Roberts, W. H. Orme-Johnson, *J. Am. Chem. Soc.* **1982**, *104*, 860-862.
- [22] R. V. Hageman, R. H. Burris, *Proc. Natl. Acad. Sci. U.S.A.* **1978**, *75*, 2699-2702.
- [23] R. Davydov, B. M. Hoffman, *Arch. Biochem. Biophys.* **2011**, *507*, 36-43.
- [24] R. Davydov, M. Laryukhin, A. Ledbetter-Rogers, M. Sono, J. H. Dawson, B. M. Hoffman, *Biochemistry* **2014**, *53*, 4894-4903.
- [25] R. Davydov, S. Chemerisov, D. E. Werst, T. Rajh, T. Matsui, M. Ikeda-Saito, B. M. Hoffman, *J. Am. Chem. Soc.* **2004**, *126*, 15960-15961.
- [26] J. Christiansen, P. J. Goodwin, W. N. Lanzilotta, L. C. Seefeldt, D. R. Dean, *Biochemistry* **1998**, *37*, 12611-12623.
- [27] P. K. Glasoe, F. A. Long, *J. Phys. Chem.* **1960**, *64*, 188-190.
- [28] C. E. Davoust, P. E. Doan, B. M. Hoffman, *J. Magn. Reson.* **1996**, *119*, 38-44.
- [29] H. Zipse, E. Artin, S. Wnuk, G. J. S. Lohman, D. Martino, R. G. Griffin, S. Kacprzak, M. Kaupp, B. Hoffman, M. Bennati, J. Stubbe, N. Lees, *J. Am. Chem. Soc.* **2009**, *131*, 200-211.
- [30] D. Lukoyanov, Z. Y. Yang, S. Duval, K. Danyal, D. R. Dean, L. C. Seefeldt, B. M. Hoffman, *Inorg. Chem.* **2014**, *53*, 3688-3693.
- [31] K. Fisher, W. E. Newton, D. J. Lowe, *Biochemistry* **2001**, *40*, 3333-3339.
- [32] R. Davydov, B. M. Hoffman, *J. Biol. Inorg. Chem* **2008**, *13*, 357-369.



- [33] Cryoirradiation further creates weak features in the low-field region at  $g = 4.91$  and  $5.31$  (Fig 4), as well as again causing the appearance of a weak  $S = \frac{1}{2} P^{\text{ox}}$  signal (not shown).
- [34] Those spectra also show an additional feature at  $g = 1.78$  that can be assigned to a second conformer of cryogenerated Pox, which relaxes to the  $g = 1.82$  conformation during step-annealing.
- [35] D. Lukoyanov, B. M. Barney, D. R. Dean, L. C. Seefeldt, B. M. Hoffman, *Proc. Natl. Acad. Sci. U.S.A.* **2007**, *104*, 1451-1455.
- [36] K. Rupnik, Y. Hu, C. C. Lee, J. A. Wiig, M. W. Ribbe, B. J. Hales, *J. Am. Chem. Soc.* **2012**, *134*, 13749-13754.
- [37] P. E. Wilson, A. C. Nyborg, G. D. Watt, *Biophys. Chem.* **2001**, *91*, 281-304.
- [38] D. Lukoyanov, Z.-Y. Yang, D. R. Dean, L. C. Seefeldt, B. M. Hoffman, *J. Am. Chem. Soc.* **2010**, *132*, 2526-2527.
- [39] J. Christiansen, R. C. Tittsworth, B. J. Hales, S. P. Cramer, *J. Am. Chem. Soc.* **1995**, *117*, 10017-10024.
- [40] T. Spatzal, M. Aksoyoglu, L. M. Zhang, S. L. A. Andrade, E. Schleicher, S. Weber, D. C. Rees, O. Einsle, *Science* **2011**, *334*, 940-940.
- [41] K. M. Lancaster, M. Roemelt, P. Eitzenhuber, Y. Hu, M. W. Ribbe, F. Neese, U. Bergmann, S. DeBeer, *Science* **2011**, *334*, 974-977.
- [42] J. S. Anderson, J. Rittle, J. C. Peters, *Nature* **2013**, *501*, 84-87.
- [43] M. C. Durrant, *Biochem. J.* **2001**, *355*, 569-576.
- [44] I. Dance, *Inorg. Chem.* **2013**, *52*, 13068-13077.

## **APPENDIX**

### **SUPPLEMENTARY INFORMATION**

**EXPLORING ELECTRON/PROTON TRANSFER AND CONFORMATIONAL  
CHANGES IN THE NITROGENASE MOFE PROTEIN AND FEMO-  
COFACTOR THROUGH CRYOREDUCTION/EPR MEASUREMENTS**

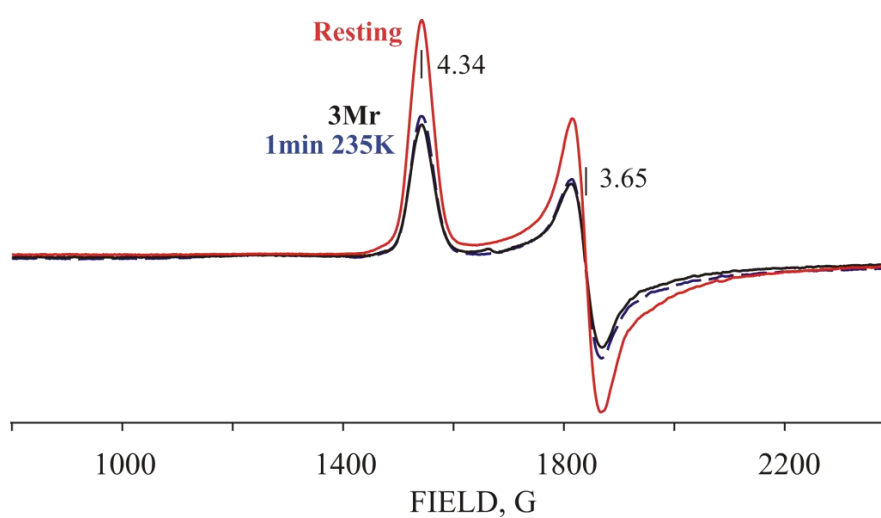


**Figure 2-S1a X-band EPR spectra of resting state nitrogenase before (red) and after radiolytic cryoreduction (3 Mrad, black) and subsequent it's annealing at 235K for 1 min (blue dashed). Instrument conditions: microwave power 5 mW, modulation amplitude of 10G, microwave frequency 9.367 GHz, T = 4 K.**

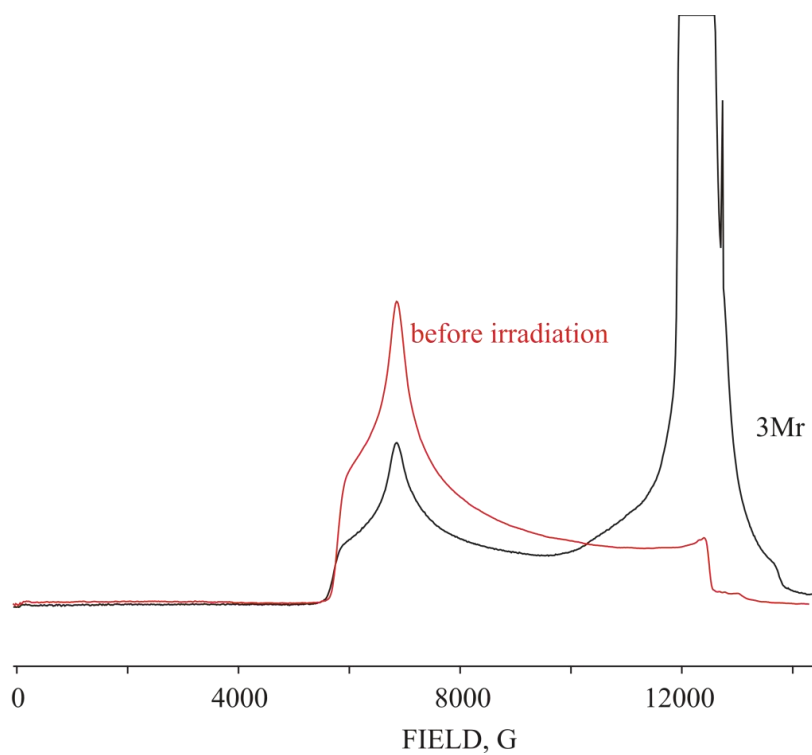


**Figure 2-S1b 2 K 35 GHz EPR spectra of resting state nitrogenase before (red) and after radiolytic cryoreduction (3 Mrad, black).** Instrument conditions: modulation amplitude of 1G, microwave frequency =34.98 GHz, T=2 K.

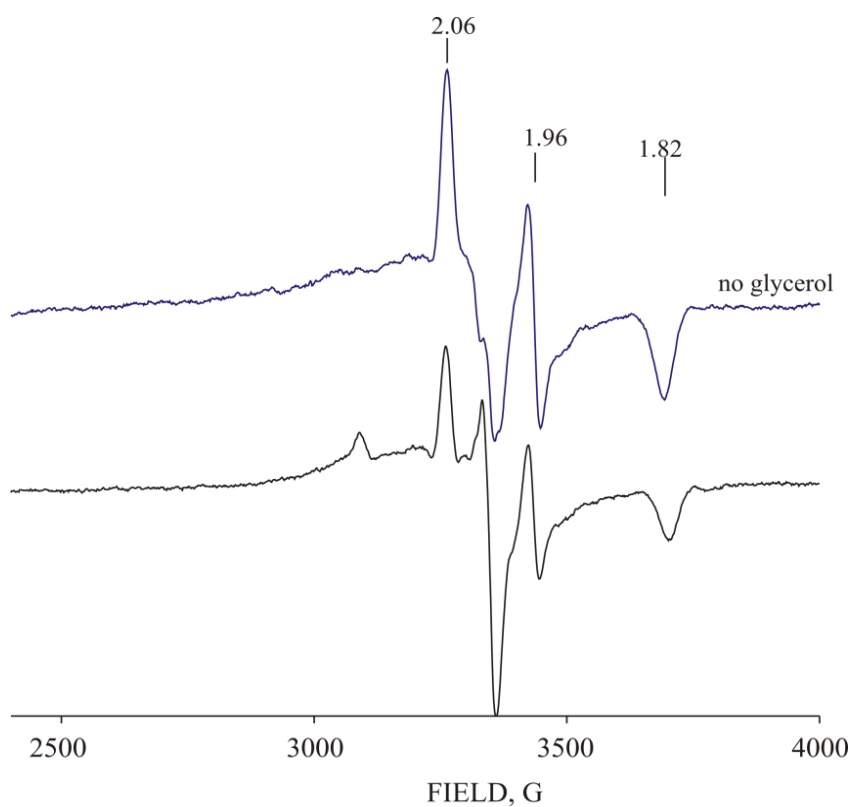


**Figure 2-S2 X-band EPR spectra of cryogenerated oxidized P cluster in  $\gamma$ -irradiated resting state nitrogenase prepared without and in the presence of 10% glycerol.** Instrument conditions: Microwave power 5mW, modulation amplitude of 5 G, microwave frequency 9.367 GHz; T=11 K.

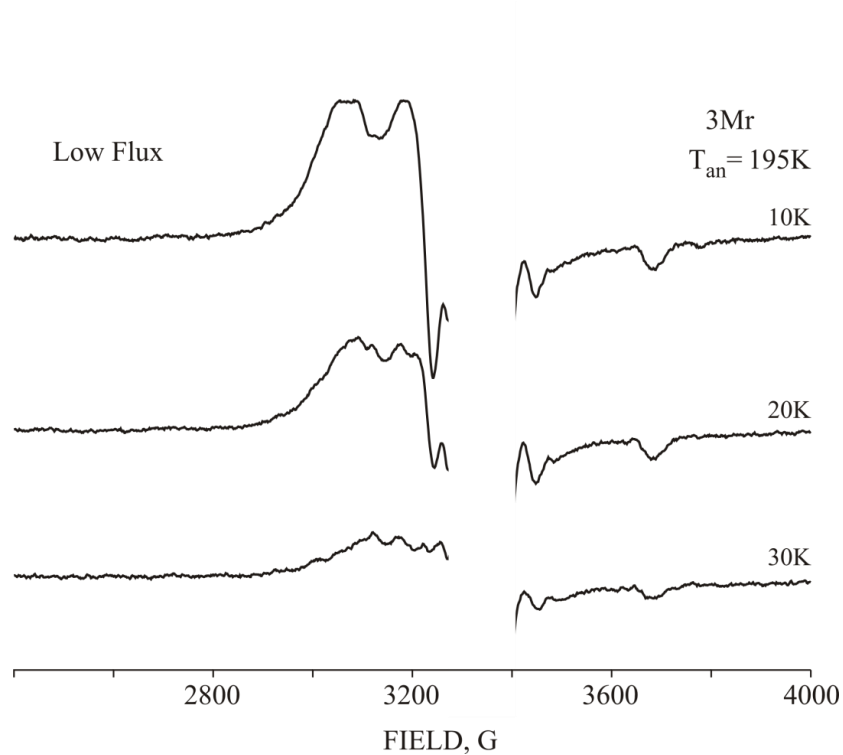


**Figure 2-S3 Effect of temperature on EPR spectra of the cryogenerated  $S = 1/2$  intermediate of cryoreduced low-flux Ar turnover nitrogenase.** Instrument conditions as in **Figure 2-S2**. (Strong radical signal within range 3300 – 3400G was omitted for clarity)

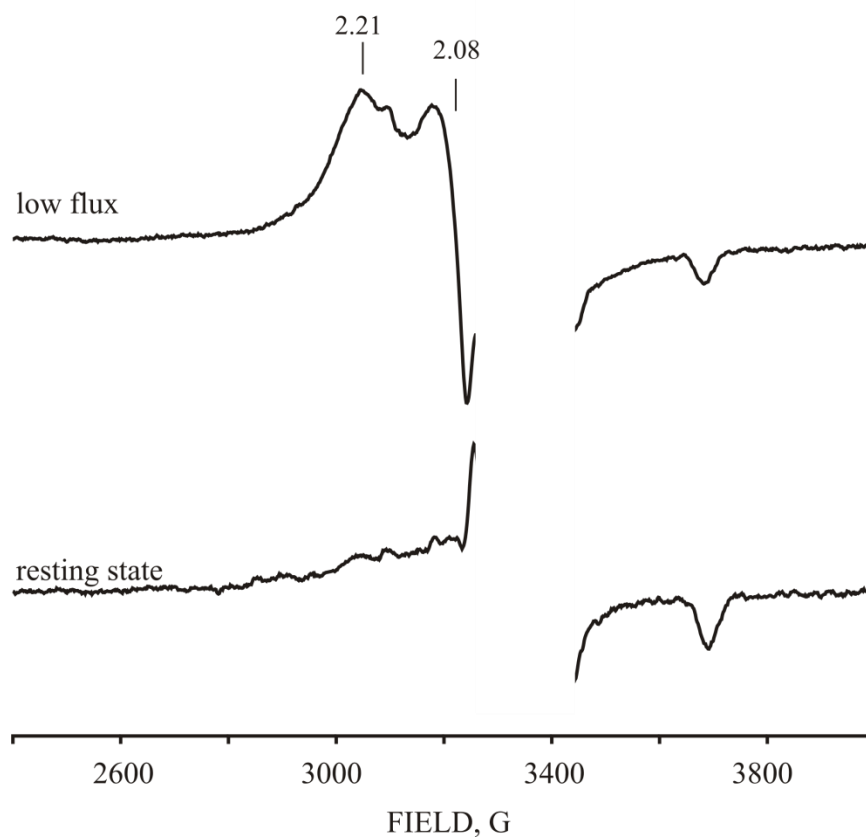


**Figure 2-S4. High field EPR spectra of cryoreduced nitrogenase in resting state and prepared at low flux under Ar turnover annealed at 160 K for 1 min.** Instrument conditions as in **Figure 2-S2**. (The radiolytically generated radical signal was omitted for clarity)

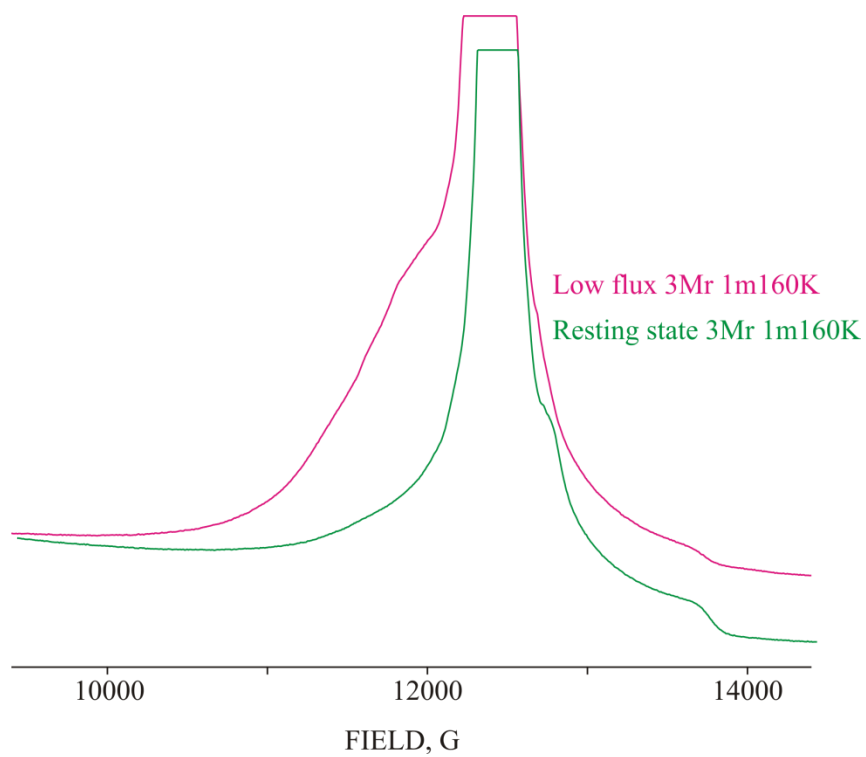


**Figure 2-S5. 2K 35GHz EPR spectra of cryoreduced resting state and low flux TO nitrogenase annealed at 160 K for 1 min. Instrument conditions as in Figure 2-S1a.**



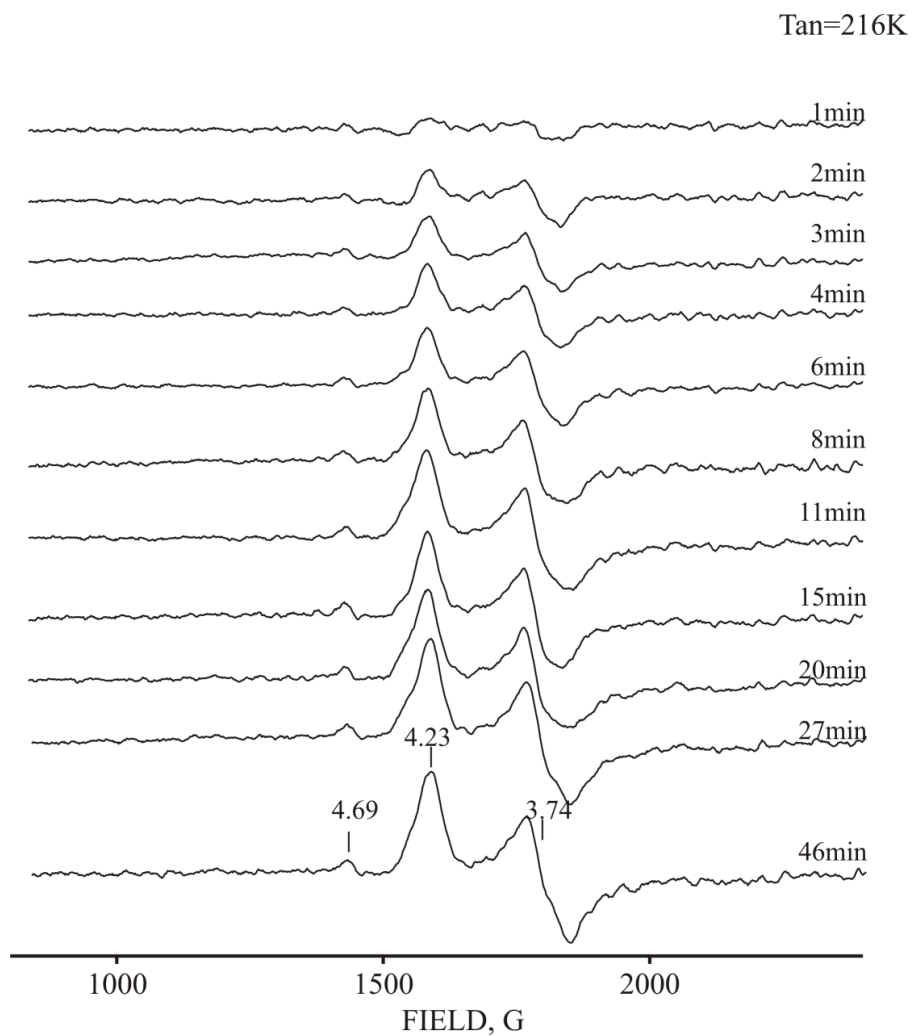


**Figure 2-S6 Time course of growth of S=3/2 1b EPR signal (difference spectrum, see Figure 2-4A) during annealing cryoreduced low-flux Ar turnover nitrogenase at 216 K.** Instrument conditions: Microwave power of 5 mW, modulation amplitude of 5 G; microwave frequency = 9.375 GHz; T=4 K.

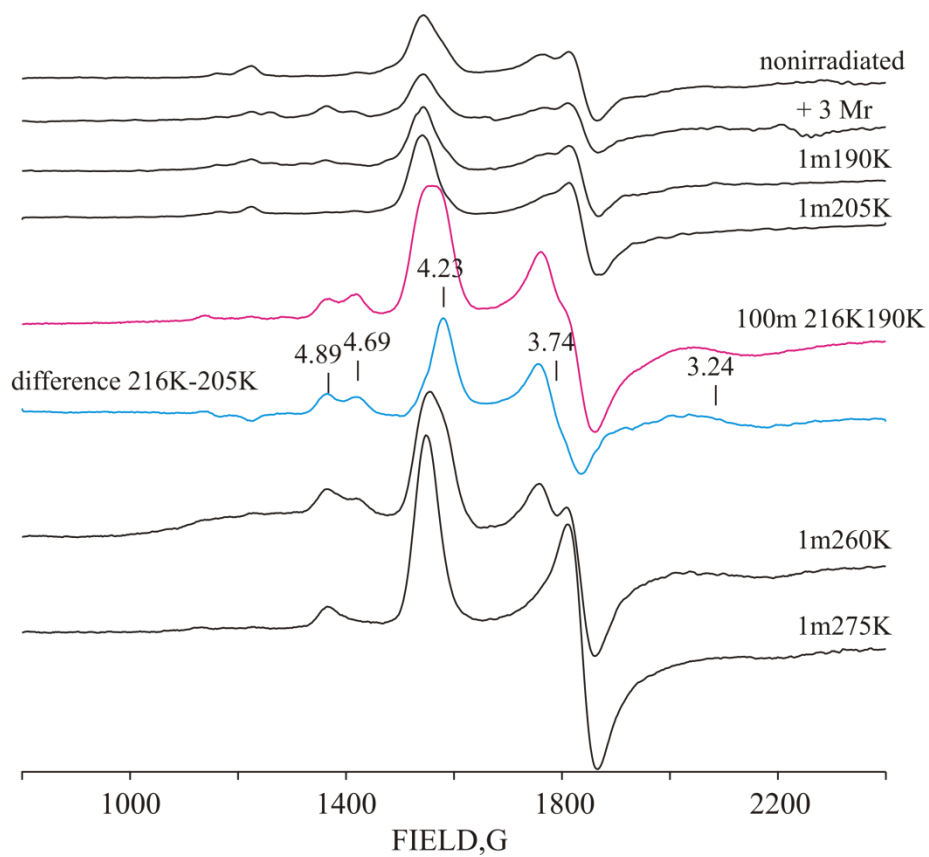


**Figure 2-S7. EPR spectra of the cryoreduced high flux Ar turnover nitrogenase annealed at indicated temperatures. Instrument conditions as in Figure 2-S6.**

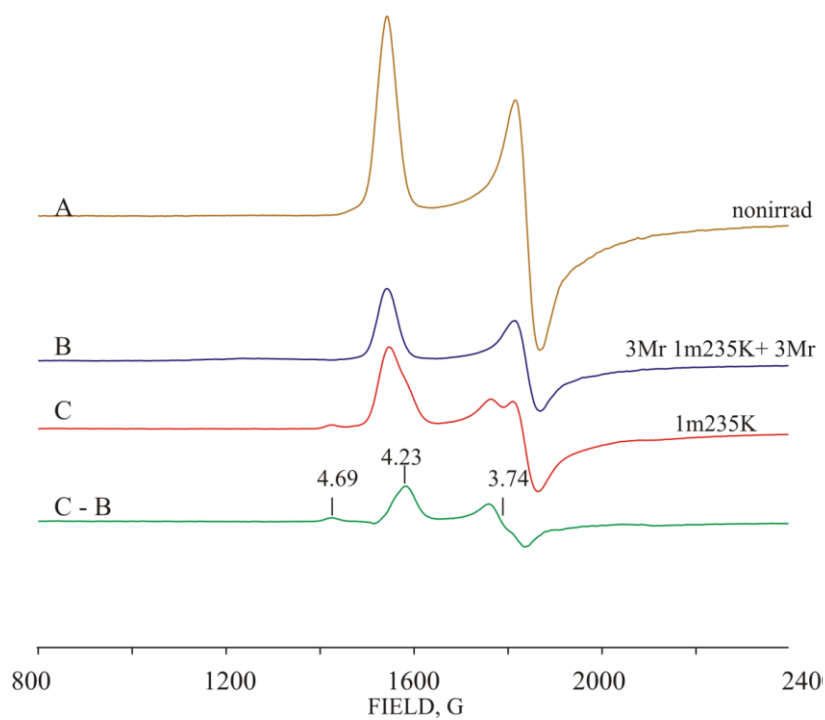


**Figure 2-S8.** Low field EPR spectra of the cryoreduced  $E_1$  state (B) that was generated by cryoreduction of nitrogenase in resting state (A) and followed subsequent annealing at 235 K (C) EPR spectrum of (B) after annealing at 235 K for 1 min. Instrument conditions as in Figure 2-S6.

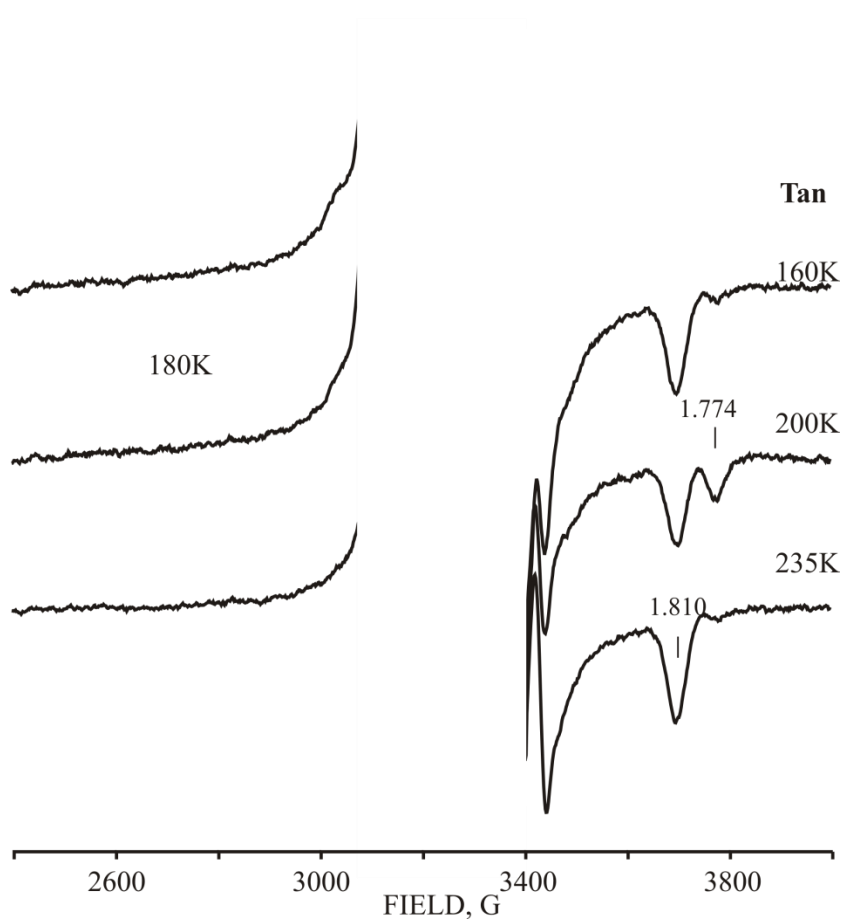


**Figure 2-S9. EPR spectra of cryogenerated oxidized P cluster in resting state nitrogenase exposed to  $\gamma$ -irradiation at 77 K with dose 9 Mrad after annealing at 160 -235 K for 1 min.** Instrument conditions as in **Figure 2-S2.**(The strong radiolitically generated radical signal within the 3100-3300 G range was omitted for clarity)

## CHAPTER 3

CO<sub>2</sub> REDUCTION CATALYZED BY NITROGENASE: PATHWAYS TO  
FORMATE, CARBON MONOXIDE, AND METHANE**Abstract**

The reduction of N<sub>2</sub> to NH<sub>3</sub> by Mo-dependent nitrogenase at its active-site metal cluster FeMo-cofactor utilizes reductive elimination (*re*) of Fe-bound hydrides with obligatory loss of H<sub>2</sub> to activate the enzyme for binding/reduction of N<sub>2</sub>. Earlier work showed that wild type nitrogenase and a nitrogenase with amino acid substitutions in the MoFe protein near FeMo-cofactor can catalytically reduce CO<sub>2</sub> by 2 or 8 electrons/protons to carbon monoxide (CO) and methane (CH<sub>4</sub>) at low rates. Here, it is demonstrated that nitrogenase preferentially reduces CO<sub>2</sub> by 2 electrons/protons to formate (HCOO<sup>-</sup>) at rates >10 times higher than rates of CO<sub>2</sub> reduction to CO and CH<sub>4</sub>. Quantum mechanical (QM) calculations on the doubly-reduced FeMo-cofactor with a Fe-bound hydride and S-bound proton (E<sub>2</sub>(2H) state) favor a direct reaction of CO<sub>2</sub> with the hydride ('direct hydride transfer' reaction pathway), with facile hydride transfer to CO<sub>2</sub> yielding formate. In contrast, a significant barrier is observed for reaction of Fe-bound CO<sub>2</sub> with the hydride ('associative' reaction pathway), which leads to CO and CH<sub>4</sub>. Remarkably, in the direct hydride transfer pathway, the Fe-H behaves as a hydridic hydrogen, whereas in the associative pathway it acts as a protic hydrogen. MoFe proteins with amino acid substitutions near FeMo-cofactor ( $\alpha$ -70<sup>Val→Ala</sup>,  $\alpha$ -195<sup>His→Gln</sup>) are found to

---

\*Coauthored by Nimesh Khadka, Dennis R. Dean, Dayle Smith, Brian M. Hoffman, Simone Raugei, Lance C. Seefeldt, (2016) *Inorganic Chemistry* **55** (17), 8321-8330]. Copyright © [2016] American Chemical Society. Reprinted with permission.

significantly alter the distribution of products between formate and CO/CH<sub>4</sub>.

## Introduction

Nitrogenase catalyzes the reduction of dinitrogen (N<sub>2</sub>) to two ammonia (NH<sub>3</sub>) molecules,<sup>1</sup> the largest contribution of ‘fixed nitrogen’ in the global biogeochemical nitrogen cycle.<sup>2</sup> The reduction of N<sub>2</sub> by Mo-dependent nitrogenase occurs at the FeMo-cofactor (7Fe-9S-1Mo-1C-1R homocitrate) contained within the nitrogenase MoFe protein (**Figure 3-1a**).<sup>3</sup>

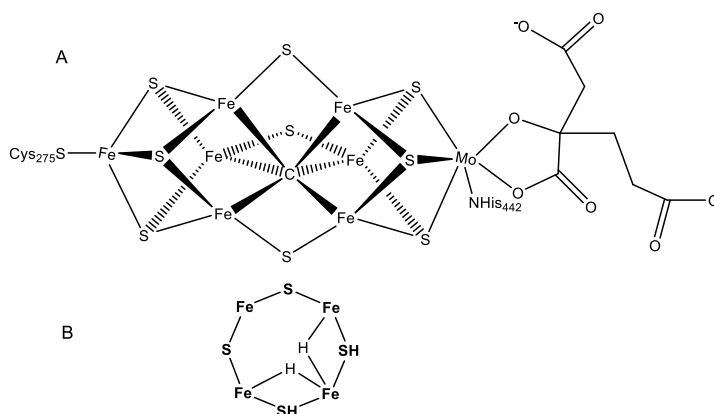


**Figure 3-1: FeMo-co of nitrogenase.** (A) Shown is FeMo-co with the  $\alpha$ -Cys275 and  $\alpha$ -His442 ligands and *R*-homocitrate (right). (B) One FeS face of FeMo-co is shown in the proposed bridging dihydride E<sub>4</sub> state with two protons associated with sulfides. Not shown are several possible binding modes for the hydrides.

Early kinetic studies indicated that FeMo-co must accumulate 4 electrons and protons (the E<sub>4</sub>(4H) state in the Lowe and Thorneley (LT) kinetic model) before the first step of N<sub>2</sub> reduction,<sup>4</sup> with the electrons delivered one at a time by the nitrogenase Fe protein,<sup>5</sup> before N<sub>2</sub> can be reduced, and that N<sub>2</sub> binding coincides with the evolution of one equivalent of H<sub>2</sub>.<sup>6</sup> Recently, analysis of the reactivity of proteins with amino acid substitutions, coupled with advanced spectroscopic studies of trapped intermediates

isotopically labelled at the metal ions and substrates, has identified the intermediates postulated in this kinetic model.<sup>7-10</sup> In particular, the reactive  $E_4(4H)$  state has been revealed to contain two [Fe-H-Fe] bridging hydrides bound to a particular 4Fe-4S FeMo-co face (**Figure 3-1b**).<sup>7,8,11-13</sup> For charge balance, the  $E_4$  state is also assumed to contain 2 bound protons, likely bound to one or more of the sulfides of FeMo-co, hence the notation,  $E_4(4H)$ .<sup>9</sup>

These experiments have further established that  $E_4(4H)$  *necessarily* undergoes a loss of  $H_2$  during  $N_2$  binding/reduction, with the consequence that  $N_2$  reduction requires the delivery of a total of eight electrons/protons to the MoFe protein.<sup>12,13,12,13</sup> This kinetically and thermodynamically reversible equilibrium binding of  $N_2$  to  $E_4(4H)$  with  $H_2$  release has been proposed to involve reductive elimination (*re*) of the two hydrides forming  $H_2$ , with concomitant reduction of  $N_2$  to a diazenido-level, metal-bound state  $M(2N_2H)$  (**Figure 3-2**, right side).<sup>9</sup> Four subsequent electron/proton addition steps ultimately lead to the formation of two  $NH_3$  molecules and return FeMo-co to the resting ( $E_0$ ) state.

In addition to reducing  $N_2$  and protons, nitrogenase can reduce a number of small, multiply bonded compounds.<sup>14,15</sup> Reduction of acetylene ( $C_2H_2$ ) to ethylene ( $C_2H_4$ ) is commonly used as an activity assay.<sup>16</sup> We recently showed acetylene reduction involves migratory insertion (*mi*) of bound  $C_2H_2$  into a Fe-H bond to form an Fe-alkenyl intermediate, followed by reductive elimination of ethylene.<sup>17</sup> Substitution of one or more 'gatekeeper' amino acids in the protein environment surrounding FeMo-co has been shown to relax the native enzyme's size restriction on compounds that can gain access to

FeMo-co for reduction, and to control the distribution of electrons between competing

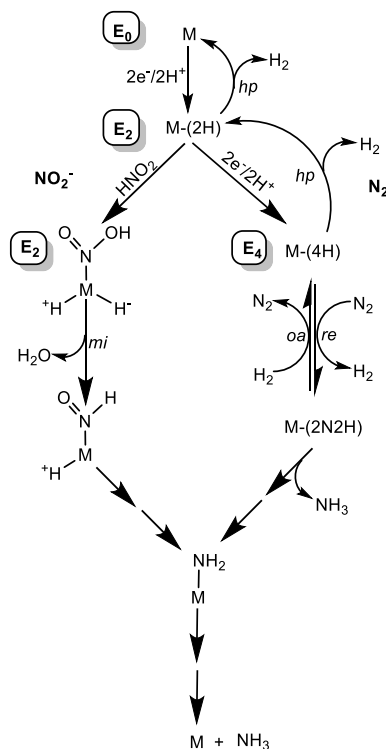


**Figure 3-2. Pathways for N<sub>2</sub> and nitrite reduction.** Proposed pathways for H<sub>2</sub> evolution (top), N<sub>2</sub> reduction (right), and nitrite reduction (left), where M represents FeMo-co and the E<sub>n</sub> state is noted. Hydride protonation (*hp*) is proposed to make H<sub>2</sub>, reductive elimination (*re*) for the activation of N<sub>2</sub>, while hydride migratory insertion (*mi*) has been proposed in the reduction of nitrite. Oxidative addition (*oa*) is shown for the binding of H<sub>2</sub> concomitant with the release of N<sub>2</sub> (right).

substrates.<sup>18</sup> Most recently, we demonstrated that nitrogenase remodeled in this way can reduce nitrite (NO<sub>2</sub><sup>-</sup>) to NH<sub>3</sub>.<sup>19</sup> Intermediates along the NO<sub>2</sub><sup>-</sup> reaction pathway were trapped by a freeze-quench method and characterized by Q-band ENDOR/Non-Kramers ESEEM spectroscopy. A pair of intermediates consistent with M-NH<sub>2</sub> and M-NH<sub>3</sub> (M = FeMo-co) species were trapped and identified as the same as intermediates trapped during the reduction of diazene (HN=NH) and hydrazine (H<sub>2</sub>N-NH<sub>2</sub>).<sup>11</sup> From this observation, and the fact that the two-electron/two-proton trapped state of the FeMo-co



likely contains a metal-bound hydride and a proton ( $E_2(2H)$ ), we proposed a mechanism for  $NO_2^-$  reduction that again invokes migratory hydride insertion, with the substrate fragment of the M-NOOH state inserting into the M-H, with proton addition and loss of  $H_2O$  to yield the M-NHO intermediate (**Figure 3-2**, left).<sup>19</sup> Subsequent reduction leads to the observed M-NH<sub>2</sub> and M-NH<sub>3</sub> intermediates and ultimate release of NH<sub>3</sub>.

From these findings, it can be seen that hydrides on FeMo-cofactor can undergo at least two different types of reaction: (i) reductive elimination (*re*) of H<sub>2</sub> by the state containing two hydrides activates FeMo-co for N<sub>2</sub> binding and reaction; (ii) and migratory insertion (*mi*) into the M-H by substrates, such as acetylene and nitrite, and most likely some of the N<sub>2</sub>H<sub>x</sub> intermediate states of N<sub>2</sub> reduction.

It has been demonstrated that in a MoFe protein with substituted amino acids near FeMo-co, carbon dioxide (CO<sub>2</sub>) can be catalytically reduced by 2 or 8 electrons/protons to carbon monoxide (CO) or methane (CH<sub>4</sub>) at low rates.<sup>20,21</sup> A better understanding of the mechanism by which nitrogenase catalyzes CO<sub>2</sub> reduction would provide insight into the challenging and environmentally important reduction of CO<sub>2</sub>. Here, we report that wild type nitrogenase reduces CO<sub>2</sub> by two electrons/protons to make formate (HCOO<sup>-</sup>) at rates up to 10-times faster than the rates of CO and CH<sub>4</sub> formation reported earlier. To understand the alternative reaction mechanisms, we have explored possible pathways for CO<sub>2</sub> reduction on FeMo-co using density functional theory (DFT) calculations. These pathways involve reactions of Fe-hydrides and yield energies that are consistent with the observed product distribution for CO<sub>2</sub> reduction. In addition, we show that amino acid substitutions near FeMo-co in the MoFe protein can significantly alter the product

distribution between formate and CO/CH<sub>4</sub>.

## **Materials and Methods**

*Reagents and protein purification:* All reagents were obtained from SigmaAldrich (St.Louis, MO) or Fisher Scientific (Fair Lawn, NJ) and were used without further purification. Carbon dioxide (CO<sub>2</sub>) was purchased from Air Liquide (Walnut Creek, CA) and methane from Air Gas (Radnor, PA). *Azotobacter vinelandii* strains DJ995 (wild-type), DJ997 ( $\alpha$ -195<sup>Gln</sup>), DJ1310 ( $\alpha$ -70<sup>Ala</sup>), and DJ1316 ( $\alpha$ -70<sup>Ala</sup>/ $\alpha$ -195<sup>Gln</sup>) were grown, and the corresponding nitrogenase MoFe proteins having a seven-His tag addition near the carboxyl-terminal end of the  $\alpha$ -subunit, were expressed and purified as previously described.<sup>22</sup> Protein concentrations were determined by the Biuret assay using bovine serum albumin as standard. Handling of proteins and buffers was done in septum-sealed serum vials under an argon atmosphere or on a Schlenk vacuum line. All gases and liquids were transferred using gas-tight syringes.

*Carbon dioxide reduction assay:* CO<sub>2</sub> reduction to CH<sub>4</sub> was carried out at 0.45 atm CO<sub>2</sub> in 9.4 mL serum vials containing 2 mL of an assay buffer consisting of 100 mM sodium dithionite, a MgATP regenerating system (13.4 mM MgCl<sub>2</sub>, 10 mM ATP, 60 mM phosphocreatine, 0.6 mg/mL bovine serum albumin, and 0.4 mg/mL creatine phosphokinase) in 100 mM MOPS buffer at pH 7.2. Addition of CO<sub>2</sub> was followed by 10 min of incubation at room temperature to allow equilibration. MoFe protein was added and then the assay vials were ventilated to atmospheric pressure. Reactions were initiated by the addition of Fe protein and incubated at 30°C for the noted times. To each was

added 500  $\mu\text{L}$  of 400 mM EDTA at pH 8.0 to quench the reaction. From the gas phase, 300  $\mu\text{L}$  was injected into a gas chromatograph with a flame ionization detector to quantify  $\text{CH}_4$ . From the same samples, 50  $\mu\text{L}$  of the gas phase was injected into a gas chromatograph with a thermal conductivity detector to quantify  $\text{H}_2$ .

$\text{CO}_2$  reduction to CO was measured using a hemoglobin (0.3 mg/mL) binding assay as described before.<sup>23</sup> The buffer composition was the same as used for  $\text{CO}_2$  reduction to  $\text{CH}_4$  except 0.3 mg/mL hemoglobin was added in the assay buffer. 1.2 mL of assay buffer was transferred to 9.4 mL serum vial containing 0.45 atm  $\text{CO}_2$  and 20 min of equilibration time was allowed. Then, MoFe protein was added (0.5 mg/mL). One mL of  $\text{CO}_2$  saturated assay buffer was transferred to a 2.2 mL (1 cm path length) quartz cuvette that had been modified to maintain a defined gas atmosphere. Fe protein was added to initiate the reaction. The increase in the absorbance at 418 nm corresponding to the binding of CO to the hemoglobin was monitored using an UV-visible spectrophotometer.

$\text{CO}_2$  reduction to formate was established using a 300 MHz JOEL NMR spectrometer. To a 9.4 mL vial was added 0.026 mg of  $\text{H}^{13}\text{CO}_3^-$  under Ar. To this vial was added 2 mL of anaerobic assay buffer, followed by addition of 1 mg MoFe protein. The reaction was initiated by addition of 1 mg of Fe protein. The reaction was allowed to run for 1 h, after which 500  $\mu\text{L}$  of the liquid phase was transferred to a sealed NMR tube. A  $\text{D}_2\text{O}$  containing capillary tube was placed inside of the NMR tube.  $^{13}\text{C}$  NMR was carried out to ascertain the formation of formate during the reduction of  $\text{H}^{13}\text{CO}_3^-$  (**Figure 3- S1**). The NMR probe temperature was set to 25  $^\circ\text{C}$  and the magnetic field was locked using  $\text{D}_2\text{O}$  as solvent. The probe was tuned for both  $^1\text{H}$  and  $^{13}\text{C}$  nuclei. Single pulse

decoupled NMR was carried out using the following parameters:- X-offset 90 ppm, X-sweep 180 ppm, scan 6000, pulse X-angle 30, relaxation delay 3 s, and both NOE and decoupling on. The  $^1J_{C-H}$  for formate was also determined using the same parameters except turning the decoupling parameter off (data not shown). A colorimetric assay was used to quantify the formation of formate using a protocol previously reported.<sup>24</sup> In a 9.4 mL serum vial, 3.5 mL of 100% acetic anhydride, 50  $\mu$ L of 30% (w/v) sodium acetate, and 1 mL isopropanol solution containing 0.5% (w/v) citric acid and 10% (w/v) acetamide were added. To this assay solution was added 500  $\mu$ L of sample with 5 hours of incubation time at room temperature. Using a UV-Visible spectrophotometer, the absorbance was determined at 514 nm (**Figure 3-S2**). The formate standard calibration curve was made as follows: first, the assay buffer with MoFe and Fe protein was left to turnover for an hour under an Ar atmosphere; then, the appropriate concentration of formate was added. From this, 500  $\mu$ L of samples was used for the colorimetric assay.

*Calculations:* Two models of the FeMo-co and the enzyme environment of increasing complexity were employed for the DFT calculations. The first model comprises the FeMo-co ligands  $\alpha$ -275<sup>Cys</sup>,  $\alpha$ -442<sup>His</sup> (*Azotobacter vinelandii* numbering), and *R*-homocitrate, which were modeled as methylthiolate, imidazole (or 4-methyl-imidazole), and dimethyl glycolate, respectively (**Figure 3-S3a**). The second model adds residues  $\alpha$ -70<sup>Val</sup> and  $\alpha$ -96<sup>Arg</sup> located on top the FeMo-co reactive face, which was modeled as tert-butyl and methylguanidinium, respectively (**Figure 3-S3b**). The atoms of the protein and FeMo-co that were truncated were kept frozen to their crystallographic position. In model 2 the steric confinement exerted by the protein matrix on  $\alpha$ -70<sup>Val</sup> and  $\alpha$ -96<sup>Arg</sup> during the

CO<sub>2</sub> insertion in the direct hydride transfer pathway (see Results) was included, adding two ethane molecules next to  $\alpha$ -70<sup>Val</sup> and  $\alpha$ -96<sup>Arg</sup> at the location of the backbone C atoms of  $\alpha$ -66<sup>Gly</sup> and  $\alpha$ -98<sup>Asn</sup>. The C atoms of the ethane molecules were kept fixed at their equilibrium distance. Model 1 was used for all of the reactions considered in the present work, whereas model 2 was employed only for selected reactions as discussed.

The electronic structure of the FeMo-co was described within the DFT framework using the gradient-corrected Becke<sup>25</sup> exchange and Perdew<sup>26</sup> correlation functional. The Ahlrichs VTZ basis set was employed for all Fe atoms,<sup>27</sup> the Los Alamos National Laboratory basis set LANL2TZ with an effective core potential was employed for the Mo atom<sup>28</sup>, and the 6-311++G\*\* basis set was employed for all atoms coordinated to metal atoms, protic and hydridic hydrogen atoms, and finally the 6-31G\* basis<sup>29</sup> set was adopted for all of the other atoms. Harmonic vibrational frequencies were calculated at the optimized geometries using the same level of theory to estimate the zero-point energy and the thermal contributions (298.1 K and 1 atm) to the gas-phase free energy. The protein environment around FeMo-co was described with a polarizable continuum with a dielectric constant  $\epsilon = 4$ .<sup>30</sup> Standard state corrections were applied to solvation free energies. Calculations for the reference state E<sub>0</sub> were performed for the observed  $S = 3/2$  spin state. For the E<sub>2</sub> state, the  $S = 3/2$  spin state was used, while for the E<sub>4</sub> state, the  $S = 1/2$  spin state was used, consistent with the spin states observed experimentally.<sup>9</sup> In agreement with previous reports,<sup>31</sup> we found that the ground state of all the structures considered are characterized by the highest alternating antiferromagnetic couplings possible between the Fe centers compatible with the chosen spin multiplicity.

Different locations of the hydridic and protic hydrogen atoms on the reactive face of the FeMo-cofactor (identified by the atoms Fe2, Fe3, Fe6, and Fe7) were explored. The two models of the active site yielded similar reaction thermodynamic (differences within 3 kcal/mol) as detailed in **Figure 3-S4**. In particular, model 1 and 2 yielded a similar lowest-free energy  $E_2$  state, with a “protic” hydrogen located on a sulfur atom and an “hydridic” hydrogen located on one Fe center or bridging two Fe atoms. In the lowest free energy structure, the hydridic hydrogen is located between Fe2 and Fe6 and the protic hydrogen is bound to S2B (**Figure 3-S3**). In model 1, the hydridic hydrogen is asymmetrically positioned between the two Fe atoms (Fe2-H and F6-H distances of 1.60 Å and 1.75 Å), whereas in model 2 the hydridic hydrogen is in a nearly symmetric location (Fe<sub>2</sub>-H and F<sub>6</sub>-H distances of 1.63 Å and 1.68 Å). Both models also predict that the protic hydrogen is preferentially bound to a bridging  $\mu$ -S atom (the S2B atom in the lowest free energy isomer, **Figure 3-S5**). These lowest free energy  $E_2$  isomers were employed as a starting point for the calculations. All of the calculations were performed with the NWChem quantum chemistry package.<sup>32</sup>

## Results

***CO<sub>2</sub> reduction to formate:*** Earlier studies revealed that the wild type MoFe protein reduces CO<sub>2</sub> to CO at a very low rate (~0.03 nmol CO/nmol MoFe protein/min at 30°C),<sup>20</sup> a result repeated here (**Table 3-1**). In agreement with those earlier results, we find that under these conditions most of the electron flux through nitrogenase goes to the reduction of protons to make H<sub>2</sub>, which occurs with a roughly 3x10<sup>3</sup>-fold greater rate (83 nmol H<sub>2</sub>/nmol MoFe protein/min at 30°C) than CO formation, and we detect no CH<sub>4</sub>. In a

subsequent study, it was found that substitution of two amino acids within the MoFe protein located near the active site FeMo-co,  $\alpha$ -70<sup>Val→Ala</sup>/ $\alpha$ -195<sup>His→Gln</sup>, resulted in a MoFe protein that could reduce CO<sub>2</sub> by 8 e<sup>-</sup>/H<sup>+</sup> to methane (CH<sub>4</sub>) at a rate of ~1 nmol CH<sub>4</sub>/nmol MoFe protein/min, with most of the electron flux going to proton reduction (~62 nmol H<sub>2</sub>/nmol MoFe protein/min).<sup>21</sup> The reduction of CO<sub>2</sub> to CO and CH<sub>4</sub> are expected to follow the same reaction pathway, with CO formed after 2e<sup>-</sup>/H<sup>+</sup> reduction and CH<sub>4</sub> after addition of a further 6 e<sup>-</sup>/H<sup>+</sup>.

**Table 3-1. Product accumulation and electron distribution for wild-type MoFe protein**

	Product							
	H <sub>2</sub>		HCOO <sup>-</sup>		CH <sub>4</sub>		CO	
Gas	nmol/nmol/min <sup>a</sup>	% e <sup>-</sup>	nmol/nmol/min	% e <sup>-</sup>	nmol/nmol/min	% e <sup>-</sup>	nmol/nmol/min	% e <sup>-</sup>
Ar	83 ± 1.55	100	ND <sup>b</sup>	ND	ND	ND	ND	ND
CO <sub>2</sub>	70 ± 1.8	85	9.8 ± 1.5	12	ND	ND	0.03	1

<sup>a</sup>nmol product/nmol MoFe protein/min. Rates are the average over the 60 min assay at 30°C with 1 mg MoFe protein and 1 mg Fe protein. CO<sub>2</sub> was at a partial pressure of 0.45 atm.

<sup>b</sup>ND, not detected.

An examination of CO<sub>2</sub> reduction catalyzed by a range of small molecules that utilize metal hydrides reveals that an alternative product for CO<sub>2</sub> reduction is formate (HCOO<sup>-</sup>).<sup>33-37</sup> The pathway to CO and CH<sub>4</sub> formation is believed to involve the addition of H to the O atom of CO<sub>2</sub>, whereas the pathway to HCOO<sup>-</sup> formation is believed to involve the addition of H to the C atom of CO<sub>2</sub>.<sup>38,39</sup> In this context, we tested whether wild type nitrogenase could reduce CO<sub>2</sub> to HCOO<sup>-</sup>, a reaction that had not been reported before.

Wild type nitrogenase that was allowed to turn over for 60 min in the presence of <sup>13</sup>CO<sub>2</sub> as substrate catalyzed the formation of formate, as established by <sup>13</sup>C NMR, which showed a peak at 171.083 ppm associated with H<sup>13</sup>CO<sub>3</sub><sup>-</sup> (**Figure 3-S1**). Formate was quantified by a colorimetric assay (**Figure 3-S2**). As can be seen from the data in **Table 3-1**, the wild-type MoFe protein reduces CO<sub>2</sub> to formate at a substantial rate (~10 nmol HCOO<sup>-</sup>/nmol MoFe protein/min at 30°C). Under these conditions, ~12% of the electron flux through nitrogenase goes to produce formate, whereas about 1% goes to form CO. The remaining electron flux (77%) makes H<sub>2</sub>. Thus, the present measurements reveal that the conversion of CO<sub>2</sub> to formate represents a significant catalytic process for nitrogenase.

***Does CO<sub>2</sub> reduction involve reductive elimination?*** Although the reduction of CO<sub>2</sub> to formate involves only 2e<sup>-</sup>/H<sup>+</sup>, and likely involves binding at the E<sub>2</sub> state, the 6/8 e<sup>-</sup>/H<sup>+</sup> reduction to CO/CH<sub>4</sub> could occur by a process that parallels the reduction of N<sub>2</sub>, namely a reductive elimination (*re*) mechanism (**Figure 3-2, right**).<sup>10</sup> A key feature of the *re* mechanism for N<sub>2</sub> reduction is the reversible reductive elimination/oxidative



addition in which the FeMo-co is activated for the binding/reduction of  $N_2$  through the re

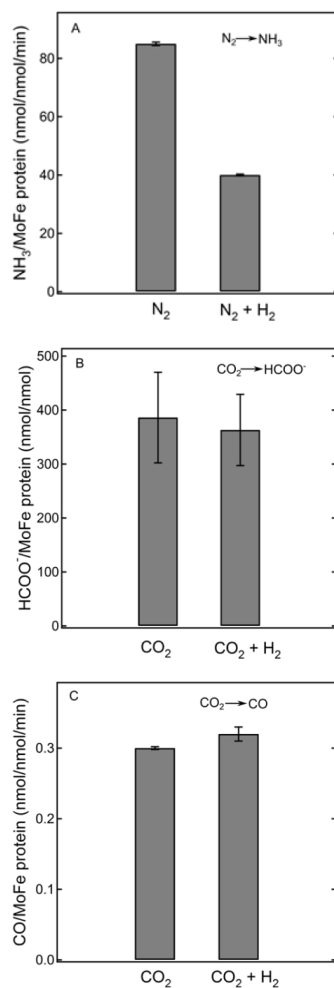


**Figure 3-3. Effect of  $H_2$  on  $N_2$  and  $CO_2$  reduction.** Specific activities (nmol product/nmol MoFe protein/min) are shown for  $N_2$  reduction to  $NH_3$  (panel A),  $CO_2$  reduction to formate (panel B), and  $CO_2$  reduction to CO (panel C) either with or without the addition of  $H_2$ . All assays were done with wild type MoFe protein at  $30^\circ C$  as described in the **Materials and Methods**. Reaction conditions were: 0.2 atm  $N_2$  + 0.8 atm Ar or 0.2 atm  $N_2$  + 0.8 atm  $H_2$  for panel A; 40 mM  $HCO_3^-$  + 1 atm Ar or 40 mM  $HCO_3^-$  + 1 atm  $H_2$  for panel B; 0.15 atm  $CO_2$  + 0.85 atm Ar or 0.15 atm  $CO_2$  + 0.85 atm  $H_2$  for panel C.

loss of  $H_2$ . As a result of this reversible equilibrium,  $H_2$  inhibits  $N_2$  reduction to  $NH_3$  by displacement of the bound  $N_2$  (**Figure 3-2, right**).<sup>13</sup> This inhibition is recapitulated here

by activity measurements that show inclusion of 0.8 atm H<sub>2</sub> in place of 0.8 atm of Ar along with 0.2 atm N<sub>2</sub>, results in ~50% inhibition of the NH<sub>3</sub> formation rate for wild type nitrogenase (**Figure 3-3**). If CO<sub>2</sub> reduction also followed a reversible *re* mechanism, this process likewise should be inhibited by the addition of H<sub>2</sub>. However, as can be seen (**Figure 3-3, panel B**), the inclusion of 1 atm H<sub>2</sub> caused no detectable inhibition of the reduction of CO<sub>2</sub> to formate, relative to the Ar control. Inclusion of 0.85 atm of H<sub>2</sub> also had no effect on the rate of reduction of CO<sub>2</sub> to CO compared to the Ar control (**Figure 3-3, panel C**). These results indicate that CO<sub>2</sub> reduction catalyzed by nitrogenase does not involve the reversible *re* step that is operative in N<sub>2</sub> reduction.

*Alternative mechanisms of CO<sub>2</sub> reduction by hydride insertion:* With the *re* mechanism having been eliminated, the most plausible mechanisms for CO<sub>2</sub> reduction catalyzed by nitrogenase involves migratory insertion of CO<sub>2</sub> into the Fe-H bond of reduced FeMo-co, in analogy to the proposed mechanisms of C<sub>2</sub>H<sub>2</sub> and NO<sub>2</sub><sup>-</sup> reduction.<sup>17,19</sup> **Figure 3-4** presents two alternative hydride insertion reaction pathways for the reduction of CO<sub>2</sub> to formate based on studies of inorganic complexes: the ‘direct hydride transfer’ reaction of CO<sub>2</sub> with the FeMo-co Fe-H, and an ‘associative’ pathway with hydride insertion by Fe-bound CO<sub>2</sub>.<sup>40</sup> As incorporated into **Figure 3-4**, the formation of CO and CH<sub>4</sub> can be viewed as a shunt off of the associative pathway. The ~10:1 product ratio of formate:CO/CH<sub>4</sub> observed for CO<sub>2</sub> reduction by wild-type nitrogenase indicates that the pathways to formate formation are energetically favorable compared to the pathway to CO/CH<sub>4</sub> formation.

*Testing possible pathways by calculations:* We used DFT calculations to

evaluate the possible pathways for CO<sub>2</sub> reduction catalyzed at FeMo-co, presented in **Figure 3-4**. The starting point for the calculations is the E<sub>2</sub>(2H) state, which has

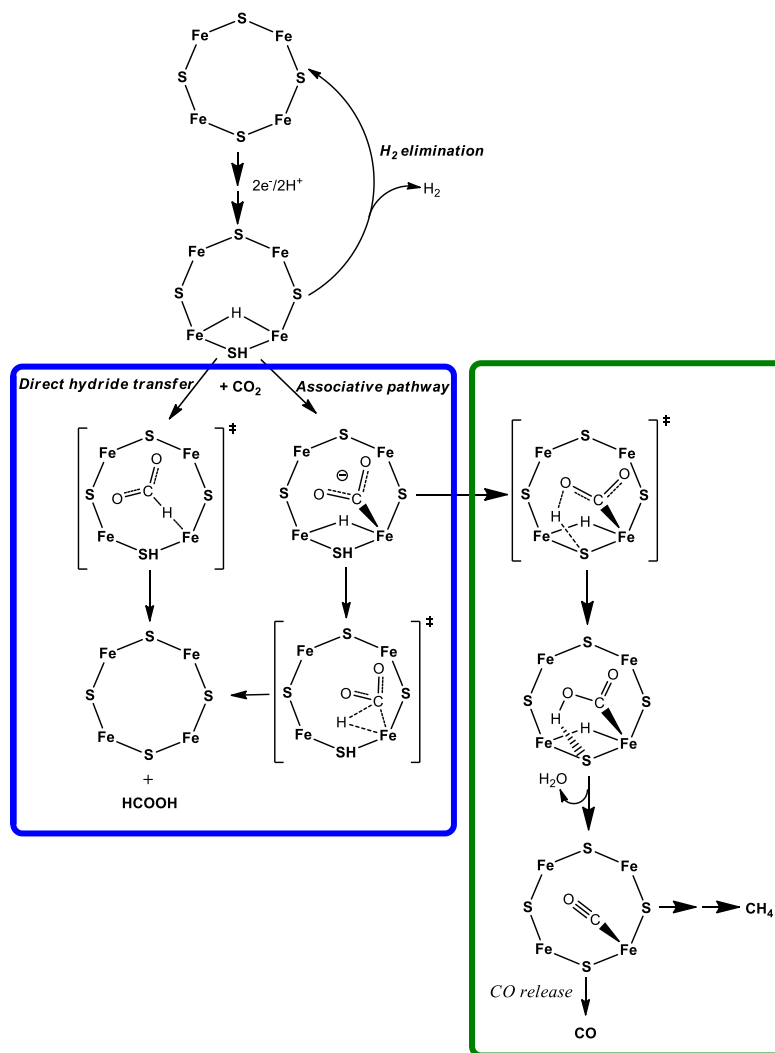


**Figure 3-4. Possible pathways for CO<sub>2</sub> reduction.** CO<sub>2</sub> activation at one FeS face of the E<sub>2</sub> state of FeMo-co is shown. The E<sub>2</sub> state is proposed to contain a single Fe-hydride and a proton bound to a sulfide shown bound to one face of FeMo-co. Reduction to formate (blue box) can go by either a direct hydride transfer or an associative pathway. A pathway to formation of CO and CH<sub>4</sub> is shown in the green box. Six additional electrons and protons are added to the bottom structure to achieve reduction to CH<sub>4</sub>.

accumulated 2 [e<sup>-</sup>/H<sup>+</sup>], which optimization shows to be present as 1 Fe-bound hydride

and 1 sulfido-bound proton (**Figure 3-S3**).

Geometry optimization of model 1 in the presence of CO<sub>2</sub> in the vicinity of the Fe-hydride center of the E<sub>2</sub>(2H) state (at C-H distance longer than 3.5 Å) leads to spontaneous ‘direct hydride’ transfer to carbon, with the formation of formate (**Figure 3-5**, blue pathway). In turn, according to the adopted computation model, the newly formed formate deprotonates the S-H of FeMo-co with the formation of formic acid. Isomers of FeMo-co differing in the location of the proton and the hydride provided similar scenarios. Calculations carried out on model 2, which includes residues  $\alpha$ -70<sup>Val</sup> and  $\alpha$ -96<sup>Arg</sup> above the reactive face of FeMo-co, revealed that the local environment around the cofactor limits CO<sub>2</sub> access to the catalytic center and introduces a barrier for the direct hydride transfer ( $\Delta G^\ddagger = +9.6$  kcal/mol, see **Figure 3-5**), forcing CO<sub>2</sub> to approach the hydridic hydrogen sideways (**Figure 3-S6**) with respect to the FeMo-co face rather than perpendicularly as in model 1. It is important to point out that while model 1 and model 2 largely differ in the description of the kinetics of the direct hydride transfer, they provide comparable reaction free energies ( $\Delta G^0 = -25.8$  kcal and  $-23.0$  kcal/mol, respectively). An analysis of the electronic properties of FeMo-co during the hydride transfer, carried out within the natural bond orbital (NBO) framework,<sup>41</sup> revealed a strong charge transfer from the  $\sigma$  (Fe-H) bonding orbital to the  $\sigma^*$  (C=O) anti-bonding orbital (see **Supporting Information**), which results in the heterolytic Fe-H  $\rightarrow$  Fe<sup>+</sup> + H<sup>-</sup> bond cleavage and the transfer of the hydride to CO<sub>2</sub>. The exergonic nature of the direct hydride transfer suggests that the hydricity of the E<sub>2</sub> state,  $\Delta G_{H^-}$ , is sufficient to transfer a hydride to CO<sub>2</sub> to generate formate, i.e., the hydricity is below that of formate (HCOO<sup>-</sup>  $\rightarrow$  CO<sub>2</sub> + H<sup>-</sup>,

$$\Delta G_{H^-} = +24.1 \text{ kcal/mol}.^{42}$$

In contrast, the ‘associative’ pathway for CO<sub>2</sub> reduction, whereby CO<sub>2</sub> first coordinates sideways to Fe<sub>2</sub> via the C atom (**Figure 3-S7**), was found to be thermodynamically and kinetically unfavorable. Indeed, the formation of the E<sub>2</sub>(2H)-CO<sub>2</sub> adduct is endergonic by  $\Delta G^0 = +10.8 \text{ kcal/mol}$  ( $\Delta G^0 = +8.7 \text{ kcal/mol}$ , model 2), and the calculated barrier for the subsequent hydrogen transfer to CO<sub>2</sub> is  $\Delta G^\ddagger = +11.1 \text{ kcal/mol}$  (**Figure 3-5**, blue pathway). The computed overall barrier for CO<sub>2</sub> reduction to HCOOH via the associative pathway is +21.9 kcal/mol. Upon CO<sub>2</sub> binding to Fe<sub>2</sub>, the Fe<sub>2</sub>-S bond in the Fe<sub>2</sub>-S-Fe<sub>6</sub> bridge breaks (**Figure 3-S7A**) and it is reformed when the product is released. The NBO analysis of the associative pathway indicates that the hydrogen transfer is driven by a strong charge transfer from  $\pi$  (Fe-C) of the Fe-bound CO<sub>2</sub> moiety to  $\sigma^*$  (Fe-H) and from FeMo-co localized orbitals to CO<sub>2</sub>, which results in the heterolytic Fe-H  $\rightarrow$  Fe<sup>-</sup> + H<sup>+</sup> bond dissociation with the net transfer of a proton to the C atom and the breaking of the Fe-C bond. During the proton transfer the two  $\sigma$  (Fe-C) electrons are used to make the C-H bond. The different behaviors of the Fe-H in the direct hydride transfer pathway and the associative pathway are truly remarkable: in the former the Fe-H hydrogen behaves as a hydridic hydrogen and in the latter as a protic hydrogen.

A pathway leading to the formation of CO from E<sub>2</sub>(2H)-CO<sub>2</sub> was also found. The lowest free energy path for this reaction starts with the transfer of the protic S-H hydrogen to one of the oxygen atoms of CO<sub>2</sub>, which is an exergonic reaction ( $\Delta G^0 = -7.6 \text{ kcal/mol}$ ) with an activation barrier of  $\Delta G^\ddagger = +7.7 \text{ kcal/mol}$  (**Figure 5**, green pathway). The presence of ionizable residues near the reactive FeMo-co face, most notably  $\alpha$ -96<sup>Arg</sup>,

raises the question whether one of these residues can act as a proton relay to the CO<sub>2</sub> rather than the protonated FeMo-Co S atom. The size of the present computational models cannot fully address this question. However calculations carried out with model 2 indicate that protonation from  $\alpha$ -96<sup>Arg</sup> is extremely unlikely, given that this reaction is endergonic by 13.4 kcal/mol.

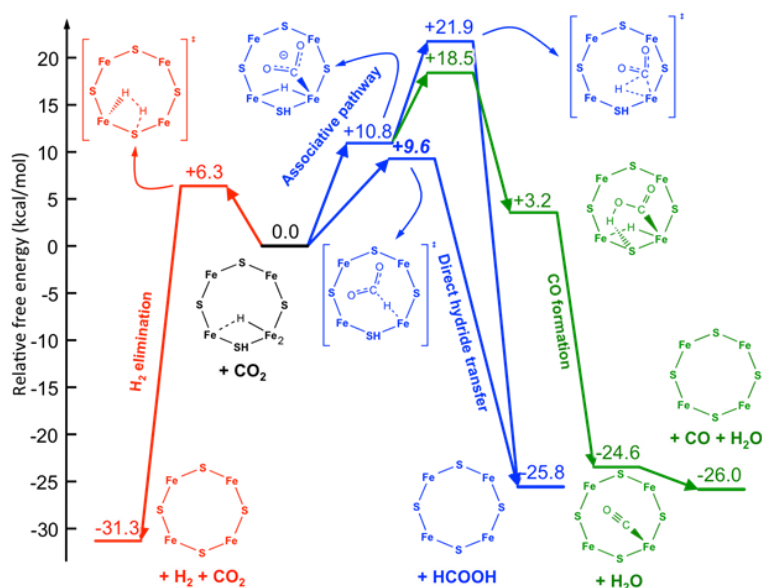


**Figure 3-5. Computed free energy diagram for CO<sub>2</sub> reduction and H<sub>2</sub> formation occurring at the E<sub>2</sub> state of FeMo-cofactor.** Calculations start with the E<sub>2</sub> state that contains one bridging hydride and one H<sup>+</sup> associated with a sulfide. This starting state is assigned a relative free energy of 0 kcal/mol and all other free energy changes are relative to this state. Going to the left (red) is the pathway for heterolytic formation of H<sub>2</sub>. To the right (blue) is the direct hydride transfer or associative pathway going to a CO<sub>2</sub> bound to FeMo-co. Further to the right (green) is the pathway to CO formation. Reported data were calculated with model 1 except for the activation barrier for the direct hydride transfer, which was calculated with model 2. For a more detailed comparison between model 1 and model 2, see Figure 3-S3.

The formation of CO proceeds with the transfer of the Fe-H hydrogen (as a proton) to that oxygen, which results in the spontaneous and very exoergic dissociation of a water

molecule ( $\Delta G^0 = -27.8$  kcal/mol), followed by the slightly exergonic dissociation of CO ( $\Delta G^0 = -1.4$  kcal/mol). Thus, in this case, the Fe-H again behaves as a proton donor.

For completeness, we also investigated computationally the release of H<sub>2</sub> from the E<sub>2</sub>(2H) state. We found that formation of H<sub>2</sub> is a facile ( $\Delta G^\ddagger = +6.3$  kcal/mol) and very exergonic process ( $\Delta G^0 = -31.3$  kcal/mol; **Figure 3-5**, red pathway). This result is consistent with our recent explanation of why H<sub>2</sub> cannot reduce FeMo-co: it is too far ‘uphill’.<sup>9</sup> As with the direct hydride pathway, the Fe-H behaves as a hydride that is protonated by S-H, with the overall H<sub>2</sub> elimination driven by a  $\sigma$  (Fe-H) to  $\sigma^*$  (S-H) charge transfer.

***Experimentally altering product distribution during CO<sub>2</sub> reduction through MoFe protein modification:*** We sought to alter the selectivity of CO<sub>2</sub> reduction to different products by changing the environment around the active site FeMo-co by amino acid substitutions (**Figure 3-S8**). Earlier studies identified the  $\alpha$ -70<sup>Val</sup> and  $\alpha$ -195<sup>Gln</sup> as key residues that, when substituted, alter the reactivity of nitrogenase toward substrate reduction.<sup>21,43,44</sup> We therefore assessed how changing these amino acids would alter the ratio of the products when reacting with CO<sub>2</sub> (**Figure 3-6 and Table 3-S1**). For the wild type MoFe protein under these conditions, about 20% of the electrons are utilized for CO<sub>2</sub> reduction, formate being the primary product, with a trace of CO. The remaining 80% of electron flux is used to make H<sub>2</sub>. In the  $\alpha$ -70<sup>Val->Ala</sup> substituted MoFe protein, the electron flux is shifted in favor of CO<sub>2</sub> reduction to make formate (~30%), with the remainder going to make H<sub>2</sub>. The  $\alpha$ -195<sup>His->Gln</sup> substituted MoFe protein shows essentially 100% electron flux going to make H<sub>2</sub>. Substitution of both  $\alpha$ -70<sup>Ala</sup>/  $\alpha$ -195<sup>Gln</sup>,

however, results in a protein that shows considerable reduction of CO<sub>2</sub> to formate (~20%), but with detectable formation of CH<sub>4</sub> (~2%), the remaining flux going to make H<sub>2</sub>. These findings reveal that subtle changes around the active site can indeed alter the reaction pathway energy landscape, thereby altering the distribution of electrons passing through nitrogenase to CO<sub>2</sub> reduction.

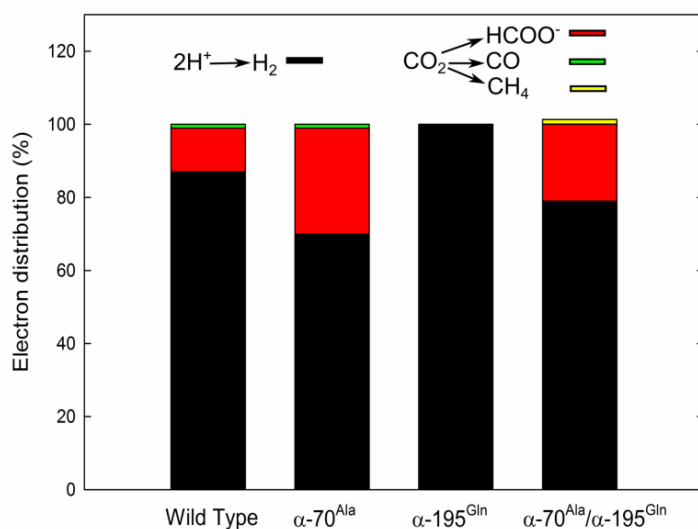


**Figure 3-6. Product distribution under CO<sub>2</sub> for different MoFe proteins.** Shown are the electron distribution to different products with CO<sub>2</sub> for the wild-type, α-70<sup>Ala</sup>, α-195<sup>Gln</sup>, and α-70<sup>Ala</sup>/α-195<sup>Gln</sup> MoFe proteins. Assay conditions: 1 mg MoFe, 6 mg Fe, 0.45 atm CO<sub>2</sub> with an incubation time of 60 min at 30°C.

## Discussion

The discovery reported here that nitrogenase can reduce CO<sub>2</sub> to formate, coupled with the earlier reports of reduction to CO<sup>20</sup> and to CH<sub>4</sub>,<sup>21</sup> makes nitrogenase unique in its ability to catalyze the reduction of CO<sub>2</sub> to a range of products. For example, CO dehydrogenase and formate dehydrogenase efficiently catalyze 2 e<sup>-</sup>/H<sup>+</sup> reduction of CO<sub>2</sub>



to CO and HCOO<sup>-</sup>, respectively, but do not catalyze reduction of CO<sub>2</sub> to CH<sub>4</sub>.<sup>45,46</sup> Indeed, few known organometallic complexes can reduce CO<sub>2</sub> to this suite of products,<sup>47,48</sup> making the study of the mechanism of CO<sub>2</sub> reduction by nitrogenase important to gain mechanistic insights into how to reduce CO<sub>2</sub>. Studies during the last few years have revealed the presence of Fe-bound hydrides in reduced states of nitrogenase, as well as their importance in the nitrogenase N<sub>2</sub> reduction mechanism.<sup>9</sup> Activation of nitrogenase by the accumulation of 4e<sup>-</sup>/H<sup>+</sup> on FeMo-co (E<sub>4</sub>(4H) state) results in the storage of these reducing equivalents as two bridging hydrides (Fe-H-Fe) in the central E<sub>4</sub>(4H) state. There is ample evidence now that the binding of N<sub>2</sub> to this activated state is associated with the loss of H<sub>2</sub> by a reductive elimination (*re*) mechanism, with two hydrides combining to make H<sub>2</sub> coupled to the reduction of N<sub>2</sub> to a diazene-level state.<sup>9-13</sup> It has been shown that the binding of N<sub>2</sub> to the E<sub>4</sub>(4H) state with loss of H<sub>2</sub> involves the thermodynamically and kinetically reversible *re* equilibrium (**eqn 3-1**)



that activates FeMo-co for the addition of the first two electrons and protons to N<sub>2</sub>, the most difficult step in N<sub>2</sub> reduction. Subsequent steps of reduction are likely to involve migratory insertion (*mi*) of this bound species into M-H on FeMo-co, ultimately leading to the formation of two NH<sub>3</sub>. The ability of FeMo-co to simultaneously hold the partially reduced N<sub>2</sub> species juxtaposed to one or more Fe-hydrides offers an attractive way to achieve the stepwise reduction of N<sub>2</sub> all the way to NH<sub>3</sub> without release of intermediates

that might be toxic to the cell.

An important consequence of an obligatory loss of H<sub>2</sub> during reduction of any substrate through a *re* equilibrium means that added H<sub>2</sub> will inhibit reduction of the substrate through such a *re* mechanism by ‘driving’ the equilibrium to the left.<sup>13</sup> The findings presented here, that CO<sub>2</sub> reduction to formate and to CO and CH<sub>4</sub> are not inhibited by H<sub>2</sub>, eliminates the possibility that CO<sub>2</sub> binding and reduction is coupled to reversible *re/oa* mechanism in which N<sub>2</sub> binding/reduction is coupled to the *re* loss of H<sub>2</sub>. This finding directed our attention to alternative mechanisms involving proton coupled electron transfer or migratory hydride insertion, as is proposed for CO dehydrogenase and formate dehydrogenase.<sup>45,46</sup>

Studies on inorganic metal-hydride complexes indicate there are two pathways for the participation of metal-hydrides in reduction of CO<sub>2</sub> to formate.<sup>40</sup> One is an associative pathway, in which CO<sub>2</sub> binds through its C atom to an Fe of FeMo-co that has at least one bound hydride (**Figure 3-4**); the presence of a bound hydride increases the  $\pi$  back-donation ability of the metal and the nucleophilicity of the metal. The bound C then undergoes *mi* into the Fe-H bond and accepts a proton bound to sulfur to release HCOOH. Alternatively, (**Figure 3-4**) in a direct hydride transfer mechanism, CO<sub>2</sub> does not bind to a metal ion, but rather the C atom of CO<sub>2</sub> associates with the metal bound hydride and the hydride is directly transferred to the C of CO<sub>2</sub>, to generate formate with transfer of the proton bound to sulfur again giving HCOOH.

Both of these mechanisms seem reasonable and it would be difficult to distinguish

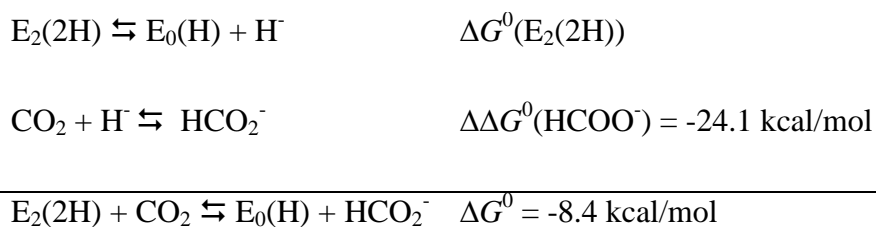
between them from experimental evidence. Instead, this is an ideal situation where calculations can distinguish between possible pathways. Exploratory DFT calculations have been carried out by starting the reaction pathway from an  $E_2(2H)$  state, the state with which  $CO_2$  is proposed to initially interact. These calculations employed simplified models of the nitrogenase active site, which includes FeMo-co with truncated Cys, His, and homocitrate ligands (model 1), similar to previous investigations,<sup>49,50</sup> and additionally truncated  $\alpha$ -70<sup>Val</sup> and  $\alpha$ -96<sup>Arg</sup> residues (model 2) to examine the energetics of the possible direct hydride and associative reaction pathways, and, at the same time, to analyze the chemical bonding and the reorganization of the electron density distribution upon bond breaking and forming.

The calculations reveal a significant barrier between  $CO_2$  and formate along the associative pathway. For this pathway, the coordination of  $CO_2$  to  $E_2(2H)$  is endergonic by +10.8 kcal/mol, with the overall activation free energy for forming formate being endergonic by +21.8 kcal/mol relative to the  $E_2(2H)$  state. In contrast, the direct hydride pathway is found to have a barrier of only 9.6 kcal/mol. Comparison between model 1 and model 2 indicates that this barrier is basically due to protein residues above the reactive face of the FeMo-co, which limit the  $CO_2$  access to the hydridic hydrogen. These environmental effects are demonstrated by the changes in product ratios introduced by amino acid substitutions in the vicinity of the active sites on FeMo-co. The lack of a barrier when  $CO_2$  has free access to the hydridic hydrogen is notable, suggesting that the hydride donor ability of the Fe-H on the  $E_2(2H)$  state is considerably more favorable (smaller hydricity) than that of formate. Using the experimental hydride donor ability of

formate in aqueous solution,  $\Delta G^0(\text{HCOO}^-) = 24.1 \text{ kcal/mol}$ ,<sup>42</sup> as a reference value, we can obtain a conservative estimate of the hydride donor ability (hydricity) of  $\text{E}_2(2\text{H})$  from the half reactions<sup>51</sup> reported in the thermodynamic cycle of **Scheme 1** as  $\Delta G^0(\text{E}_2(2\text{H})) = \Delta G^0 + \Delta G^0(\text{HCOO}^-)$ . Using the calculated (model 1) value  $\Delta G^0 = -8.4 \text{ kcal/mol}$  for the free energy change of the hydride transfer reaction from  $\text{E}_2(2\text{H})$  to  $\text{CO}_2$ , yields  $\Delta G^0(\text{E}_2(2\text{H})) = +15.7 \text{ kcal/mol}$ .

Following similar arguments (Scheme S1), we can obtain an estimate of the  $\text{p}K_a$  for the protonated  $\text{E}_0(\text{H})$  state of  $-9.1 \text{ p}K_a$  units. The extremely high acidity of  $\text{E}_0(\text{H})$  suggests that, in the formation of  $\text{E}_1(\text{H})$ ,  $\text{E}_0$  is first reduced then protonated probably through a proton coupled electron transfer reaction.

**Scheme 1. Thermodynamic cycle for determining the hydride donor ability of  $\text{E}_2(2\text{H})$ .**



These calculations demonstrate that hydride-bound FeMo-co can act as a strong  $\text{H}^-$  donor. On the other hand, the same hydride ligand can act as a proton donor in the less active associative pathway. Our results highlight several of the numerous fallacies in a recent misanalysis of nitrogenase catalysis.<sup>49</sup> A hydrogen atom bonded to a metal is

*defined* formally as a hydride, and the present results show that it is incorrect to attempt to define an M-H moiety as a hydride or proton based on atomic point charges derived from electron density partitioning schemes, rather than reactivity (see **Supporting Information**). The calculations reported in the present paper, together with other recent reports, show little differences between atomic charges on H atoms bound to Fe or S, with variation smaller than differences between the different flavor of the partitioning scheme employed (**Tables 3-S2 and 3-S3**).<sup>49</sup> Correspondingly, the NBO analysis reported here indicates that the Fe-H and S-H bonds are covalent with a small polarization as expected from the difference in electronegativity of the atoms involved (see **Supporting Information**). Nonetheless, the Fe-H and S-H bonds show dramatically different reactivity patterns. We also would like to point out that, as a consequence of the strong covalent character of the Fe-H and S-H bonds, during the accumulation of  $e^-/H^+$  to form  $E_2(2H)$  and, in turn,  $E_4(4H)$ , electrons are neither stored on the FeMo-co metal core, in particular on the Fe atoms, nor in hydridic  $H^-$  atoms. Rather the added electrons are nearly equally shared between the atoms involved in the new chemical bonds as substantiated by the electron configurations reported in **Table 3-S4**.

In contrast to the formation of formate, the reduction of  $CO_2$  to CO, and on to  $CH_4$ , are likely to follow an associative reaction pathway, involving the binding of  $CO_2$  to FeMo-co through the C (**Figures 3-4 and 3-5**). The common early step in this pathway for both formate and CO formation is the endergonic coordination of the  $CO_2$  to the Fe of FeMo-co. On the pathway to CO formation, the  $H^+$  associated with the S has been modeled to interact with one O of the bound  $CO_2$ , with the hydride bound to the Fe acting

as a proton donor to the O, resulting in the reduction of the O to water and a bound CO. The overall barrier to the formation of the intermediate leading to CO is found to be +18.5 kcal/mol relative to the E<sub>2</sub>(2H) state. Thus, the calculations are consistent with the experimental observations that the wild type nitrogenase exhibits a larger formate/CO product ratio during CO<sub>2</sub> reduction. The calculations indicate that the direct hydride transfer pathway will be substantially favorable compared to the associative pathway that leads to CO and CH<sub>4</sub> production. For comparison, calculations were also done for the conversion of the E<sub>2</sub>(2H) state to the E<sub>0</sub> +H<sub>2</sub> state, revealing an exergonic process of -31.3 kcal/mol compared to the E<sub>2</sub>(2H) baseline state, with an activation barrier of 6.3 kcal/mol.

In summary, wild type nitrogenase is shown here to be effective in CO<sub>2</sub> reduction to formate. The most favorable pathway for formate production is calculated to be direct hydride transfer to the C with subsequent proton transfer from an SH. The alternative associative pathway to formate, the binding of CO<sub>2</sub> to Fe followed by *mi* of the CO<sub>2</sub> into Fe-H and protonation, is calculated to have a much higher energy barrier. The higher barrier on the associative pathway is consistent with the modest rates observed for CO formation, with essentially undetectable CH<sub>4</sub> formation. The observation that substitution of amino acids around FeMo-co can alter the product distribution between formate and CO/CH<sub>4</sub> reveals that subtle changes in the protein environment around FeMo-co can tune the energetics of the two pathways. Further experimental and computational studies may provide insights into how to design amino acid substitutions that influence the energetics of the competing pathways in favorable ways.

**References**

- (1) Burgess, B. K.; Lowe, D. J. *Chem. Rev* **1996**, *96*, 2983–3012.
- (2) Smil, V. *Enriching the earth: Fritz Haber, Carl Bosch, and the transformation of world food production*; MIT Press: Cambridge, Mass, 2001.
- (3) Shah, V. K.; Brill, W. J. *Proc. Natl. Acad. Sci. U.S.A.* **1977**, *74*, 3249–3253.
- (4) Thorneley, R. N. F.; Lowe, D. J. In *Molybdenum Enzymes*; Spiro, T. G., Ed.; Metal Ions in Biology; Wiley-Interscience Publications: New York, 1985; Vol. 7, pp 221–284.
- (5) Hageman, R. V.; Burris, R. H. *Proc. Natl. Acad. Sci. U.S.A.* **1978**, *75*, 2699–2702.
- (6) Thorneley, R. N.; Lowe, D. J. *Biochem. J.* **1984**, *224*, 887–894.
- (7) Igarashi, R. Y.; Laryukhin, M.; Dos Santos, P. C.; Lee, H.-I.; Dean, D. R.; Seefeldt, L. C.; Hoffman, B. M. *J. Am. Chem. Soc.* **2005**, *127*, 6231–6241.
- (8) Lukoyanov, D.; Barney, B. M.; Dean, D. R.; Seefeldt, L. C.; Hoffman, B. M. *Proc. Natl. Acad. Sci. U.S.A* **2007**, *104*, 1451–1455.
- (9) Hoffman, B. M.; Lukoyanov, D.; Yang, Z.-Y.; Dean, D. R.; Seefeldt, L. C. *Chem. Rev.* **2014**, *114*, 4041–4062.
- (10) Hoffman, B. M.; Lukoyanov, D.; Dean, D. R.; Seefeldt, L. C. *Acc. Chem. Res.* **2013**, *46*, 587–595.
- (11) Lukoyanov, D.; Yang, Z.-Y.; Barney, B. M.; Dean, D. R.; Seefeldt, L. C.; Hoffman, B. M. *Proc. Natl. Acad. Sci. U.S.A* **2012**, *109*, 5583–5587.
- (12) Yang, Z.-Y.; Khadka, N.; Lukoyanov, D.; Hoffman, B. M.; Dean, D. R.; Seefeldt, L. C. *Proc. Natl. Acad. Sci. U.S.A.* **2013**, *110*, 16327–16332.

- (13) Lukoyanov, D.; Yang, Z.-Y.; Khadka, N.; Dean, D. R.; Seefeldt, L. C.; Hoffman, B. M. *J. Am. Chem. Soc.* **2015**, *137*, 3610–3615.
- (14) Seefeldt, L. C.; Yang, Z.-Y.; Duval, S.; Dean, D. R. *Biochim. Biophys. Acta* **2013**, *1827*, 1102–1111.
- (15) Rivera-Ortiz, J. M.; Burris, R. H. *J. Bacteriol.* **1975**, *123*, 537–545.
- (16) Dilworth, M. J. *Biochim. Biophys. Acta* **1966**, *127*, 285–294.
- (17) Lee, H.-I.; Sørliie, M.; Christiansen, J.; Yang, T.-C.; Shao, J.; Dean, D. R.; Hales, B. J.; Hoffman, B. M. *J. Am. Chem. Soc.* **2005**, *127* (45), 15880–15890.
- (18) Mayer, S. M.; Niehaus, W. G.; Dean, D. R. *J. Chem. Soc. Dalton Trans.* **2002**, 802–807.
- (19) Shaw, S.; Lukoyanov, D.; Danyal, K.; Dean, D. R.; Hoffman, B. M.; Seefeldt, L. C. *J. Am. Chem. Soc.* **2014**, *136*, 12776–12783.
- (20) Seefeldt, L. C.; Rasche, M. E.; Ensign, S. A. *Biochemistry* **1995**, *34*, 5382–5389.
- (21) Yang, Z.-Y.; Moure, V. R.; Dean, D. R.; Seefeldt, L. C. *Proc. Natl. Acad. Sci. U.S.A.* **2012**, *109*, 19644–19648.
- (22) Christiansen, J.; Goodwin, P. J.; Lanzilotta, W. N.; Seefeldt, L. C.; Dean, D. R. *Biochemistry* **1998**, *37*, 12611–12623.
- (23) Bonam, D.; Murrell, S. A.; Ludden, P. W. *J. Bacteriol.* **1984**, *159*, 693–699.
- (24) Sleat, R.; Mah, R. A. *Appl. Environ. Microbiol.* **1984**, *47*, 884–885.
- (25) Becke, A. D. *Phys. Rev. A* **1988**, *38*, 3098–3100.
- (26) Perdew, J. P. *Phys. Rev. B* **1986**, *33*, 8822–8824.
- (27) Schäfer, A.; Horn, H.; Ahlrichs, R. *J. Chem. Phys.* **1992**, *97*, 2571–2577.



- (28) Roy, L. E.; Hay, P. J.; Martin, R. L. *J. Chem. Theory Comput.* **2008**, *4*, 1029–1031.
- (29) Ditchfield, R. *J. Chem. Phys.* **1971**, *54*, 724–728.
- (30) Klamt, A.; Schüürmann, G. *J. Chem. Soc., Perkin Trans. 2* **1993**, 799–805.
- (31) Lovell, T.; Li, J.; Liu, T.; Case, D. A.; Noodleman, L. *J. Am. Chem. Soc.* **2001**, *123*, 12392–12410.
- (32) Valiev, M.; Bylaska, E. J.; Govind, N.; Kowalski, K.; Straatsma, T. P.; Van Dam, H. J. J.; Wang, D.; Nieplocha, J.; Apra, E.; Windus, T. L.; de Jong, W. A. *Comput. Phys. Commun.* **2010**, *181*, 1477–1489.
- (33) Kang, P.; Cheng, C.; Chen, Z.; Schauer, C. K.; Meyer, T. J.; Brookhart, M. *J. Am. Chem. Soc.* **2012**, *134*, 5500–5503.
- (34) Pugh, J. R.; Bruce, M. R. M.; Sullivan, B. P.; Meyer, T. J. *Inorg. Chem.* **1991**, *30*, 86–91.
- (35) Schmeier, T. J.; Dobereiner, G. E.; Crabtree, R. H.; Hazari, N. *J. Am. Chem. Soc.* **2011**, *133*, 9274–9277.
- (36) Sullivan, B. P.; Meyer, T. J. *Organometallics* **1986**, *5*, 1500–1502.
- (37) Rail, M. D.; Berben, L. A. *J. Am. Chem. Soc.* **2011**, *133*, 18577–18579.
- (38) Machan, C. W.; Sampson, M. D.; Kubiak, C. P. *J. Am. Chem. Soc.* **2015**, *137*, 8564–8571.
- (39) Song, J.; Klein, E. L.; Neese, F.; Ye, S. *Inorg. Chem.* **2014**, *53*, 7500–7507.
- (40) Kumar, N.; Camaioni, D. M.; Dupuis, M.; Raugai, S.; Appel, A. M. *Dalton Trans.* **2014**, 11803–11806.

- (41) Reed, A. E.; Curtiss, L. A.; Weinhold, F. *Chem. Rev.* **1988**, *88*, 899–926.
- (42) Connelly, S. J.; Wiedner, E. S.; Appel, A. M. *Dalton Trans.* **2015**, *44*, 5933–5938.
- (43) Kim, C. H.; Newton, W. E.; Dean, D. R. *Biochemistry* **1995**, *34*, 2798–2808.
- (44) Dilworth, M. J.; Fisher, K.; Kim, C.-H.; Newton, W. E. *Biochemistry* **1998**, *37*, 17495–17505.
- (45) Can, M.; Armstrong, F. A.; Ragsdale, S. W. *Chem. Rev.* **2014**, *114*, 4149–4174.
- (46) Mondal, B.; Song, J.; Neese, F.; Ye, S. *Curr. Opin. Chem. Biol.* **2015**, *25*, 103–109.
- (47) Jessop, P. G.; Ikariya, T.; Noyori, R. *Chem. Rev.* **1995**, *95*, 259–272.
- (48) Appel, A. M.; Bercaw, J. E.; Bocarsly, A. B.; Dobbek, H.; DuBois, D. L.; Dupuis, M.; Ferry, J. G.; Fujita, E.; Hille, R.; Kenis, P. J. A.; Kerfeld, C. A.; Morris, R. H.; Peden, C. H. F.; Portis, A. R.; Ragsdale, S. W.; Rauchfuss, T. B.; Reek, J. N. H.; Seefeldt, L. C.; Thauer, R. K.; Waldrop, G. L. *Chem. Rev.* **2013**, *113*, 6621–6658.
- (49) Dance, I. *Dalton Trans.* **2015**, *44*, 9027–9037.
- (50) Varley, J. B.; Wang, Y.; Chan, K.; Studt, F.; Nørskov, J. K. *Phys. Chem. Chem. Phys.* **2015**, *17*, 29541–29547.
- (51) Muckerman, J. T.; Achord, P.; Creutz, C.; Polyansky, D. E.; Fujita, E. *Proc. Natl. Acad. Sci. U.S.A* **2012**, *109*, 15657–15662.

**APPENDIX****SUPPLEMENTARY INFORMATION****CO<sub>2</sub> REDUCTION CATALYZED BY NITROGENASE: PATHWAYS TO  
FORMATE, CARBON MONOXIDE, AND METHANE**

### **Natural Bond Orbital Analysis**

The natural bond orbital (NBO) analysis was developed to study hybridization and covalency in molecules in terms of concepts similar to Lewis chemical structures, then extended to the analysis of intermolecular charge transfer due to localized orbital interactions. In this appendix, we will briefly review a few main concepts and quantities of NBO theory, which we used to characterize and quantify bonding and orbital interactions in the catalytic intermediates and transition states involved in the CO<sub>2</sub> reduction by E<sub>2</sub>(2H). For consistency all of the NBO analysis was performed on species obtained from model 1 (**Figure 3-S3a**).

The NBO of a localized orbital,  $\phi$ , between two atoms A and B is formed by a linear combination of two orthonormal hybrid orbitals,  $h_A$  and  $h_B$ , defined in terms of atomic orbitals centered on A and B:

$$\phi(\text{A-B}) = c_A h_A + c_B h_B$$

where  $|c_A|^2 + |c_B|^2 = 1$ . The relative magnitude of the coefficients  $c_A$  and  $c_B$  can be taken as a measure of the bond polarization due to the different electronegativity of A and B. For a perfectly apolar bond  $c_A = c_B = 2^{-1/2} \approx 0.707$ . The coefficients  $c_A$  and  $c_B$ , and the occupation of selected NBOs for crucial species are reported in Table S1. In addition to the species involved in the CO<sub>2</sub> reduction by E<sub>2</sub>(2H), data for the E<sub>4</sub>(4H) state is also shown. From Table S1, it is evident that the Fe-H is properly described has a covalent bond with a small polarization toward the H atom. As discussed in the main text, for the truncated nitrogenase model used in the present study, direct hydride transfer to CO<sub>2</sub> was found to be an exergonic, barrier less process. Therefore, in Table S1, for this pathway

we report data relative to a (Fe)H...C distance of 2 Å to analyze the nature of the intermolecular interactions as CO<sub>2</sub> approaches Fe-H. This (Fe)H...C distance is comparable with the corresponding TS distance characterized from model 2 (Fig S5). It is interesting to point out that, while the population of the  $\sigma^*(\text{Fe-H})$  antibonding orbital is typically negligible, in the case of the E<sub>2</sub>(2H)-CO<sub>2</sub> adduct,  $\sigma^*(\text{Fe-H})$  has an appreciable population (0.470 *e*) because of the strong charge transfer from the geminal  $\sigma(\text{Fe-C})$  orbital, which in turn has an unexpectedly low population for a bonding orbital (0.825 *e*). As discussed in the main text, and reiterated below, the  $\sigma(\text{Fe-C}) \rightarrow \sigma^*(\text{Fe-H})$  drives the proton transfer from Fe to C with the formation of HCOO<sup>-</sup>. It should also be noted that because of  $\sigma(\text{Fe-C}) \rightarrow \sigma^*(\text{Fe-H})$  charge transfer, a population analysis based on charge partitioning yields the substantial negative charge of -0.214 *e* on the hydrogen of the Fe-H bond (Table S4), providing the misleading suggestion that Fe-H has a partial “hydridic character”.

The strength  $\Delta E^{(2)}$  of charge transfer interaction  $\phi_1(\text{A-B}) \rightarrow \phi_2(\text{C-D})$  between two orbitals can be estimated from the second order perturbative formula

$$\Delta E^{(2)} = -2 \frac{|\langle \phi_1 | \hat{F} | \phi_2 \rangle|^2}{\varepsilon_2 - \varepsilon_1}$$

where  $\hat{F}$  is the Fock operator, and  $\varepsilon_2$  and  $\varepsilon_1$  are the NBO energies associated to  $\phi_1$  and  $\phi_2$ .

In turn, from  $\Delta E^{(2)}$  the charge  $q_{\text{CT}}$  transferred from  $\phi_1(\text{A-B})$  to  $\phi_2(\text{C-D})$  is obtained as  $q_{\text{CT}} = |\Delta E^{(2)}|/(\varepsilon_2 - \varepsilon_1)$  (in electron charge, *e*).

Table S2 reports the value of  $q_{\text{CT}}$  relative to the major interactions between E<sub>2</sub>(2H) and CO<sub>2</sub> for five situations: the (i) E<sub>2</sub>(2H)/CO<sub>2</sub> system with (Fe)H interacting with CO<sub>2</sub> at a

distance of 2 Å (direct hydride transfer mechanism), (ii) the  $E_2(2H)-CO_2$  adduct, the transition state for  $CO_2$  reduction to (iii) formate and (iv) CO according to the associative mechanism, and, finally (v) the transition state for  $H_2$  evolution from  $E_2(2H)$ . This data clearly shows the different behavior of the hydrogen atom bound to Fe. Indeed, in the direct “hydride” transfer mechanism, the hydrogen atom moves to C of  $CO_2$  bringing with it the electron density of the Fe-H covalent bond as indicated by the large  $\sigma(Fe-H) \rightarrow \pi^*(C-O)$  charge transfer. In the associative mechanism for the  $CO_2$  reduction to formate, an appreciable amount of charge is transferred from the  $\sigma(Fe-C)$  bond to the  $\sigma^*(Fe-H)$  antibond, weakening the Fe-H bond, and at the same time an even larger amount of charge is transferred from FeMoco localized  $\sigma(Fe-X)$  bonds to  $\sigma^*(Fe-C)$  and  $\pi^*(C-O)$  antibonds, which leads to the dissociation of the Fe-H bond, with the departure of H as a proton rather than an hydride, and the breaking of the Fe-C bond. At the transition state the dominant charge transfer is from  $\sigma(Fe-X)$  to  $\pi^*(C-O)$ . Finally, in the  $H_2$  elimination, Fe-H bond behaves again as a hydride donor, and the reaction can be described as a protonation of the hydride by the S-H group.

**Table 3-S1. Coefficients ( $c_A$  and  $c_B$ ) and occupation of selected Natural Bond Orbitals,  $\phi(A-B)$ , where  $\phi = \sigma$  (sigma bonding),  $\sigma^*$  (sigma antibonding), and  $\pi^*$  (pi antibonding). The reported values are relative to the spin up orbitals. Similar trends are observed for the spin down.**

Species	Orbital	$c_A$	$c_B$	Occupation ( $e$ )
E <sub>2</sub> (2H)	$\sigma(\text{Fe-H})$	0.690	0.724	0.911
	$\sigma(\text{S-H})$	0.761	0.647	0.997
	$\sigma^*(\text{Fe-H})$	0.724	-0.689	0.057
	$\sigma^*(\text{S-H})$	0.647	-0.762	0.023
E <sub>2</sub> (2H)...CO <sub>2</sub>	$\sigma(\text{Fe-H})$	0.609	0.7928	0.850
Direct pathway	$\sigma(\text{S-H})$	0.763	0.646	0.996
(H...CO <sub>2</sub> distance = 2 Å)	$\sigma^*(\text{Fe-H})$	0.793	-0.609	0.091
	$\sigma^*(\text{S-H})$	0.646	0.763	0.023
	$\sigma^*(\text{C=O})$	0.591	0.806	0.411
E <sub>2</sub> (2H)-CO <sub>2</sub>	$\sigma(\text{Fe-H})$	0.838	0.546	0.861
Associative pathway	$\sigma(\text{S-H})$	0.662	0.750	0.996
	$\sigma(\text{Fe-C})$	0.838	0.546	0.825
	$\sigma^*(\text{Fe-H})$	0.546	-0.838	0.470
	$\sigma^*(\text{S-H})$	0.662	0.750	0.010
E <sub>4</sub> (4H)	$\sigma_1(\text{Fe-H})$	0.647	0.763	0.800
	$\sigma_2(\text{Fe-H})$	0.782	0.623	0.719
	$\sigma_1(\text{S-H})$	0.755	0.655	0.995
	$\sigma_2(\text{S-H})$	0.777	0.630	0.967

**Table 3-S2. Magnitude of the charge  $q_{CT}$  transferred from the NBOs  $\phi_1$  and to the NBO  $\phi_2$ ,  $\phi_1(A-B) \rightarrow \phi_2(C-D)$ , for selected species, where  $\phi_{2=1,2} = \sigma$  (sigma bonding),  $\sigma^*$ (antibonding),  $\pi^*$  (pi antibonding), and  $n$  (lone pair). Both spin up and spin down orbital have been considered for the calculation of  $q_{CT}$ .**

Species	Interaction	$q_{CT}$ ( $e$ )
$E_2(2H) \dots CO_2(\text{Direct pathway})$	$\sigma(\text{Fe-H}) \rightarrow \pi^*(\text{C-O})$	0.182
$E_2(2H)-CO_2$	$\sigma(\text{Fe-C}) \rightarrow \sigma^*(\text{Fe-H})$	0.108
	$\sigma(\text{Fe-C}) \rightarrow \sigma^*(\text{Fe-C})$	0.116
	$\sigma(\text{Fe-X}) \rightarrow \pi^*(\text{C=O})$	0.188
	$\sigma(\text{Fe-X}) \rightarrow \sigma^*(\text{Fe-C})$	0.307
$E_2(2H)-CO_2 \rightarrow E_2(H) + HCOO^-$ (TS)	$\sigma(\text{Fe-X}) \rightarrow \sigma^*(\text{Fe-C})$	0.218
	$\sigma(\text{C-H}) \rightarrow \sigma^*(\text{Fe-S})$	0.118
$E_2(2H)-CO_2 \rightarrow E_2(H)-COOH$ (TS)	$n(O) \rightarrow \sigma^*(\text{S-H})$	0.211
$E_2(2H) \rightarrow E_0 + H_2$ (TS)	$\sigma(\text{Fe-H}) \rightarrow \sigma^*(\text{S-H})$	0.290



**Table 3-S3. NBO point charges ( $e$ ) on the FeMoco cluster in various catalytic intermediates.** The values of the Fe atoms in E<sub>2</sub>(2H), E<sub>2</sub>(2H)-CO<sub>2</sub> and E<sub>4</sub>(4H) to which the hydrogen is bound are reported in bold. Hydrogen bound to Fe and S atoms are indicated as H<sub>*i*</sub><sup>-</sup> and H<sub>*i*</sub><sup>+</sup>, respectively.

	E <sub>0</sub>	E <sub>2</sub> (2H)	E <sub>2</sub> (2H)-CO <sub>2</sub>	E <sub>4</sub> (4H)
Fe1	0.859	0.874	0.724	0.831
Fe2	0.749	<b>0.467</b>	<b>0.647</b>	<b>0.518</b>
Fe3	0.695	0.766	-0.689	0.757
Fe4	0.695	0.656	-0.762	0.772
Fe5	0.636	0.628	0.7928	0.789
Fe6	0.671	0.519	0.646	<b>0.535</b>
Fe7	0.705	0.726	-0.609	0.418
S1A	-0.719	-0.813	-0.759	-0.831
S2A	-0.807	-0.768	-0.730	<b>-0.685</b>
S3A	-0.886	-0.887	-0.838	-1.136
S4A	-0.747	-0.776	-0.766	-0.706
S5A	-0.854	-0.926	-0.826	-0.926
S1B	-0.310	-0.318	-0.395	-0.364
S2B	-0.890	<b>-0.483</b>	<b>-0.569</b>	<b>-0.516</b>
S3B	-0.357	-0.379	-0.315	-0.253
S4B	-0.367	-0.387	-0.361	-0.418
Mo	-0.033	-0.011	-0.089	0.021
C <sup>4+</sup>	-1.131	-1.097	-0.990	-1.197

---

$H_1^-$	-0.137	-0.214	-0.031
$H_2^-$			-0.004
$H_1^+$	0.128	-0.132	0.097
$H_2^+$			0.023

---

---



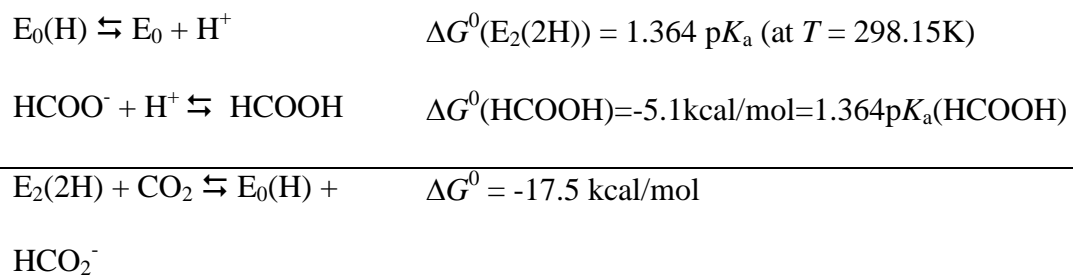
**Table 3-S5: Product accumulation and electron distribution for MoFe protein variants**

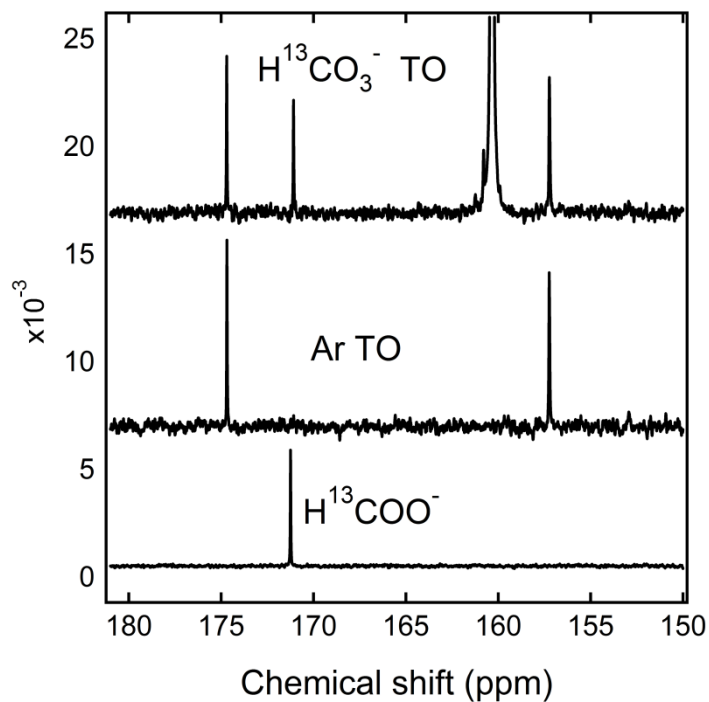
	Product							
	H <sub>2</sub>		HCOO <sup>-</sup>		CH <sub>4</sub>		CO	
	nmol/nmol/min <sup>a</sup>	% e <sup>-</sup>	nmol/nmol/min	% e <sup>-</sup>	nmol/nmol/min	% e <sup>-</sup>	nmol/nmol/min	% e <sup>-</sup>
<b><u>α-70<sup>Ala</sup></u></b>								
Ar	78±1	100	ND <sup>b</sup>	ND	ND	ND	ND	ND
CO <sub>2</sub>	47±2	70	21±3	29	ND	ND	0.14±0.01	1
<b><u>α-195<sup>Gln</sup></u></b>								
Ar	74±2	100	ND	ND	ND	ND	ND	ND
CO <sub>2</sub>	73±2	100	ND	ND	ND	ND	ND	Trace
<b><u>α-70<sup>Ala</sup> / α-195<sup>Gln</sup></u></b>								
Ar	103±1	100	ND	ND	ND	ND	ND	ND
CO <sub>2</sub>	79±2	78	21±6	21	0.32±0.01	1.24	0.0007	Trace

<sup>a</sup>nmol product/nmol MoFe protein/min. Rates are the average over the 60 min assay at 30°C with 1 mg MoFe protein and 1 mg Fe protein. CO<sub>2</sub> was at a partial pressure of 0.45 atm.

<sup>b</sup>Not detected

**Scheme 3-S1. Thermodynamic cycle for determining the  $pK_a$   $E_0(H)$ .** The value  $\Delta G^0(HCOOH) = 5.1$  kcal/mol is derived from the experimental  $pK_a$  of formic acid (3.77) [Brown, H. C. et al., in Braude, E. A. and Nachod, F. C., *Determination of Organic Structures by Physical Methods*, Academic Press, New York, 1955]. The value  $\Delta G^0 = -17.5$  kcal/mol was calculated in the present work.



**Figures:**

**Figure 3-S1.  $\text{HCOO}^-$  via  $^{13}\text{C}$  NMR.**  $^{13}\text{C}$  formate was detected at  $\delta=171.083$  ppm only during  $\text{H}^{13}\text{CO}_3^-$  turnover but not under Ar turnover. Natural abundance  $^{13}\text{C}$  formate was used as reference to get the chemical shift for formate. Conditions: 50 mM  $\text{H}^{13}\text{CO}_3^-$ , 1 mg wild type MoFe protein, 1 mg Fe was used to carry out the turnover for 60 min at 30  $^\circ\text{C}$ .

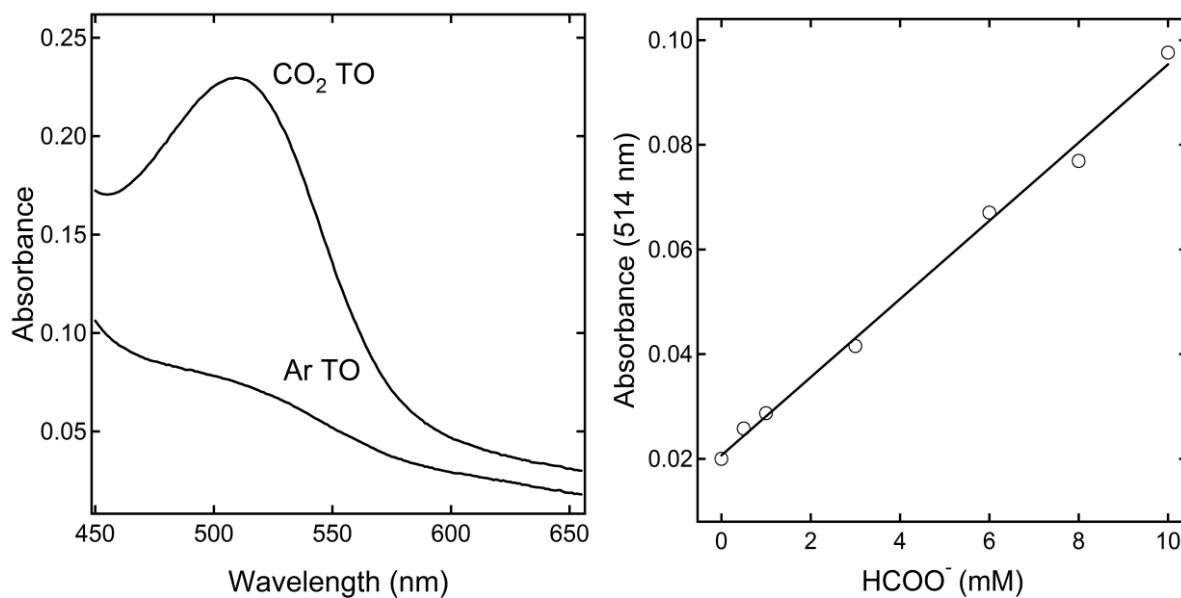


**Figure 3-S2. Colorimetric assay for formate.** (Left) Absorbance versus wavelength of a sample following turnover under CO<sub>2</sub> (top) or Ar (bottom) in the formate assay. (Right) Standard calibration curve for the formate colorimetric assay.

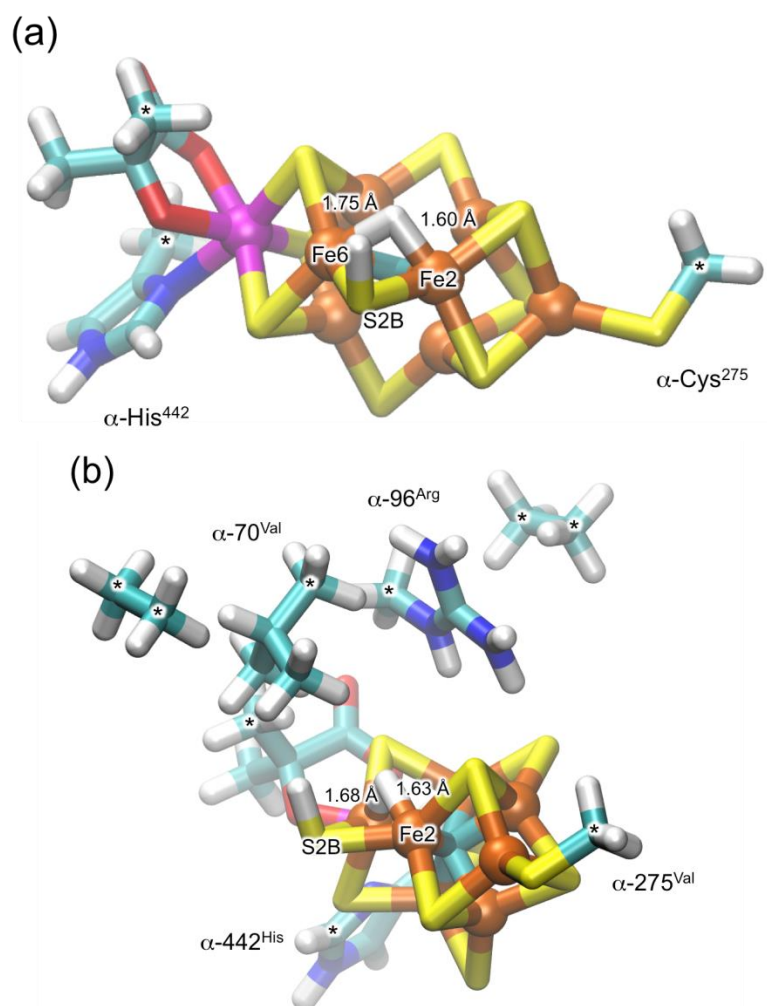


**Figure 3-S3. Structures of the models used for the DFT calculations.** Atom coloring is as follows: rust, iron; magenta, molybdenum; yellow, sulfur; cyan, carbon; blue, nitrogen; red, oxygen; grey, hydrogen. The atoms marked with asterisks were kept frozen to their crystallographic position during the geometry optimizations. Selected Fe-H distances are shown. (a) minimal model and (b) extended model that includes key amino acid side chains.



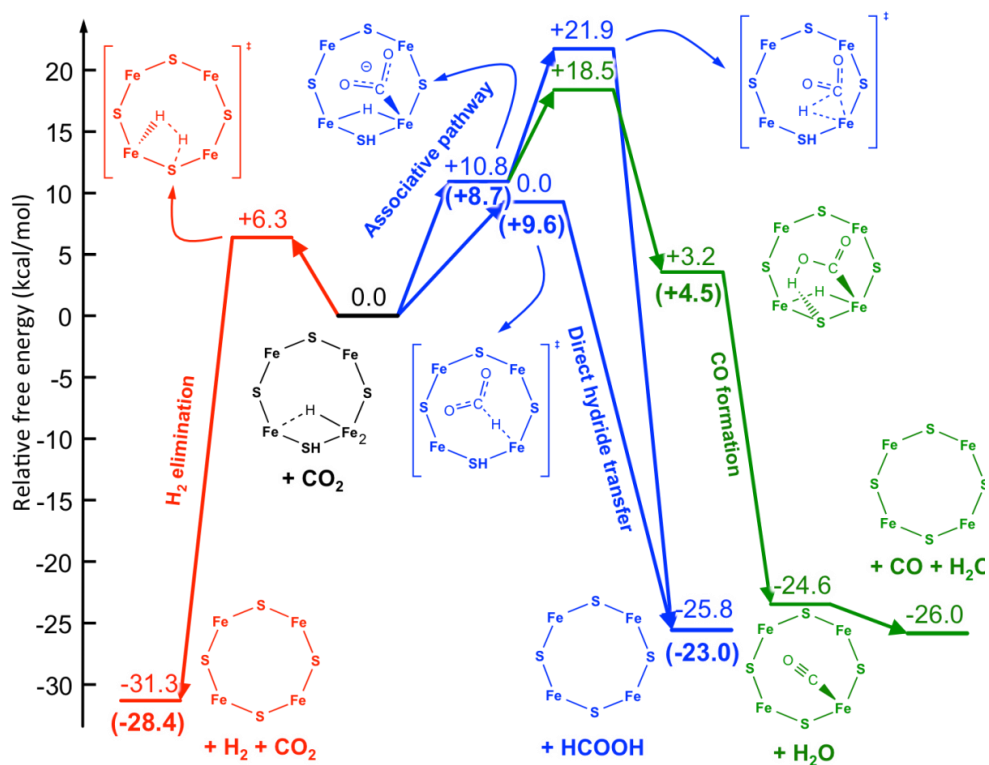


**Figure 3-S4. Computed free energy diagram for CO<sub>2</sub> reduction and H<sub>2</sub> formation occurring at the E<sub>2</sub> state of FeMo-cofactor.** Values reported for model 1 (Figure S3a) and model 2 (Figure S3b, values given in parenthesis).

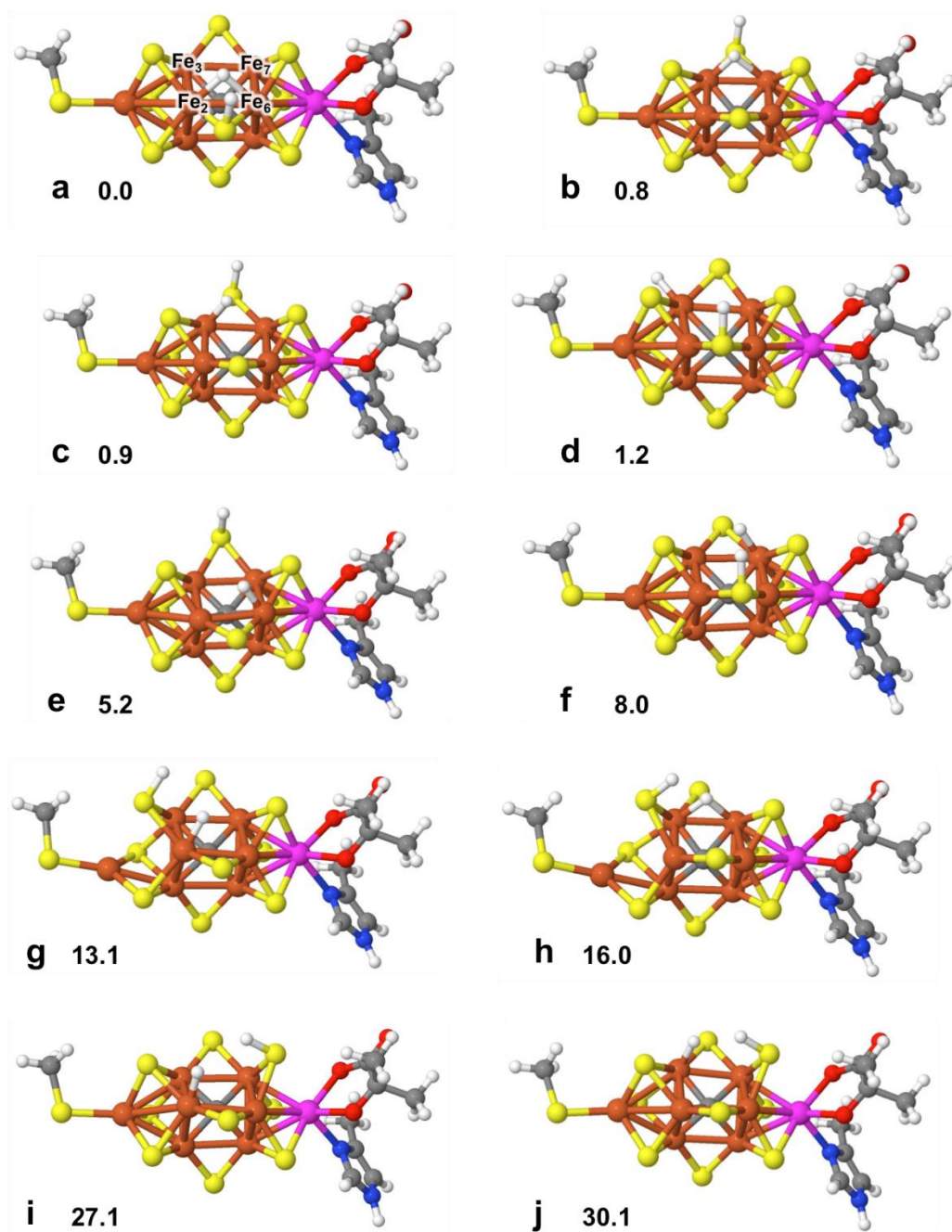


**Figure 3-S5. Structure and relative free energy of various  $E_2$  states examined computationally.** The DFT calculations indicate a preference for a hydric hydrogen shared between two Fe centers and a protic hydrogen located on a  $\mu$ -S atom. Protonation of a  $\mu_3$ -S atom is highly unfavorable (structure g, h, i and j). All free energies are given in kcal/mol.

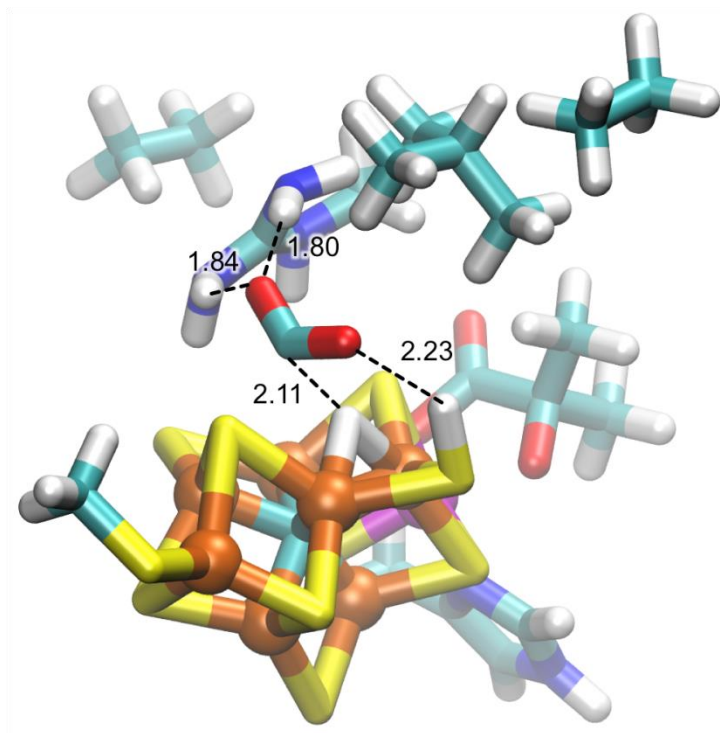


**Figure 3-S6. Structure of the transition state for the direct hydride transfer to CO<sub>2</sub> as computed from model 2. Relevant distances are given in Å.**

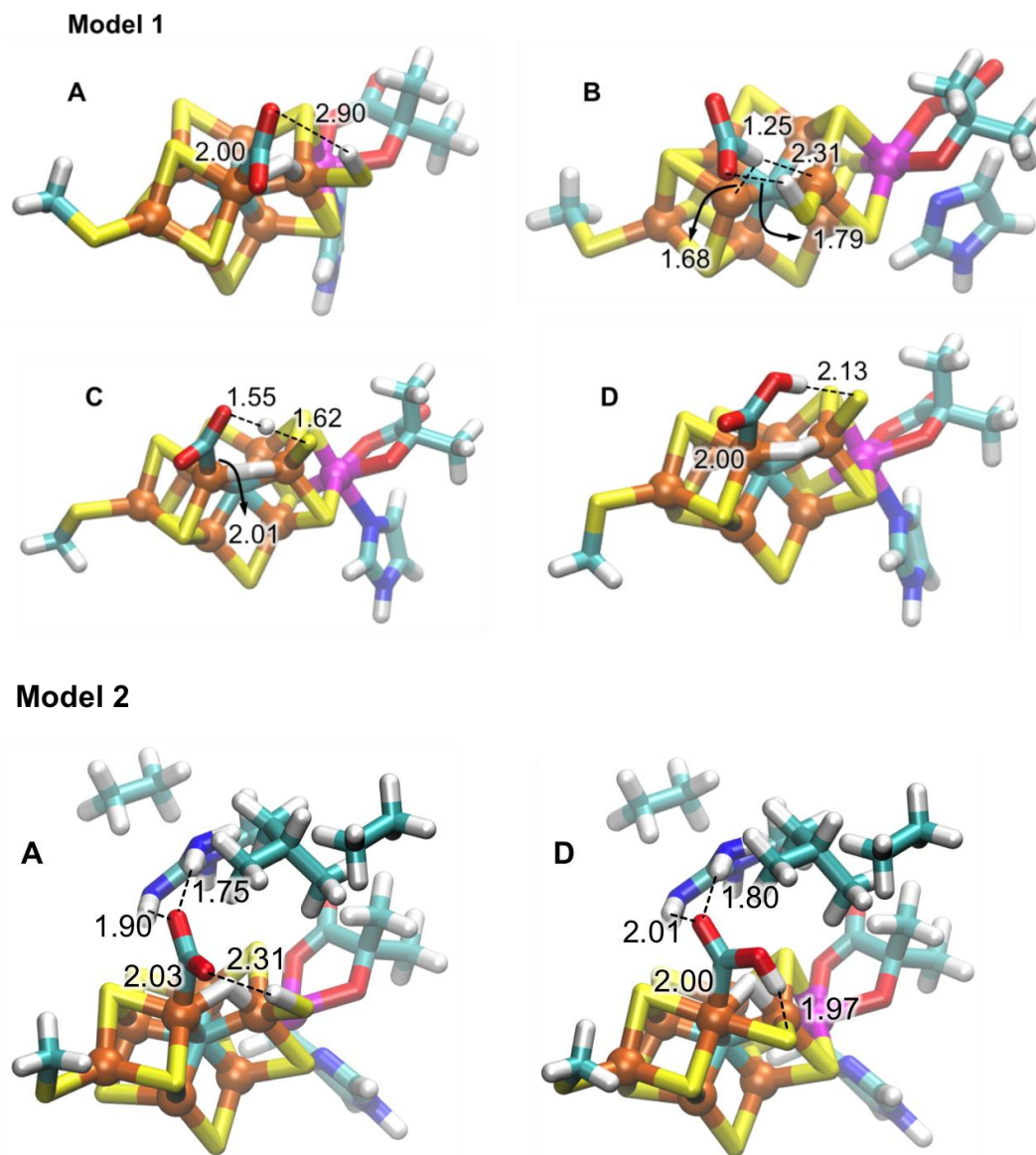


**Figure 3-S7. Selected structures of species leading to the formation of formate (associative pathway) and CO as computed from model 1 and model 2. A: E<sub>2</sub>-CO<sub>2</sub> adduct; B: transition state for the hydride transfer to the C atom of CO<sub>2</sub>; C: transition state for the proton transfer to the O atom of CO<sub>2</sub> bound to E<sub>2</sub>; D: E<sub>2</sub>-COOH adduct. Relevant distances are given in Å.**

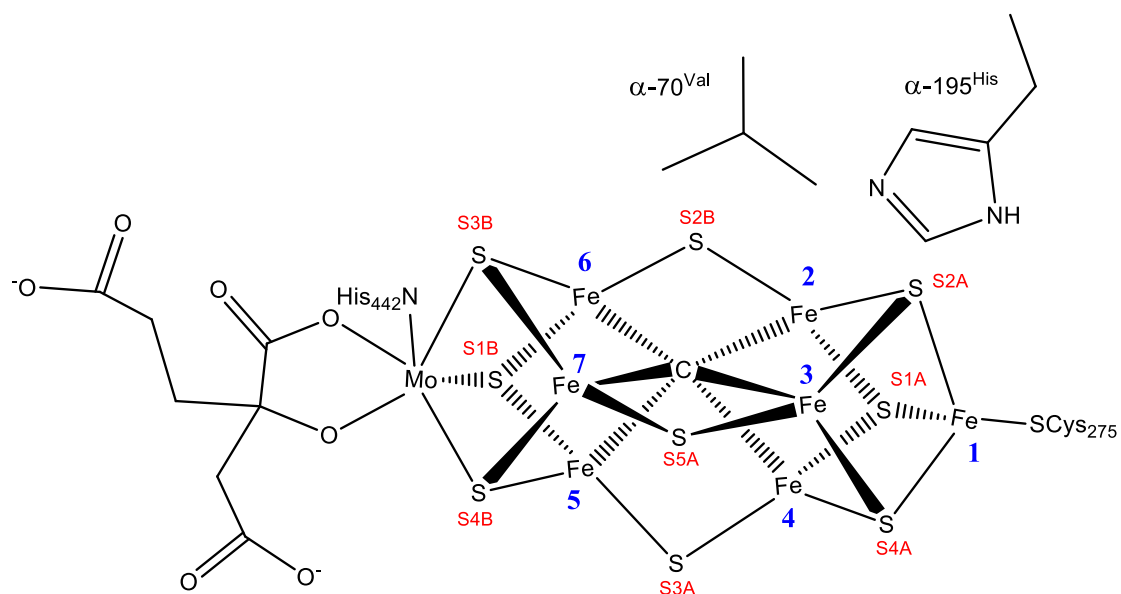


**Figure 3-S8. Key catalytic residue around FeMo-cofactor that modulate catalytic selectivity.**  $\alpha$ -70<sup>Ala</sup> is above the catalytic 4Fe-4S face and acts as a “gatekeeper” to control the access of substrate to the FeMo-cofactor.  $\alpha$ -195<sup>His</sup> is presumed to be one of the proton donors to the cofactor.

CHAPTER 4  
PATHWAY OF CO<sub>2</sub> REDUCTION TO CH<sub>4</sub> AND C-C BOND FORMATION  
CATALYZED BY NITROGENASE

**Abstract**

Nitrogenase catalyzes multi electrons/protons reduction of many unsaturated molecules besides its physiological substrate, dinitrogen (N<sub>2</sub>). Decades of exploration of the nitrogenase catalysis reveal that it uses diverse mechanisms to overcome the kinetics and thermodynamics barriers associated with the reduction processes, namely proton-coupled electron transfer (PCET), migratory insertion (*mi*), deprotonation of the metal hydride, and reductive elimination (*re*). In this study, we show how nitrogenase uses various mechanisms for the reduction of carbon dioxide (CO<sub>2</sub>) to methane (CH<sub>4</sub>) and for the functionalization of CO<sub>2</sub> through the C-C bond. The activation of CO<sub>2</sub> to CO involves an unfavorable deprotonation of bridging hydride while in the subsequent step it uses a reversible hydride transfer mechanism to activate and reduce CO to formyl intermediate. Kinetics studies with different MoFe proteins show that the thermodynamics associated with CO/formyl equilibrium is, in fact, the rate-determining step for the overall reduction of CO<sub>2</sub> to CH<sub>4</sub>. In addition, we show through the C-C bond formation reactions that nitrogenase uses different mechanisms for the activation of different carbon-containing substrates but ultimately “funnels” the reduction pathways into the common intermediates that are released from the FeMo-co via the reductive elimination mechanism.

---

\*Coauthored by Nimesh Khadka, Dennis R Dean, Brian M. Hoffmann, and Lance C. Seefeldt. *Manuscript in preparation.*

## Introduction

Nitrogenase catalyzes the reduction of an inert dinitrogen ( $N_2$ ) to the two molecules of ammonia ( $NH_3$ ) and is one of the dominant contributors of fixed nitrogen in the biogeochemical nitrogen cycle.<sup>1,2</sup> The most active and heavily studied Mo-nitrogenase has two components: (i) MoFe protein that contains a multi-metallic FeMo-co ( $7Fe-9S-1Mo-1C-R$  homocitrate; denoted **M**; **Figure 4-1**) in its active site and (ii) Fe protein that has a redox active  $[4Fe-4S]$  center.<sup>3</sup>

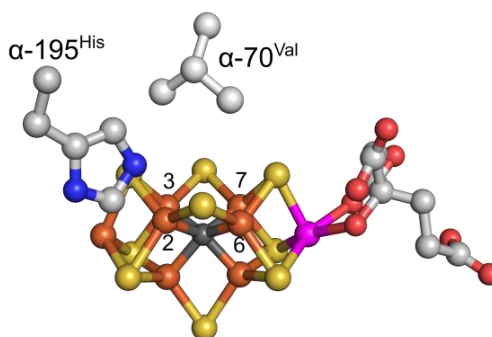


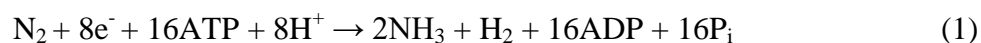
**Figure 4-1: Crystal structure of FeMo-co.** Fe is shown in rust, S in yellow, Mo in magenta, carbide in dark-grey, carbon in gray, N in blue and O in red. The four Fe atoms of the catalytic  $[4Fe-4S]$  face are labeled as 2, 3, 6, and 7. Two amino acids,  $\alpha-70^{Val}$  and  $\alpha-195^{His}$ , around the FeMo-co are also shown; the former or both are modified in enzyme used in this study. The image was created using PDB coordinate 2AFI.

Substrates reduction is initiated by the transfer of electrons  $[e^-]$  from the reduced  $[4Fe-4S]$  center of the Fe protein to the FeMo-co of the MoFe protein in a reaction that is coupled to the hydrolysis of 2 MgATP per  $[e^-]$  transfer.<sup>4-6</sup> The addition of each electron to the FeMo-co is associated with a coupled proton transfer from the network of proton donors; hence, the overall mechanism being proton-coupled electron transfer (PCET) as represented in the simplified Lowe-Thorneley (LT) kinetic scheme for nitrogenase catalysis (**Figure 4-2**).<sup>4,7</sup> Each state of the MoFe protein in LT catalytic cycle is denoted



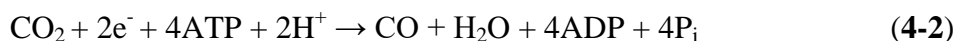


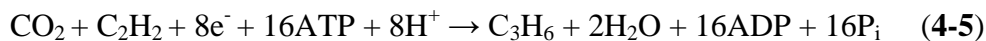
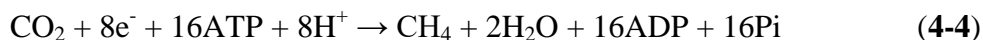
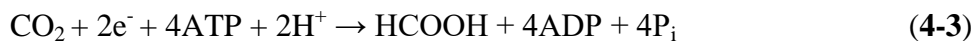
transforms the inactivated  $E_4(4H)$  to a new activated state,  $E_4(2H)^*$ , that has propensity to bind  $N_2$  through an oxidative addition (*oa*).<sup>10,12,13</sup> The *oa* of  $N_2$  to  $E_4(2H)^*$  promptly transfers 2 [ $e^-$ ] from FeMo-co to  $\pi^*$  orbital of  $N_2$  followed by the concerted transfer of 2 protons from adjacent protonated sulfides ( $-SH^+$ ) that hydrogenate  $N_2$  to a diazene level intermediate,  $E_4(2N_2H)$ .<sup>12</sup> This mechanistic requirement of obligatory dihydrogen ( $H_2$ ) evolution during the activation of  $N_2$  explains the need of 8 PCET steps rather than 6 as required for the chemical reduction of  $N_2$  to  $2NH_3$  (Eq. 1),



In the latter half of catalysis, nitrogenase acquires additional 4 [ $e^-/H^+$ ] through 4 steps of PCET and likely uses two different mechanisms, namely migratory insertion (*mi*) into metal hydride and PCET, to form two molecules of  $NH_3$ .<sup>7,12,14</sup> Decades of studies on the  $N_2$  reduction mechanism show that nitrogenase uses various mechanisms at different stages of the reduction pathway to overcome both the thermodynamic and the kinetic barriers. Such an ability of nitrogenase to orchestrate varieties of mechanisms allows it not only to reduce  $N_2$  but many other small, unsaturated molecules including carbon dioxide ( $CO_2$ ), a potent greenhouse gas and a major contributor to the global climate change.<sup>15-17</sup>

Previous studies report that the wild type MoFe protein reduces carbon dioxide ( $CO_2$ ) by 2 [ $e^-/H^+$ ] to carbon monoxide (CO) and formate ( $HCOO^-$ ) while only the remodeled  $\alpha$ -70<sup>Ala</sup>/ $\alpha$ -195<sup>Gln</sup> MoFe protein reduces  $CO_2$  by 8 [ $e^-/H^+$ ] to methane ( $CH_4$ ) and catalyzes the C-C bond formation with following stoichiometry (**Eqn 4-2,5**),<sup>16-18</sup>





Reduction of  $\text{CO}_2$  by 2 [ $\text{e}^-/\text{H}^+$ ] to  $\text{HCOO}^-$  ( $E^{\circ'} = -0.43$  V vs NHE) or CO ( $E^{\circ'} = -0.52$  V vs NHE) or by 8 [ $\text{e}^-/\text{H}^+$ ] to  $\text{CH}_4$  ( $E^{\circ'} = -0.24$  V vs NHE) are all thermodynamically favorable, yet the kinetic barrier associated with the activation of  $\text{CO}_2$  limits the number of available catalyst.<sup>19</sup> Nitrogenase is the only single catalyst (enzyme) that catalyzes the reduction of two most challenging and mechanistically different reactions: -  $\text{N}_2$  and  $\text{CO}_2$  reduction. Therefore, understanding different activation mechanisms by nitrogenase might insights into developing a single molecular catalyst with diverse substrate selectivity. In this study, we demonstrate how nitrogenase uses different pathways for the reduction of  $\text{CO}_2$  to  $\text{CH}_4$  and how it couples the reduced intermediates to form the C-C bond.

## Materials and Methods

*Reagents and Protein purification.* All reagents were obtained from SigmaAldrich (St. Louis, MO) or Fisher Scientific (Fair Lawn, NJ) and were used without further purification. Gasses were purchased from Air Liquide ( $\text{CO}_2$ ,  $\text{C}_2\text{H}_2$ ,  $\text{C}_3\text{H}_6$ ; Huston, TX), Matheson tri.gas (CO; Basking Ridge, NJ) and Air gas ( $\text{CH}_4$ ; Radnor, PA). *Azotobacter vinelandii* strains DJ995 (wild-type), DJ997 ( $\alpha$ -195<sup>Gln</sup>), DJ1310 ( $\alpha$ -70<sup>Ala</sup>), and DJ1316 ( $\alpha$ -70<sup>Ala</sup>/ $\alpha$ -195<sup>Gln</sup>) were grown and the corresponding MoFe proteins, having a seven-His tag near the carboxyl-terminal end of the  $\alpha$ -subunit, were expressed and purified as described.<sup>20</sup> Protein concentrations were determined using Biuret assay. The purities of

all proteins were >95% based on SDS/PAGE analysis with Coomassie staining. The handling of all buffers and proteins were done anaerobically under Ar atmosphere or under Schlenk vacuum line.

*CO reduction Assay.* Time dependent CO<sub>2</sub> reduction to CH<sub>4</sub> was carried out under 0.45 atm CO<sub>2</sub> in 9.4 mL serum vials with 1 mL of an assay buffer containing 50 mM sodium dithionite and a MgATP regenerating system (13.4 mM MgCl<sub>2</sub>, 10 mM ATP, 60 mM phosphocreatine, 0.6 mg/mL BSA, and 0.4 mg/mL creatine phosphokinase) in 100 mM MOPS buffer at pH 7.2. After addition of CO<sub>2</sub>, samples were incubated for 10 min at room temperature to equilibrate CO<sub>2</sub> in gas and liquid phase. 2.1 μM MoFe protein was then added. The assay vials were further incubated in a water bath at 30 °C for 15 min. After equilibrating the vials to the atmospheric pressure, reactions were initiated by the addition of 51.4 μM Fe protein. The reactions were allowed to run for the designated time at 30 °C and quenched by adding 700 μL of 400 mM EDTA at pH 8.0. 500 μL of headspace gas was injected into gas chromatography with FID detector to quantify CH<sub>4</sub>.

Time dependent CO<sub>2</sub> reduction to CO was quantified using hemoglobin as described.<sup>17,21</sup> The composition of assay buffer was same as above except 0.1 mg/mL hemoglobin was also included. 1.2 mL of assay buffer was transferred to 9.4 mL serum vials maintained with 0.45 atm CO<sub>2</sub> and the vials were allowed to equilibrate for 10 min at room temperature. MoFe protein was then added (0.5 mg/mL or 2.1 μM). 1 mL of this mixture was transferred to 2.2 mL (1 cm path length) quartz cuvette that is modified to maintain a defined gas atmosphere. A quartz top was fused onto the cuvettes to accommodate a 13 mm butyl rubber septum and a crimp aluminum seal. The partial

pressure of the cuvette was also adjusted to 0.45 atm CO<sub>2</sub>. The sample holder on Cary Bio UV-Visible spectrophotometer was set to 30 °C and the cuvette was placed on the holder for 15 min before the initiation of turnover. 51.4 μM Fe proteins were added to initiate the reaction. The increase in the absorbance at 418 nm was monitored that corresponds to the formation of CO-Hb complex.

*Solvent Isotope effect on CO formation.* Both H<sub>2</sub>O and D<sub>2</sub>O buffer had the same constituents as mentioned above. For D<sub>2</sub>O buffer pD was adjusted to 7.2 (pH reading of 6.8 on the scale).<sup>22</sup> The assays were conducted with fixed MoFe protein (2.1 μM) but the varying concentration of Fe protein. The rate of formation of CO was monitored by the increase of absorbance at 418 nm. The standard curves were made in both H<sub>2</sub>O and D<sub>2</sub>O buffer. The effect of H<sub>2</sub>O and D<sub>2</sub>O on the rate of CO binding to hemoglobin and the difference in molar extinction coefficient were monitored using the stop-flow spectrophotometer.

*Formamide and Formic hydrazide reduction.* Stocks of 1 M Formamide and Formic hydrazide were made in 100 mM MOPS and pH adjusted to 7.2. From this stock, appropriate volume was added to 1 mL assay buffer. Formation of CH<sub>4</sub> and CO were monitored as described above.

*EPR and photolysis.* X-band EPR samples were prepared in H<sub>2</sub>O buffer with the standard protocol using 100 μM α-70<sup>Ala</sup>/α-195<sup>Gln</sup> MoFe protein, 150 μM Fe protein, 50 μM of formic hydrazide, and 40% (v/v) ethylene glycol as a glassy agent. EPR spectra were recorded on a Bruker CW Elexsys-II E500 instrument connected to a Bruker SHQE-W resonator at 10 K. Cryogenic temperatures were achieved with an Oxford ESR-900 He-

flow cryostat. Temperature was controlled using an Oxford Instruments Model ITC 503 temperature controller. Photolysis was performed using a xenon arc lamp (Sutter Instrument Company, Model: LB-LS/30) with the time intervals of 1 min, 6.5 min, 11.5 min, 21.5 min and 31.5 min.

*C-C coupling assay.* Coupling assays were carried out in 9.4 mL serum vials containing 1 mL of assay buffer. 0.45 atm CO<sub>2</sub>, 0.005 atm CO, 50 mM HCONHNH<sub>2</sub>, 5 mM HCN/CN<sup>-</sup> and varying concentration of C<sub>2</sub>H<sub>2</sub>. 500 mM stock of KCN was made in deoxygenated 2 M MOPS pH=7.2 to counter the change in pH. 4.2 μM MoFe proteins was added to each vial and finally, the reactions were initiated by the addition of 16.8 μM Fe protein. All reactions were run for 60 min at 30 °C. 500 μL of 400 mM EDTA (pH 8.0) solution was added to quench the reaction and the gaseous products were quantified as described. Briefly, CH<sub>4</sub>, C<sub>2</sub>H<sub>4</sub> and C<sub>3</sub>H<sub>6</sub> were quantified by injecting 300 μL of headspace gas into gas chromatography with FID detector and from the same sample 50 μL of headspace gas was injected into gas chromatography with TCD detector to quantify H<sub>2</sub>.

## Results

**CO<sub>2</sub> reduction to CH<sub>4</sub>.** Substitution of two amino acid residues within the MoFe protein located near FeMo-co allows the remodeled MoFe protein ( $\alpha$ -70<sup>Ala</sup>/ $\alpha$ -195<sup>Gln</sup>) to reduce CO<sub>2</sub> by 8 [e<sup>-</sup>/H<sup>+</sup>] to methane (CH<sub>4</sub>).<sup>16,23</sup> Time dependent CO<sub>2</sub> reduction to CH<sub>4</sub> shows a lag phase of about 1 min. that proceeds before the steady state formation of CH<sub>4</sub> (**Figure 4-3**).

The lag phase corresponds to the intermediate accumulation phase that accepts

further  $[e^-/H^+]$  and gets reduce to  $CH_4$ . Recent findings have established that  $\alpha$ -70<sup>Ala</sup>/ $\alpha$ -195<sup>Gln</sup> MoFe protein reduces  $CO_2$  by 2  $[e^-/H^+]$  to  $CO$  and  $HCOO^-$  but no other reduced intermediates (like  $CH_3OH$ ,  $HCOH$ ) were detected in  $^{13}C$  or  $^1H$  NMR.<sup>18</sup> This opens two possibilities for the formation of  $CH_4$ , namely “CO pathway” or “ $HCOO^-$  pathway”.

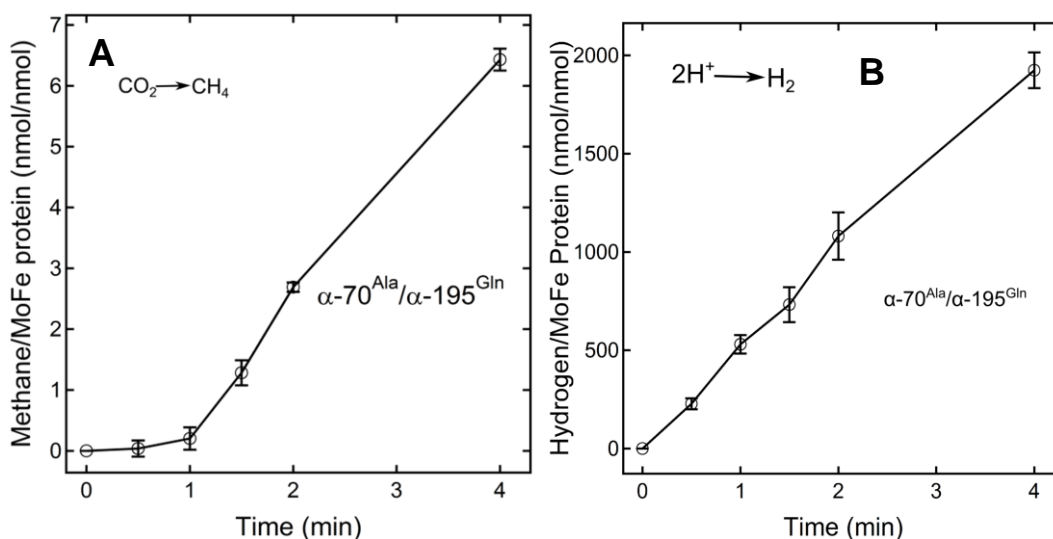


**Figure 4-3: Time dependent  $CO_2$  reduction to  $CH_4$ .** (A) A lag phase precedes the steady state formation of  $CH_4$ . This lag phase corresponds to the intermediate accumulation phase. (B) No lag phase was observed for proton reduction in the same samples used to generate data on panel A. Assay conditions: 0.45 atm  $CO_2$ , 2.1  $\mu M$  MoFe protein, and 51.4  $\mu M$  Fe protein. The reaction was done as described in the Materials and Methods.

Nitrogenase turnover in the presence of  $CO$  or  $HCOO^-$  demonstrate that  $\alpha$ -70<sup>Ala</sup>/ $\alpha$ -195<sup>Gln</sup> MoFe protein can reduce  $CO$  to  $CH_4$  but no  $CH_4$  was detected in  $HCOO^-$  turnover samples (Figure 4-4).

Furthermore, no  $CH_4$  was detected when turnover was carried out in the presence of 70 mM methanol ( $CH_3OH$ ) and formaldehyde ( $HCOH$ ), which excludes the possibility of these intermediates being accumulated during the lag phase (data not shown).

If the lag phase for CH<sub>4</sub> formation refers to CO accumulation phase, there should not be any lag phase for CO formation during this period. As predicted, only a steady state CO formation was observed (**Figure 4-S1, A**). To test if CO is kinetically and/or thermodynamically compatible as an intermediate, turnover in the presence of CO was

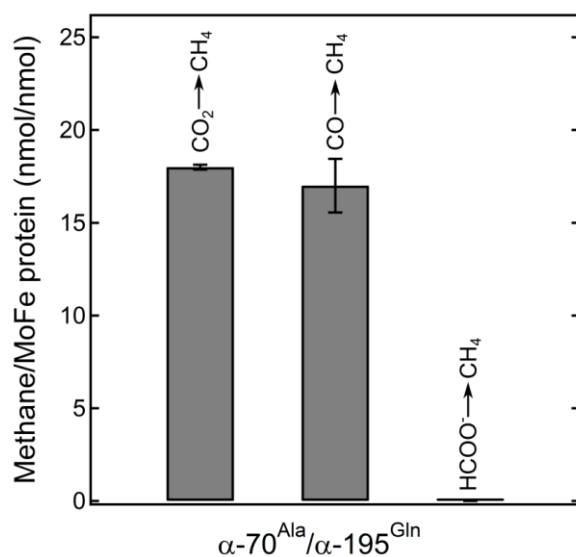


**Figure 4-4: CO<sub>2</sub> reduction to CH<sub>4</sub> likely follows CO pathway:**  $\alpha$ -70<sup>Ala</sup>/ $\alpha$ -195<sup>Gln</sup> MoFe protein catalyzes the reduction of both CO<sub>2</sub> and CO to CH<sub>4</sub>. No CH<sub>4</sub> was detected on HCOO<sup>-</sup> turnover samples. Assay conditions: 0.45 atm CO<sub>2</sub>, 0.005 atm CO, 50 mM HCOO<sup>-</sup>, 4.2  $\mu$ M MoFe protein and 104  $\mu$ M Fe protein were used. The assays were run for 20 min at 30 °C.

carried out. The reduction of CO to CH<sub>4</sub> at an approximate concentration produced during the lag phase of CO<sub>2</sub> reduction is kinetically comparable to rate of CO<sub>2</sub> reduction to CH<sub>4</sub> (~1 nmol CH<sub>4</sub>/nmol MoFe protein/min at 30 °C) (**Figure 4-S1, B**), which strongly suggests that the reduction of CO<sub>2</sub> to CH<sub>4</sub> follows “CO pathway”. To further exclude the possibility of CO formation through the isomerization of metallo-formate complex (M-OCOH), hemoglobin assay in presence of HCOO<sup>-</sup> was carried out. No CO formation was

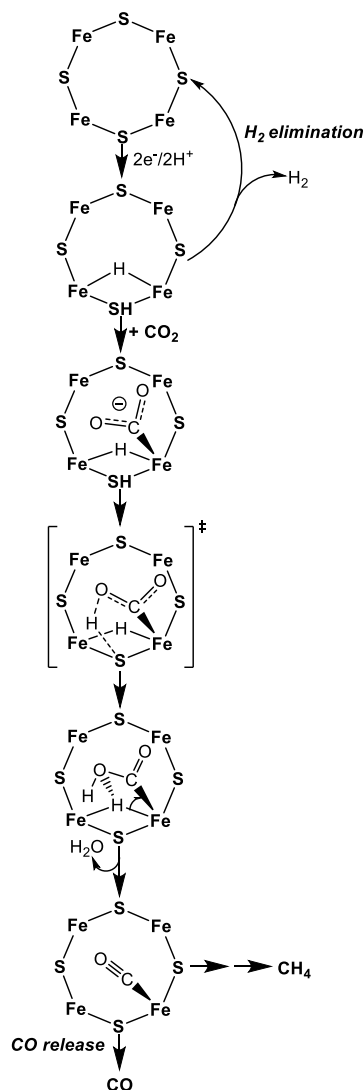


**Figure 4-5: Predicted pathway for activation of CO<sub>2</sub> toward CO formation.** DFT calculations suggest that the binding of CO<sub>2</sub> to E<sub>2</sub>(2H) state through C atom is accompanied by the transfer of electron density from FeMo-co to adsorbed CO<sub>2</sub>, however, the 2 equivalent of electron density is transferred only after coupled proton transfer from protonated sulfide (-SH). This decrease in electron density in FeMo-co causes the H attached to Fe to act as proton which is then transferred to the hydroxyl functional group of metal carboxylate species (M-COOH) that causes the cleavage of the C-O bond. The release of H<sub>2</sub>O molecules then yields CO.

detected during HCOO<sup>-</sup> turnover (**Figure 4-S2**). These observations conclude that the reduction of CO<sub>2</sub> to CH<sub>4</sub> by nitrogenase is a two-step process: (i) 2 [e<sup>-</sup>/H<sup>+</sup>] reduction of



CO<sub>2</sub> to CO and (ii) 6 [e<sup>-</sup>/H<sup>+</sup>] reduction of accumulated CO to CH<sub>4</sub>.

**Mechanism of the reduction of CO<sub>2</sub> to CO.** Our initial DFT calculations suggest that the binding and activation of CO<sub>2</sub> toward CO formation involves a mechanism of deprotonation of metal hydride (**Figure 4-5**).<sup>18</sup>

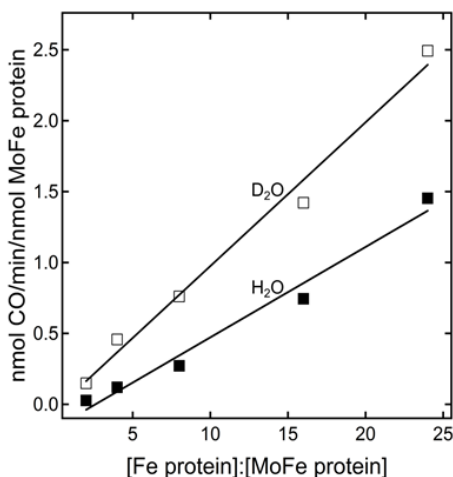


**Figure 4-6: Solvent Isotope effect on  $\alpha$ -70<sup>Ala</sup>/ $\alpha$ -195<sup>Gln</sup> MoFe protein catalyzed steady state formation of CO with changing electron flux [Fe protein]:[MoFe protein].** The steady state formation of CO during the reduction of CO<sub>2</sub> is greater in D<sub>2</sub>O as compared to H<sub>2</sub>O at all the fluxes tested. As explained above, this is expected if metal hydride were involved in the binding of CO<sub>2</sub>. The fit shown in the figure has no physical meaning. Shown data is the average of 3 different experiments. Assay conditions: - 0.45 atm CO<sub>2</sub>, 2.1  $\mu$ M MoFe protein and varying Fe protein concentration.

A competing reaction during this process is the protonolysis of metal hydride to form H<sub>2</sub>. Early temperature dependent Cryo-annealing/EPR experiments establish that protonolysis of metal hydride to form H<sub>2</sub>/ D<sub>2</sub> exhibit a normal kinetic isotope effect (KIE ( $k_H/k_D$ )  $\sim$  3-4).<sup>9</sup> As shown in the proposed mechanism (**Figure 4-5**), the presence of deuteride should disfavor the loss of reducing equivalent through hydride protonolysis and, therefore, should favor the binding of CO<sub>2</sub> to FeMo-co. The presence of hydride or

deuteride on FeMo-co should have no or negligible effect on the back-donation of electron density from FeMo-co to CO<sub>2</sub> as it involves only electronic interaction but no nuclear movement. Hence, this would predict a solvent inverse isotope effect for the steady state formation of CO if metal hydride were involved in binding of CO<sub>2</sub>. To test the hypothesis, the reactions were carried in H<sub>2</sub>O and D<sub>2</sub>O buffer.

As predicted, the steady state reduction of CO<sub>2</sub> to CO monitored by hemoglobin assay displays an inverse kinetic isotope effect (**Figure 4-6 and Figure 4-S3**). D<sub>2</sub>O has no effect either on the rate of CO binding to Hb or the molar extinction coefficient of CO-Hb complex (**Figure 4-S4**). This result corroborates our initial proposed mechanism for the reduction of CO<sub>2</sub> to CO through a pathway that involves the metal hydride for binding and subsequent reduction.

**Formyl is an intermediate in the pathway to CH<sub>4</sub> formation:** Formyl (-CHO) is an intermediate in Fisher-Tropsch chemistry and in several homogeneous catalysts that catalyze hydrogenation of CO.<sup>24</sup> It is, therefore, likely that formyl is one of the intermediates in the pathway of CO<sub>2</sub> reduction to CH<sub>4</sub> by nitrogenase. However, there is no direct spectroscopic evidence of formyl species being formed or trapped during nitrogenase turnover. We, therefore, used an “intermediate interception” strategy, previously used to elucidate the reduction pathways for N<sub>2</sub> and NO<sub>2</sub><sup>-</sup>.<sup>14,25</sup> For this, formamide (HCONH<sub>2</sub>) and formic hydrazide (HCONHNH<sub>2</sub>) were explored as new substrates for nitrogenase. This hypothesis is based on the chemical properties of carbonyl carbon. The carbonyl carbon of both formamide and formic hydrazide are electron deficient and susceptible to nucleophilic attack either by the hydride or the

electron rich metal center. When the metal center of the FeMo-co act as nucleophile, there is a possibility of C-N bond cleavage with the release of  $\text{NH}_x$  species and the transfer of the formyl group to the FeMo-co. The covalently bound formyl group further accepts 4  $[\text{e}^-/\text{H}^+]$  and gets reduce to  $\text{CH}_4$ . Hence, if formyl is an intermediate in the pathway leading to  $\text{CH}_4$ , we would expect both formamide and/or formic hydrazide to release  $\text{CH}_4$  as a reduced product. As expected, both formamide and formic hydrazide are substrates for  $\alpha\text{-}70^{\text{Ala}}/\alpha\text{-}195^{\text{Gln}}$  MoFe protein and are reduced to  $\text{CH}_4$ . Surprisingly, formic hydrazide, even more sterically hindered to reach the active site, produced more  $\text{CH}_4$  than formamide; and therefore used for further analysis (**Figure 4-7**).

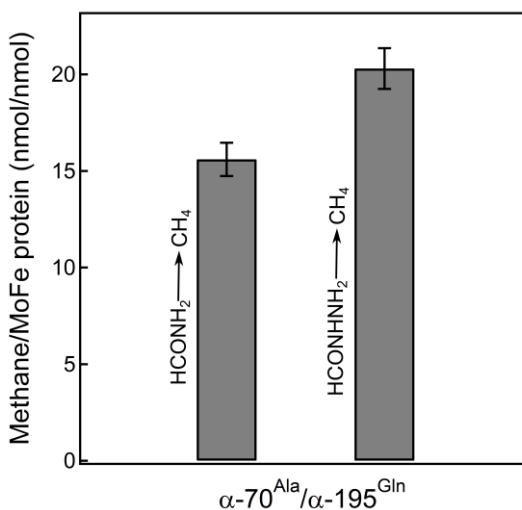


**Figure 4-7: Formamide and formic hydrazide reduction to  $\text{CH}_4$  by  $\alpha\text{-}70^{\text{Ala}}/\alpha\text{-}195^{\text{Gln}}$  MoFe protein.** Both formamide and formic hydrazide can be reduced to  $\text{CH}_4$ . The formation of  $\text{CH}_4$  is high when formic hydrazide is used as the substrate. Assay conditions: 50 mM formamide, 50 mM formic hydrazide, 2.1  $\mu\text{M}$  MoFe protein, 51.4  $\mu\text{M}$  Fe protein and 15 min of turnover time.

The formation of  $\text{CH}_4$  was confirmed using gas chromatography-mass

spectrometry (GC-MS). Analysis of head space gas formed after formic hydrazide turnover showed a peak, that is absent in Ar turnover, with the same retention time as that of methane and mass over charge ( $m/z$ ) ratio of 16 (**Figure 4-S5**). The formation of  $\text{CH}_4$  is catalytic and all the components required for the nitrogenase turnover must be present for this catalysis to occur (**Figure 4-S6**). Also, the formation of  $\text{CH}_4$  is found to show dependence on formic hydrazide concentration and a fit to this data using Michaelis-Menten equation gave a  $V_{\text{max}}$  of 1.68 nmol  $\text{CH}_4/\text{nmol MoFe protein}/\text{min}$  and  $K_m$  of 0.98 mM (**Figure 4-S7**).

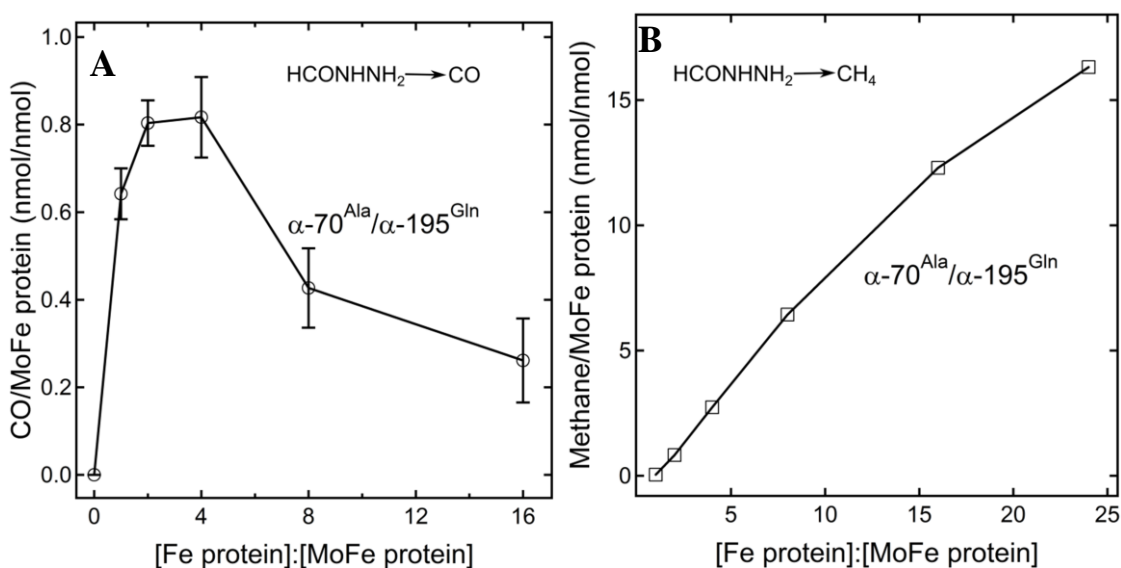


**Figure 4-8: Effect of electron flux on the formation of CO and  $\text{CH}_4$  during formic hydrazide turnover using  $\alpha\text{-70}^{\text{Ala}}/\alpha\text{-195}^{\text{Gln}}$  MoFe protein. (A) Showing the formation of CO with varying electron flux during formic hydrazide turnover. Lower electron flux favors the formation of CO. (B) Formation of  $\text{CH}_4$  is high when high electron flux is used. Assay conditions: - 50 mM formic hydrazide, 2.1  $\mu\text{M}$  MoFe protein and varying Fe protein concentration. CO detection assays were run for 8 min while assays for  $\text{CH}_4$  formation were allowed to run for 15 min.**

**Oxidation of Formyl to CO occurs at FeMo-co.** Studies on various model

complexes show that the high thermodynamic stability of CO relative to formyl shift the reaction equilibrium in the reverse direction i.e., in favor of CO.<sup>24,26</sup> To test if such unfavorable thermodynamic exists during nitrogenase catalysis, the formation of CO was monitored during formic hydrazide turnover.

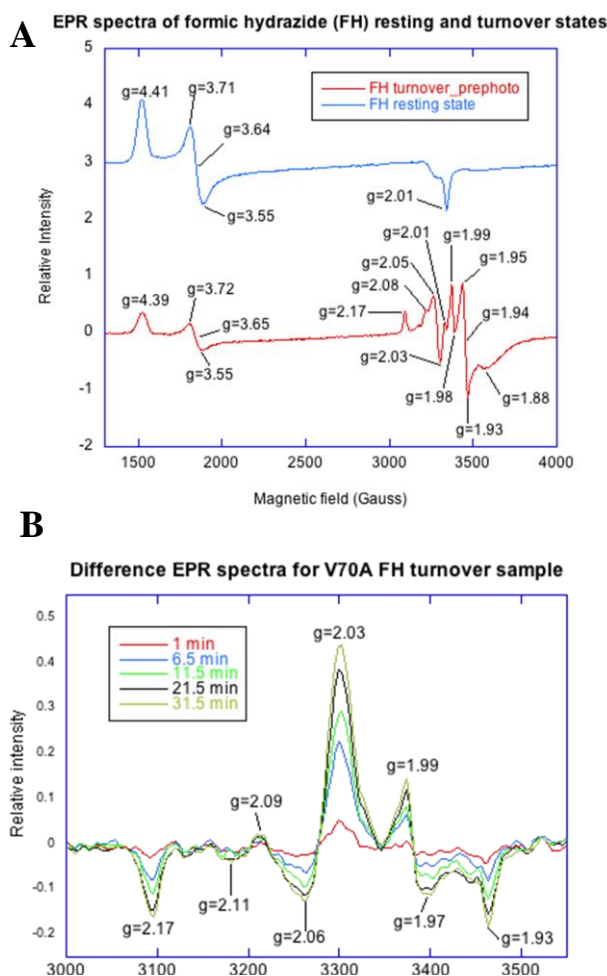


**Figure 4-9: EPR / Photolysis of freeze quench sample of formic hydrazide turnover with  $\alpha$ -70<sup>Ala</sup>/ $\alpha$ -195<sup>Gln</sup> MoFe protein. (A)** Both hi-CO and low-CO were trapped in the freeze quenched samples as represented by their respective  $g$  values. **(B)** The presence of hi-CO species was further confirmed by photolyzing it to a low-CO species. high-CO signal disappeared with the increase of low CO signal. Conditions:- 50  $\mu$ M MoFe protein, 75  $\mu$ M Fe protein, and 50 mM Formic hydrazide. EPR was run at 10 K with 2 mW power and photolysis was carried out using an arch lamp.

Hemoglobin assay confirmed the formation of CO when formic hydrazide is used as substrate (**Figure 4-S8**). Electron flux, defined as the ratio of [Fe protein]:[MoFe protein], showed a significant effect in the formation of CO and CH<sub>4</sub> during formic hydrazide reduction (**Figure 4-8A,B**). High flux favored the reduction of formyl to CH<sub>4</sub> while low flux assisted the oxidation of formyl to CO.

**EPR and photolysis confirm CO trapped state during formic hydrazide turnover.** To further confirm the relaxation of formyl species to CO, samples were freeze trapped during formic hydrazide turnover and EPR/photolysis experiments were carried out. X-band CW EPR shows the disappearance of resting state FeMo-co signal (rhombic,  $S = 3/2$ ) and a raise of a two new  $S = 1/2$  rhombic signal in the high field region centered toward  $g = 2$  region (**Figure 4-9 A**).

The signal associated with  $g = [2.17, 2.05]$  and  $g = [2.09, 1.99, 1.93]$  were identical to the signals trapped during CO turnover.<sup>27</sup> Hence, as reported before, these signals were assigned to the high CO (hi-CO) and the low CO respectively. Previous studies shows that the hi-CO state has two terminally bound CO and one of them is photo labile, which leads to the transition of the hi-CO to the low-CO state during photolysis.<sup>28,</sup><sup>29</sup> When the formic hydrazide freeze quench samples were illuminated with the arc lamp (450 nm), the peak associated with  $g = [2.09, 1.99, 1.93]$  grew in intensity while a decrease of intensity was observed at  $g = [2.17, 2.05]$  (**Figure 4-9 B**). This observation is consistent with the photolysis of hi-CO to low-CO. Undoubtedly, the oxidation of formyl to CO occurs at the FeMo-co.

**Stabilization of formyl intermediate is the key step during the reduction of CO<sub>2</sub> to CH<sub>4</sub>:** Early studies establish that all MoFe proteins reduce CO<sub>2</sub> by 2 [e<sup>-</sup>/H<sup>+</sup>] to CO and HCOO<sup>-</sup> but only  $\alpha$ -70<sup>Ala</sup>/ $\alpha$ -195<sup>Gln</sup> MoFe protein catalyzes 8 [e<sup>-</sup>/H<sup>+</sup>] reduction of CO<sub>2</sub> to CH<sub>4</sub> (**Figure 4-10 A**). Since, the CO<sub>2</sub> reduction follows CO pathway so one of the possibilities for  $\alpha$ -70<sup>Ala</sup>/ $\alpha$ -195<sup>Gln</sup> MoFe protein to catalyze the CO<sub>2</sub> reduction to CH<sub>4</sub> is its enhanced catalytic ability to reduce CO<sub>2</sub> to CO. Steady state analysis indeed demonstrates that in comparison with other nitrogenase,  $\alpha$ -70<sup>Ala</sup>/ $\alpha$ -195<sup>Gln</sup> MoFe protein catalyzes reduction of CO<sub>2</sub> to CO at a high rate (**Figure 4-10 B**).

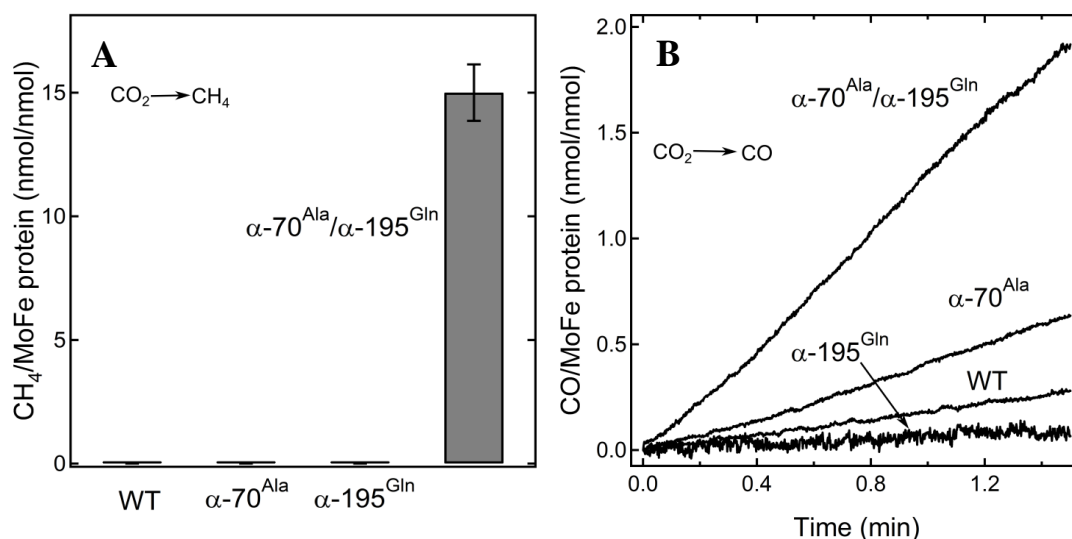


**Figure 4-10: Activity of different MoFe protein for reducing CO<sub>2</sub> to CH<sub>4</sub> and CO<sub>2</sub> to CO.** (A) Reduction of CO<sub>2</sub> to CH<sub>4</sub> as catalyzed by various nitrogenase. Only  $\alpha$ -70<sup>Ala</sup>/ $\alpha$ -195<sup>Gln</sup> MoFe protein catalyzes this chemistry with a significant rate. (B) Showing rate of CO formation during CO<sub>2</sub> reduction using various MoFe proteins. As predicted,  $\alpha$ -70<sup>Ala</sup>/ $\alpha$ -195<sup>Gln</sup> MoFe protein reduces CO<sub>2</sub> to CO at a high rate. Assay conditions:- 0.45 atm CO<sub>2</sub>, 2.1  $\mu$ M MoFe protein and 51.4  $\mu$ M Fe protein and 0.1 mg/mL Hb for CO release assay and 30 min assay time for CO<sub>2</sub> reduction to CH<sub>4</sub> assay.

However, if the concentration of accumulated CO was limiting factor for other

nitrogenase, external addition of CO at sufficient concentration should result in the formation of CH<sub>4</sub> for all MoFe proteins. Turnover under CO concentration ( $P_{CO} = 0.0005$  to .005 atm) shows that only  $\alpha$ -70<sup>Ala</sup>/ $\alpha$ -195<sup>Gln</sup> MoFe protein is able to reduce CO to CH<sub>4</sub> at that concentration (**Figure 4-11**). Hence, any of the chemical steps after the formation of CO intermediate governs the overall catalysis of CO<sub>2</sub> reduction to CH<sub>4</sub>.

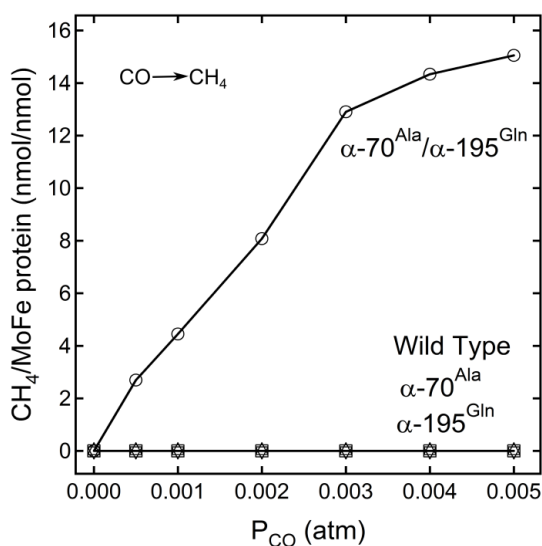


**Figure 4-11: Reduction of CO to CH<sub>4</sub> using different MoFe proteins.** Showing the reduction of CO to CH<sub>4</sub> at a lower partial pressure of CO that mimics the CO accumulation phase during CO<sub>2</sub> reduction. Only,  $\alpha$ -70<sup>Ala</sup>/ $\alpha$ -195<sup>Gln</sup> MoFe protein is able to yield CH<sub>4</sub> under the condition used. Assay conditions: - 2.1  $\mu$ M MoFe, 51.4  $\mu$ M Fe protein and 8 min of assay time.

To test if the rate-determining step for CO<sub>2</sub> reduction to CH<sub>4</sub> is before or after the formyl intermediate, turnovers were carried out in presence of formic hydrazide (**Figure 4-12**). Thermodynamically, all variants of MoFe protein were able to reduce formyl to CH<sub>4</sub> indicating that a kinetic barrier associated with the activation of CO to formyl is the most likely the rate-determining step for CO<sub>2</sub> reduction to CH<sub>4</sub>.



**Convergence of reduction pathways and Metal alkyl (M-CH<sub>3</sub>) a common intermediate.** Studies with N<sub>2</sub> and NO<sub>2</sub><sup>-</sup> reduction have shown that nitrogenase uses different mechanisms for activation of different substrates but ultimately “funnels” the reduced intermediates into a common pathway.<sup>14,25</sup> Such convergence of pathways can

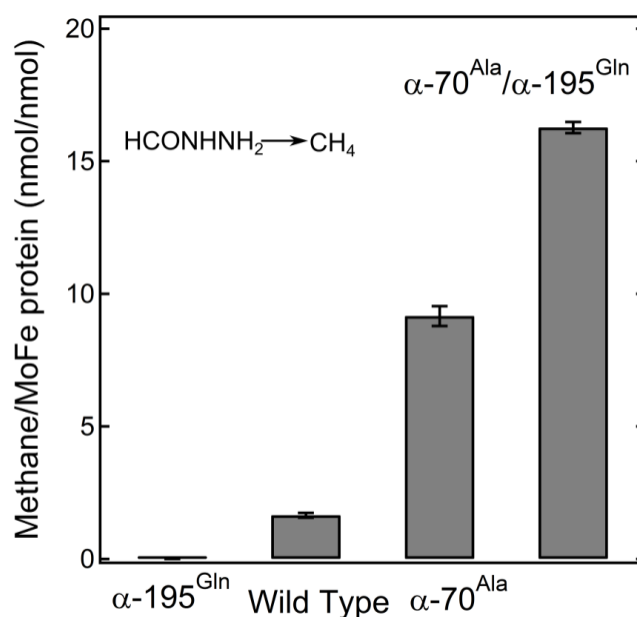


**Figure 4-12: Reduction of formic hydrazide to CH<sub>4</sub> using different MoFe proteins.** All variants including wild type MoFe protein were capable of reducing formyl to CH<sub>4</sub>. Assay conditions:- 2.1  $\mu$ M MoFe, 51.4  $\mu$ M Fe protein, 50mM Formic hydrazide and 30 min of assay time.

be expected for C containing substrates as well. To test this hypothesis, C-C coupling assays are carried out with different substrates that are reduced to CH<sub>4</sub> (CO<sub>2</sub>, CO, HCONHNH<sub>2</sub>, and HCN/CN<sup>-</sup>). A logical hypothesis would predict that nitrogenase would reduce these substrates to a common species, likely metal alkyl (M-CH<sub>3</sub>), which reductively coupled with acetylene to form propylene. As expected, propylene formation

was observed for all these substrates (**Figure 4-13**).

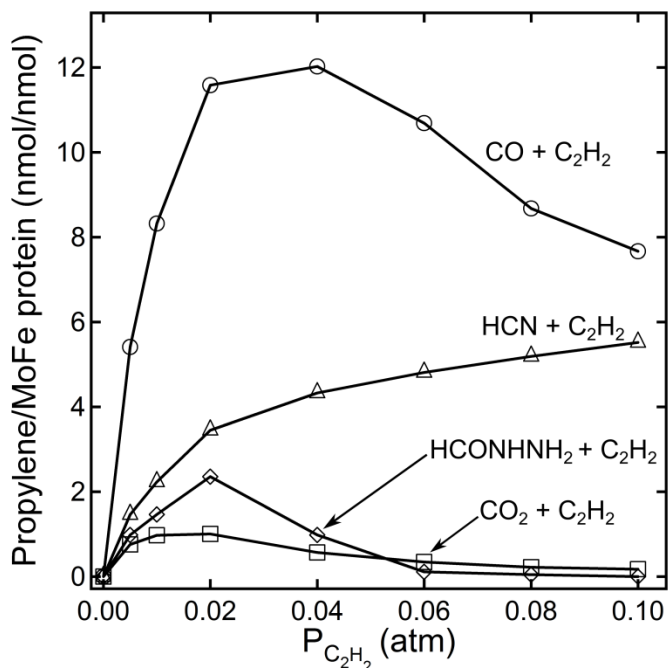


**Figure 4-13: Formation of C-C bond during co-reduction of CO<sub>2</sub>, CO, HCONHNH<sub>2</sub>, and HCN with C<sub>2</sub>H<sub>2</sub>.** Consistent with the hypothesis as mentioned above, the reduction of CO<sub>2</sub>, CO, HCONHNH<sub>2</sub> or HCN converses to a common intermediate, most likely M-CH<sub>3</sub>, which is intercepted by C<sub>2</sub>H<sub>2</sub> to form propylene. Assay conditions:- 0.45 atm CO<sub>2</sub>, 0.005 atm CO, 50 mM HCONHNH<sub>2</sub>, 5 mM HCN/CN<sup>-</sup>, 4.2 μM MoFe protein, 16.8 μM Fe protein and 60 min turnover time.

## Discussion

The multi-metallic FeMo-co uses deprotonation of metal hydride as the pathway for the reduction of CO<sub>2</sub> to CO, which contrast with the mechanisms broadly accepted for CO dehydrogenase or well-characterized Ni-cyclam complexes.<sup>18,19,30</sup> In CO dehydrogenase or Ni-cyclam complexes, CO<sub>2</sub> binds to the reduced Ni-center followed by the transfer of electron density from the filled d orbital of metal to the π\* orbital of CO<sub>2</sub> that causes the bending of CO<sub>2</sub> molecule as well as increase of C-O bond length, a feature

associated with CO<sub>2</sub> activation (**Figure 4-14**).

CO<sub>2</sub> activation is a high energy demanding process.<sup>19</sup> In CO dehydrogenase, the activation energy is significantly lowered by charge stabilization. The charge developed on oxygen atom of metal coordinated CO<sub>2</sub> (M-COO) complex is stabilized by the electrostatic interaction with the adjacent Lewis acid metal (Fe<sup>2+</sup>) as well as hydrogen (H) bonding between surrounding H donor (His residue). In a subsequent step, the coupled proton transfer from the network of H-bonding allows the further transfer of electron density from the metal center to the π\* orbital of CO<sub>2</sub> in M-COO complex that finally results in the formation of metal carboxylate (M-COOH) intermediate. A further transfer

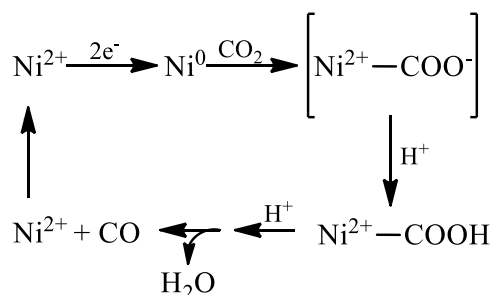


**Figure 4-14: Simplified mechanism of Ni-Fe CO dehydrogenase.** The additions of 2e<sup>-</sup> to the active site reduces Ni<sup>2+</sup> to Ni<sup>0</sup> to which linear CO<sub>2</sub> molecule binds and gets activated as evident by the decrease of bond angle and the increase of C-O bond length represented by [Ni<sup>2+</sup>-COO<sup>-</sup>] in the graphic. Lewis acid metal center (Fe<sup>2+</sup>) of the active site and the first sphere protonated histidine stabilizes the charge developed on [Ni<sup>2+</sup>-COO<sup>-</sup>] species. The transfer of H<sup>+</sup> from histidine yields Ni<sup>2+</sup>-COOH species which is further protonated to cleave C-O bond and releases H<sub>2</sub>O and CO molecule.

of one more H<sup>+</sup> to the metal carboxylate intermediate cleave C-O bond with the release of CO and H<sub>2</sub>O as the product.<sup>31</sup> Such PCET mechanism using a reduced metal center for the reduction of CO<sub>2</sub> to CO is very efficient in increasing both catalytic selectivity and frequency.<sup>32</sup> However, for nitrogenase, such a mechanism is very likely. Recent findings

have demonstrated that the transfer of  $H^+$  is so efficiently coupled with the  $e^-$  transfer that even at cryogenic temperature (77 K) they occur in a concerted manner.<sup>7</sup> This implies that when  $2[e^-/H^+]$  are added to the FeMo-co, rapid protonation of the metal center occurs to form metal hydride instead of reduced metal center. Consequently, for reactions that involve concerted  $2[e^-/H^+]$  transfer; nitrogenase preferentially uses the hydride rather than the metal as nucleophile. This feature of nitrogenase is well evident in products profile when compared to CO-dehydrogenase or Ni-cyclam. Both CO dehydrogenase and Ni-cyclam shows high catalytic selectivity for CO formation with only a trace of electrons diverted toward formate or  $H_2$  formation.<sup>33</sup> In contrast, less CO but more  $H_2$  and formate are observed for nitrogenase catalysis: - an attribute of hydride participation.<sup>18</sup>

Metal hydrides are involved in varieties of reaction, namely hydride transfer, proton transfer and hydrogen atom transfer.<sup>34</sup>



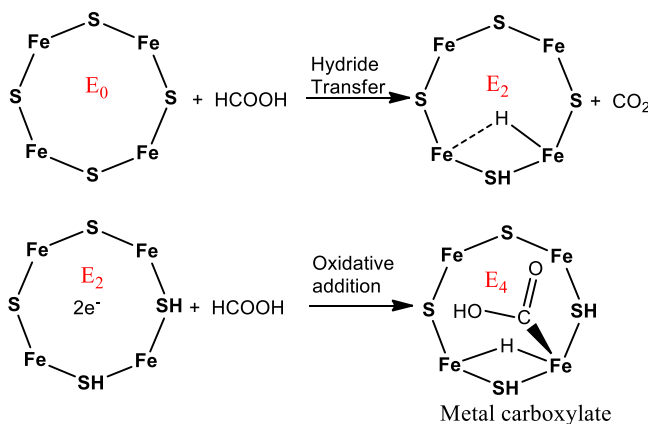
Unique structural and electronic properties of the hydride formed on the FeMo-co allow it to involve in multiple classes of reaction. The hydride formed on the FeMo-co are bridging hydride (Fe-H-Fe) and natural bond orbital (NBO) analysis on these bridging hydrides shows that the electron density is shared equally between Fe and H atom with only a small polarization of Fe-H bond as expected from the difference in electronegativity of Fe and H atoms. Therefore, Fe-H-Fe can be formally characterized as

a covalent bond. The presence of such bridging hydride increases the back donation from the metal core of the FeMo-co and allows initial binding of CO<sub>2</sub> through C atom. Binding of CO<sub>2</sub> to the Fe core of the FeMo-co involves transfer of the electron density from the filled d orbital of the Fe core to the  $\pi^*$  of CO<sub>2</sub>. Transfer of a H<sup>+</sup> from the protonated sulfide to the oxygen atom of metal bound CO<sub>2</sub> stabilizes charge transfer to CO<sub>2</sub> and results in the formation of metal carboxylate intermediate (M-COOH). M-COOH represents a state where CO<sub>2</sub> has accepted two electrons from FeMo-co. At this stage, the FeMo-co is electron deficient and, therefore, accepts the electron density from Fe-H-Fe bond that allows the associated hydride to act as proton in a mechanism known as the reductive elimination. The transfer of H<sup>+</sup> from the bridging hydride to the protonate hydroxyl functional group of M-COOH causes C-O bond cleavage and results in the formation of CO as shown in **Figure 4-5**.<sup>18</sup>

DFT calculations on the pathway leading to CO formation reveal that the energetics of the intermediates is uphill up to the formation of M-COOH. This means that one of the multiple steps involved between the bindings of CO<sub>2</sub> to the formation of M-COOH governs the rate of catalysis. A normal kinetic isotope effect on the protonation of metal hydride (M-H) to form H<sub>2</sub>/D<sub>2</sub> would increase the collision frequency of metal deuteride (M-D) with CO<sub>2</sub> relative to M-H. In addition, the proposed mechanism involves the transfer of the proton from -SH to oxygen of the CO<sub>2</sub>. Physical measurement of the fractionation factor for thiol have shown an inverse fractionation factor ranging from  $\Phi^R = 0.4$  to  $0.6$ .<sup>35</sup> Therefore, the transfer of deuteride (D<sup>+</sup>) from -SD to the oxygen atom of the CO<sub>2</sub> is thermodynamically favored over the transfer of H<sup>+</sup> from -SH. This

cumulative effect of stability of M-D against protonolysis and the presence of inverse fractionation factor for thiol explain the observation of solvent inverse isotope effect (sIIE) for the formation of CO (**Figure 4-6**). A similar sIIE for CO formation has been reported for vanadium nitrogenase which suggests that both molybdenum and vanadium nitrogenase uses the similar mechanism for the activation of CO<sub>2</sub> toward the CO formation. An interesting feature of this sIIE is the dependence of its magnitude on electron flux defined as the ratio of Fe protein to MoFe protein at a fixed CO<sub>2</sub> concentration (**Figure 4-S3**). The rate of CO formation is low at lower flux but the magnitude of sIIE is at maximum, which suggests that sIIE is revealed to the maximum magnitude under the condition when the CO<sub>2</sub> reduction becomes extremely difficult. At electron flux of 2:1 (Fe protein:MoFe protein), the magnitude of sIIE is ~5. Given that the KIE for protonation of M-H is ~4, the proposed mechanism would predict a sIIE ≥ 4. The true sIIE cannot be measured in this study but nonetheless, the observed sIIE of ~5 undoubtedly supports the proposed mechanism.

**Chart 1**

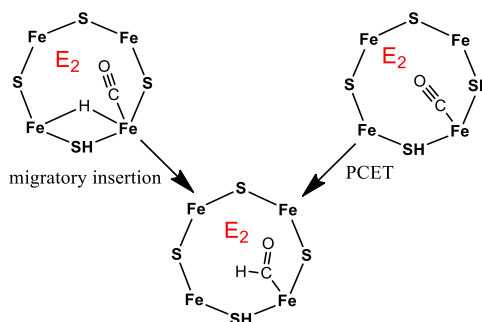


The other possibility of the formation of CO is through the isomerization of metal

formate complex (M-OCHO) that is unlikely because of the thermodynamic and the kinetic factor.<sup>36</sup> The first requirement for this process is the breakage of C-H bond of formate which can occur through two different mechanisms (**Chart 1**).

The first pathway involves the transfer of a hydride from formate to the FeMo-co that is thermodynamically unfavorable ( $\Delta G^\circ = +24$  kCal/mol). The other pathway involves the breakage of C-H bond of formate through oxidative addition to the reduced Fe atom of FeMo-co. But, given the concerted protonation of FeMo-co with the transfer of electron at 77 K, it is unlikely that formate can compete against the protonation of reduced metal to favor the oxidative addition at room temperature. Hence, it is logical to conclude that the formation of CO occurs through the direct reduction of CO<sub>2</sub> rather than the reduction of CO<sub>2</sub> to formate followed by the isomerization of formate to CO.

**Chart 2**



Having CO as an intermediate in the reduction pathway has a kinetic consequence. CO is a stable molecule with bond dissociation energy of about 1075 kJ/mol. Thus, activation of CO involves a significant barrier. Studies on model complexes show two different mechanisms for the reduction of CO to formyl (**Chart 2**). The first is the migratory insertion in which the binding of CO to metal center is followed

by the transfer of hydride to the C atom.<sup>26</sup> The other possibility is the proton coupled electron transfer mechanism (PCET), a mechanism observed for rhodium catalyst where electrons are donated through a reduced metal atom and a proton through a donor.<sup>24</sup> Computational studies on these two pathways suggest that the hydride transfer is favored over PCET to hydrogenate CO to formyl species.<sup>37</sup>

Studies on numerous  $\eta^1$ -C formyl complexes (M-CHO) shows that, because of the thermodynamic stability of M-CO,  $\eta^1$ -C formyl are very strong hydride donor.<sup>26</sup> This suggests that the activation of CO to formyl possibly involves an equilibrium process (M-H + CO  $\leftrightarrow$  M-CHO) and the equilibrium constant for this step favors the reverse direction. Indeed, the formation of CO formed during the formic hydrazide turnover corroborates such a reverse favored equilibrium. The loading of formyl group to the FeMo-co during formic hydrazide turnover creates a  $\eta^1$ -C bound metal formyl species that transfers hydride back to the FeMo-co and generates CO as a thermodynamic product. Similarly, the forward reaction of this equilibrium is a second order reaction and, therefore, depends on the concentration of M-H and CO. This is in consistent with the increase of CH<sub>4</sub> formation with increasing CO concentration (**Figure 4-11**), the lag phase needed to accumulate CO during CO<sub>2</sub> reduction(**Figure 4-1**) and the increase of CH<sub>4</sub> with increasing electron flow. All these factors push the equilibrium in the forward direction toward the formation of formyl. Besides the formation of the CO, the formyl intermediate also accepts further  $6[e^-/H^+]$  and forms CH<sub>4</sub>. The electronics of the FeMo-co determines if the formyl relaxes to CO or proceeds to CH<sub>4</sub>. Increasing electron flux through MoFe protein by increasing Fe protein to MoFe protein ratio increases the



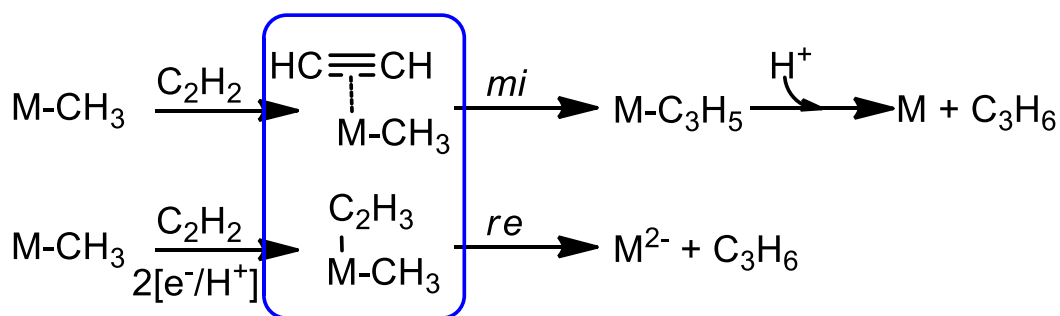


One of the features for nitrogenase catalysis is the convergence of different reduction pathways to a common intermediate as observed for nitrogen containing substrates (**Figure 4-15**).<sup>14,25</sup>

A similar feature also exists for C containing substrates. Nitrogenase uses different mechanisms for activation of different C containing substrates ( $\text{CO}_2$ ,  $\text{CO}$ ,  $\text{HCONHNH}_2$ , and  $\text{HCN}$ ) but “funnels” the different pathways into a common intermediate (**Figure 4-16**). One of the common intermediates is metal alkyl ( $\text{M-CH}_3$ ) which is intercepted by acetylene to form propylene.

Based on the literature, two possible mechanisms are likely for the formation of the C-C bond. One is the migratory insertion (*mi*) of acetylene to metal alkyl species ( $\text{M-CH}_3$ ) and the other is the reduction of acetylene to metal alkenyl species ( $\text{M-C}_2\text{H}_3$ ) which then undergo reductive elimination (*re*) with metal alkyl ( $\text{M-CH}_3$ ) to form the propylene (**Chart 3**).

**Chart 3**



According to the *mi* mechanism, the formation of propylene broadly depends on the concentration of metal alkyl species ( $\text{M-CH}_3$ ) as well as the activation energy ( $E_{act}$ ) associated with the transfer of the alkyl group to the metal  $\pi$ -coordinated acetylene. The

$E_{act}$  is substrate independent and, therefore, according to the *mi* mechanism the formation of propylene only depends on the concentration of  $M-CH_3$  formed.

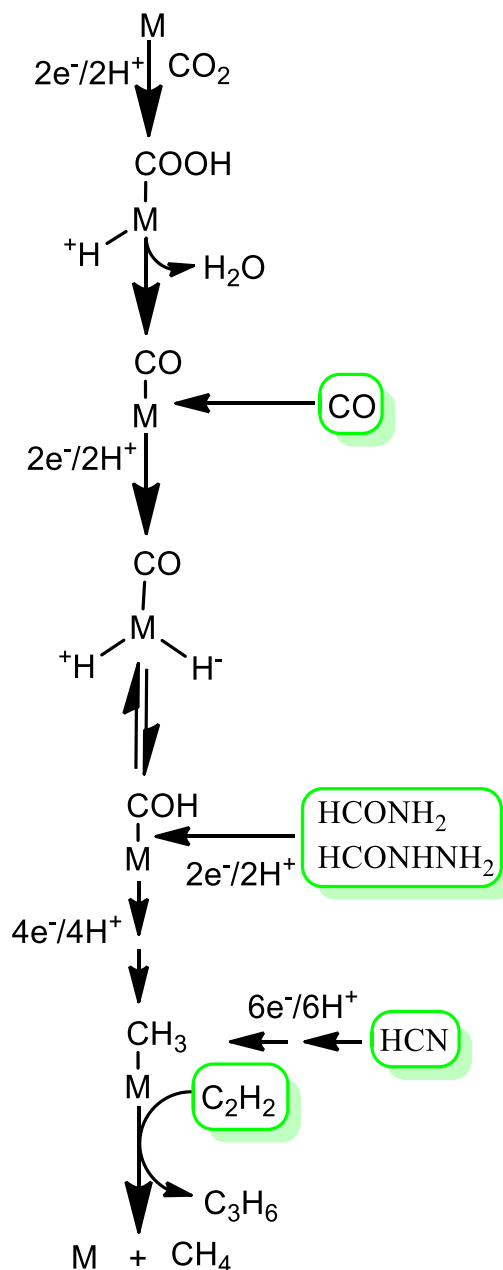
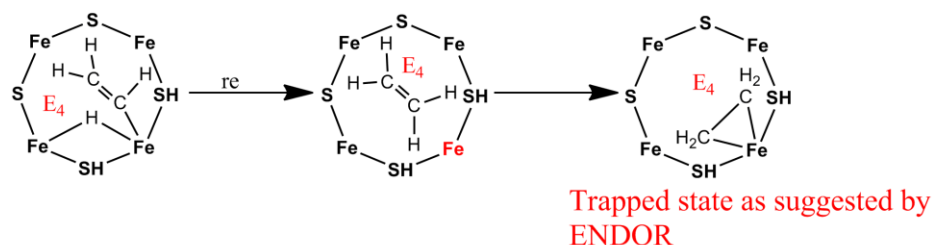


**Figure 4-16: Proposed mechanism of  $CO_2$  reduction to  $CH_4$  and the formation of the C-C bond.** The  $2[e^-/H^+]$  reduction of  $CO_2$  to  $CO$  is followed by the migratory insertion of  $CO$  into metal hydride to form formyl intermediate. The formyl intermediate can either relax back to the  $CO$  or commit to further reduction by the addition of  $[e^-/H^+]$ . Metal alkyl ( $M-CH_3$ ) is a proposed intermediate that most likely couples with acetylene to form propylene.

Hence, the prediction would be an increase in the formation of propylene with an increase of the concentration of M-CH<sub>3</sub>. In contrast to this prediction, even though reduction of HCN is ~450 folds higher as compared to CO<sub>2</sub> that in turn corresponds to ~450 folds more M-CH<sub>3</sub> formed, there is only a marginal increase in propylene formation (**Figure 4-SI Table 1**). This suggests that *mi* mechanism is not operative for the formation of the C-C bond.

On the other hand, the *re* mechanism requires the co-existence of metal alkyl (M-CH<sub>3</sub>) and metal alkenyl (M-C<sub>2</sub>H<sub>3</sub>) on the FeMo-co. This introduces additional constraints for the formation of propylene besides the concentration of M-CH<sub>3</sub> and E<sub>act</sub> as required the *mi* mechanism. The co-existence of metal alkyl (M-CH<sub>3</sub>) and metal alkenyl (M-C<sub>2</sub>H<sub>3</sub>) is affected by many other factors including the concentration of substrates, kinetic barrier associated with substrate reduction, and electron flux through MoFe protein. Thus, *re* mechanism explains why the formation of propylene is minimal even the formation of M-CH<sub>3</sub> species is enhanced by ~450 folds.

**Chart 4**



The *re* mechanism is not uncommon for the release of C product during

nitrogenase catalysis. As explained elsewhere when turnover is carried out in presence of  $N_2/D_2/C_2H_2$ , di-deuterated ethylene ( $C_2H_2D_2$ ) is formed which unequivocally confirms the release of ethylene by *re* mechanism.<sup>13</sup> In addition, the trapped species under acetylene turnover is also proposed to form through *re* mechanism (**Chart 4**).<sup>39</sup>

Therefore, the C-C bond formation must likely involve the reductive elimination of co-existed metal alkyl and metal alkenyl species from the FeMo-co.

### **Conclusion:**

Nitrogenase catalyzed reduction of  $CO_2$  to  $CH_4$  proceed via. CO pathway. Consistent with the proposed mechanism, the reduction of  $CO_2$  to CO involves the metal hydride to facilitate the binding of  $CO_2$  and the transfer of 2 electrons equivalence through an unfavorable mechanism that involves the deprotonation of metal hydride. The accumulated CO is activated to the formyl intermediate through a reversible hydride transfer mechanism with the equilibrium constant favoring the reverse direction (CO state). Kinetic studies suggest that the stabilization of the transition state during the formation of formyl is the rate determining step in the overall reduction of  $CO_2$  to  $CH_4$ . The details of the mechanism for the reduction of formyl to  $CH_4$  are unknown but data suggest that all these steps should be a downhill process and cannot be the rate-determining step for the reduction of  $CO_2$  to  $CH_4$ . Finally, analogous to the reduction of nitrogen containing substrates, nitrogenase uses different mechanisms for the activation of carbon containing molecules but ultimately converge the different reduction pathways into a common intermediate.

**References**

- (1) Burgess, B. K.; Lowe, D. J. *Chem. Rev.* **1996**, *96* (7), 2983–3012.
- (2) Smil, V. *Enriching the Earth: Fritz Haber, Carl Bosch, and the Transformation of World Food Production*; MIT Press, 2004.
- (3) Shah, V. K.; Brill, W. J. *Proc. Natl. Acad. Sci. U.S.A.* **1977**, *74*, 3249–3253.
- (4) Thorneley, R. N. F.; Lowe, D. J. In *Molybdenum Enzymes*; Spiro, T. G., Ed.; Metal Ions in Biology; Wiley-Interscience Publications: New York, 1985; Vol. 7, pp 221–284.
- (5) Hageman, R. V.; Burris, R. H. *Proc. Natl. Acad. Sci. U.S.A.* **1978**, *75*, 2699–2702.
- (6) Thorneley, R. N.; Lowe, D. J. *Biochem. J.* **1984**, *224*, 887–894.
- (7) Davydov, R.; Khadka, N.; Yang, Z.-Y.; Fielding, A. J.; Lukoyanov, D.; Dean, D. R.; Seefeldt, L. C.; Hoffman, B. M. *Isr. J. Chem.* **2016**, *56* (9-10), 841–851.
- (8) Igarashi, R. Y.; Laryukhin, M.; Dos Santos, P. C.; Lee, H.-I.; Dean, D. R.; Seefeldt, L. C.; Hoffman, B. M. *J. Am. Chem. Soc.* **2005**, *127*, 6231–6241.
- (9) Lukoyanov, D.; Barney, B. M.; Dean, D. R.; Seefeldt, L. C.; Hoffman, B. M. *Proc. Natl. Acad. Sci. U.S.A* **2007**, *104*, 1451–1455.
- (10) Lukoyanov, D.; Yang, Z.-Y.; Khadka, N.; Dean, D. R.; Seefeldt, L. C.; Hoffman, B. M. *J. Am. Chem. Soc.* **2015**, *137*, 3610–3615.
- (11) Doan, P. E.; Telsler, J.; Barney, B. M.; Igarashi, R. Y.; Dean, D. R.; Seefeldt, L. C.; Hoffman, B. M. *J. Am. Chem. Soc.* **2011**, *133* (43), 17329–17340.
- (12) Hoffman, B. M.; Lukoyanov, D.; Yang, Z.-Y.; Dean, D. R.; Seefeldt, L. C. *Chem. Rev.* **2014**, *114*, 4041–4062.

- (13) Yang, Z.-Y.; Khadka, N.; Lukoyanov, D.; Hoffman, B. M.; Dean, D. R.; Seefeldt, L. C. *Proc. Natl. Acad. Sci. U.S.A.* **2013**, *110*, 16327–16332.
- (14) Lukoyanov, D.; Yang, Z.-Y.; Barney, B. M.; Dean, D. R.; Seefeldt, L. C.; Hoffman, B. M. *Proc. Natl. Acad. Sci. U.S.A.* **2012**, *109*, 5583–5587.
- (15) Seefeldt, L. C.; Yang, Z.-Y.; Duval, S.; Dean, D. R. *Biochim. Biophys. Acta* **2013**, *1827*, 1102–1111.
- (16) Yang, Z.-Y.; Moure, V. R.; Dean, D. R.; Seefeldt, L. C. *Proc. Natl. Acad. Sci. U.S.A.* **2012**, *109*, 19644–19648.
- (17) Seefeldt, L. C.; Rasche, M. E.; Ensign, S. A. *Biochemistry* **1995**, *34*, 5382–5389.
- (18) Khadka, N.; Dean, D. R.; Smith, D.; Hoffman, B. M.; Raugei, S.; Seefeldt, L. C. *Inorg. Chem.* **2016**, *55* (17), 8321–8330.
- (19) Appel, A. M.; Bercaw, J. E.; Bocarsly, A. B.; Dobbek, H.; DuBois, D. L.; Dupuis, M.; Ferry, J. G.; Fujita, E.; Hille, R.; Kenis, P. J. A.; Kerfeld, C. A.; Morris, R. H.; Peden, C. H. F.; Portis, A. R.; Ragsdale, S. W.; Rauchfuss, T. B.; Reek, J. N. H.; Seefeldt, L. C.; Thauer, R. K.; Waldrop, G. L. *Chem. Rev.* **2013**, *113*, 6621–6658.
- (20) Christiansen, J.; Goodwin, P. J.; Lanzilotta, W. N.; Seefeldt, L. C.; Dean, D. R. *Biochemistry* **1998**, *37*, 12611–12623.
- (21) Bonam, D.; Murrell, S. A.; Ludden, P. W. *J. Bacteriol.* **1984**, *159*, 693–699.
- (22) Glasoe, P. K.; Long, F. A. *J. Phys. Chem.* **1960**, *64* (1), 188–190.
- (23) Fixen, K. R.; Zheng, Y.; Harris, D. F.; Shaw, S.; Yang, Z.-Y.; Dean, D. R.; Seefeldt, L. C.; Harwood, C. S. *PNAS* **2016**, *113* (36), 10163–10167.

- (24) Imler, G. H.; Zdilla, M. J.; Wayland, B. B. *J. Am. Chem. Soc.* **2014**, *136* (16), 5856–5859.
- (25) Shaw, S.; Lukoyanov, D.; Danyal, K.; Dean, D. R.; Hoffman, B. M.; Seefeldt, L. *C. J. Am. Chem. Soc.* **2014**, *136*, 12776–12783.
- (26) Ellis, W. W.; Miedaner, A.; Curtis, C. J.; Gibson, D. H.; DuBois, D. L. *J. Am. Chem. Soc.* **2002**, *124* (9), 1926–1932.
- (27) Cameron, L. M.; Hales, B. J. *Biochemistry* **1998**, *37* (26), 9449–9456.
- (28) Maskos, Z.; Hales, B. J. *J. Inorg. Biochem.* **2003**, *93* (1–2), 11–17.
- (29) Lee, H.-I.; Cameron, L. M.; Hales, B. J.; Hoffman, B. M. *J. Am. Chem. Soc.* **1997**, *119* (42), 10121–10126.
- (30) Amara, P.; Mouesca, J.-M.; Volbeda, A.; Fontecilla-Camps, J. C. *Inorg. Chem.* **2011**, *50* (5), 1868–1878.
- (31) Can, M.; Armstrong, F. A.; Ragsdale, S. W. *Chem. Rev.* **2014**, *114*, 4149–4174.
- (32) Song, J.; Klein, E. L.; Neese, F.; Ye, S. *Inorg. Chem.* **2014**, *53*, 7500–7507.
- (33) Wang, V. C.-C.; Islam, S. T. A.; Can, M.; Ragsdale, S. W.; Armstrong, F. A. *J. Phys Chem B* **2015**, *119* (43), 13690–13697.
- (34) Bullock, R. M. *Comments on Inorganic Chemistry* **1991**, *12* (1), 1–33.
- (35) Kohen, A.; Limbach, H.-H. *Isotope effects in chemistry and biology*; Taylor & Francis: Boca Raton, 2006.
- (36) Machan, C. W.; Sampson, M. D.; Kubiak, C. P. *J. Am. Chem. Soc.* **2015**, *137*, 8564–8571.
- (37) Dance, I. *Dalton Trans* **2011**, *40* (20), 5516–5527.



- (38) Scott, A. D.; Pelmeshikov, V.; Guo, Y.; Yan, L.; Wang, H.; George, S. J.; Dapper, C. H.; Newton, W. E.; Yoda, Y.; Tanaka, Y.; Cramer, S. P. *J. Am. Chem. Soc.* **2014**, *136* (45), 15942–15954.
- (39) Lee, H.-I.; Sørli, M.; Christiansen, J.; Song, R.; Dean, D. R.; Hales, B. J.; Hoffman, B. M. *J. Am. Chem. Soc.* **2000**, *122* (23), 5582–5587.

**APPENDIX****SUPPLEMENTARY INFORMATION****PATHWAY OF CO<sub>2</sub> REDUCTION TO CH<sub>4</sub> AND C-C BOND FORMATION****CATALYZED BY NITROGENASE**

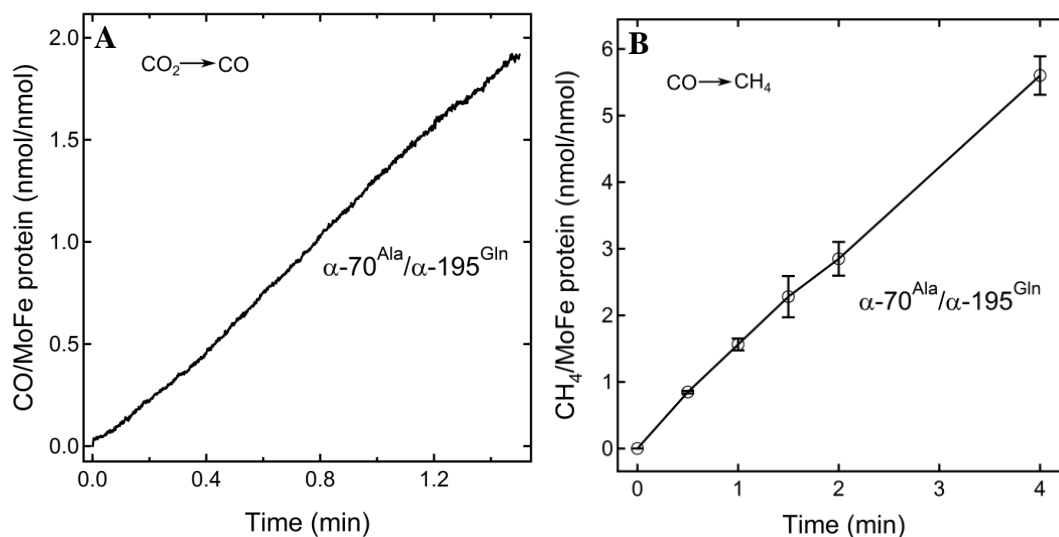


**Figure 4-S1:  $\alpha\text{-70}^{\text{Ala}}/\alpha\text{-195}^{\text{Gln}}$  MoFe protein catalyzed time dependent  $\text{CO}_2$  reduction to CO formation and CO to  $\text{CH}_4$ .** (A) Showing the time dependent CO formation during  $\text{CO}_2$  reduction. No lag phase is observed for CO formation. (B) Monitoring CO reduction to  $\text{CH}_4$  at approximately the same concentration ( $1.3 \mu\text{M}$ ) produced in solution during 1 min of lag phase during  $\text{CO}_2$  reduction to  $\text{CH}_4$ . Assay conditions:- 0.45 atm  $\text{CO}_2$ , 0.002 atm CO,  $2.1 \mu\text{M}$  MoFe protein and  $51.4 \mu\text{M}$  Fe protein.

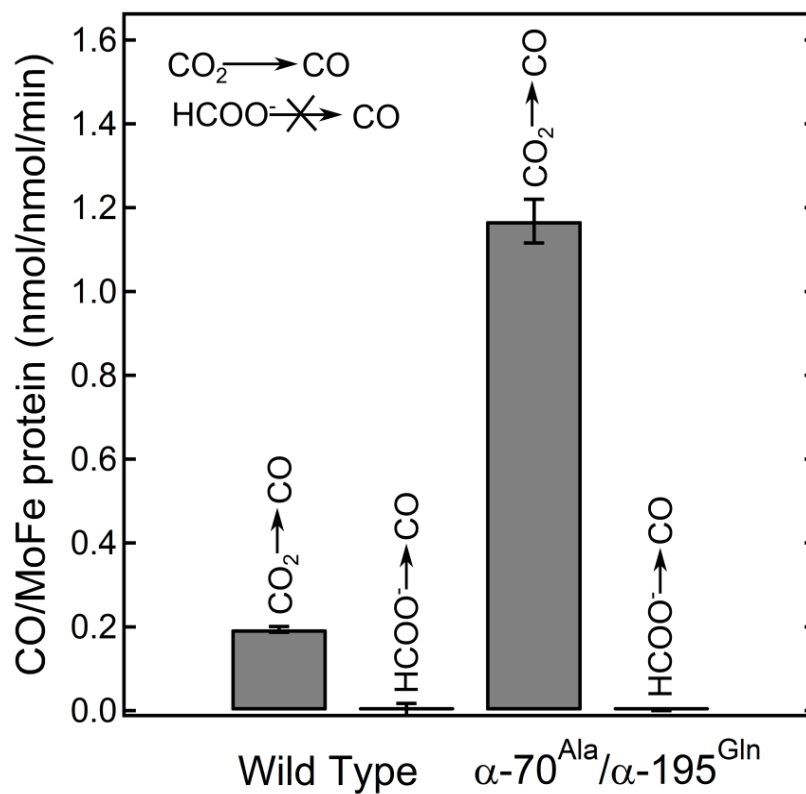


**Figure 4-S2: Test if metal formate (M-(OCOH)) isomerizes to yield CO.** Hemoglobin assay was used to measure the formation of CO during turnover under CO<sub>2</sub> and HCOO<sup>-</sup>. No CO was detected using HCOO<sup>-</sup> as substrate. CO formation occurs through CO<sub>2</sub> reduction and not through isomerization of metal bound HCOO<sup>-</sup>. Assay conditions:- 0.45 atm CO<sub>2</sub>, 70 mM HCOO<sup>-</sup>, 0.3 mg/mL Hb, 2.1 μM MoFe protein and 51.4 μM Fe protein.

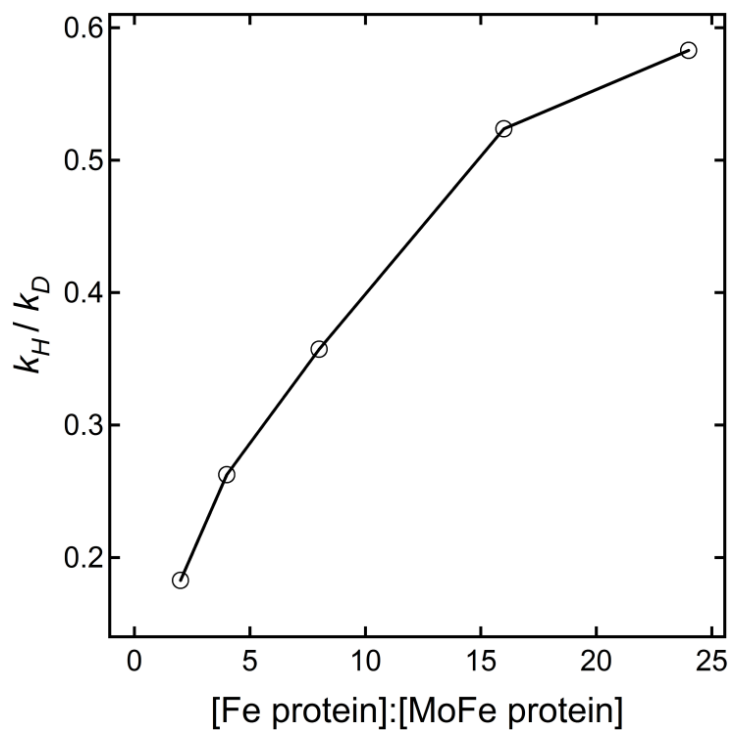


**Figure 4-S3: Ratio of steady state of CO formation in H<sub>2</sub>O and D<sub>2</sub>O during CO<sub>2</sub> reduction by  $\alpha$ -70<sup>Ala</sup>/ $\alpha$ -195<sup>Gln</sup> MoFe protein.** Replotting the data as shown in Fig. 3. The inverse isotopic effect in the formation of CO increases with lowering the flux and reaches the maximum of 5 folds at the low flux tested.

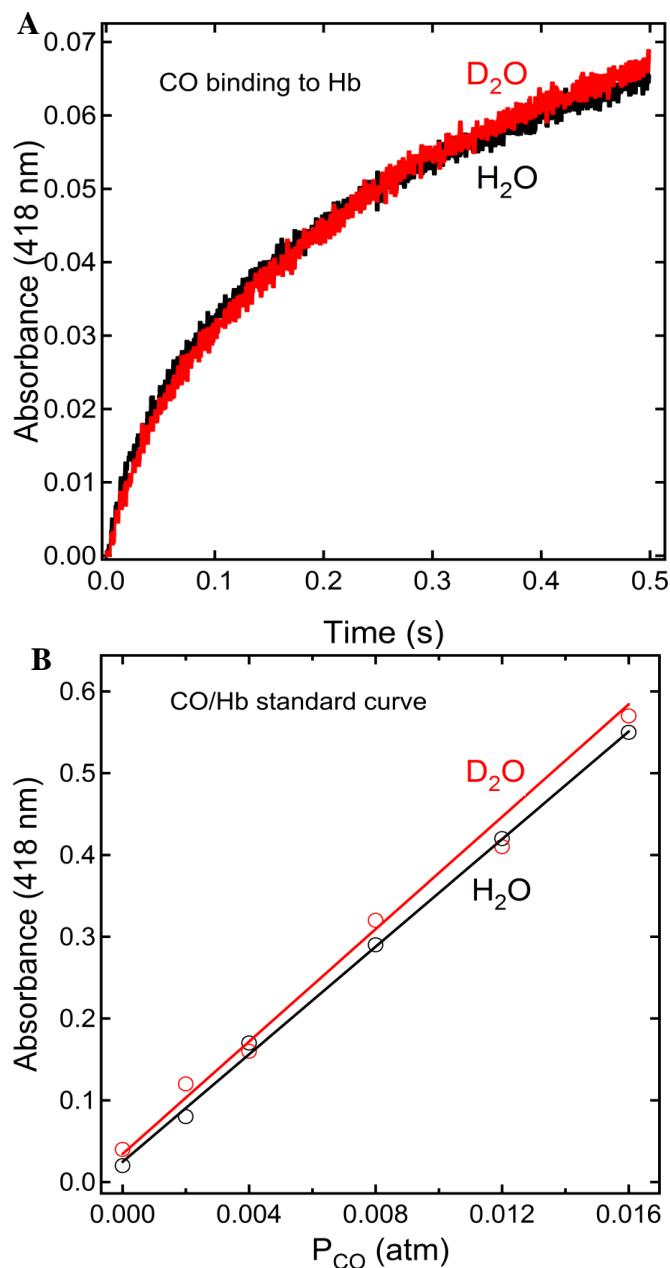


**Figure 4-S4: Test of solvent isotope effect for the rate of CO binding and change of molar extinction coefficient of CO-Hb complex.** (A) The rate of CO binding to Hemoglobin as well as the amplitude did not differ significantly in  $H_2O$  and  $D_2O$ . (B) The plot of the absorbance at 418 nm using different partial pressure of CO. Conditions: 100 mM MOPS pH=7.2 (pD=7.2 or 6.8 on the pH meter scale), 0.45 atm  $CO_2$  and the other components of the assay buffer stated above except MoFe and Fe protein.

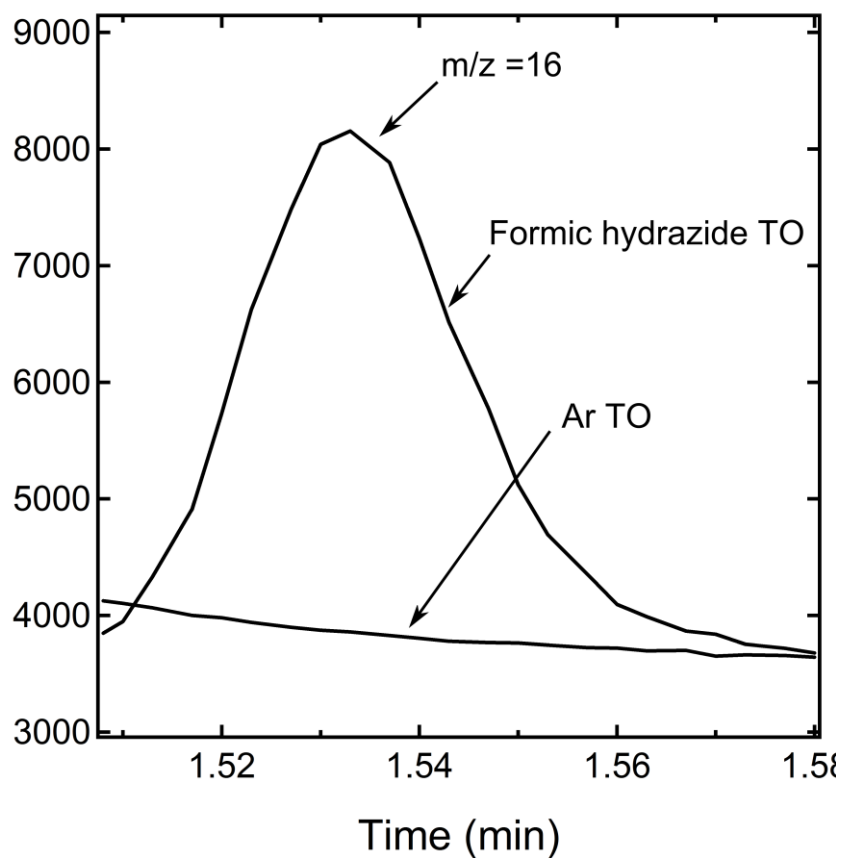


**Figure 4-S5: Showing CH<sub>4</sub> formation during formic hydrazide turnover using  $\alpha$ -<sup>70</sup>Ala/ $\alpha$ -<sup>195</sup>Gln MoFe protein.** CH<sub>4</sub> peak was observed only in presence of formic hydrazide. Conditions: 100 mM MOPS pH=7.2, 50 mM formic hydrazide, 2.1  $\mu$ M MoFe protein, 51.4  $\mu$ M Fe protein and 1 h of turnover time.

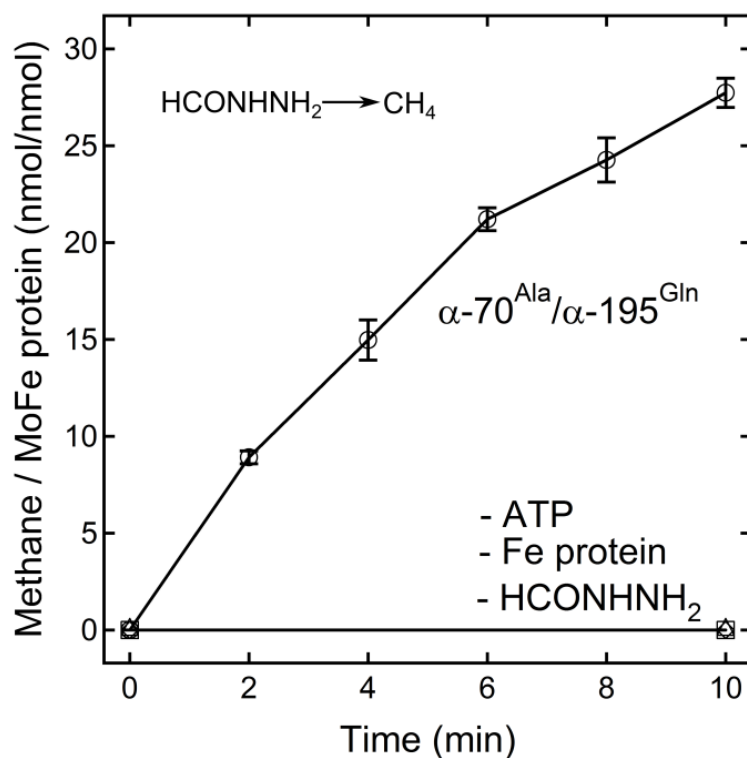


**Figure 4-S6: Catalytic reduction of formic hydrazide (HCONHNH<sub>2</sub>) to CH<sub>4</sub> by  $\alpha$ -70<sup>Ala</sup>/ $\alpha$ -195<sup>Gln</sup> MoFe protein.** The formation of CH<sub>4</sub> is observed only when the full components needed for nitrogenase turnover and formic hydrazide are present. Assay condition: 50 mM formic hydrazide, 2.1  $\mu$ M MoFe protein, and 51.4  $\mu$ M Fe protein.



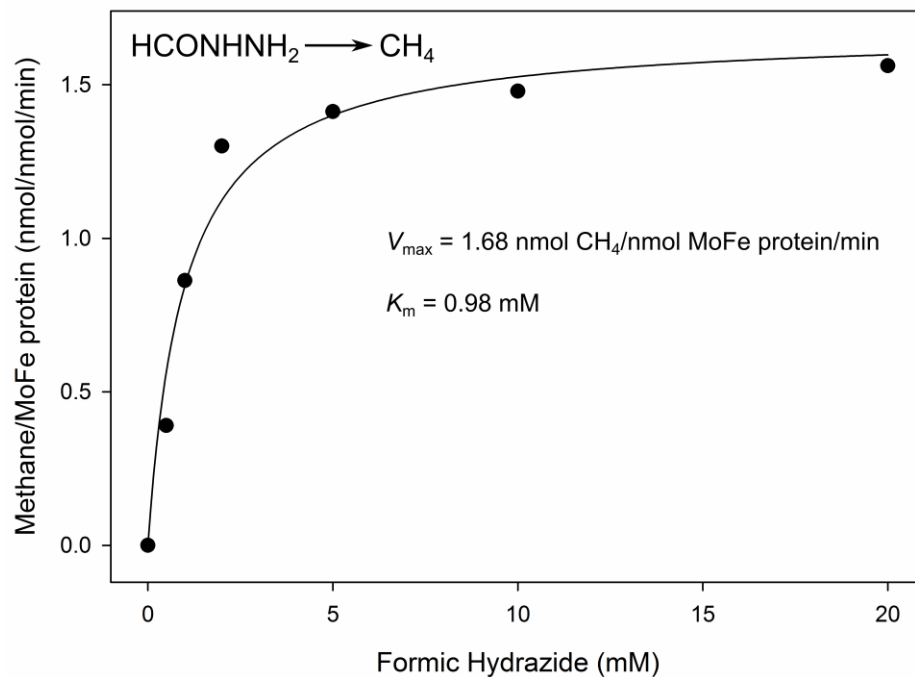


**Figure 4-S7: Concentration dependence formic hydrazide reduction to CH<sub>4</sub> by  $\alpha$ -70<sup>Ala</sup>/ $\alpha$ -195<sup>Gln</sup> MoFe protein.** The formation of CH<sub>4</sub> is dependent on formic hydrazide concentration. Fitting the data to Michaelis-Menten equation gave a  $V_{\max}$  of 1.68 nmol CH<sub>4</sub>/nmol MoFe protein/min and  $K_m$  of 0.98 mM. Assay condition: 50 mM formic hydrazide, 2.1  $\mu$ M MoFe protein, and 51.4  $\mu$ M Fe protein.

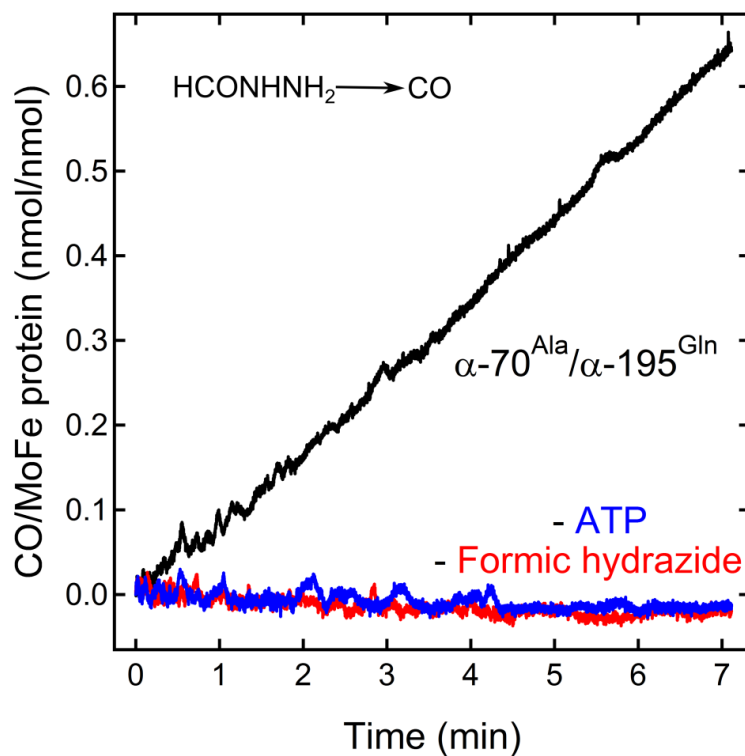


**Figure 4-S8: Formation of CO during formic hydrazide turnover with  $\alpha\text{-70}^{\text{Ala}}/\alpha\text{-195}^{\text{Gln}}$  MoFe protein.** The formation of CO is monitored using Hemoglobin assay. The increase of absorbance at 418 nm confirmed the formation of CO during formic hydrazide turnover. Lack of ATP or formic hydrazide in the reaction buffer did not show any formation of CO. Assay condition: 50 mM formic hydrazide, 0.3 mg/mL Hemoglobin, 2.1  $\mu\text{M}$  MoFe protein, and 4.2  $\mu\text{M}$  Fe protein.

**Table 4-S1: Formation of propylene with various substrates.**

MoFe protein	Flux [MoFe protein]:[Fe protein]	Solvent	Substrate	Methane/ MoFe protein (nmol/nmol)	Propylene/MoFe protein (nmol/nmol)
V70A H195Q	1:4	H <sub>2</sub> O	0.4atm CO <sub>2</sub>	1.05±0.071	0.94±0.03
V70A H195Q	1:4	H <sub>2</sub> O	0.005atm CO	2.65±0.13	5.98±0.10
V70A H195Q	1:4	H <sub>2</sub> O	5mM HCN/CN <sup>-</sup>	449±5.4	3.12±0.06

## CHAPTER 5

REVERSIBLE PHOTOINDUCED REDUCTIVE ELIMINATION OF H<sub>2</sub> FROM THE  
NITROGENASE DIHYDRIDE STATE, THE E<sub>4</sub>(4H) JANUS INTERMEDIATE**ABSTRACT**

We recently demonstrated that N<sub>2</sub> reduction by nitrogenase involves the obligatory release of one H<sub>2</sub> per N<sub>2</sub> reduced. These studies focused on the E<sub>4</sub>(4H) ‘Janus intermediate’, which has accumulated four reducing equivalents as two [Fe-H-Fe] bridging hydrides. E<sub>4</sub>(4H) is poised to bind and reduce N<sub>2</sub> through reductive elimination (*re*) of the two hydrides as H<sub>2</sub>, coupled to the binding/reduction of N<sub>2</sub>. To obtain atomic-level details of the *re* activation process, we carried out *in situ* 450 nm photolysis of E<sub>4</sub>(4H) in an EPR cavity at temperatures below 20 K. ENDOR and EPR measurements show that photolysis generates a new FeMo-co state, denoted E<sub>4</sub>(2H)\*, through the photoinduced *re* of the two bridging hydrides of E<sub>4</sub>(4H) as H<sub>2</sub>. During cryoannealing at temperatures above 175 K, E<sub>4</sub>(2H)\* reverts to E<sub>4</sub>(4H) through the oxidative addition (*oa*) of the H<sub>2</sub>. The photolysis quantum yield is temperature invariant at liquid helium temperatures and shows a rather large kinetic isotope effect, KIE = 10. These observations imply that photoinduced release of H<sub>2</sub> involves a barrier to the combination of the two nascent H atoms, in contrast to a barrier less process for mono-metallic inorganic complexes, and further suggest that H<sub>2</sub> formation involves nuclear tunneling through that barrier. The *oa* recombination of E<sub>4</sub>(2H)\* with the liberated H<sub>2</sub> offers

---

\*Coauthored by Dmitriy Lukoyanov, Nimesh Khadka, Zhi-Yong Yang, Dennis R. Dean, Lance C. Seefeldt, Brian M. Hoffman (2016) *JACS* **138** (4), 1320-1327. Copyright © [2016] American Chemical Society. Reprinted with permission.

compelling evidence for the Janus intermediate as the point at which  $H_2$  is necessarily lost during  $N_2$  reduction; this mechanistically coupled loss must be gated by  $N_2$  addition that drives the *re/oa* equilibrium toward reductive elimination of  $H_2$  with  $N_2$  binding/reduction.

### Introduction

Biological nitrogen fixation — the reduction of  $N_2$  to two  $NH_3$  molecules — is primarily catalyzed by the Mo-dependent nitrogenase. This enzyme comprises two component proteins, denoted the Fe protein and the MoFe protein. The former delivers electrons one-at-a-time to the MoFe protein, where they are utilized at the active site iron-molybdenum cofactor ([7Fe-9S-Mo-C-R-homocitrate]; FeMo-co), **Figure 5-1**, to reduce substrate.<sup>1,2</sup>

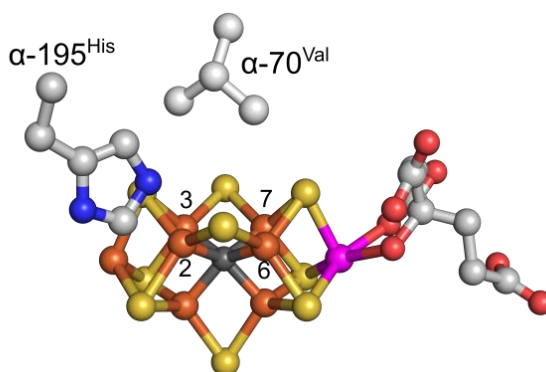
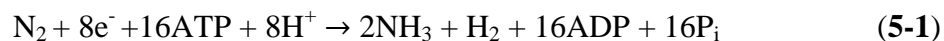


**Figure 5-1: Crystal structure of FeMo-co.** Fe is shown in rust, Mo in magenta, S in yellow, carbide in dark-grey, carbon in gray, N in blue and O in red. The Fe atoms of catalytic 4Fe-4S face are labelled as 2, 3, 6, and 7. Two amino acids,  $\alpha$ -70<sup>Val</sup> and  $\alpha$ -195<sup>His</sup>, around the FeMo-co are also shown; the former or both are modified in enzyme used in this study (see text). The image was created using PDB coordinate 2AFI.

Kinetic studies of  $N_2$  reduction by nitrogenase, carried out in the 1970's and 1980's by many groups, especially by Lowe and Thorneley and their coworkers,

culminated in the Lowe-Thorneley (LT) kinetic model for nitrogenase function.<sup>1,3,4</sup> It describes the kinetics of transformations among catalytic intermediates, denoted E<sub>n</sub> where *n* is the number of electron/proton deliveries to the catalytic FeMo-co, with electron transfer from the partner Fe protein in each of these steps being driven by the binding and hydrolysis of two MgATP within the Fe protein.<sup>5</sup> A central defining feature of this scheme is a mysterious and puzzling, obligatory (mechanistic) requirement for the formation of one H<sub>2</sub> for each N<sub>2</sub> reduced. This, in turn, leads to a limiting enzymatic stoichiometry for enzyme-catalyzed nitrogen fixation, given by **eqn 5-1**,



a conclusion in agreement with stoichiometric experiments by Simpson and Burris.<sup>6</sup> However, obligatory requirement for H<sub>2</sub> formation has not been universally accepted.<sup>7</sup> Most tellingly, in their magisterial review, Burgess and Lowe themselves questioned this requirement: “Thus the data that support the obligatory evolution of one H<sub>2</sub> for every N<sub>2</sub> reduced are much less compelling than the data that require us to believe that some H<sub>2</sub> will always be evolved during N<sub>2</sub> reduction.”<sup>1</sup>

We recently proposed<sup>8,9</sup> that obligatory H<sub>2</sub> formation was required to explain the multitude of mechanistic observations by numerous investigators that had accumulated over decades.<sup>1</sup> This proposal focuses on the E<sub>4</sub>(4H) ‘Janus intermediate’ (See **Figure 5-2** for notation), which has accumulated four of the eight required reducing equivalents, storing them as two [Fe-H-Fe] bridging hydrides.<sup>10-12</sup>

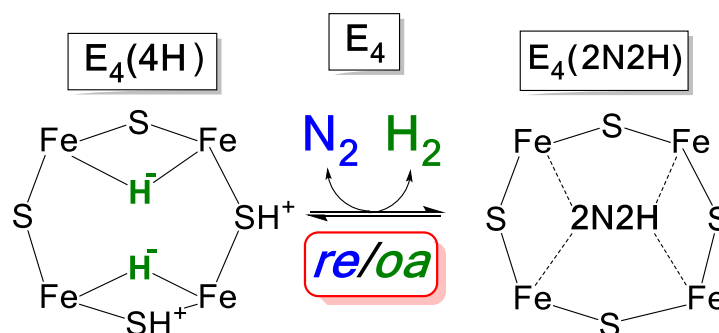


**Figure 5-2: Schematic of *re/oa* Equilibrium.** The cartoon represents the Fe 2,3,6,7 face of FeMo-co, and the ‘2N<sub>2</sub>H’ implies a species at the diazene reduction level of unknown structure and coordination geometry. In the indicated equilibrium the binding and activation of N<sub>2</sub> is mechanistically coupled to the *re* of H<sub>2</sub>, as described in the text. In the E<sub>n</sub> notation, *n* = number of [e<sup>-</sup>/H<sup>+</sup>] added to FeMo-co; parenthesis denotes the stoichiometry of H/N bound to FeMo-co.

E<sub>4</sub>(4H) sits at a transition in the N<sub>2</sub> reduction pathway, poised to ‘fall back’ to E<sub>0</sub> by release of two H<sub>2</sub>, but equally poised to bind and reduce N<sub>2</sub> through the accumulation of four more equivalents, hence the appellation.<sup>9</sup> The bridging mode of hydride binding plays a key mechanistic role. Bridging hydrides are less susceptible to protonation than terminal hydrides, and so they diminish the tendency of FeMo-co to ‘fall back’ by losing reducing equivalents through the formation of H<sub>2</sub>. However, the bridging mode also lowers hydride reactivity, relative to that of terminal hydrides.<sup>13,14</sup> How this ‘deactivated’ intermediate becomes activated through the release of H<sub>2</sub> coupled to N<sub>2</sub> binding forms part of the ‘mystery’ of dinitrogen fixation by nitrogenase.

We proposed that the E<sub>4</sub>(4H) state becomes activated for the binding of N<sub>2</sub> and its hydrogenation to a N<sub>2</sub>H<sub>2</sub>-level moiety through the reductive elimination (*re*) of the two hydrides as H<sub>2</sub>, the forward direction of the equilibrium in **Figure 5-2**.<sup>8,9</sup> This proposal

was initially supported<sup>8,9</sup> by showing that the behavior of nitrogenase during the reverse of this equilibrium, the oxidative addition (*oa*) of H<sub>2</sub> with loss of N<sub>2</sub>, explains the key constraints on nitrogenase mechanism that had been revealed over the years.<sup>1</sup> In particular it explains the previously baffling observation that D<sub>2</sub> can only react with nitrogenase during turnover with N<sub>2</sub> present, and then is stoichiometrically reduced to two HD.<sup>1</sup> Promptly thereafter we confirmed the mechanistic prediction that during turnover under N<sub>2</sub>/D<sub>2</sub>, the reverse of the equilibrium of **Figure 5-2**, the *oa* of D<sub>2</sub> by the E<sub>4</sub>(2N<sub>2</sub>H) intermediate with the loss of N<sub>2</sub>, must generate the E<sub>4</sub>(2D<sub>2</sub>H) isotopologue with D<sub>2</sub> having been converted selectively into two bridging deuterides, a state which could form in no other way.<sup>15</sup> This observation established the *re/oa* equilibrium is thermodynamically reversible. More recently, we demonstrated that the (*re/oa*) activation equilibrium of **Figure 5-2** is not only thermodynamically, but also kinetically reversible. The overall result of these several findings is to establish the mechanistic requirement for the formation of one H<sub>2</sub> per N<sub>2</sub>. This in turn implies the limiting stoichiometry of eight electrons/protons for the reduction of N<sub>2</sub> to two NH<sub>3</sub> (**eq 5-1**).<sup>16</sup>

But these efforts, while establishing the *re/oa* mechanism for nitrogenase activation, do not provide atomic-level details of the *re* activation process. For example, in rough analogy to nucleophilic substitution in organic chemistry, we can imagine a spectrum of reaction pathways for *re/oa*, as illustrated in **Figure 5-3**: Is the conversion concerted? associative? dissociative? If a discrete intermediate (*e.g.* **Y**, or **Z**) exists, what are its properties?

To obtain atomic-level details of the *re* activation process requires deeper



understanding of the inorganic chemistry of the bridging hydrides of  $E_4(4H)$ : what are their properties and what properties do they confer on this enzyme state? We here present the initial results of a photochemical approach inspired by the properties of inorganic dihydride complexes.

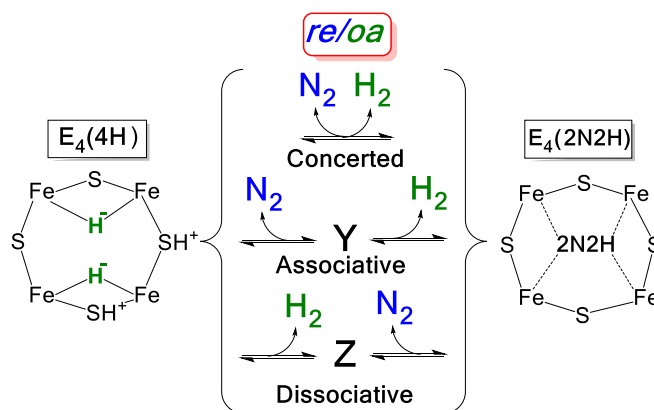


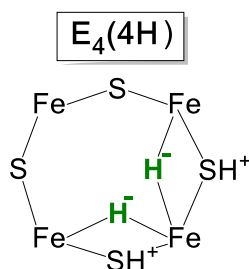
**Figure 5-3: Schematic of alternative limiting mechanisms for  $re/oa$  equilibrium.**

The photolysis of transition metal dihydride complexes with mutually *cis* hydride ligands commonly results in the release of  $H_2$ .<sup>17-25 26</sup> As noted by Perutz,<sup>17</sup> “The photochemical reaction causes a reduction in oxidation state of two and is a typical example of reductive elimination. The reverse reaction will usually proceed thermally and is the prototype example of an oxidative addition reaction.” Regardless of the precise nature of the thermal  $re/oa$  equilibrium process in nitrogenase, **Figure 5-2**, photo-induced  $re$  would cleanly give an activated version of the doubly reduced  $E_2(2H)$  intermediate, which we denote  $E_4(2H)^*$ , that would be analogous to the intermediate that would form upon thermal dissociative  $re$  loss of  $H_2$  prior to  $N_2$  binding (**Z**; **Figure 5-3**). Our cartoon depictions of  $E_4(4H)$  frequently have shown the two  $[Fe-H-Fe]$  hydrides with a common

vertex, **Chart 1**, in order to emphasize the analogy between *re* of H<sub>2</sub> by mononuclear metal di-hydrides, and the activation of FeMo-co through *re* of H<sub>2</sub>.

However, we do not yet know their exact disposition, and know of no precedent for *re*, either thermal or photochemical, for the ‘parallel’ hydrides drawn in the cartoon, **Figure 5-2**, a geometry that is suggested by preliminary DFT computations.<sup>27</sup> On the

**Chart 1**



other hand, no inorganic multimetallic dihydride of which we are aware exhibits a 4Fe ‘face’, as does FeMo-co, and therefore none could have the adjacent, parallel hydrides drawn in the cartoon. Thus, photolysis of the Janus E<sub>4</sub>(4H) intermediate embeds FeMo-co even more deeply within the body of organometallic chemistry, yet breaks new ground.

### Materials and Methods

*Materials and Protein purifications:* All the reagents were obtained from SigmaAldrich (St. Louis, MO) or Fisher Scientific (Fair Lawn, NJ) and were used without further purification. Argon, N<sub>2</sub>, and acetylene gases were purchased from Air Liquide America Specialty Gases LLC (Plumsteadville, PA).

Remodeling the active site of MoFe protein by the  $\alpha$ -70<sup>Val→Ile</sup> mutation permits the freeze trapping of MoFe with high populations of E<sub>4</sub>(4H).<sup>10</sup> Experiments were carried

out both with the singly substituted,  $\alpha$ -70<sup>Ile</sup> MoFe protein and with the doubly-substituted  $\alpha$ -70<sup>Val→Ile</sup>/ $\alpha$ -195<sup>His→Gln</sup> MoFe proteins. As shown in **Table 5-S1**, this protein functions similarly to the single mutant. The two proteins were obtained from the corresponding *Azotobacter vinelandii* strains. They were grown, and the corresponding nitrogenase MoFe proteins were expressed and purified as described elsewhere.<sup>28</sup> The handling of all buffers and proteins were done anaerobically under Ar atmosphere or under Schlenk vacuum line unless stated otherwise.

*EPR and ENDOR samples:* The E<sub>4</sub>(4H) intermediate and its deuterated analogue, E<sub>4</sub>(4D), are prepared by turnover of the MoFe protein in H<sub>2</sub>O and D<sub>2</sub>O buffers, respectively. Depending on the buffer used, all exchangeable sites are thereby populated with H or D, not only the hydride bridges. Thus, measured kinetic isotope effects associated with *re* and *oa* steps of the equilibrium of **Figure 5-2**<sup>29,30</sup> are a composite of primary isotope effects associated with hydride *re* or H<sub>2</sub> *oa* plus any, smaller, solvent isotope effects.

EPR samples were prepared in a dioxygen free buffer containing a MgATP regeneration system with final concentrations of 13 mM ATP, 15 mM MgCl<sub>2</sub>, 20 mM phosphocreatine, 2.0 mg/mL bovine serum albumin, and 0.3 mg/ mL phosphocreatine kinase in a 200 mM MOPS buffer at pH 7.3 (H<sub>2</sub>O buffer) or pD=7.3 (D<sub>2</sub>O buffer; pH meter reading of 6.9)<sup>31</sup> with 50 mM dithionite. MoFe protein was added at ~50  $\mu$ M final concentration and the reaction was initiated by addition of Fe protein at ~36  $\mu$ M concentration. The reaction was allowed to run at room temperature under Ar atmosphere for 20-25 s before freeze-quenching the samples. The samples for ENDOR experiments were prepared similarly, but typically with three-fold higher concentrations.

*EPR and ENDOR Measurements:* X-band EPR spectra were recorded on a Bruker ESP 300 spectrometer equipped with an Oxford Instruments ESR 900 continuous He flow cryostat.

To allow illumination, a Bruker ER4104R cavity was employed. This cavity allows front-face optical access through a waveguide beyond cutoff (microwave non-transmitting) on the cavity front face, with a 4x10 mm optical transmission path. *In situ* photolysis of a sample held within the cryostat at the chosen temperature initially employed a 15 mW blue LED inserted into this illumination port. Subsequently it employed a Thorlabs Inc (Newton, New Jersey) PL450B, 450 nm, 80 mW Osram Laser Diode mounted on the port through use of the corresponding diode mount with focusing lenses. Thermal relaxation was monitored by the step-annealing procedure in which the sample was quickly warmed to a desired temperature, held there for a fixed time, then promptly returned to 77K, and then examined by EPR at a still lower temperature.

Q-band CW EPR and  $^1\text{H}$  ENDOR spectra were collected on a spectrometer with a helium immersion Dewar as previously reported.<sup>32</sup> The stochastic field-modulation detected ENDOR technique, first reported by Brueggeman and Niklas,<sup>33</sup> was also utilized. In the stochastic ENDOR sequence, RF is randomly hopped over the frequency range of the spectrum, with subtraction of a background signal (RF off) at each frequency. All measurements were done at 2 K. As desired, Q-band samples were photolyzed by placing them in liquid nitrogen in an X-band finger Dewar and illuminating them with a 1000 mW blue LED. The samples were then transferred to a liquid helium cryostat for EPR/ENDOR study.

## Results and Discussion

**Figures 5-4** and **5-S1** present X-band and **Fig 5-S2** Q-band EPR spectra of the  $S = \frac{1}{2} E_4(4H)$  intermediate freeze-trapped during turnover of MoFe protein that was remodeled with the  $\alpha$ -70<sup>Val→Ile</sup> substitution; similar results are seen for MoFe with the double substitution,  $\alpha$ -70<sup>Val→Ile</sup>,  $\alpha$ -194<sup>His→Gln</sup> (**Figure 5-1**). Both single and double substitutions prevent access of substrates other than protons without perturbing FeMo-co function (**Table 5-S1**), and enhance the accumulation of  $E_4(4H)$ .<sup>10-12</sup>

**Figure 5-4** includes spectra collected during *in situ* photolysis with 450 nm light with the sample held at 12 K; equivalent spectra are obtained by photolysis at 77 K (e.g., **Figure 5-S2**). Although it has not yet proven possible to create optically transparent freeze-quenched samples of this intermediate, the figures show that irradiation nonetheless causes the progressive loss of the  $E_4(4H)$  signal,  $g = [2.15, 2.007, 1.965]$ , and accompanying appearance of a new signal,  $S$ , with  $g = [2.098, 2.0, 1.956]$ . EPR spectra collected over temperatures between 12 K and 50 K (**Figure 5-S1**) show the  $E_4(4H)$  signal disappears by  $\sim 40$ -50 K because of rapid spin relaxation, whereas for  $S$ , the EPR signal is clearly visible at 50 K, demonstrating differences between excited spin-state manifolds of  $S$  and  $E_4(4H)$ .

Careful examination of the timecourse of photolysis shows no new signals that are generated, other than  $S$ . In particular, **Figures 5-4, 5-S1, 5-S2** show *no* other photo-induced change in the spectrum in the vicinity of  $g \sim 2$ ; likewise, there is *no* change at lower fields (not shown), where the signal from residual resting state ( $E_0$ ) appears and where signals would appear from the state which has accumulated two  $[e^-/H^+]$  ( $E_2(2H)$ ).<sup>34</sup>

The photolysis product, *S*, completely relaxes back to  $E_4(4H)$  when annealed for 2 minutes at 217 K, with *no* other change in the EPR spectrum, either in the  $g \sim 2$  region, **Figure 5-4**, or the high- $g$  (low-field) region (not shown). Thus, *photolysis/annealing cause the reversible, and kinetically direct, conversion,  $E_4(4H) \rightleftharpoons S$ .*

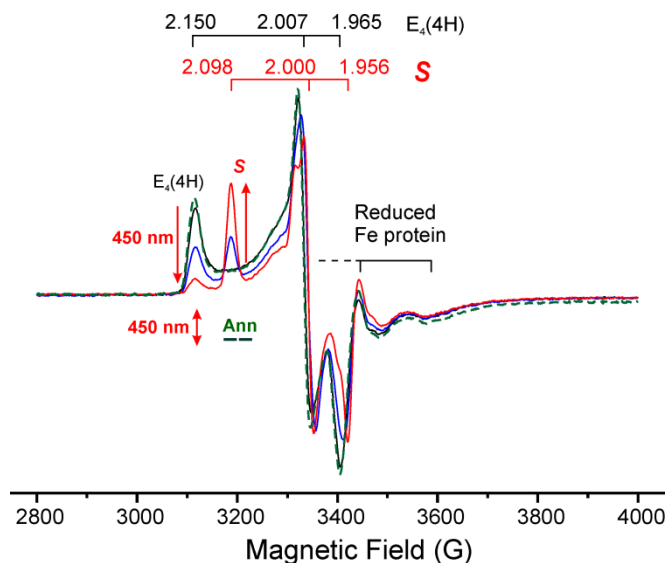


**Figure 5-4:** X-band EPR spectra of MoFe protein ( $\alpha$ -70<sup>Ile</sup>) freeze-trapped during Ar turnover in H<sub>2</sub>O before (*black*) and during irradiation with 450 nm diode laser at 12 K (*blue* (2.5 min) and *red* (20 min) traces); *Red* arrows highlight the conversion of  $E_4(4H)$  to the photoinduced *S* state. *Dashed Green* spectrum shows that annealing (Ann) the illuminated sample at 217 K for 2 minutes causes complete reversion of *S* to  $E_4(4H)$ . EPR conditions: T = 12 K; microwave frequency, 9.36 GHz; microwave power, 10 mW; modulation amplitude, 13 G; time constant, 160 ms; field sweep speed, 20 G/s.

<sup>1</sup>H ENDOR spectroscopy was used to determine the fate of the [Fe-H-Fe] bridging hydrides during the photolytic  $E_4(4H) \Rightarrow S$  conversion. **Figure 5-5** shows 2 K Q-band stochastic CW <sup>1</sup>H ENDOR spectra collected at two different  $g$ -values from  $E_4(4H)$  before and after photolysis; **Figure 5-S2** presents corresponding ‘conventional’ CW spectra. In both figures, the spectra represent components of the 2D field-frequency pattern of spectra collected across the EPR envelope, which has been thoroughly

analyzed in terms of two hydrides with anisotropic hyperfine tensor components that are virtually identical, but with tensors that are differently oriented with respect to  $\mathbf{g}$ .<sup>10</sup> In the  $g = 2.01$  spectrum of  $E_4(4H)$  in **Figure 5-5**, the strongly-coupled  $^1H$  signals from the two hydrides ( $A \lesssim 40$  MHz) are completely overlapped; at  $g = 2.00$ , the signals again overlap, but distinct peaks also are seen from the individual hydrides, most noticeably the two doublets with couplings of  $A \sim 22$  and  $28$  MHz.<sup>10 35</sup>

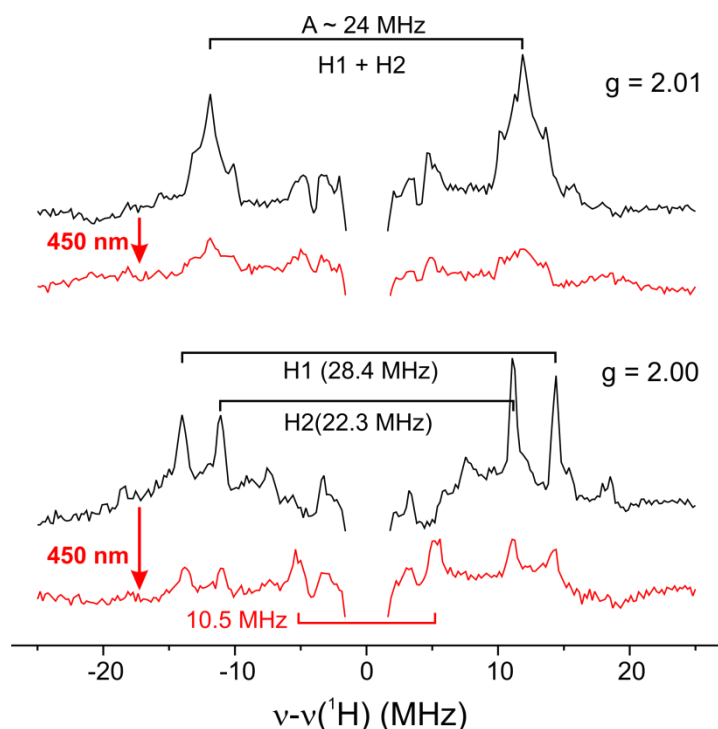


**Figure 5-5:** Q-band stochastic  $^1H$  CW ENDOR spectra showing loss of signals from hydrides, H1 and H2, through photolysis. (Black) Before and (red) after 450 nm photolysis of MoFe protein ( $\alpha$ -70<sup>lle</sup>/ $\alpha$ -195<sup>Gln</sup>) trapped during Ar turnover in  $H_2O$  buffer. ENDOR conditions: microwave frequency,  $\sim 34.99$  GHz; modulation amplitude, 6.3 G; RF duration 3 ms; RF cycle, 200 Hz; bandwidth of RF broadened to 100 kHz; 2000 scans; temperature, 2 K.

For the sample that gave the ENDOR spectra in **Figure 5-5**, the photolysis had reduced the intensity of the  $E_4(4H)$  EPR signal by  $\sim$  threefold, with the corresponding

appearance of EPR intensity from *S*. **Figure 5-5** shows that the photolysis decreases the intensity of the  $^1\text{H}$  ENDOR signals from the strongly-coupled hydrides by a comparable amount, *without* the appearance of new strongly-coupled signals that can be associated with a metal-hydride ‘isomer’. At  $g = 2.01$  *no* new signal appears; at  $g = 2.0$  a signal appears with the relatively small coupling,  $A \sim 10$  MHz, which likely is associated with one of the protonated sulfides that must be present in *S*. CW ENDOR spectra taken on a sample with an even greater extent of photolysis show essentially complete loss of the ENDOR signals at a field where the two hydrides show distinct features (**Figure 5-S2**). Correspondingly,  $^2\text{H}$  ENDOR measurements of *S* created by photolysis of  $\text{E}_4(4\text{D})$  prepared in  $\text{D}_2\text{O}$  buffer show the loss of the  $[\text{Fe-D-Fe}]$  signals associated with  $\text{E}_4(4\text{D})$ , again with no new strongly-coupled signal appearing (not shown).

The absence of new strongly-coupled signals in the  $^{1,2}\text{H}$  ENDOR responses further rules out the possibility that *S* is an  $\text{H}_2$  complex of  $\text{FeMo-co}$ , either with strongly-hindered or free rotation of  $\text{H}_2$ , rather than having released  $\text{H}_2$ . A bound  $\text{H}_2$  complex with strongly hindered rotation would show new strongly-coupled  $^1\text{H}$  ENDOR signals, contrary to observation.<sup>36</sup> Quantum statistical arguments show that freely rotating  $\text{H}_2$ , which can occur even at 2 K, would not show  $^1\text{H}$  ENDOR signals, but would show new strongly-coupled  $^2\text{H}$  ENDOR signals for the corresponding  $\text{D}_2\text{O}$  sample.<sup>37</sup> The absence of such new signals for *S* means that it does not contain a freely-rotating bound  $\text{D}_2$ .

*We thus infer that the state S generated by photolysis of  $\text{E}_4(4\text{H})$  has indeed lost the metal-bound hydrides through the release of one or two  $\text{H}_2$ .*

*Mechanism of Photoconversion:* Three mechanisms must be considered for the



$E_4(4H) \Rightarrow S$  photo-conversion through loss of both hydrides and release of  $H_2$ , **Figure 5-6**, which we denote, *re*, *hp*, and *L*.

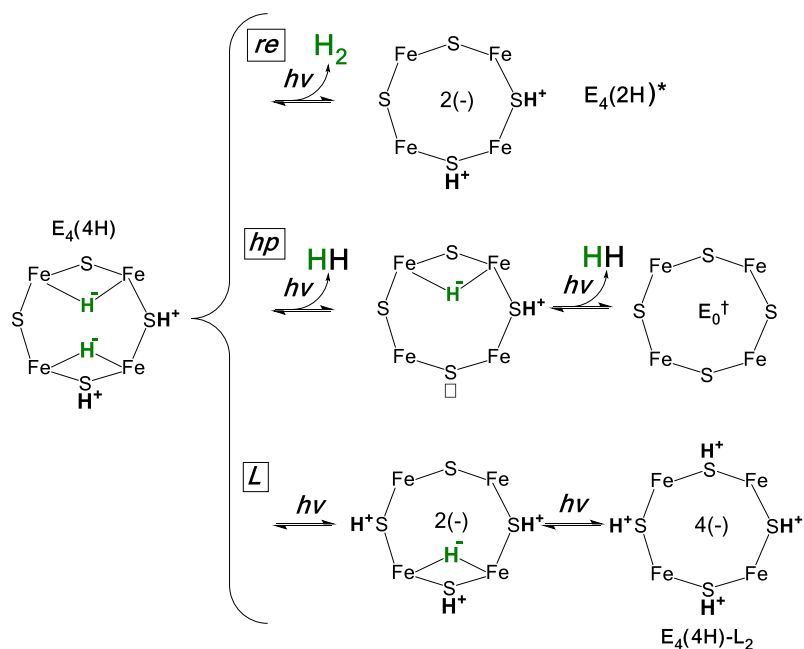


**Figure 5-6: Alternative mechanisms for the  $E_4(4H) \Rightarrow S$  photo-conversion through loss of both hydrides and release of  $H_2$  and thermal reverse.**

The first would be precisely the photo-induced reductive-elimination of one  $H_2$ , as discussed above, yielding a non-thermal form of the doubly-reduced state of the cluster, which we denote  $E_4(2H)^*$ . The second postulates two steps of photo-induced hydride protonolysis (*hp*), each with loss of  $H_2$ , in which case  $S$  must be a low-spin ( $S = 1/2$ ) ‘spin-isomer’ of the  $E_0$ ,  $S = 3/2$  resting state, which we can denote  $E_0^\dagger$ . Thermal *hp* processes are responsible for  $H_2$  formation by nitrogenase,<sup>1,8,9</sup> as well as by hydrogenases.<sup>38,39</sup> The third mechanism differs from the other two in that it does not involve generation of  $H_2$ . Instead it would involve two steps of photo-induced *re* of a

hydride, with transfer of the proton ‘released’ to a bridging sulfide. We denote this the ‘*L* mechanism’ because it is inspired by the photoinduced conversion of the Ni-C state of the Ni-Fe hydrogenases.<sup>38,39</sup> Ni-C exhibits a [Ni(III)-H-Fe(II)] bridging hydride and a cysteinyl thiolate bound to Ni. Photolysis generates a state, denoted Ni-L, which contains [Ni(I), Fe(II)] metal ions, and with the proton formed by photoinduced reductive elimination of the hydride having been transferred to the bound sulfur. Any one of these three imagined processes would yield a final photoproduct without metal hydrides.

The observation that *S* thermally relaxes to E<sub>4</sub>(4H) immediately rules out the *hp* mechanism for photo-induced E<sub>4</sub>(4H) ⇒ *S* conversion. This conversion would involve the loss of four reducing equivalents as two H<sub>2</sub> molecules, and its reverse must involve two steps of reduction of FeMo-co by H<sub>2</sub>: E<sub>0</sub><sup>†</sup> + H<sub>2</sub> ⇒ E<sub>2</sub>(2H); E<sub>2</sub>(2H) + H<sub>2</sub> ⇒ E<sub>4</sub>(4H). However, it is one of the foundational facts about nitrogenase mechanism that H<sub>2</sub> cannot react with any thermally generated state of FeMo-co except the N<sub>2</sub>-bound state produced by *re* of H<sub>2</sub>; as we have explained, the reactions are uphill by ~ 30 kcal/mol.<sup>8</sup> Even if the E<sub>0</sub><sup>†</sup> photo-generated spin isomer were sufficiently activated as to react with H<sub>2</sub>, the first step of reduction would necessarily produce the thermally equilibrated E<sub>2</sub>(2H), which could not react with H<sub>2</sub>: hence E<sub>4</sub>(4H) could not be regenerated from *S* during cryoannealing.

The complete absence during photolysis of a second new EPR signal in addition to *S* (see above) in fact not only independently rules out *hp*, but also rules out *L*. Both mechanisms involve sequential steps of photon absorption. Under the constant low-level illumination of this experiment this necessarily implies the buildup then loss of the EPR

signal from the intermediate stage that has absorbed one photon. *Thus we conclude that photolysis indeed generates a FeMo-co state,  $S = E_4(2H)^*$ , through the photoinduced reductive elimination of the two bridging hydrides of  $E_4(4H)$  with accompanying production of one  $H_2$ , and that the relaxation of  $E_4(2H)^*$  to  $E_4(4H)$  during cryoannealing corresponds to the oxidative addition of  $H_2$  to the photo-generated state,  $E_4(2H)^*$ .*

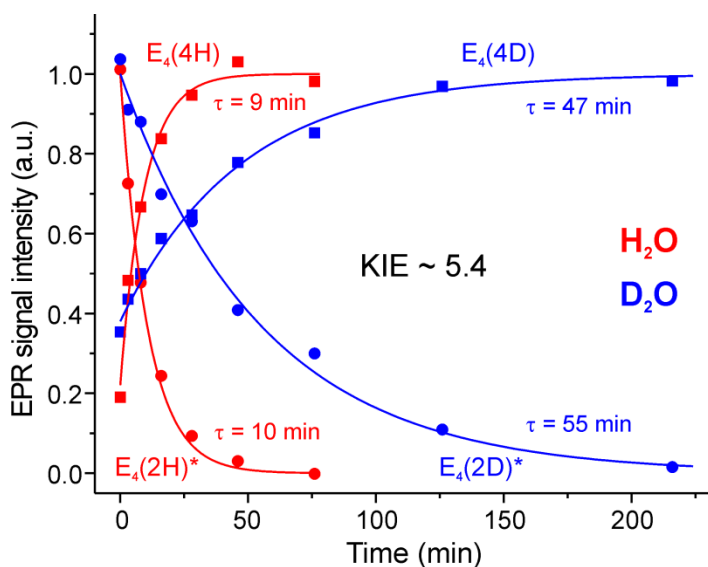


**Figure 5-7: Decay during 193 K annealing of  $E_4(2H)^*$  photoinduced in MoFe ( $\alpha$ -70<sup>Ile</sup>) freeze-trapped during turnover in  $H_2O$  (red) and  $D_2O$  (blue), along with the parallel recoveries of  $E_4(4H)$ . Data points obtained as intensities of  $g_1$  feature of the corresponding  $S=1/2$  EPR signals, normalized to the maximum signal; they were fit with an exponential function, with time constants shown in the figure. *EPR conditions:* as in **Figure 5-4**.**

*Kinetics of  $H_2/D_2$  oa:* To characterize the isotope dependence of the thermal *oa* process,  $E_4(2H)^* + H_2 \Rightarrow E_4(4H)$  versus  $E_4(2D)^* + D_2 \Rightarrow E_4(4D)$ ,<sup>29,30,40</sup> we measured the kinetics of the 193 K relaxation of  $E_4(2H)^*$  and  $E_4(2D)^*$  in samples prepared, respectively, in  $H_2O$  and  $D_2O$  buffers. In these experiments the sample was annealed at 193 K for multiple time intervals, with cooling to 12 K for collection of EPR spectra

between intervals. For both H<sub>2</sub>O and D<sub>2</sub>O buffers the relaxation is well-modeled as a one-step process, **Figure 5-7**. This is consistent with, but not proof of, the absence of an intermediate state(s), for example an H<sub>2</sub> complex.<sup>41</sup>

With *S* in H<sub>2</sub>O buffer, the exponential decay time-constant is,  $\tau = 10$  min; decay is slowed in D<sub>2</sub>O buffer, to the decay time,  $\tau = 55$  min. The E<sub>4</sub>(4H) state recovers in synchrony with the loss of *S*, as the recovery also is exponential, and exhibits the same time-constants,  $\tau = 9$  min for H<sub>2</sub>O sample and  $\tau = 47$  min for D<sub>2</sub>O. This kinetic isotope effect during *oa*, KIE  $\sim 5.4$ , is larger than typical for closed-shell monometallic complexes.<sup>42,43</sup> Combined with a strong temperature dependence in the time-constant (not shown), this KIE implies that *oa* of H<sub>2</sub> involves traversal of an energy barrier associated with H<sub>2</sub> binding and/or bond cleavage. The exponential decay of *S* and appearance of E<sub>4</sub>(4H) suggest that in the frozen solution the H<sub>2</sub> formed by photoinduced *re* is trapped adjacent to FeMo-co and undergoes *oa* ‘intramolecularly’, presumably in some part because the incorporation of isoleucine over the active face of FeMo-co prevents H<sub>2</sub> diffusion away. Indeed, although we presume that the relatively weakly coupled, but clearly resolved <sup>1</sup>H ENDOR signal seen for *S* is associated with a sulfur-bound proton, we cannot rule out the possibility that it comes from the H<sub>2</sub> trapped nearby.

*KIE of photoinduced re:* We know of only two studies of the KIE for photoinduced *re* of H<sub>2</sub>/D<sub>2</sub>, and these found small<sup>44</sup> or negligible isotope effects.<sup>21</sup> For completeness, we nonetheless used *in situ* photolysis to compare the time-dependent loss of the E<sub>4</sub>(4H) and corresponding E<sub>4</sub>(4D) signals as a function of temperature, **Figure 5-8**.

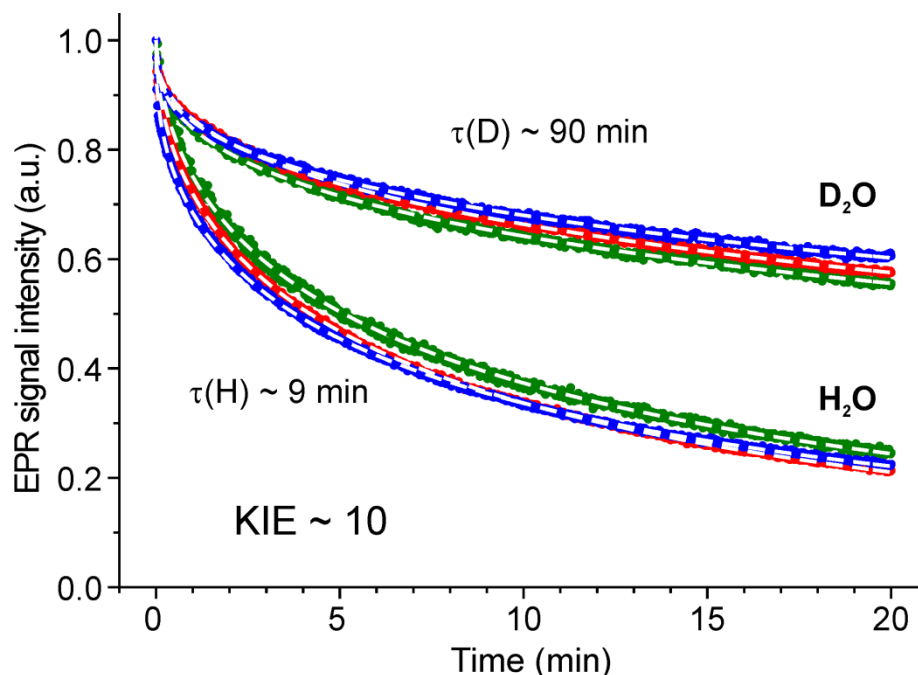


**Figure 5-8: Timecourse of *in situ* 450 nm photoinduced conversion of  $E_4(4H)$  intermediate trapped during MoFe protein ( $\alpha\text{-}70^{\text{IIe}}$ ) turnover in  $\text{H}_2\text{O}$  (lower) and  $\text{D}_2\text{O}$  (upper).** Photolysis at 3.8 K (green), 8 K (red) and 12 K (blue). Signal measured directly as intensity of the  $g_1$  feature of the  $E_4(4H)$   $S=1/2$  EPR signal, normalized to the maximum signal and fit with a stretched exponential decay function,  $I = \exp(-[t/\tau]^n)$ , with ‘1/e’ time constant,  $\tau$ ;  $0 < n \leq 1$  equals unity for exponential decay and decreases with the spread of the distribution. Time constants for fits (white dashed lines) are given in figure; in all cases  $n \sim 0.4$  (see SI for details). *EPR conditions:* microwave frequency, 9.36 GHz; microwave power, 10 mW (1 mW for measurements at 3.8 K); modulation amplitude, 13 G; time constant, 160 ms.

In a clear solution of low optical density, photolysis under constant illumination would cause an exponential loss of the signal with rate constant ( $k$ ) proportional to the light intensity ( $I_0$ ) and quantum yield ( $\phi$ ), for *re*,  $k(\phi) = \tau^{-1}(\phi) \propto I_0\phi$ , where  $\tau(\phi)$  is the corresponding time-constant for decay. However, it proved impossible to prepare clear frozen samples with high population of  $E_4(4H)$ , only frozen ‘snows’. The decay of the signal during photolysis of a ‘snow’ is *necessarily* non-exponential because light

scattering diminishes the photon flux across the sample (See **5-SI**); instead, as shown in **Figure 5-8**, it can be described with a stretched exponential,  $\exp(-[t/\tau]^n)$ ,<sup>45</sup> with  $\phi$ -dependent ‘1/e’ decay time,  $\tau(\phi)$ , whose inverse is proportional to the average decay rate constant ( $\dot{k}$ )<sup>45</sup> and is thus proportional to the quantum yield for *re*:  $\tau^{-1}(\phi) \propto \dot{k}(\phi) \propto \phi$  (See **SI**).

The decay time for photoinduced *re* of dihydrogen from  $E_4(4H)$  measured in *both*  $H_2O$  and  $D_2O$  buffers is temperature invariant, within error, from 4-12 K, **Figure 5-8**, **Table 5-S2**, a variation in the thermal energy ( $k_B T$ ) by a factor of  $\sim 3$ . Contrary to expectation, the decay slows markedly in  $D_2O$  buffer; the KIE for *re* over this range, defined as the ratio of the ‘1/e’ decay times for  $D_2O$  and  $H_2O$  buffers is large, KIE  $\sim 10$ . *These observations together imply that photoinduced re involves a barrier to the combination of the two nascent H atoms, in contrast to the barrierless process inferred for mono-metallic metal complexes,<sup>17,21</sup> and suggest that the photoinduced formation of  $H_2$  involves nuclear tunneling through that barrier.* Whether the process involves an actual intermediate  $H_2$  complex remains to be determined. In combination with the evidence for a barrier crossing in the *oa* of  $H_2$  to  $E_4(2H)^*$  to regenerate  $E_4(4H)$ , this leads us to the picture of the energy surfaces for photoinduced *re/oa* for the Janus intermediate presented in **Figure 5-9**.

*A Second Channel for Photoinduced Reaction:* Intriguingly, the slowed conversion of  $E_4(4D)$  to  $E_4(2D)^*$  in  $D_2O$  buffer uncovered a second channel for the photoinduced loss of  $E_4(4D)$ , one which could not compete with the more rapid conversion to  $E_4(2H)^*$  in  $H_2O$ . During photolysis of  $E_4(4D)$  in  $D_2O$  buffer at  $\sim 10$  K we

observed a very weak photoinduced spin -  $\frac{1}{2}$  EPR signal in addition to that of  $E_4(2D)^*$  (not shown). This state is much less stable than  $E_4(2D)^*$ , and decays completely within

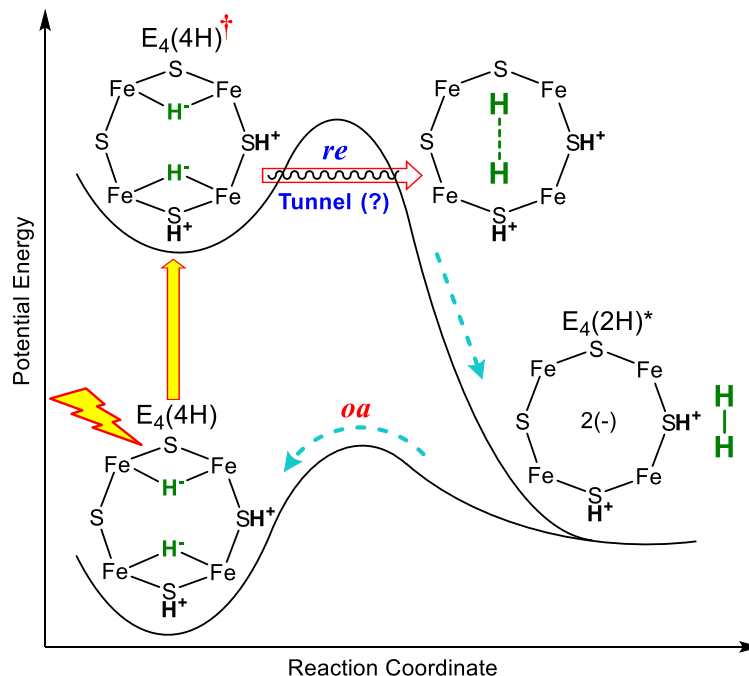


**Figure 5-9: Idealized energy surfaces for photoinduced *re/oa* of the Janus intermediate,  $E_4(4H)$ .** Among issues to be resolved are the possibility of tunneling on the excited-state surface, '(?)', and whether there are stable intermediates along *re* or *oa* paths.

two minutes upon raising the temperature to 77 K. Its low population and instability have precluded detailed analysis, and it has proven impossible to determine its mechanism of formation (for example, whether it is generated by the *L* mechanism).

*Excited-State Molecular Orbitals:* The photo-induced *re* of mutually *cis* hydrides on a single metal ion (M) has been studied computationally,<sup>46,47</sup> and is thought to occur

from a ligand-field excited state that is H-H bonding and that weakens M-(H-H) bonding and/or is actually M-(H-H) ( $\sigma^*$ ) antibonding, as shown in **Figure 5-10**.

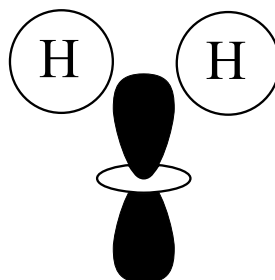


**Figure 5-10.** Cartoon showing nodal properties of an excited MO for an  $M(H)_2$  complex that is bonding between the two hydrides and antibonding between each one and the metal  $dz^2$  orbital.

The process is thought to be concerted, and to occur on a barrierless repulsive energy surface, with the H's freely coming together for release as  $H_2$ .<sup>17,21</sup> This view is compatible with measurements showing prompt release of  $H_2$  after photolysis ( $< 6$  ps),<sup>18</sup> and with the absence of a KIE for  $H_2/D_2$  photorelease.<sup>21</sup> The large KIE and tunneling-like behavior for the photo-*re* of  $E_4(4H)$  in contrast imply that its excited energy surface must instead have a barrier to  $H_2$  formation, and suggest that at the low temperature of our experiments  $H_2$  is formed by H-atom tunneling through the barrier. This behavior in turn suggests to us that the hydrides of  $E_4(4H)$  do not have a common vertex..

What type of excited state can generate the release of bridging hydrides? Regardless of whether the two bridging hydrides share a vertex (**Chart 1**) or are otherwise displayed, as in the 'parallel' arrangement in **Figures 5-2, 5-3, 5-6**, by analogy to the mononuclear case we would suggest that the optical excitation generates a  $M_2-(H-H)$  ( $\sigma^*$ ) antibonding ligand-field excited state of one of the two bridging hydrides, as



exemplified in **Figure 5-11**.

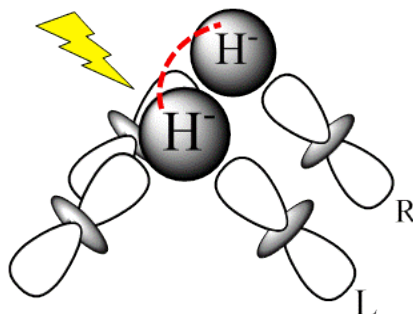


**Figure 5-11.** Cartoon showing nodal properties of the excited MO's for bridging hydrides (parallel arrangement), each antibonding between the hydride and the two  $dz^2$  orbitals on the Fe ions it bridges.

This could couple to the equivalent state of the other bridging hydride, delocalizing the excitation and generating a *cluster* excited state from which  $H_2$  is liberated, or alternatively, the excited hydride state might undergo reductive elimination through an *L*-like mechanism, with the 'liberated' proton attacking its neighbor hydride, liberating  $H_2$ . In any case, the formation of  $H_2$  appears to involve nuclear tunneling through a barrier, as discussed above.

### Summary and Prospects

These measurements have shown that *in situ* 450 nm photolysis of the Janus Intermediate,  $E_4(4H)$ , in an EPR cavity at temperatures below 20 K generates a new FeMo-co state, denoted  $E_4(2H)^*$ , that has lost the hyperfine couplings characteristic of the two bridging hydrides. We have concluded that this state is neither a 'hydride isomer' nor an  $H_2$  complex, but instead  $E_4(4H)$  has undergone photoinduced *re* of the two bridging hydrides of  $E_4(4H)$  to generate  $E_4(2H)^*$  with the release of  $H_2$ . During cryoannealing at temperatures above 175 K,  $E_4(2H)^*$  reverts to  $E_4(4H)$  through the

oxidative addition (*oa*) of H<sub>2</sub>. Our observations further imply that photoinduced release of H<sub>2</sub> involves a barrier to the combination of the two nascent H atoms, in contrast to a barrierless process for mono-metallic inorganic complexes, and further suggest that H<sub>2</sub> formation involves nuclear tunneling through that barrier. The *oa* recombination of E<sub>4</sub>(2H)\* with the liberated H<sub>2</sub> offers compelling evidence for the Janus intermediate as the point at which H<sub>2</sub> is necessarily lost during N<sub>2</sub> reduction; this mechanistically coupled loss must be gated by N<sub>2</sub> addition that drives the *re/oa* equilibrium toward reductive elimination of H<sub>2</sub> with N<sub>2</sub> binding/reduction.<sup>48</sup>

There are many issues to be addressed concerning this remarkable observation of photo-induced *re* of the bridging hydrides of E<sub>4</sub>(4H) and its thermal reverse, *oa* of H<sub>2</sub> by the photo-generated *S* = E<sub>4</sub>(2H)\* intermediate. Most obvious, is further characterization of the energy surfaces for photoinduced *re/oa* of the Janus intermediate, E<sub>4</sub>(4H), through experiments that address the indications of tunneling during photoinduced *re* and the possibility of stable intermediates during either or both, *re* and *oa*, as noted in the legend to **Figure 5-9**. In addition, we anticipate characterizing E<sub>4</sub>(2H)\* by <sup>57</sup>Fe and <sup>95</sup>Mo ENDOR spectroscopy.

Expanding the perspective, it is of particular interest to examine the reactivity of the photogenerated state E<sub>4</sub>(2H)\*. We know that E<sub>4</sub>(2H)\* is in some way more reactive than all thermally generated states of FeMo-co *except* the E<sub>4</sub>(2N2H) state produced by *re* of H<sub>2</sub> (**Figure 5-2**), as this latter is the only turnover state that can react with H<sub>2</sub>, through the *oa* reverse of the *re/oa* equilibrium with loss of N<sub>2</sub>. It seems unlikely that this equilibrium in fact involves the Dissociative pathway of **Figure 5-3**, as E<sub>4</sub>(4H) *re* does

not occur unless N<sub>2</sub> is present. Nevertheless, it is important to test whether E<sub>4</sub>(2H)\* binds and reacts with N<sub>2</sub>, as would be the case if *re* did occur in this fashion and E<sub>4</sub>(2H)\* were equivalent to **Z**, **Figure 5-3**. Indeed, as there is keen interest in using nitrogenase to reduce substrates other than N<sub>2</sub>,<sup>49-51</sup> it is of fundamental importance to test if E<sub>4</sub>(2H)\* can react with other possible substrates (CO<sub>2</sub>; C<sub>2</sub>H<sub>2</sub>, C<sub>2</sub>H<sub>4</sub>, etc.), as occurs with the coordinatively unsaturated states produced by photo-*re* of single-metal complexes.<sup>17,20,52</sup>

Of course, the use of  $\alpha$ -70<sup>lle</sup> MoFe protein precludes such experiments. Although this active-site change is central to the present report in allowing the accumulation of high populations of E<sub>4</sub>(4H), it does so at the cost of blocking access to the FeMo-co active site to all substrates *but* protons.<sup>10</sup> There is, however, an excellent prospect of overcoming this limitation. We find that under certain conditions of turnover with the wild-type enzyme, the E<sub>4</sub>(4H) EPR signal can be observed. Efforts are under way to maximize its population; photochemical studies of this state will be undertaken subsequently. These may help us to distinguish between the alternative Concerted and Associative mechanisms for *re/oa*, **Figure 5-3**.

## References

- (1) Burgess, B. K.; Lowe, D. J. *Chem. Rev.* **1996**, 96, 2983.
- (2) Seefeldt, L. C.; Hoffman, B. M.; Dean, D. R. *Annu. Rev. Biochem.* **2009**, 78, 701.
- (3) Thorneley, R. N. F.; Lowe, D. J. *Metal Ions in Biology* **1985**, 7, 221.
- (4) Wilson, P. E.; Nyborg, A. C.; Watt, G. D. *Biophys. Chem.* **2001**, 91, 281.
- (5) Duval, S.; Danyal, K.; Shaw, S.; Lytle, A. K.; Dean, D. R.; Hoffman, B.

- M.; Antony, E.; Seefeldt, L. C. *Proc. Natl. Acad. Sci. U.S.A.* **2013**, *110*, 16414.
- (6) Simpson, F. B.; Burris, R. H. *Science* **1984**, *224*, 1095.
- (7) For example, during the decades after the definitive formulation of the LT scheme (ref 3), with its obligatory loss of H<sub>2</sub> and resulting eight-electron/proton stoichiometry (eq 1), numerous computational studies described ‘mechanisms’ with only six electrons/protons. Indeed, one investigator even published multiple six-electron/proton mechanisms without acknowledging or addressing the contradiction to LT: eg., Dance, I. *Chem. Asian J.* 2007, *2*, 936
- (8) Hoffman, B. M.; Lukoyanov, D.; Yang, Z. Y.; Dean, D. R.; Seefeldt, L. C. *Chem. Rev.* **2014**, *114*, 4041.
- (9) Hoffman, B. M.; Lukoyanov, D.; Dean, D. R.; Seefeldt, L. C. *Acc. Chem. Res.* **2013**, *46*, 587.
- (10) Igarashi, R. Y.; Laryukhin, M.; Dos Santos, P. C.; Lee, H. I.; Dean, D. R.; Seefeldt, L. C.; Hoffman, B. M. *J. Am. Chem. Soc.* **2005**, *127*, 6231.
- (11) Lukoyanov, D.; Yang, Z.-Y.; Dean, D. R.; Seefeldt, L. C.; Hoffman, B. M. *J. Am. Chem. Soc.* **2010**, *132*, 2526.
- (12) Lukoyanov, D.; Barney, B. M.; Dean, D. R.; Seefeldt, L. C.; Hoffman, B. M. *Proc. Natl. Acad. Sci. U.S.A.* **2007**, *104*, 1451.
- (13) Crabtree, R. H. *The organometallic chemistry of the transition metals*; 5th ed.; Wiley: Hoboken, N.J., 2009.

- (14) Peruzzini, M.; Poli, R.; Editors *Recent Advances in Hydride Chemistry*; Elsevier Science B.V.: Amsterdam, Netherlands, 2001.
- (15) Yang, Z.-Y.; Khadka, N.; Lukoyanov, D.; Hoffman B. M.; Dean D. R.; Seefeldt L. C. *Proc. Natl. Acad. Sci. U.S.A.* **2013**, *110*, 16327.
- (16) Lukoyanov, D.; Yang, Z. Y.; Khadka, N.; Dean, D. R.; Seefeldt, L. C.; Hoffman, B. M. *J. Am. Chem. Soc.* **2015**, *137*, 3610.
- (17) Perutz, R. N. *Pure and Applied Chemistry* **1998**, *70*, 2211.
- (18) Colombo, M.; George, M. W.; Moore, J. N.; Pattison, D. I.; Perutz, R. N.; Virrels, I. G.; Ye, T. Q. *J. Chem. Soc., Dalton Trans.* **1997**, 2857.
- (19) Whittlesey, M. K.; Mawby, R. J.; Osman, R.; Perutz, R. N.; Field, L. D.; Wilkinson, M. P.; George, M. W. *J. Am. Chem. Soc.* **1993**, *115*, 8627.
- (20) Ballmann, J.; Munha, R. F.; Fryzuk, M. D. *Chem. Commun.* **2010**, *46*, 1013.
- (21) Ozin, G. A.; Mccaffrey, J. G. *J. Phys. Chem.* **1984**, *88*, 645.
- (22) Dugan, T. R.; Holland, P. L. *J. Organomet. Chem.* **2009**, *694*, 2825.
- (23) Yu, Y.; Smith, J. M.; Flaschenriem, C. J.; Holland, P. L. *Inorg. Chem.* **2006**, *45*, 5742.
- (24) Smith, J. M.; Sadique, A. R.; Cundari, T. R.; Rodgers, K. R.; Lukat-Rodgers, G.; Lachicotte, R. J.; Flaschenriem, C. J.; Vela, J.; Holland, P. L. *J. Am. Chem. Soc.* **2006**, *128*, 756.
- (25) Yu, Y.; Sadique, A. R.; Smith, J. M.; Dugan, T. R.; Cowley, R. E.; Brennessel, W. W.; Flaschenriem, C. J.; Bill, E.; Cundari, T. R.; Holland,

P. L. *J. Am. Chem. Soc.* **2008**, *130*, 6624.

- (26) We particularly note the extensive reference collection in ref 22
- (27) Manuscript in preparation.
- (28) Christiansen, J.; Goodwin, P. J.; Lanzilotta, W. N.; Seefeldt, L. C.; Dean, D. R. *Biochemistry* **1998**, *37*, 12611.
- (29) Parkin, G. J. *Labelled Compd. Radiopharm.* **2007**, *50*, 1088.
- (30) Parkin, G. *Acc. Chem. Res.* **2009**, *42*, 315.
- (31) Glasoe, P. K.; Long, F. A. *J. Phys. Chem.* **1960**, *64*, 188.
- (32) Davoust, C. E.; Doan, P. E.; Hoffman, B. M. *J. Magn. Reson.* **1996**, *119*, 38.
- (33) Brueggemann, W.; Niklas, J. R. *J. Magn. Reson., Ser A* **1994**, *108*, 25.
- (34) Lukoyanov, D.; Yang, Z. Y.; Duval, S.; Danyal, K.; Dean, D. R.; Seefeldt, L. C.; Hoffman, B. M. *Inorg. Chem.* **2014**, *53*, 3688.
- (35) Manuscript in preparation.
- (36) Lee, Y.; Kinney, R. A.; Hoffman, B. M.; Peters, J. C. *J. Am. Chem. Soc.* **2011**, *133*, 16366.
- (37) Gunderson, W. A.; Suess, D. L.; Fong, H.; Wang, X.; Hoffmann, C. M.; Cutsail III, G. E.; Peters, J. C.; Hoffman, B. M. *J. Am. Chem. Soc.* **2014**, *136*, 14998.
- (38) Lubitz, W.; Ogata, H.; Rudiger, O.; Reijerse, E. *Chem. Rev.* **2014**, *114*, 4081.
- (39) Tai, H. L.; Nishikawa, K.; Suzuki, M.; Higuchi, Y.; Hirota, S. *Angew.*

*Chem. Int. Ed.* **2014**, *53*, 13817.

- (40) Bullock, R. M.; Bender, B. R. In *Encyclopedia of Catalysis*; Horváth, I. T., Ed.; Wiley: Hoboken, New Jersey, 2003; Vol. 4, p 281.
- (41) Mas-Balleste', R.; Lledos, A. In *Comprehensive Inorganic Chemistry II*; Alvarez, S., Ed.; Elsevier Ltd.: 2013; Vol. 9, p 736.
- (42) Abu-Hasanayn, F.; Goldman, A. S.; Krogh-Jespersen, K. *J. Phys. Chem.* **1993**, *97*, 5890.
- (43) Campian, M. V.; Perutz, R. N.; Procacci, B.; Thatcher, R. J.; Torres, O.; Whitwood, A. C. *J. Am. Chem. Soc.* **2012**, *134*, 3480.
- (44) Wang, W. H.; Narducci, A. A.; House, P. G.; Weitz, E. *J. Am. Chem. Soc.* **1996**, *118*, 8654.
- (45) Berberan-Santos, M. N.; Bodunov, E. N.; Valeur, B. *Chem. Phys.* **2005**, *315*, 171.
- (46) Daniel, C. *J. Phys. Chem.* **1991**, *95*, 2394.
- (47) Wang, W. H.; Weitz, E. *J. Phys. Chem. A* **1997**, *101*, 2358.
- (48) We thank an anonymous reviewer for helping us to articulate this point.
- (49) Hu, Y.; Lee, C. C.; Ribbe, M. W. *Science* **2011**, *333*, 753.
- (50) Yang, Z. Y.; Moure, V. R.; Dean, D. R.; Seefeldt, L. C. *Proc. Natl. Acad. Sci.U.S.A.* **2012**, *109*, 19644.
- (51) Seefeldt, L. C.; Yang, Z. Y.; Duval, S.; Dean, D. R. *Biochim. Biophys. Acta* **2013**, *1827*, 1102.
- (52) Calladine, J. A.; Torres, O.; Anstey, M.; Ball, G. E.; Bergman, R. G.;

Curley, J.; Duckett, S. B.; George, M. W.; Gilson, A. I.; Lawes, D. J.;

Perutz, R. N.; Sun, X. Z.; Vollhardt, K. P. C. *Chem. Sci.* **2010**, *1*, 622.



**APPENDIX****SUPPORTING INFORMATION****REVERSIBLE PHOTOINDUCED REDUCTIVE ELIMINATION OF H<sub>2</sub> FROM  
THE NITROGENASE DIHYDRIDE STATE, THE E<sub>4</sub>(4H) JANUS  
INTERMEDIATE**

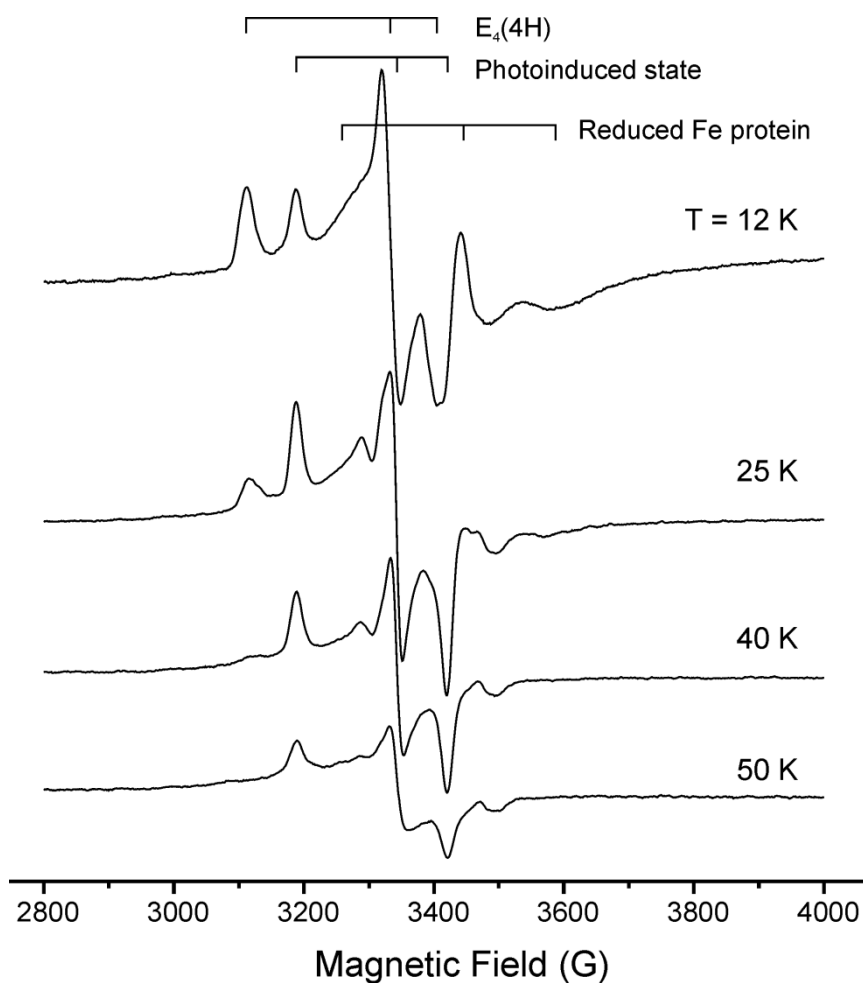


**Figure 5-S1: Temperature dependence of X-band EPR spectra of irradiated MoFe protein ( $\alpha$ -70<sup>He</sup>) trapped during Ar turnover in H<sub>2</sub>O buffer.** Additional features observed at  $T > 12$  K are assigned to ATP bound reduced Fe protein present in the turnover sample. *EPR conditions:* microwave frequency, 9.36 GHz; microwave power, 10 mW; modulation amplitude, 13 G; time constant, 160 ms; field sweep speed, 20 G/s.

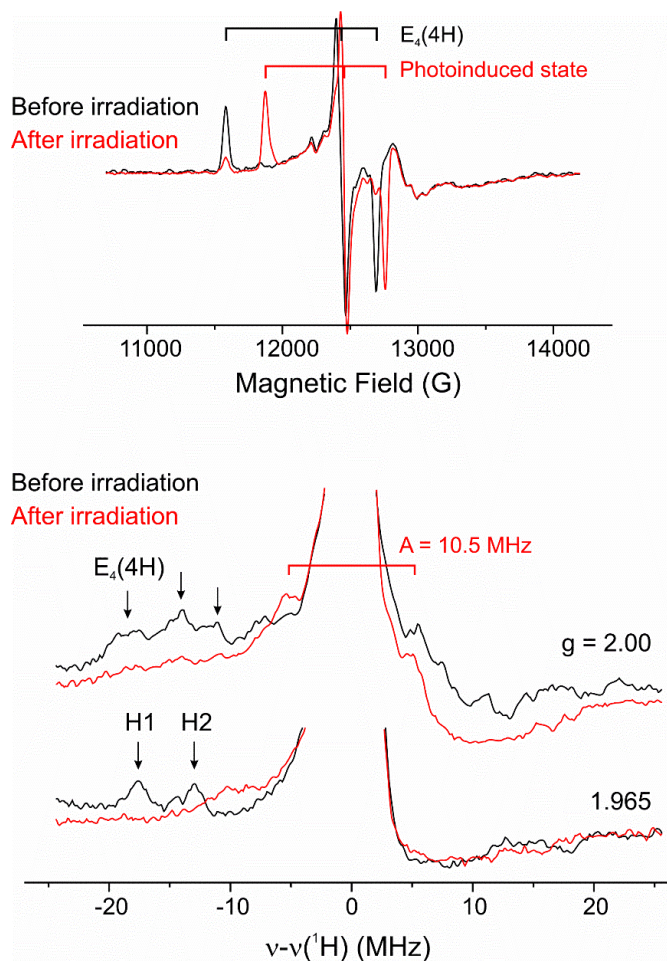


**Figure 5-S2: Photoinduced changes in Q-band CW EPR (upper) and <sup>1</sup>H field-modulated Q-band CW ENDOR (lower) spectra of MoFe protein ( $\alpha$ -70<sup>Ile</sup>) trapped during Ar turnover in H<sub>2</sub>O buffer.**  $g = 2.00$ : Arrows indicate overlapping ENDOR signals associated with the two bridging hydrides of the E<sub>4</sub>(4H) intermediate.  $g = 1.965$ : As indicated, resolved signals from the two hydrides. *EPR conditions*: microwave frequency, ~35.04 GHz; modulation amplitude, 1 G; time constant, 128 ms; field sweep speed, 17 G/sec; temperature, 2 K. *ENDOR conditions*: microwave frequency, ~35.04 GHz; modulation amplitude, 1.6 G; time constant, 64 ms; RF sweep speed, 2 MHz/sec; bandwidth of RF broadened to 60 kHz; 60-100 scans; temperature, 2 K.

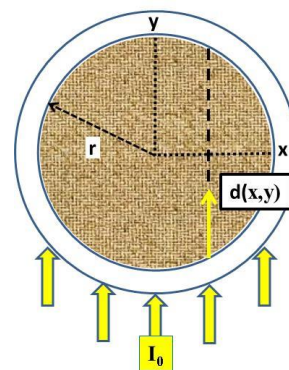
Rate Constant for photolysis.

Assume the ‘snow’ of frozen MoFe protein in an EPR tube of internal diameter  $r$  scatters light with a scattering length,  $\delta$ , and the front face is uniformly illuminated with a parallel beam of Intensity  $I_0$  incident at each point across the front tube face (no scattering off face), as depicted in **Fig S3**. Then at each point  $(x,y)$  within the tube the light intensity will be reduced by the scattering along the distance,  $d(x,y)$  through which the light travels to that point, and thus the rate constant for photolysis,  $k$ , which is proportional to the quantum yield for photolysis,  $\phi$ , and the local light intensity,  $I(x,y)$ , varies across the tube. As a result, the time course for photolysis becomes distributed, the sum of the varying decay constants over the tube. The number of unphotolyzed systems at time,  $t$ , denoted  $N(t, \phi)$ , then becomes distributed, as follows:

$$k_i(x, y, \phi) \propto \phi I_i(x, y)$$

$$\propto \phi I_0 e^{-d(x,y)/\delta}$$

$$N(t, \phi) \propto \iint_{tube} e^{-k(x,y,\phi)t} dx dy$$



As the *in situ* photolysis process is in actuality even more complicated, we model the observed photolysis progress curves with a stretched exponential,<sup>1</sup>

$$N(t, \phi) \propto e^{-(t/\tau(\phi))^n}$$

where  $\tau(\phi)$  is the median decay time whose inverse equals the median decay rate constant

and is proportional to the quantum yield for photolysis,

$$\tau^{-1}(\phi) = k_{med} \propto \phi$$

and,  $0 < n \leq 1$  equals unity for an exponential decay and decreases with the spread of the distribution.

- (1) Phillips, J. C. *Reports on Progress in Physics* **1996**, 59, 1133.

**Table 5-S1. Specific Activities for MoFe proteins at pH 7.0.**

MoFe Protein	Substrates <sup>a</sup>			
	Proton <sup>b</sup>	N <sub>2</sub> (1 atm)		Acetylene (0.1 atm)
	nmol of H <sub>2</sub> /min/mg	nmol of H <sub>2</sub> /min/m g	nmol of NH <sub>3</sub> /min/mg	nmol of H <sub>2</sub> /min/m g      nmol of C <sub>2</sub> H <sub>4</sub> /min/mg
$\alpha$ -70 <sup>Val</sup> / $\alpha$ - 195 <sup>His</sup>	2310 ± 145	714 ± 41	677 ± 6	262 ± 3      1897 ± 57
$\alpha$ -70 <sup>Val</sup> / $\alpha$ - 195 <sup>Gln</sup>	1900 ± 53	1345 ± 16	28 ± 1	738 ± 4      1012 ± 24
$\alpha$ -70 <sup>Ile</sup> / $\alpha$ - 195 <sup>His</sup>	2739 ± 114	2595 ± 72	116 ± 4	2371 ± 43      92 ± 1
$\alpha$ -70 <sup>Ile</sup> / $\alpha$ - 195 <sup>Gln</sup>	2172 ± 57	2225 ± 108	28 ± 3	1751 ± 72      102 ± 3

<sup>a</sup> All assays were performed at 30 °C for 8 min at a molar ratio of MoFe protein to Fe protein of 1:20, and the specific activities are expressed nmol of product per min per mg of MoFe protein. <sup>b</sup> Proton reduction assays were conducted under an argon atmosphere.

**Table 5-S2. Stretched Exponential parameters describing the photoinduced *re* of E<sub>4</sub>(4H).**

	T (K)	3.8	8	12
H <sub>2</sub> O	$\tau$ (min)	9.6	8.5	8.9
	n	0.50	0.52	0.48
D <sub>2</sub> O	$\tau$ (min)	75	80	114
	n	0.41	0.44	0.41
sKIE	$\tau(\text{D}_2\text{O})/\tau(\text{H}_2\text{O})$	7.8	9.4	12.8

## CHAPTER 6

REDUCTIVE ELIMINATION OF H<sub>2</sub> ACTIVATES NITROGENASE TO REDUCE  
THE N≡N TRIPLE BOND: CHARACTERIZATION OF THE E<sub>4</sub>(4H) JANUS  
INTERMEDIATE IN WILD-TYPE ENZYME**Abstract**

We have proposed a reductive elimination/oxidative addition (*re/oa*) mechanism for reduction of N<sub>2</sub> to 2NH<sub>3</sub> by nitrogenase, based on identification of a freeze-trapped intermediate of the  $\alpha$ -70<sup>Val→Ile</sup> substituted MoFe protein as the Janus intermediate that stores four reducing equivalents on FeMo-co as two [Fe-H-Fe] bridging hydrides (denoted E<sub>4</sub>(4H)). The mechanism postulates that obligatory *re* of the hydrides as H<sub>2</sub> drives reduction of N<sub>2</sub> to a state (denoted E<sub>4</sub>(2N2H)) with a moiety at the diazene (HN=NH) reduction level bound to the catalytic FeMo-cofactor. In the present work, EPR/ENDOR and photophysical measurements show that a state freeze-trapped during N<sub>2</sub> reduction by wild type (WT) MoFe protein is the same Janus intermediate, thereby establishing the  $\alpha$ -70<sup>Val→Ile</sup> intermediate as a reliable guide to mechanism, and enabling new experimental tests of the *re/oa* mechanism with WT enzyme. These allow us to show that the *re/oa* mechanism accounts for the longstanding *Key Constraints* on mechanism. Monitoring the  $S = 1/2$  FeMo-co EPR signal of Janus in WT MoFe during N<sub>2</sub> reduction under mixed-isotope condition, H<sub>2</sub>O buffer/D<sub>2</sub>, and the converse, establishes that the bridging hydrides/deuterides do not exchange with solvent during enzymatic turnover,

---

\*Coauthored by Dmitry Lukoyanov, Nimesh Khadka, Zhi-Yong Yang, Dennis R. Dean, Lance C. Seefeldt, Brian M. Hoffman (2016) *JACS* **138** (33), 10674-10683. Copyright © [2016] American Chemical Society. Reprinted with permission.

thereby explaining earlier observations and verifying the *re/oa* mechanism. Relaxation of  $E_4(2N_2H)$  to the WT resting-state is shown to occur via *oa* of  $H_2$  and release of  $N_2$  to form Janus, followed by sequential release of two  $H_2$ , demonstrating the kinetic reversibility of the *re/oa* equilibrium. The relative populations of  $E_4(2N_2H)$  and  $E_4(4H)$  freeze-trapped during WT turnover furthermore show that the rapidly reversible *re/oa* equilibrium between  $[E_4(4H) + N_2]$  and  $[E_4(2N_2H) + H_2]$  is roughly thermoneutral ( $\Delta_{re}G^0 \sim -2$  kcal/mol), whereas hydrogenation of gas-phase  $N_2$  would be highly endergonic. These findings establish (i) that *re/oa* satisfies all key constraints on mechanism, (ii) that Janus is the key to  $N_2$  reduction by WT enzyme, which (iii) indeed occurs via the *re/oa* mechanism. Thus emerges a picture of the central mechanistic steps by which the nitrogenase MoFe protein carries out one of the most challenging chemical transformation in biology, the reduction of the  $N\equiv N$  triple bond.

## Introduction

By catalyzing biological nitrogen fixation — the reduction of  $N_2$  to two  $NH_3$  molecules — nitrogenase generates the nitrogen-containing nutrients that support most of

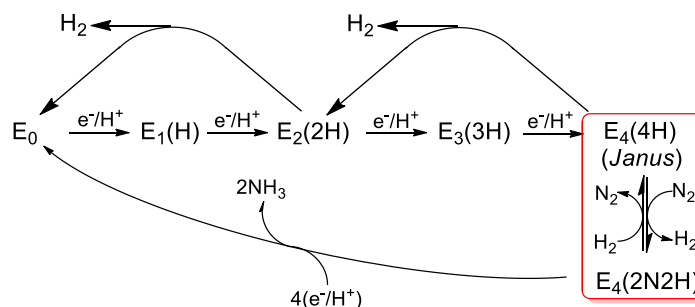


**Figure 6-1: Simplified Lowe-Thorneley (LT) kinetic scheme for nitrogen reduction<sup>2-4</sup> that focus on the electron-accumulation and FeMo-co activation (boxed) stages.** In the  $E_n$  notation,  $n$  = number of  $[e^-/H^+]$  added to FeMo-co; in parentheses, the stoichiometry of H/N bound to FeMo-co, except  $n = 7, 8$ , where structures are shown.



the biosphere, including over half the human population.<sup>1</sup>

But an understanding of the mechanism of N<sub>2</sub> reduction by nitrogenase has been elusive. A ‘kinetic’ foundation for the mechanism of the Mo-dependent nitrogenase was developed through extensive studies in the 1970’s and 1980’s.<sup>2-4</sup> The culmination of these measurements was the Lowe-Thorneley (LT) kinetic scheme for nitrogenase function, **Figure 6-1**,<sup>2-4</sup> which describes the transformations among catalytic intermediates, denoted E<sub>n</sub> where *n* is the number of steps of electrons/protons delivered from the nitrogenase Fe protein to the MoFe protein, which contains the active site iron-molybdenum cofactor ([7Fe-9S-Mo-C-R-homocitrate, denoted **M**]; FeMo-co) **Figure 6-2**.

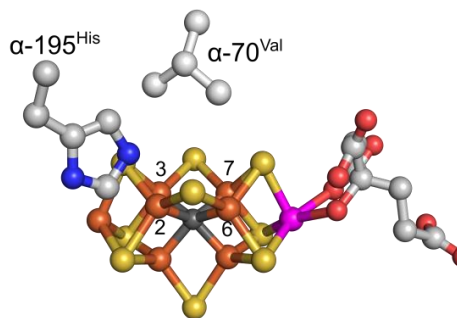


**Figure 6-2: Crystal structure of FeMo-co.** Fe is shown in rust, Mo in magenta, S in yellow, carbide in dark-grey, carbon in grey, N in blue and O in red. The Fe atoms of catalytic 4Fe-4S face are labelled as 2, 3, 6, and 7. Two amino acids,  $\alpha$ -70<sup>Val</sup> and  $\alpha$ -195<sup>His</sup>, that approach the FeMo-co are also shown. The image was created using PDB coordinate 2AFI.

A defining feature of this scheme is the obligatory formation of one mole of H<sub>2</sub> per mole of N<sub>2</sub> reduced, which leads to a limiting stoichiometry for enzyme-catalyzed nitrogen fixation given by **eq 6-1**,



in agreement with stoichiometric measurements by Simpson and Burris.<sup>5</sup> However, the

obligatory requirement for H<sub>2</sub> formation has not been universally accepted, and was even questioned in the culminating review of Burgess and Lowe: “Thus the data that support the obligatory evolution of one H<sub>2</sub> for every N<sub>2</sub> reduced are much less compelling than the data that require us to believe that some H<sub>2</sub> will always be evolved during N<sub>2</sub> reduction.”<sup>2</sup>

We recently proposed<sup>6,7</sup> that obligatory H<sub>2</sub> formation during nitrogenase N<sub>2</sub> reduction is in fact required to explain the catalytic function of nitrogenase. This proposal originates with the characterization of an intermediate (FeMo-co spin  $S = \frac{1}{2}$ ) trapped during turnover of MoFe protein having the  $\alpha$ -70<sup>Val→Ile</sup> substitution, which apparently inhibits access by all substrates to the active site, other than protons.<sup>8</sup> A combination of <sup>1,2</sup>H/<sup>95</sup>Mo ENDOR spectroscopy<sup>8,9</sup> and cryoannealing ‘electron counting’<sup>10</sup> showed this state to be the key E<sub>4</sub>(4H) ‘Janus’ intermediate, which has accumulated four of the eight reducing equivalents required by **eq 6-1**, storing them as two [Fe-H-Fe] bridging hydrides.<sup>8-10</sup> E<sub>4</sub>(4H) sits at a transition in the N<sub>2</sub> reduction pathway, **Figure 6-1**, poised to ‘fall back’ to the E<sub>0</sub> resting state by successive release of two H<sub>2</sub>,<sup>10</sup> but equally poised to eliminate H<sub>2</sub> and proceed to the reduction of N<sub>2</sub> to two NH<sub>3</sub> through the accumulation of four more equivalents, hence the appellation, ‘Janus’.<sup>7</sup>

The discovery that the four reducing equivalents accumulated by E<sub>4</sub>(4H) are stored as bridging hydrides forged a connection between nitrogenase catalysis and the organometallic chemistry of metal hydrides<sup>11-13</sup> that offered explanations of a multitude of features of nitrogenase mechanism that had defied explanation for decades.<sup>2</sup> At the most basic level, this hydride formation helped to explain how a constant-potential

electron donor, reduced Fe protein ( $\text{Fe}^{\text{red}}$ ), could reduce FeMo-co by four equivalents. Moreover, bridging hydrides are less susceptible to protonation to form  $\text{H}_2$ , or to solvent exchange, than terminal hydrides. As a consequence of the latter, bridging hydrides diminish the tendency of FeMo-co to ‘fall back’ to resting state through the formation of two  $\text{H}_2$  (**Figure 6-1**) However, the bridging mode also lowers hydride reactivity, relative to that of terminal hydrides. How the release of  $\text{H}_2$  contributes to the activation of this ‘deactivated’ intermediate for the hydrogenation of  $\text{N}_2$  to a moiety at the  $\text{N}_2\text{H}_2$ -reduction level is thus a central ‘mystery’ of  $\text{N}_2$  reduction by nitrogenase.

Importantly, reference to the inorganic chemistry of metal-dihydrides offered an explanation to this mystery, as well. Once it is recognized that  $\text{E}_4(4\text{H})$  contains two bridging hydrides, then the chemistry of metal-dihydride complexes<sup>11-13</sup> identifies the LT  $\text{E}_4(4\text{H}) \leftrightarrow \text{E}_4(2\text{N}_2\text{H})$  mechanistically coupled equilibrium (**Figure 6-1**) as the reductive elimination (*re*) of  $\text{H}_2$  and its reverse, the oxidative addition (*oa*) of  $\text{H}_2$ , **Figure 6-3**.

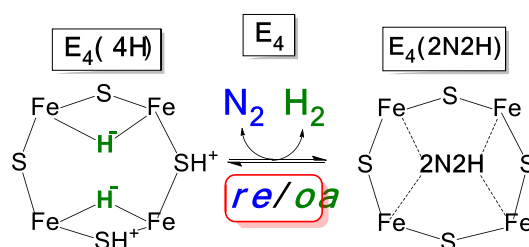


**Figure 6-3: Schematic of *re/oa* equilibrium.** The cartoon represents the Fe 2,3,6,7 face of FeMo-co, and the ‘ $2\text{N}_2\text{H}$ ’ implies a species at the diazene reduction level of unknown structure and coordination geometry. In the indicated equilibrium the binding and activation of  $\text{N}_2$  is mechanistically coupled to the *re* of  $\text{H}_2$ , as described in the text. Some of the potential complexities associated with this enzymatic process that underlie this cartoon are discussed in reference 18.

We proposed that for nitrogenase, the *re* of  $\text{H}_2$  carries off two of the four reducing equivalents formally stored as the  $\text{H}^-$ , driving the first, and most difficult, step of  $\text{N}_2$

cleavage; reduction of the N<sub>2</sub> triple bond to a diazene-level (2N2H) moiety bound to FeMo-cofactor, **Figure 6-3**, by the remaining two reducing equivalents. This process fulfills one of the long-standing key constraints on mechanism: **Chart 1, (i)**.<sup>2</sup>

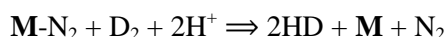
**Chart 1: Key Constraints on Nitrogenase Mechanism<sup>2</sup>**

(i) State when N<sub>2</sub> is Reduced:

N<sub>2</sub> is reduced at the E<sub>4</sub> stage of [e<sup>-</sup>/H<sup>+</sup>] accumulation

(ii) D<sub>2</sub> or T<sub>2</sub> only react during N<sub>2</sub> Turnover, during which:

(a) 2HD form stoichiometrically:



(b) No Scrambling with solvent:

‘No’ T<sup>+</sup> released to solvent under T<sub>2</sub>

(c) Reduction Level of this reaction:

D<sub>2</sub>/T<sub>2</sub> reacts at E<sub>4</sub>(2N2H) level

The proposal that N<sub>2</sub> fixation requires the obligatory *re* of H<sub>2</sub> was first supported by its ability to provide explanations of key constraints on nitrogenase mechanism summarized in **Chart 1**.<sup>2</sup> These include not only the E<sub>n</sub> state at which N<sub>2</sub> is first reduced (*Key Constraint (i)*), but most especially previously baffling results from turnover in the presence of D<sub>2</sub>/T<sub>2</sub>. It was found that: *Key Constraints (ii)*, D<sub>2</sub> only reacts with nitrogenase during turnover under an N<sub>2</sub>/D<sub>2</sub> atmosphere; *(iia)* in this reaction D<sub>2</sub> is stoichiometrically reduced to two HD (with H<sub>2</sub>O buffer); *(iib)*, corresponding turnover with T<sub>2</sub> does not lead to exchange of T<sup>+</sup> into H<sub>2</sub>O solvent.<sup>2</sup> These constraints are explained as arising through the reverse of the *re* process, **Figure 6-3**, namely the

oxidative addition (*oa*) of  $H_2$  with loss of  $N_2$ .<sup>6,7</sup> According to the mechanism, during turnover under  $D_2/N_2$ , reaction of the  $E_4(2N_2H)$  intermediate with  $D_2$  generates dideutero- $E_4$  with two  $[Fe-D-Fe]$  bridging deuterides which do not exchange with solvent.<sup>14</sup> This  $E_4(4H)$  isotopologue, which we denote  $E_4(2D^-;2H^+)$  (**Chart 2**), would relax through  $E_2(D^-;H^+)$  to  $E_0$  with successive loss of two  $HD$  <sup>7,10</sup>.

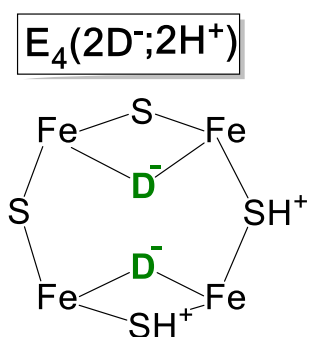


**Chart 2**

The proposed formation of the  $E_4(2D^-;2H^+)$  and  $E_2(D^-;H^+)$  states through the *thermodynamically* allowed reverse of *re*, the *oa* of  $D_2$  with accompanying release of  $N_2$ , led to a successful test of their formation. During turnover under  $N_2/D_2$ , the non-physiological substrate acetylene ( $C_2H_2$ ) intercepted these states to generate deuterated ethylenes ( $C_2H_3D$  and  $C_2H_2D_2$ ).<sup>14</sup> More recently, we identified an  $S = 1/2$  EPR signal that appears during  $N_2$  reduction by wild type (WT) MoFe protein as arising from FeMo-co of the  $E_4(2N_2H)$  state formed by *re* of  $H_2$  with  $N_2$  reduction, **Figure 6-3**, and in so doing confirmed the prediction that the (*re/oa*) activation equilibrium is not only thermodynamically, but also *kinetically* reversible.<sup>15</sup> Characterization of the  $E_4(4H)$  ‘Janus’ intermediate as carrying four reducing equivalents in the form of two  $[Fe-H-Fe]$

bridging hydrides thus laid the foundation for the *re/oa* mechanism, **Figure 6-3**, with its obligatory formation of one H<sub>2</sub> per N<sub>2</sub> reduced and resultant limiting stoichiometry of **eq 6-1**,<sup>15</sup> while the success of predictions based on the mechanism provides powerful support for the mechanism.

We here report *two* major types of advance in our understanding of nitrogenase catalysis. The *first* was motivated by our recognition that, although the predictions of *re/oa* were tested in WT MoFe, the mechanism was founded on the presence and properties of the two [Fe-H-Fe] bridging hydrides in the Janus intermediate trapped and characterized in the  $\alpha$ -70<sup>Val→Ile</sup> MoFe protein, which shows a much decreased ability to bind and reduce N<sub>2</sub>. This raised the question: *Do the properties of the Janus intermediate in the MoFe variant accurately reflect those of the WT intermediate, and are mechanistic conclusions based on studies of the variant applicable to WT enzyme? This report answers these coupled questions: yes.* We here establish that the same E<sub>4</sub>(4H) Janus intermediate, with its two [Fe-H-Fe] bridging hydrides, in fact does participate in catalysis by the WT enzyme through the *re/oa* mechanism for N<sub>2</sub> reduction, thereby showing the  $\alpha$ -70<sup>Val→Ile</sup> Janus intermediate as a reliable guide to mechanism.

The *second* is a set of advances founded on the ability to monitor both the E<sub>4</sub>(4H) and E<sub>4</sub>(2N<sub>2</sub>H) partners of the *re/oa* equilibrium in WT enzyme (**Figure 6-3**). This ability enables us to experimentally demonstrate that the *re/oa* mechanism indeed satisfies the *Key Constraints* of **Chart 1**, and beyond that to measure the energetics and kinetics of the equilibrium interconversion. Overall, this report yields a picture of the key mechanistic steps by which nitrogenase carries out one of the most challenging chemical

transformation in biology, the reduction of the N≡N triple bond.<sup>16</sup>

## Materials and Methods

*Materials and Protein purifications:* All the reagents were obtained from SigmaAldrich (St. Louis, MO) or Fisher Scientific (Fair Lawn, NJ) and were used without further purification. Argon and N<sub>2</sub> gases were purchased from Air Liquide America Specialty Gases LLC (Plumsteadville, PA). Experiments were carried out with WT *Azotobacter vinelandii* MoFe protein expressed and purified as described elsewhere.<sup>17</sup> The handling of all buffers and proteins were done anaerobically unless stated otherwise.

*EPR and ENDOR samples:* Samples were prepared as described under turnover conditions specified in figure legends; X-band samples contain 50 μM MoFe protein, 75 μM Fe protein, and the concentration of intermediates trapped during turnover is typically ~ 20 μM.<sup>15,18</sup> For Q band samples, 100 μM MoFe and 150 μM Fe was used. All the samples were allowed to turnover for 20-25s, transferred to a X or Q band tube, and frozen with liquid nitrogen..<sup>15,18</sup> It was found that during turnover of WT enzyme under low partial pressures of N<sub>2</sub> a g<sub>1</sub> = 2.15 species, shown below to be the E<sub>4</sub>(4H) intermediate in WT enzyme could be trapped in populations adequate for study, typically along with its ‘equilibrium partner’ the E<sub>4</sub>(2N2H) intermediate. The properties of g<sub>1</sub> = 2.15, E<sub>4</sub>(4H) are compared with those of E<sub>4</sub>(4H) trapped in the α-70<sup>Val→Ile</sup> and α-70<sup>Val→Ile</sup>/α-195<sup>His→Gln</sup> MoFe proteins as described.<sup>17,18</sup>

*EPR and ENDOR Measurements:* X-band CW EPR spectra and Q-band CW EPR and <sup>1,2</sup>H ENDOR spectra, including those during *in situ* photolysis by constant 450nm diode laser illumination, were collected as described.<sup>18</sup> Data points for kinetics of photolysis

and annealing were obtained as amplitudes of EPR signals at the well-resolved  $g_1$  features of the  $E_4$  states linked by *re/oa*. Tests of this protocol by EPR simulations show that the error of this quantitation approach should not exceed 15% when both  $E_4(4H)$  and  $E_4(4D)$  intermediates are present. We recall a time constant for photolysis is inversely proportional to the intensity of illumination and photolysis quantum yield.<sup>18</sup> As a result the kinetic isotope effect on photolysis corresponds to the effect on quantum yield.

## Results and Discussion

### *Enhancing the population of the WT $g_1 = 2.15$ intermediate*

**Figure 6-4** presents EPR spectra of WT MoFe protein freeze-quenched under turnover at high and low partial pressure of  $N_2$ , along with a spectrum of the  $E_4(4H)$  intermediate trapped during turnover of  $\alpha$ -70<sup>Val→Ile</sup> MoFe protein. The spectrum for the  $\alpha$ -70<sup>Val→Ile</sup> enzyme shows the signal from the  $E_4(4H)$  Janus intermediate,  $\mathbf{g} = [2.15, 2.007, 1.965]$ . The WT enzyme turned over under high partial pressure of  $N_2$  ( $P(N_2)$ ) shows the EPR signal from the  $E_4(2N2H)$  intermediate, in which FeMo-co binds a diazene-level product of  $N_2$  binding/reduction,  $\mathbf{g} = [2.09, 1.99, 1.97]$ . However, WT enzyme freeze-trapped under low  $P(N_2)$  turnover with high solution concentration of  $H_2$  (high effective  $P(H_2)$ , see figure legend and ref<sup>15</sup>) shows only traces of the signal from  $E_4(2N2H)$ , and instead shows an EPR signal of an intermediate with  $g_1 = 2.15$ , which is indistinguishable from that of  $E_4(4H)$  in the MoFe  $\alpha$ -70<sup>Val→Ile</sup> variant.<sup>8,10</sup> Closer inspection of the high- $P(N_2)$  signal then shows a trace of the  $g_1 = 2.15$  feature, associated with a very low population of this intermediate, confirming its presence under all turnover conditions. Such a correlation of relative intensities with  $P(N_2)$  and effective  $P(H_2)$  is as expected if



this  $g_1 = 2.15$  signal is indeed from WT  $E_4(4H)$ . In this case its concentration relative to that of  $E_4(2N_2H)$  is governed by the equilibrium of **Figure 6-3**, when, as expected, the forward and reverse steps of the *re/oa* equilibrium are rapid compared to the slow delivery of the next electron from  $Fe^{red}$  (**Figure 6-1**).

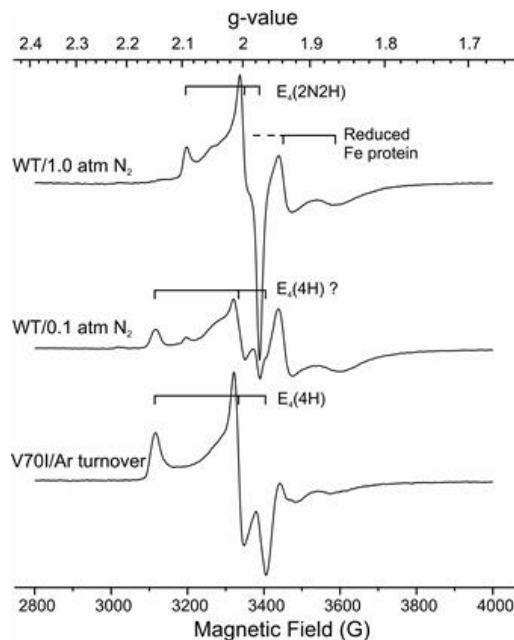


**Figure 6-4: X-band EPR spectra of WT nitrogenase turnover samples trapped under different conditions.** EPR spectrum under 1 atm of  $N_2$  (with stirring to facilitate transfer of  $H_2$  formed during turnover into the headspace<sup>15</sup>), and under low  $P(N_2)$  in  $H_2O$  buffer (without stirring) shown in comparison with spectrum of  $E_4(4H)$  state trapped during turnover of  $\alpha$ -70<sup>Val→Ile</sup> MoFe protein of the same concentration (see M&M). *EPR conditions:* temperature, 12 K; microwave frequency, 9.36 GHz; microwave power, 10 mW; modulation amplitude, 9 G; time constant, 160 ms; field sweep speed, 20 G/s.

$$\frac{E_4(2N_2H)}{E_4(4H)} = K_{re} \frac{P(N_2)}{P(H_2)} \propto P(N_2)$$

Here  $K_{re}$  is the equilibrium constant for the *re/oa* equilibrium, and a simple proportionality to  $P(N_2)$  follows from our observation that at these high enzyme concentrations, turnover produces a roughly constant (saturating) concentration of  $H_2$

regardless of  $P(N_2)$ .<sup>15</sup> Not only does this  $P(N_2)$  dependence supports the idea that the  $g_1 = 2.15$  state is indeed the WT  $E_4(4H)$ , but of central importance to this study, the ability to prepare samples whose dominant EPR signal is that of the  $g_1 = 2.15$  state enables its characterization and identification, as now described.

### $^{1,2}H$ Hyperfine Coupling to Bridging $[Fe-H/D-Fe]$ in WT MoFe

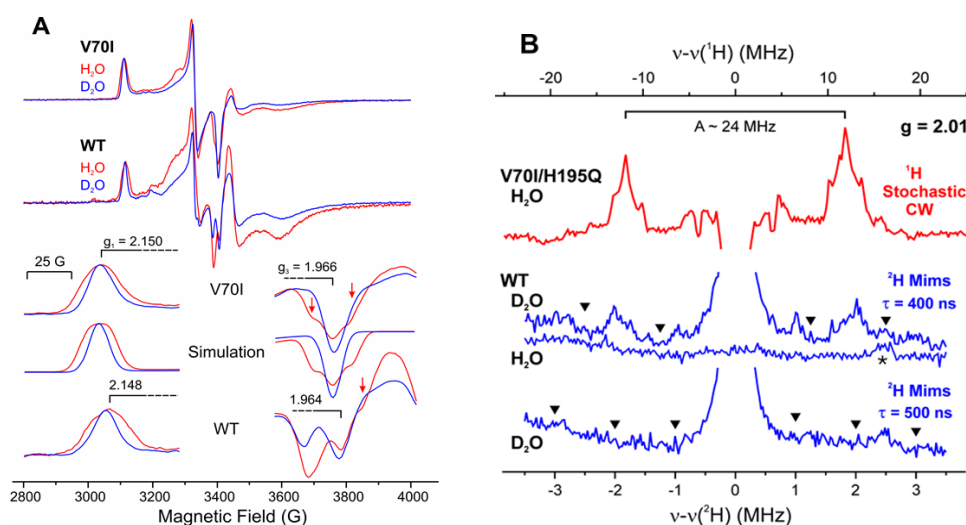


**Figure 6-5: EPR and ENDOR spectrum for WT and  $\alpha$ -70<sup>Val→Ile</sup> MoFe protein under Ar turnover.** (A) EPR spectra of WT and  $\alpha$ -70<sup>Val→Ile</sup> turnover samples trapped in H<sub>2</sub>O (red) and D<sub>2</sub>O (blue) buffers. Spectra are shown after normalization to the same  $g_1$  feature amplitude and their extended  $g_1$  and  $g_3$  fragments are compared with EPR simulations obtained with hydrides/deuterides hyperfine interaction parameters known from previous ENDOR study.<sup>8</sup> Red arrows indicate resolved features associated with hydrides hyperfine interaction. *EPR conditions:* temperature, 12 K; microwave frequency, 9.36 GHz; microwave power, 10 mW; modulation amplitude, 2.3 G; time constant, 160 ms; field sweep speed, 10 G/s; 4 scans. (B) Mims <sup>2</sup>H ENDOR spectra of WT low  $P(N_2)$  turnover in D<sub>2</sub>O (*middle*) shown in comparison with previously obtained stochastic CW ENDOR of hydrides of  $E_4(4H)$  trapped in  $\alpha$ -70<sup>Val→Ile</sup>/ $\alpha$ -195<sup>His→Gln</sup> protein during turnover in H<sub>2</sub>O (*top*).<sup>18</sup> Spectra of <sup>2</sup>H and <sup>1</sup>H are scaled to the same Larmor frequency. In D<sub>2</sub>O spectra, down triangles indicate 'blind spots' of Mims ENDOR spectra with suppressed hyperfine couplings of  $A = n/\tau$ ,  $n = 1, 2, \dots$ ; \*-labeled signal in the H<sub>2</sub>O background Mims  $\tau = 400$  ns spectrum is associated with 5<sup>th</sup> harmonics of the matrix <sup>1</sup>H response. *Mims ENDOR conditions:* microwave frequency, 34.743 GHz;  $\tau/2 = 50$  ns; RF 20  $\mu$ s; repetition time 50 ms;  $\sim 400$ -800 scans; temperature, 2 K.

ENDOR spectroscopy revealed the presence in  $E_4(4H)$  of  $\alpha$ -70<sup>Val→Ile</sup> and  $\alpha$ -70<sup>Val→Ile</sup>/ $\alpha$ -195<sup>His→Gln</sup> MoFe protein of two [Fe-H-Fe] bridging hydrides with anisotropic hyperfine tensors whose principal values are virtually identical,  $A_1 = [11, 25, 37]$  MHz,  $A_2 = [10, 24, 33]$  MHz, but whose orientations differ.<sup>8</sup> To begin this investigation, we examined how the hyperfine coupling to the two hydrides influence the EPR spectrum of  $E_4(4H)$  of  $\alpha$ -70<sup>Val→Ile</sup> MoFe protein. **Figure 6-5A** presents CW X-band EPR spectra of this intermediate prepared in H<sub>2</sub>O and D<sub>2</sub>O buffers, along with expansion of the  $g_1$  and  $g_3$  regions of the spectra plus simulations that incorporate the ENDOR-derived hyperfine couplings to the hydrides/deuterides (the accompanying protons have only small couplings and do not significantly contribute). The difference in breadth of the  $g_1$  feature in H<sub>2</sub>O and D<sub>2</sub>O buffers is well-captured by the simulated <sup>1</sup>H hyperfine broadening from the two hydrides, as calculated using the ENDOR-derived couplings. In particular, at  $g_3$ , the EPR spectrum of the intermediate in H<sub>2</sub>O buffer even shows the 1-2-1 pattern arising from comparable couplings to the two <sup>1</sup>H hydrides, and this too is reproduced by the simulation. The loss of this pattern in D<sub>2</sub>O buffer definitively confirms its identification with coupling to the two hydrides.

The EPR spectrum of the WT  $g_1 = 2.15$  species in H<sub>2</sub>O buffer has the same breadth at  $g_1 = 2.15$  as that of  $E_4(4H)$  of  $\alpha$ -70<sup>Val→Ile</sup>, and shows the same narrowing in D<sub>2</sub>O. At  $g_3$  the signals from residual Fe<sup>red</sup> and  $E_4(2N2H)$  largely obscure the  $g_1 = 2.15$  intermediate signal for the WT enzyme, but the spectrum in H<sub>2</sub>O buffer nonetheless shows clear evidence for the same 1-2-1 hyperfine-coupling pattern from two [Fe-H-Fe] hydrides as seen for the  $\alpha$ -70<sup>Val→Ile</sup> variant, a feature that is lost in D<sub>2</sub>O buffer as with the

$\alpha$ -70<sup>Val→Ile</sup> intermediate. Thus, the WT and  $\alpha$ -70<sup>Val→Ile</sup> enzymes have equivalent hyperfine-coupled hydrides.

Comparison of ENDOR responses from E<sub>4</sub>(4H) in  $\alpha$ -70<sup>Val→Ile</sup> MoFe protein and the  $g_1 = 2.15$  intermediate of WT enzyme confirms the presence of the two bridging hydrides in the WT intermediate. **Figure 6-5B** shows a 2 K Q-band stochastic CW <sup>1</sup>H ENDOR spectrum collected at  $g_2 = 2.01$  for E<sub>4</sub>(4H)  $\alpha$ -70<sup>Val→Ile</sup>/ $\alpha$ -195<sup>His→Gln</sup>.<sup>18</sup> This spectrum is one component of the 2D field-frequency pattern of spectra collected across the EPR envelope used to carry out the ENDOR analysis. In this spectrum, taken at the field of maximum EPR intensity,<sup>8</sup> the strongly-coupled <sup>1</sup>H signals from the two hydrides are completely overlapped, yielding a single composite (structured) doublet whose feature of maximum intensity corresponds to a hyperfine splitting,  $A(^1\text{H}) \sim 24$  MHz.

The population of the  $g_1 = 2.15$  intermediate trapped during turnover of WT enzyme in H<sub>2</sub>O buffer is low, even when enhanced by low P(N<sub>2</sub>), which prevented collection of a satisfactory ENDOR response for strongly-coupled [Fe-<sup>1</sup>H-Fe] protons. However, during turnover of the WT enzyme in D<sub>2</sub>O buffer the intermediate is trapped with a more than two-fold higher population. As a result, we could obtain <sup>2</sup>H ENDOR signals from strongly-coupled [Fe-<sup>2</sup>H-Fe] deuterons. The Q-band <sup>2</sup>H Mims pulsed-ENDOR spectrum at  $g = 2.01$  shows a narrow ‘distant deuteron’ signal centered at the <sup>2</sup>H Larmor frequency (**Figure 6-5B**), but in addition shows a pair of peaks offset from the <sup>2</sup>H Larmor frequency by  $\sim \pm 1.85$  MHz. The identification of this pair as a hyperfine-split doublet with  $A(^2\text{H}) \sim 3.7$  MHz is confirmed by its suppression when the interval,  $\tau$ , in the Mims microwave pulse sequence is chosen appropriately for the hyperfine coupling, in

this case  $A(^2\text{H})\tau \sim 2$ , and by the absence of the signal in a sample prepared in  $\text{H}_2\text{O}$  buffer, **Figure 6-5B.**<sup>19</sup> When scaled by the nuclear g-factors, the coupling for this feature corresponds to a proton coupling of  $A(^1\text{H}) \sim 24$  MHz, the value seen in the  $^1\text{H}$  spectrum from  $\text{E}_4(4\text{H})$   $\alpha\text{-70}^{\text{Val}\rightarrow\text{Ile}}/\alpha\text{-195}^{\text{His}\rightarrow\text{Gln}}$ .

Together, the EPR and ENDOR measurements demonstrate that the WT  $g_1 = 2.15$  intermediate not only has the same g-values as  $\alpha\text{-70}^{\text{Val}\rightarrow\text{Ile}}$   $\text{E}_4(4\text{H})$  (*vide supra*), but also exhibits hyperfine couplings that correspond to the pair of [Fe-H-Fe] bridging hydrides of  $\alpha\text{-70}^{\text{Val}\rightarrow\text{Ile}}$   $\text{E}_4(4\text{H})$ , *thereby establishing that the intermediate in WT MoFe protein corresponds to that in the  $\alpha\text{-70}^{\text{Val}\rightarrow\text{Ile}}$  variant: it is the  $\text{E}_4(4\text{H})$  Janus intermediate of  $\text{N}_2$  reduction by the WT enzyme.*

***Photoinduced re of WT and  $\alpha\text{-70}^{\text{Val}\rightarrow\text{Ile}}$   $\text{E}_4(4\text{H})$  Hydrides; oa of  $\text{H}_2$  by cryoannealing  $\text{E}_4(2\text{H})^*$***

The assignment of the WT  $g_1 = 2.15$  intermediate to  $\text{E}_4(4\text{H})$ , with its two [Fe-H-Fe] bridging hydrides, is confirmed by the behavior of this intermediate under photolysis. We were inspired to take this approach by considering that the photolysis of transition metal dihydride complexes (with mutually *cis* hydride ligands) commonly results in the release of  $\text{H}_2$ ,<sup>20-28</sup> which represents “a typical example of reductive elimination”, while the thermal reverse reaction “is the prototype example of an oxidative addition reaction.”<sup>20</sup> Thus, we tested whether the two bridging hydrides of  $\text{E}_4(4\text{H})$  would behave in this fashion. ENDOR and EPR measurements showed that photolysis of  $\text{E}_4(4\text{H})$   $\alpha\text{-70}^{\text{Val}\rightarrow\text{Ile}}$  at 4 K and above generates a new FeMo-co state, denoted  $\text{E}_4(2\text{H})^*$ , through the

photoinduced *re* of the two bridging hydrides as  $H_2$ . The  $E_4(2H)^*$  thus trapped relaxes to the initial, equilibrium,  $E_4(4H)$  form during cryoannealing of the frozen solid at temperatures above 175 K, where the oxidative addition (*oa*) of the eliminated  $H_2$  by  $E_4(2H)^*$  becomes kinetically allowed. The photolysis quantum yield is temperature invariant at liquid helium temperatures and shows a large kinetic isotope effect,  $KIE \approx 10$ . These observations imply the photoinduced release of  $H_2$  involves a barrier to the combination of the two nascent H atoms and further suggest that  $H_2$  involves nuclear tunneling through that barrier.

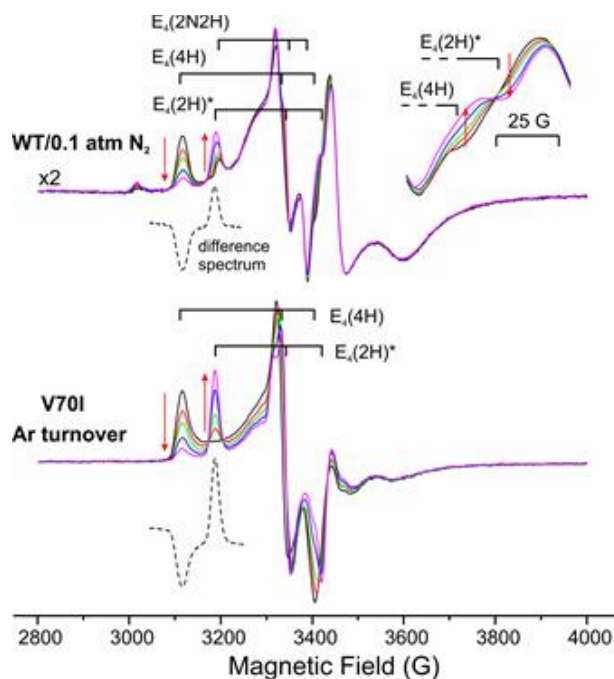


**Figure 6-6:** Photoinduced changes in EPR spectra of WT and  $\alpha$ -70<sup>Val→Ile</sup> freeze-trapped during enzymatic turnover in  $H_2O$  during 24.5 minutes of 450 nm diode laser irradiation at 12 K. EPR conditions: the same as in Figure 6-4.

Figure 6-6 compares EPR signals collected during the *in situ* irradiation by 450

nm light of  $E_4(4H)$   $\alpha$ -70<sup>Val→Ile</sup>, WT  $E_4(4H)$ , and  $E_4(2N2H)$  held at 12 K in an EPR cavity. **Figure 6-7A** plots the time course for the intensity of the EPR signals of these intermediates during the *in situ* photolysis. Irradiation converts  $E_4(4H)$   $\alpha$ -70<sup>Val→Ile</sup> ( $g = [2.15, 2.007, 1.965]$ ) to  $E_4(2H)^*$  ( $g = [2.098, 2.0, 1.956]$ ), **Figure 6-6**. The figure shows that irradiation of WT  $E_4(4H)$  likewise converts this state to an  $E_4(2H)^*$  state with  $g$ -values identical to those in the  $\alpha$ -70<sup>Val→Ile</sup> MoFe variant.

In contrast, the EPR spectra of **Figure 6-6** and progress curves of **Figure 6-7A**, show that the  $E_4(2N2H)$  signal is unaffected by photolysis. That a bound nitrogenous moiety, the  $N_2$ -derived 2N2H moiety of  $E_4(2N2H)$ , is not photodissociable supports the idea that the photosensitivity is associated with the presence of bound hydrides. *The photolysis results thus confirm the presence of the two bridging hydrides in the WT  $g = 2.15$  intermediate, and its identification as  $E_4(4H)$ .*

The progress curves for *in situ* irradiation of  $E_4(4H)$  in WT and  $\alpha$ -70<sup>Val→Ile</sup> MoFe protein (**Figure 6-7A**) are the same, within error, showing that the quantum yield for *re* of  $H_2$  is independent of environment - WT enzyme vs  $\alpha$ -70<sup>Val→Ile</sup> variant. As a result, the *re* progress curves for WT and  $\alpha$ -70<sup>Val→Ile</sup> in  $H_2O$  buffer have been jointly fit to the stretched exponential behavior  $(\exp(-(t/\tau)^m))^{29,30}$  that is a consequence of photolysis in a non-glassy sample,<sup>18</sup> and likewise for those in  $D_2O$  buffer. As reported for photolysis of  $E_4(4H)$   $\alpha$ -70<sup>Val→Ile</sup>, the joint progress curves show a large KIE, defined as the ratio of the median decay times for  $D_2O$  and  $H_2O$  buffers,  $KIE \sim 9$ , which implies that photoinduced *re* of the two hydrides and release of  $H_2$  involves a barrier to the combination of the two nascent H atoms. Likewise, as reported for the  $\alpha$ -70<sup>Val→Ile</sup> intermediate, the decay time for

the WT intermediate is temperature invariant, within error, for  $T = 4\text{--}12\text{ K}$ , which suggests that the formation of  $\text{H}_2$  involves nuclear tunneling through that barrier.<sup>31</sup>

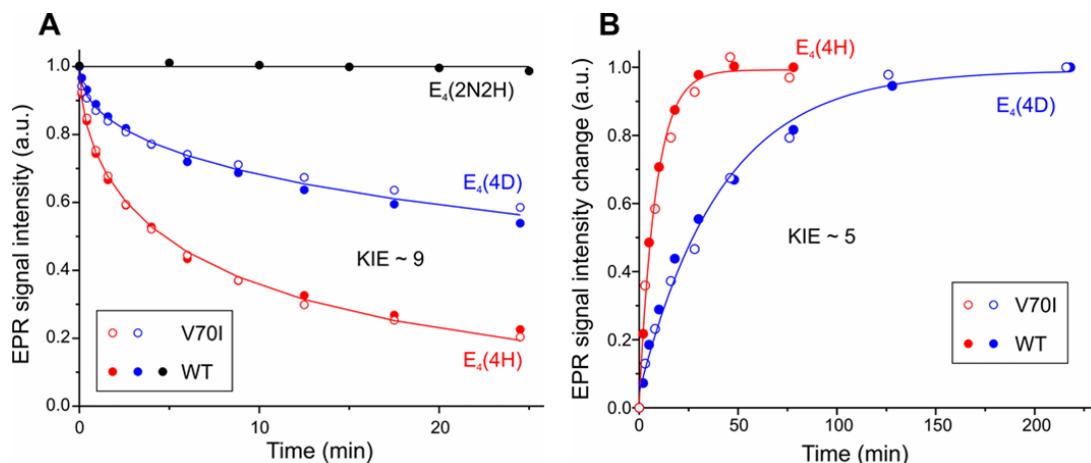


**Figure 6-7: Kinetic isotope effect on photolysis of  $E_4(4H)$  state in WT MoFe protein.** (A) Time courses of  $E_4(4H)$  and  $E_4(4D)$  states in  $\alpha\text{-}70^{\text{Val}\rightarrow\text{Ile}}$  and WT and  $E_4(2N2H)$  in WT 1 atm  $\text{N}_2$  turnover in  $\text{H}_2\text{O}$  during irradiation with 450 nm diode laser at 12 K. Data points in this and following kinetics plots were obtained as described in Materials and Methods; decays of  $E_4(4H)$  and  $E_4(4D)$  are fitted as stretched exponential with following parameters:  $\tau = 9.2\text{ min}$ ,  $m = 0.51$  for  $\text{H}_2\text{O}$  and  $\tau = 83.3\text{ min}$ ,  $m = 0.45$  for  $\text{D}_2\text{O}$ . *EPR conditions:* for this and the following kinetics figures are the same as in **Figure 6-4**. (B) Time courses of  $E_4(4H)/E_4(4D)$  recovery during 193 K annealing of irradiated WT and  $\alpha\text{-}70^{\text{Val}\rightarrow\text{Ile}}$  turnovers in  $\text{H}_2\text{O}/\text{D}_2\text{O}$ . Time constants obtained from exponential fit: 8.4 min ( $\text{H}_2\text{O}$ ) and 41.5 min ( $\text{D}_2\text{O}$ ), KIE  $\sim 5$ .

**Figure 6-7B** plots the timecourse for the *oa* of  $\text{H}_2$  by the  $E_4(2H)^*$  and  $E_4(2D)^*$  to regenerate the corresponding  $E_4(4H)/E_4(4D)$  states during 193 K cryoannealing of WT and  $\alpha\text{-}70^{\text{Val}\rightarrow\text{Ile}}$  MoFe samples.<sup>18</sup> In these experiments the sample is annealed at 193 K multiple times, with cooling for collection of EPR spectra at 12 K between annealing periods. For both  $\text{H}_2\text{O}$  and  $\text{D}_2\text{O}$  buffers the relaxation of  $E_4(2H)^*$  *oa* of  $\text{H}_2$  regenerates the  $E_4(4H)$  state formed during turnover, and the progress curves are well-fitted as a single-exponential processes. As with photoinduced *re*, the progress curves during cryoannealing *oa* are the same for the two MoFe variants, and their joint fit yields KIE  $\sim$



5, rather larger than seen for closed-shell monometallic complexes.<sup>32,33</sup> Combined with a strong temperature dependence of the time-constant (not shown), this KIE implies that *oa* of H<sub>2</sub> involves traversal of an energy barrier. Overall, the measurements of photoinduced, *re* loss of H<sub>2</sub> from E<sub>4</sub>(4H) and thermal regeneration of the E<sub>4</sub>(4H) state via *oa* of H<sub>2</sub> by the resulting E<sub>4</sub>(2H)\* confirm the identification of the WT and α-70<sup>Val→Ile</sup> intermediates as the same Janus, in showing that both the excited and ground state energy surfaces associated with these processes are essentially the same in the WT and variant MoFe proteins.

#### Accumulation of E<sub>4</sub>(4H) Isotopologues During Mixed-Isotope Turnover; Bridging Hydrides are Exchange-Inert

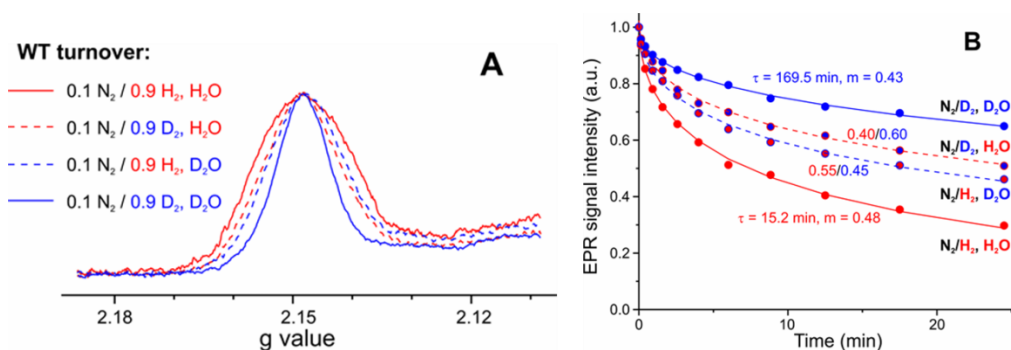


**Figure 6-8: Showing kinetic reversibility of the *re/oa* mechanism in WT MoFe protein (A)** The  $g_1$  features of Janus state EPR recorded for WT protein turnovers trapped under mixtures of 0.1 atm N<sub>2</sub> with 0.9 atm of H<sub>2</sub> or D<sub>2</sub> in H<sub>2</sub>O and D<sub>2</sub>O buffers with stirring. *EPR conditions:* temperature, 12 K; microwave frequency, ~9.36 GHz; microwave power, 10 mW; modulation amplitude, 4.5 G; time constant, 160 ms; field sweep speed, 5 G/s; 4-8 scans. **(B)** Photolysis of WT Janus intermediate formed through isotopically-mixed turnover; irradiation with 450 nm light at 12 K. Progress curves for N<sub>2</sub>/H<sub>2</sub>, H<sub>2</sub>O and N<sub>2</sub>/D<sub>2</sub>, D<sub>2</sub>O are fitted as stretched exponential decays with parameters shown in the figure. Kinetics of other two samples can be well fitted with following parameters:  $\tau = 52.6$  min,  $m = 0.47$  for N<sub>2</sub>/D<sub>2</sub> turnover in H<sub>2</sub>O and  $\tau = 38.3$  min,  $m = 0.46$  for N<sub>2</sub>/H<sub>2</sub> turnover in D<sub>2</sub>O. Dotted lines present alternative fits as sums of two decays corresponding to photolysis of E<sub>4</sub>(4H) in H<sub>2</sub>O and E<sub>4</sub>(4D) in D<sub>2</sub>O turnover samples with ratios shown in the figure.

The kinetic reversibility of the *re/oa* mechanism in WT enzyme, as well as the stability of the bridging hydrides to solvent exchange, as required by *Key Constraint (ii, b)*, **Chart 1**, are here established by the use of EPR and photolysis to measure the isotopic composition of the bridging hydrides in WT Janus trapped during N<sub>2</sub> turnover under isotopically mixed conditions: H<sub>2</sub>O buffer under an atmosphere that include D<sub>2</sub> and conversely, **Figure 6-8**. These measurements show that the *re/oa* mechanism satisfies *Key Constraints, Chart 1*, on catalysis by WT nitrogenase. According to the *re/oa* mechanism, N<sub>2</sub> turnover in H<sub>2</sub>O buffer under D<sub>2</sub> would generate E<sub>4</sub>(4H) through turnover accumulation of reducing equivalents and protons derived from solvent (**Figure 6-1**), but in addition, *oa* of D<sub>2</sub> from the gas phase by E<sub>4</sub>(2N<sub>2</sub>H) would generate E<sub>4</sub>(2D<sup>-</sup>;2H<sup>+</sup>), with two [Fe-D-Fe] bridges and two bound protons, and conversely for turnover in D<sub>2</sub>O buffer under H<sub>2</sub> (**Figure 6-3**). As a result, during N<sub>2</sub> turnover under both mixed-isotope conditions, two isotopologues of Janus are expected to accumulate, one in which the two bridges have the solvent H/D isotope, the other with the two bridges generated through *oa* of the diatomic D<sub>2</sub>/H<sub>2</sub> in the gas phase.<sup>14</sup>

**Figure 6-8A** shows that the  $g_1 = 2.15$  feature from the EPR spectrum of the WT E<sub>4</sub>(4H) intermediate, as trapped in H<sub>2</sub>O buffer during turnover under N<sub>2</sub>/D<sub>2</sub>, is distinctly narrower than for turnover under N<sub>2</sub>/H<sub>2</sub>, thus demonstrating the accumulation of an intermediate in which the reverse of the *re/oa* equilibrium has generated [Fe-D-Fe] bridging deuterides with loss of the <sup>1</sup>H hyperfine broadening (**Figure 6-5A**, above). Conversely the  $g_1 = 2.15$  feature for the WT Janus intermediate in D<sub>2</sub>O buffer is correspondingly broader for turnover under N<sub>2</sub>/H<sub>2</sub> than for turnover under N<sub>2</sub>/D<sub>2</sub>,

demonstrating the accumulation of an intermediate with bridging [Fe-H-Fe], which contribute  $^1\text{H}$  hyperfine broadening. Simulations that sum roughly equal contributions of the limiting spectra for  $\text{E}_4(4\text{H})$  and  $\text{E}_4(4\text{D})$  in fact reproduce the mixed-isotope spectrum quite well (not shown). *Note especially*, that the demonstration that deuterides/hydrides acquired by *oa* of the gas-phase diatomic accumulate in the catalytic intermediate, rather than exchanging with a solvent of opposite isotopic composition, confirms our proposal<sup>6,7</sup> that these bridging hydrides are exchange-inert, and that their formation during *oa* of a gas-phase diatomic explains why turnover under  $\text{N}_2/\text{T}_2$  does not lead to the exchange of  $\text{T}^+$  into the solvent.<sup>2</sup>

The accumulation of mixtures of  $\text{E}_4(4\text{H})$  isotopologues during turnover by *oa* of  $\text{H}_2/\text{D}_2$  under isotopically-mixed conditions is actually seen most dramatically when comparing measurements of the KIE for the photolysis of WT Janus trapped during turnover under  $\text{N}_2$  in isotopically homogeneous conditions –  $\text{H}_2\text{O}$  buffer with addition of 0.9 atm of  $\text{H}_2$ , or  $\text{D}_2\text{O}$  buffer with added  $\text{D}_2$  – with those for isotopically-mixed turnover conditions –  $\text{H}_2\text{O}$  buffer with added  $\text{D}_2$  or  $\text{D}_2\text{O}$  buffer with added  $\text{H}_2$ . As expected, the photolysis traces from isotopically homogeneous intermediates, formed in  $\text{H}_2\text{O}$  buffer with  $\text{N}_2/\text{H}_2$  and in  $\text{D}_2\text{O}$  buffer with  $\text{N}_2/\text{D}_2$ , **Figure 6-8B**, show a large KIE  $\sim 11$ , within error the same as seen for *re* of the two hydrides/deuterides formed in  $\text{H}_2\text{O}/\text{D}_2\text{O}$  buffers without the diatomics in the atmosphere (**Figure 6-7A**).

However, according to the *re/oa* mechanism, *oa* of  $\text{D}_2$  by  $\text{E}_4(2\text{N}2\text{H})$  during turnover in  $\text{H}_2\text{O}$  buffer under  $\text{D}_2$  generates  $\text{E}_4(2\text{D}^-;2\text{H}^+)$ , with two [Fe-D-Fe] bridges and two bound protons, and conversely for turnover in  $\text{D}_2\text{O}$  buffer under  $\text{H}_2$ . To a good

approximation each of these  $E_4(4H)$  mixed isotopologues should undergo photoinduced *re* with quantum yield associated with the isotopic composition of the bridges, as determined by the complementary diatomic (see above), independent of the isotopic character of the protons/deuterons on sulfur, as determined by the solvent. Thus, if the H/D bridges introduced from the diatomic do not exchange with solvent, the intermediates formed in mixed isotope turnover should have apparent rates of photolysis roughly midway between those of  $E_4(4H)$  and  $E_4(4D)$ . Indeed, **Figure 6-8B** shows that the Janus intermediate formed during turnover under  $N_2/D_2$  in  $H_2O$  buffer photolyzes more slowly than with  $N_2/H_2$  in  $H_2O$ , while the intermediate formed under  $N_2/H_2$  in  $D_2O$  buffer photolyzes more rapidly than with  $N_2/D_2$  in  $D_2O$ . The photolysis of these mixed-isotope samples each can be described by time constant roughly midway between those of the two isotopically homogeneous samples (see figure legend). Alternatively, as shown in **Figure 6-8B**, each isotopically mixed trace can be fit as the sum of a roughly  $f \sim 50\%$  contribution from the progress curve for photolysis of  $E_4(4H)$ , with two bridging hydrides, plus a contribution of  $(1-f)$  from the curve for  $E_4(4D)$  with two bridging deuterides.<sup>34</sup>

*These EPR and photochemical observations thus confirm that turnover of WT MoFe protein under  $N_2$  involves a rapidly reversible re/oa equilibrium between the  $E_4$  Janus intermediate and the  $E_4$  state with diazene-level dinitrogen reduction product, **Figure 6-3**. Furthermore, the buildup of  $E_4(2D^-; 2H^+)$  with bridging deuterides during  $N_2/D_2$  turnover in  $H_2O$  buffer, and the converse, confirm that the bridging hydrides/deuterides of the Janus intermediate do not exchange with solvent during*

turnover. Thus, these measurements show that the *re/oa* mechanism indeed satisfies Key Constraints (i), (ii)b,c, **Chart 1**, as proposed.<sup>6,7</sup>

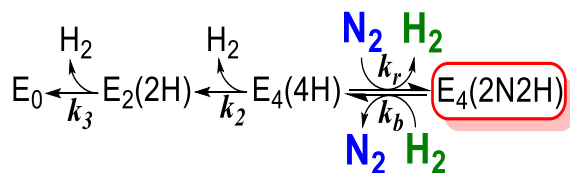
***Kinetic reversibility of the re/oa equilibrium during N<sub>2</sub> reduction by WT MoFe:***

The E<sub>4</sub>(4H) α-70<sup>Val→Ile</sup> intermediate was shown to have accumulated four reducing equivalents by a quench-cryoannealing relaxation protocol corresponding to that described above for the regeneration of E<sub>4</sub>(4H) by *oa* of H<sub>2</sub> to the photogenerated E<sub>4</sub>(2H)\*. Keeping the sample frozen prevents any additional accumulation of reducing equivalents because binding of reduced Fe protein to and release of oxidized protein from the MoFe protein both are abolished in a frozen solid. As recently confirmed,<sup>35</sup> the frozen intermediate can relax towards the resting state only through steps that release a stable species from FeMo-co, with the E<sub>n</sub> states formed prior to N<sub>2</sub> binding losing two equivalents per relaxation step in the release of H<sub>2</sub>. By this approach, E<sub>4</sub>(4H) was identified by its relaxation to the resting state E<sub>0</sub> through the release of a total of four reducing equivalents in a two-step process, each step involving hydride protonation with release of H<sub>2</sub> (two equivalents per step), with formation of E<sub>2</sub>(2H) in the first step (**Figure 6-1**).<sup>10</sup>

As an extension of this procedure, the FeMo-co S = ½ E<sub>4</sub>(2N2H) intermediate trapped during catalytic turnover of WT enzyme was identified by the finding that the decay of this state in a frozen reaction mixture is accelerated by increasing [H<sub>2</sub>] and slowed by increasing [N<sub>2</sub>], which directly demonstrated that the intermediate is the product of the kinetically, as well as thermodynamically reversible (*re/oa*) activation

equilibrium, **Figure 6-3**. However, in that study the  $E_4(4H)$  precursor to *re* was accumulated in such low levels that its kinetic progress curve during cryoannealing could not be monitored directly, and we were forced to analyze the decay of  $E_4(2N2H)$  to resting state, **Chart 3**, through a steady-state approximation for the concentration of  $E_4(4H)$ .

**Chart 3**



The preparation of freeze-quenched WT samples that contain significant populations of both  $E_4(4H)$  and  $E_4(2N2H)$ , obtained through control of  $P(N_2)$  during turnover, has now enabled us to directly monitor the progress curves in WT enzyme of all LT species on the cryoannealing relaxation pathway of  $E_4(2N2H)$  to resting state ( $E_n$  states with  $n \leq 4$ , even), **Chart 3**. In so doing we directly track the kinetics of the species linked through the *oa* reverse, of the *re/oa* equilibrium, **Figure 6-1, 6-3**. These progress curves for the relaxation of  $E_4(2N2H)$  and kinetically linked intermediates (**Chart 3**) during cryoannealing of WT enzyme at  $-50\text{ }^\circ\text{C}$  are presented in **Figure 6-9**. These are well described by the curves calculated by fitting them to the sequential kinetic scheme of **Figure 6-9**, which corresponds to the reverse of the LT scheme starting at  $E_4(2N2H)$ , **Figure 6-1** and **Chart 3**. The fitting procedure allowed for each step to exhibit distributed kinetics, and the time-constants and ‘stretch’ parameters are collected in the legend to **Figure 6-9**. The amplitudes of the kinetic phases correspond to the steady-state

turnover populations of the  $E_n$  states, and of course vary widely depending on  $P(N_2)$  and the electron flux (see **Figure 6-4**). In the sample represented by **Figure 6-9** these correspond to:  $E_0 \sim 8\%$ ;  $E_2 \sim 16\%$ ;  $E_4(4H) \sim 8\%$ ;  $E_4(2N2H) \sim 12\%$ . Thus, in this sample the two states linked by the *re/oa* equilibrium correspond to fully  $\sim 20\%$  of the MoFe protein.

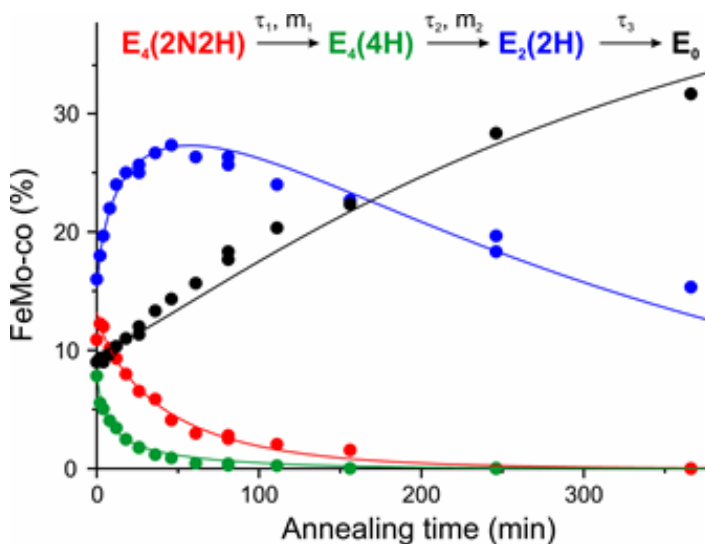


**Figure 6-9: Time courses of four EPR detected states during  $-50\text{ }^\circ\text{C}$  cryoannealing of WT low  $P(N_2) \sim 0.05$  atm turnover in  $H_2O$ .** The data colors correspond to those in the kinetic scheme (*Top*) and the lines correspond to fits to that scheme as previously described.<sup>10</sup> Stretched exponential parameters of the first two fast steps are  $\tau_1 = 43$  min,  $m_1 = 0.79$  and  $\tau_2 = 6$  min,  $m_2 = 0.8$ , the third slow step fitted as exponential with  $\tau_3 = 330$  min. Intensities of  $E_2$  and  $E_0$  states obtained and quantitated with previously described procedures;<sup>15</sup> intensities of  $E_4$  states converted to concentration units by scaling three-step kinetic scheme for corresponding decays. *EPR conditions:* for  $E_4(4H)$  spectra the same as in **Figure 6-4**; for  $E_4(2N2H)$ ,  $E_2$  and  $E_0$  the same as used in previous studies.<sup>15</sup>

*The kinetic coupling of the loss of  $E_4(2N2H)$  through oa of  $H_2$ , with the formation of  $E_4(4H)$  directly establishes the operation of the re/oa mechanism and its kinetic reversibility. The above demonstration that oa of  $D_2$  by  $E_4(2N2H)$  in  $H_2O$  yields  $E_4(2D; 2H^+)$  with exchange-inert deuteride bridges then shows that in this case each of the two*

steps by which this WT mixed-isotope intermediate relaxes to  $E_0$  would involve protonation of the deuteride bridges by protons from solvent, generating 2HD, confirming that the *re/oa* mechanism explains the final Key Constraint (ii a), **Chart 1**, as proposed.<sup>6,7</sup>

**Thermodynamic reversibility of the *re/oa* equilibrium during  $N_2$  reduction by WT MoFe:** The mere observation of both  $E_4(4H)$  and  $E_4(2N2H)$  in samples freeze-quenched during  $N_2$  fixation (**Figure 6-4**) establishes that the equilibrium constant for *re/oa*,  $K_{re} = k_r/k_b$  (**Figure 6-3; Chart 3**), is small. The cryoannealing experiments only give  $k_b$ , not  $k_r$ , but as a rough quantitative estimate of  $K_{re}$ , we assign the relative concentrations of  $E_4(2N2H)$  and  $E_4(4H)$  during turnover under low  $N_2$  partial pressure to the zero-time values determined by the fit to the annealing kinetics (**Figure 6-9**),  $E_4(2N2H)/E_4(4H) \sim 3/2$ , in keeping with the conclusion (*vide supra*) that the forward and reverse steps of the *re/oa* equilibrium are rapid compared to other steps in the catalytic cycle (**Figure 6-1**). In this case we can rewrite **eq 2** to approximate  $K_{re}$  as,

$$K_{re} = \frac{E_4(2N2H)}{E_4(4H)} \cdot \frac{P(H_2)}{P(N_2)} \quad (6-3)$$

The  $N_2$  partial pressure is fixed by the experimental conditions; earlier observations suggest that saturating concentrations of  $H_2$  are formed during turnover under all  $P(N_2)$ , which suggests an effective  $P(H_2) \sim 1\text{atm}$ .<sup>15</sup> As a result, one obtains:

$$K_{re} \sim \left( \sim \frac{3}{2} \right) * \left( \frac{\sim 1}{0.05} \right) \sim 30 \quad (6-4)$$

$$\Delta_{re}G^0 = -RT \ln(K_{re}) \sim -2 \text{ kcal / mol} \quad (6-5)$$



The LT kinetic measurements likewise yielded values for the *re* process:  $K_{re} \sim 0.7$  and  $\Delta_{re}G^0 \sim +0.2$  kcal/mol.<sup>2,4</sup> Given the difference in methodologies – direct observation of species in equilibrium in the present study, analysis of turnover kinetics in the former – and the differences in origin of the MoFe proteins – *Azotobacter vinelandii* in the present study and *Klebsiella pneumoniae* in the former - we consider the measurements to be in excellent agreement: *nitrogenase catalysis, driven by the re of H<sub>2</sub>, turns the highly endothermic first step in the reduction of the N<sub>2</sub> triple bond, (to the diazene level) into the essentially thermoneutral re/oa equilibrium conversion of **Figure 6-3**.*

### Conclusions/Summary

The *re/oa* mechanism for N<sub>2</sub> reduction by nitrogenase postulates that the reduction of the N<sub>2</sub> triple bond to a 2N2H (diazene) level is driven by the obligatory formation of one H<sub>2</sub> for each N<sub>2</sub> reduced. This proposal was based on identification of a FeMo-co  $S = 1/2$  state trapped during turnover of the  $\alpha$ -70<sup>Val→Ile</sup> MoFe protein as the Janus intermediate: the E<sub>4</sub>(4H) state, which stores four reducing equivalents as two [Fe-H-Fe] bridging hydrides. Once this identification is made, then the LT E<sub>4</sub>(4H)↔E<sub>4</sub>(2N2H) equilibrium (**Figure 6-1**) ceases to be a ‘mystery’: the connection with the organometallic chemistry of metal-dihydride complexes identifies this process as the mechanistically coupled reductive elimination (*re*) of H<sub>2</sub> (**Figure 6-3**). The H<sub>2</sub> formed during *re* carries away two of the four reducing equivalents stored in E<sub>4</sub>(4H) and drives the reaction, while the metal-ion core of FeMo-co becomes activated to reduce N<sub>2</sub> through the simultaneous acquisition of two reducing equivalents. The mechanism was first supported by its proposed explanation of the *Key Constraints* of **Chart 1**, and then two new predictions

regarding turnover by WT MoFe were promptly verified,<sup>14,15</sup> adding direct experimental support.

As we now summarize, the present report establishes the presence of Janus in WT enzyme, its participation in N<sub>2</sub> reduction, and the operation of the *re/oa* equilibrium during N<sub>2</sub> reduction. Experiments *on WT enzyme* further show that this mechanism satisfies all the Key Constraints imposed on N<sub>2</sub> reduction by decades of careful study by others summarized in **Chart 1**<sup>2</sup> and that the *re/oa* equilibrium in WT MoFe is indeed kinetically and thermodynamically reversible, thereby establishing the role of the *re/oa* equilibrium in N<sub>2</sub> reduction (**Figure 6-3**).<sup>6,7</sup>

(i) EPR/ENDOR, and photophysical measurements establish that the intermediate with  $g_1 = 2.15$  trapped during nitrogen fixation by WT MoFe in fact is the E<sub>4</sub>(4H) Janus intermediate of N<sub>2</sub> reduction, which has accumulated four reducing equivalents stored as [Fe-H-Fe] bridging hydrides, whose properties are identical to those of the Janus intermediate first trapped in the  $\alpha$ -70<sup>Val→Ile</sup> MoFe variant. This observation thereby establishes the freeze-trapped  $\alpha$ -70<sup>Val→Ile</sup> Janus intermediate as a reliable guide to mechanism, *but most importantly, enables direct observation of the participation of the Janus intermediate in N<sub>2</sub> reduction and the re/oa process during catalysis by the WT enzyme. The new findings and conclusions that build on this foundation are summarized next.*

(ii) Examination of the isotopic composition of WT Janus during turnover in H<sub>2</sub>O buffer under D<sub>2</sub> (or D<sub>2</sub>O buffer under H<sub>2</sub>) establishes that *oa* of D<sub>2</sub> from the gas phase by E<sub>4</sub>(2N2H) accumulates E<sub>4</sub>(2D<sup>-</sup>;2H<sup>+</sup>), with two [Fe-D-Fe] bridges and two bound protons

from solvent (or  $E_4(2H^-;2D^+)$ ) (**Figure 6-3**), and that the bridging hydrides/deuterides do not exchange with solvent during turnover. This demonstrates experimentally that the *re/oa* mechanism accounts for the longstanding *Key Constraints* on mechanism, **Chart 1**, (i),(ii)b,c.

(iii) The observation and successful modeling of the entire relaxation pathway of WT enzyme by which  $E_4(2N_2H)$  relaxes to the resting-state,  $E_0$ , including the *oa* of  $H_2$ , to form Janus with release of  $N_2$ , and two subsequent steps of hydride protonation each with release of  $H_2$ , **Figure 6-1**, **eq 6-2**, demonstrates the kinetic reversibility of the *re/oa* equilibrium, **Figure 6-3**, **Chart 3**, and shows that *re/oa* satisfies the last of the *Key Constraints*, (ii)a, in addition to confirming that it satisfies (ii)c.

(iv) An estimate of the free energy for the *re* of  $H_2$  by FeMo-co that has accumulated four reducing equivalents, with reduction of  $N_2$  to generate a  $2N_2H$ -level species (**Figure 6-3**) in WT enzyme, quantifies the thermodynamic reversibility of the first step in the reduction of  $N_2$  by nitrogenase: this reaction is essentially thermoneutral,  $\Delta_{re}G^0 \sim -2$  kCal/M, whereas direct hydrogenation of gas-phase  $N_2$  is highly endergonic.<sup>16</sup>

*In summary, in this report we have described the central mechanistic steps by which the WT nitrogenase carries out one of the most challenging chemical transformations in biology, the reduction of the  $N\equiv N$  triple bond.*

## References

- (1) Smil, V. *Enriching the Earth: Fritz Haber, Carl Bosch, and the Transformation of World Food Production*; MIT Press: Cambridge, MA, 2001.

- (2) Burgess, B. K.; Lowe, D. J. *Chem. Rev.* **1996**, *96*, 2983.
- (3) Thorneley, R. N. F.; Lowe, D. J. *Met. Ions Biol.* **1985**, *7*, 221.
- (4) Wilson, P. E.; Nyborg, A. C.; Watt, G. D. *Biophys. Chem.* **2001**, *91*, 281.
- (5) Simpson, F. B.; Burris, R. H. *Science* **1984**, *224*, 1095.
- (6) Hoffman, B. M.; Lukoyanov, D.; Yang, Z. Y.; Dean, D. R.; Seefeldt, L. C. *Chem. Rev.* **2014**, *114*, 4041.
- (7) Hoffman, B. M.; Lukoyanov, D.; Dean, D. R.; Seefeldt, L. C. *Acc. Chem. Res.* **2013**, *46*, 587.
- (8) Igarashi, R. Y.; Laryukhin, M.; Dos Santos, P. C.; Lee, H. I.; Dean, D. R.; Seefeldt, L. C.; Hoffman, B. M. *J. Am. Chem. Soc.* **2005**, *127*, 6231.
- (9) Lukoyanov, D.; Yang, Z.-Y.; Dean, D. R.; Seefeldt, L. C.; Hoffman, B. M. *J. Am. Chem. Soc.* **2010**, *132*, 2526.
- (10) Lukoyanov, D.; Barney, B. M.; Dean, D. R.; Seefeldt, L. C.; Hoffman, B. M. *Proc. Natl. Acad. Sci. U.S.A* **2007**, *104*, 1451.
- (11) Hartwig, J. *Organotransition metal chemistry: from bonding to catalysis*; University Science Books: Sausalito, CA, 2010.
- (12) Crabtree, R. H. *The organometallic chemistry of the transition metals*; 5th ed.; Wiley: Hoboken, N.J., 2009.
- (13) Peruzzini, M.; Poli, R.; Editors *Recent Advances in Hydride Chemistry*; Elsevier Science B.V.: Amsterdam, Netherlands, 2001.
- (14) Yang, Z.-Y.; Khadka, N.; Lukoyanov, D.; Hoffman B. M.; Dean D. R.; Seefeldt L. C. *Proc. Natl. Acad. Sci. U.S.A* **2013**, *110*, 16327.

- (15) Lukoyanov, D.; Yang, Z. Y.; Khadka, N.; Dean, D. R.; Seefeldt, L. C.; Hoffman, B. M. *J. Am. Chem. Soc.* **2015**, *137*, 3610.
- (16)  $\Delta_r G^0[\text{H}_2(\text{g}) + \text{XY}(\text{g}) \rightarrow \text{H}_2\text{XY}(\text{g})]$ ;  $\text{N}_2$ ,  $\sim +50$  kCal/mol;  $\text{CO}$ ,  $\sim +4$  kCal/mol
- (17) Christiansen, J.; Goodwin, P. J.; Lanzilotta, W. N.; Seefeldt, L. C.; Dean, D. R. *Biochemistry* **1998**, *37*, 12611.
- (18) Lukoyanov, D.; Khadka, N.; Yang, Z. Y.; Dean, D. R.; Seefeldt, L. C.; Hoffman, B. M. *J. Am. Chem. Soc.* **2016**, *138*, 1320.
- (19) Schweiger, A.; Jeschke, G. *Principles of Pulse Electron Paramagnetic Resonance*; Oxford University Press: Oxford, UK, 2001.
- (20) Perutz, R. N. *Pure Appl. Chem.* **1998**, *70*, 2211.
- (21) Colombo, M.; George, M. W.; Moore, J. N.; Pattison, D. I.; Perutz, R. N.; Virrels, I. G.; Ye, T. Q. *J. Chem. Soc., Dalton Trans.* **1997**, 2857.
- (22) Whittlesey, M. K.; Mawby, R. J.; Osman, R.; Perutz, R. N.; Field, L. D.; Wilkinson, M. P.; George, M. W. *J. Am. Chem. Soc.* **1993**, *115*, 8627.
- (23) Ballmann, J.; Munha, R. F.; Fryzuk, M. D. *Chem. Commun.* **2010**, *46*, 1013.
- (24) Ozin, G. A.; Mccaffrey, J. G. *J. Phys. Chem.* **1984**, *88*, 645.
- (25) Dugan, T. R.; Holland, P. L. *J. Organomet. Chem.* **2009**, *694*, 2825.
- (26) Yu, Y.; Smith, J. M.; Flaschenriem, C. J.; Holland, P. L. *Inorg. Chem.* **2006**, *45*, 5742.
- (27) Smith, J. M.; Sadique, A. R.; Cundari, T. R.; Rodgers, K. R.; Lukat-

Rodgers, G.; Lachicotte, R. J.; Flaschenriem, C. J.; Vela, J.; Holland, P. L.  
*J. Am. Chem. Soc.* **2006**, *128*, 756.

- (28) Yu, Y.; Sadique, A. R.; Smith, J. M.; Dugan, T. R.; Cowley, R. E.;  
Brennessel, W. W.; Flaschenriem, C. J.; Bill, E.; Cundari, T. R.; Holland,  
P. L. *J. Am. Chem. Soc.* **2008**, *130*, 6624.
- (29) Phillips, J. C. *Rep. Prog. Phys.* **1996**, *59*, 1133.
- (30) Berberan-Santos, M. N.; Bodunov, E. N.; Valeur, B. *Chem. Phys.* **2005**,  
*315*, 171.
- (31) Work in progress suggests the process involves initial formation of an H<sub>2</sub>  
complex.
- (32) Abu-Hasanayn, F.; Goldman, A. S.; Krogh-Jespersen, K. *J. Phys. Chem.*  
**1993**, *97*, 5890.
- (33) Campian, M. V.; Perutz, R. N.; Procacci, B.; Thatcher, R. J.; Torres, O.;  
Whitwood, A. C. *J. Am. Chem. Soc.* **2012**, *134*, 3480.
- (34) We are aware that this partitioning is simplified in that it does not consider  
other isotopologues that may be formed during steady-state turnover.
- (35) Lukoyanov, D.; Yang, Z. Y.; Duval, S.; Danyal, K.; Dean, D. R.; Seefeldt,  
L. C.; Hoffman, B. M. *Inorg. Chem.* **2014**, *53*, 3688.

## CHAPTER 7

### SUMMARY AND FUTURE DIRECTION

The researches presented in this dissertation address some of the fundamentals associated with the delivery of electrons and protons to the FeMo-cofactor of nitrogenase and how these accumulated electrons and protons are used through variety of mechanisms for the reduction of dinitrogen ( $N_2$ ) and carbon dioxide ( $CO_2$ ).<sup>1-4</sup> The major findings from these researches are summarized as follows:

#### **Chapter 2**

- The addition of each electron to the FeMo-cofactor is associated with a concerted proton transfer and the two events are indistinguishable even at 77 K.
- The FeMo-cofactor undergoes the conformational change after the addition of two electrons and protons that leads to the formation of an iron hydride (Fe-H) bond.

#### **Chapter 3**

- Formate is the major product formed by hydride transfer mechanism during the reduction of carbon dioxide by nitrogenase.
- Carbon monoxide, on the other hand, is formed through a less favorable mechanism called as an associative pathway that involves the deprotonation of metal hydride.
- Metal hydride of nitrogenase preferentially reacts as a hydride species but can also act as a source of proton.

#### **Chapter 4**

- Formate is an end product while carbon monoxide can accept further electrons

and protons to form methane.

- Stabilization of formyl intermediate is the key for the reduction of carbon dioxide to methane.
- Nitrogenase uses different mechanisms to activate varieties of carbon containing substrates but ultimately funnels the reduced intermediates into a common pathway.

### **Chapter 5**

- Photons ( $\lambda=450$  nm) activate dihydride on the FeMo-cofactor to undergo reductive elimination.
- During reductive elimination, one or both of the hydrides has to overcome an activation barrier as revealed by a strong kinetic isotope effect.
- The activated state generated after the photolysis can be reversed back to the dihydride state with 100% efficiency through an oxidative addition mechanism.

### **Chapter 6**

- Amino acids substitution around the FeMo-cofactor does not alter the photochemical properties of the dihydride state.
- Nitrogenase activates and cleaves the N-N triple bond of the dinitrogen molecule through a kinetically and thermodynamically reversible reductive elimination/oxidative addition mechanism.

Based on these findings, it is obvious that metal hydrides are crucial to the nitrogenase catalysis. Understanding how the metal hydride on the FeMo-cofactor react with the substrate and what factors modulates its reactivity are fundamental not only to



gain insights into the nitrogenase catalysis at molecular detail but also in rational designing of an ideal catalyst that can efficiently function for varieties of substrate reduction, including dinitrogen and carbon dioxide. In this regards, several studies are under progress which would serve which will be discussed here as guidelines for future work.

### Probing the reactivity of metal hydride

The major obstacle in probing the reactivity of metal hydride under different chemical environments introduced by amino acid substitution around the FeMo-cofactor is the Fe protein cycle. The release of phosphate during dissociation of Fe protein from MoFe protein governs the rate of overall catalysis and hence any chemical or physical perturbation introduced in the system to probe the reactivity of metal hydride is obscured by the Fe protein cycle.<sup>3</sup>

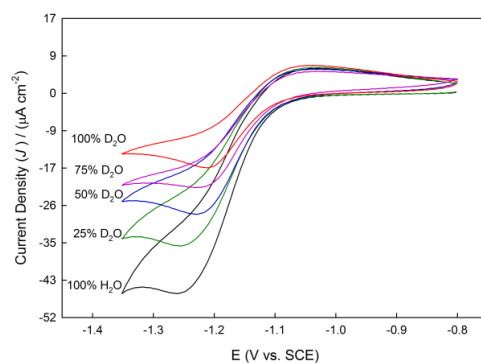


**Figure 7-1: Cyclic voltammetry (CV) for WT MoFe protein.** CV for WT MoFe protein was collected using cobaltocene as an electron mediator. The magnitude of current decreased with increasing the mole fraction of D<sub>2</sub>O. The ratio of current in H<sub>2</sub>O vs. D<sub>2</sub>O at -1.25 V gave a normal solvent isotope effect of ~2.2. No isotope effect was observed by the reduction of cobaltocene only. Condition:- 250 mM HEPES pH=7.4 (or pD=7.4), 667 μM Cc<sup>+</sup> and scan rate of 2 mV/s.

To overcome this challenges and reveal the substrate reduction occurring at the active site as the rate limiting step, delivering the electrons to the FeMo-cofactor through photo excitation or electrode might be a feasible strategy.<sup>4-6</sup> Our preliminary experiments with mediated electrocatalysis demonstrate that the solvent kinetic isotope effect observed on H<sub>2</sub> formation (H<sub>2</sub>O vs. D<sub>2</sub>O) by nitrogenase confirms that under this condition the substrate reduction is the rate limiting step (**Figure 7-1**).<sup>5</sup> In addition, the linearity of proton inventory curves for variants of MoFe protein further insights into the single proton transfer being involved in the rate limiting step (**Figure 7-2**).

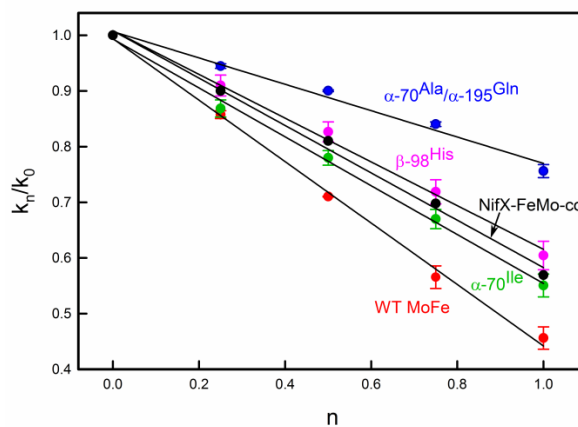


**Figure 7-2: Proton Inventory for WT (Red), β-98<sup>His</sup> (Magenta), α-70<sup>Ile</sup> (Green), α-70<sup>Ala</sup>/α-195<sup>Gln</sup> (Blue) MoFe protein and *nifX*-FeMo-co (Black).** X axis represents mole fraction of D<sub>2</sub>O while Y axis represent the ratio of current at n<sup>th</sup> fraction of D<sub>2</sub>O to current at 0 % D<sub>2</sub>O (i.e. Pure H<sub>2</sub>O). The black lines are fit to the equation defined as  $k_n/k_0 = 1 + n - nq$  where n represent mole fraction of D<sub>2</sub>O and q is the inverse of KIE obtained for each catalyst. A linear fit for all the catalyst tested suggest that (i) a single H transfer is involved in the transition state of the rate limiting step (ii) the mechanism remains unchanged for all the catalyst and (iii) amino acids around FeMo-co electronically couples to modulates the reactivity.

In our previous study we have established that the flow of current in these experiments corresponds to the steady state rate of H<sub>2</sub> formation.<sup>5</sup> In addition,

annealing/EPR and the quantum mechanical calculation (Chapter 3) have shown that protonolysis of metal hydride is the most likely mechanism for the formation of H<sub>2</sub> during nitrogenase catalysis.<sup>7,8</sup> Hence, the data shown in **Figure 7-2** that corresponds to a single proton transfer in the transition state of the rate determining step is consistent with the breakage of Fe-H bond as the rate limiting step during the hydride protonolysis. However, the same data can also be envisioned as the kinetic isotope effect on proton coupled electron transfer.

Therefore, the future direction for this research area is to determine the origin of kinetic isotope effect. This is achieved by monitoring if any kinetic isotope effect exists in the transfer of electron from the cobaltocene to the MoFe protein, most likely using UV-Vis spectroscopy. If there is no kinetic isotope effect on the proton coupled electron transfer then the breakage of Fe-H is solely the rate determining step and the difference in the magnitude of KIE must therefore reflect the strength of iron hydride bond i.e., the observed KIE is proportional to the amount of energy needed to break Fe-H bond. Hence, if breakage of iron hydride is the rate limiting step than monitoring the KIE using this strategy on different variants of MoFe protein provides a direct measurement to probe the modulation of reactivity of iron hydride bond with the change in the chemical environment. Also, this technique allows comparing the reactivity of hydride among different types of nitrogenase (FeFe, VFe and MoFe). Recent studies have already demonstrated that, unlike MoFe protein, VFe protein shows higher catalytic efficiency toward CO/CO<sub>2</sub> reduction but relatively less efficient for N<sub>2</sub> reduction.<sup>9-11</sup> We hypothesize that the difference in the catalytic selectivity of different nitrogenase is the

function of the reactivity of iron hydride on their respective active site. Hence, this research would provide the molecular details on nitrogenase catalysis by directly probing the reactivity of metal hydride.

### **Mechanism of CO<sub>2</sub> reduction**

As discussed in Chapter 3 and 4, quantum calculations suggest that carbon dioxide is reduced to carbon monoxide and formate by two different mechanisms, namely the associative pathway and the direct hydride transfer respectively. However, there are no experimental data to validate these theoretical predictions. One of the strategies is to trap the intermediates during steady state turnover and characterize the trapped intermediates using various advanced spectroscopic techniques. Such a strategy has proven extremely successful in elucidating the mechanism of N<sub>2</sub> reduction by nitrogenase. Therefore, as a future direction to understand the mechanism of carbon dioxide reduction by nitrogenase, it is essential to trap and characterize the intermediates along the reaction pathway. This may be achieved by freeze-quench technique in which variants of MoFe protein are turnover under carbon dioxide atmosphere at different conditions (change in pH, substrate concentration, temperature, and Fe protein concentration) and rapidly freezing the samples at liquid nitrogen temperature. If any paramagnetic species is trapped, advanced spectroscopy techniques like ENDOR or ESEEM can be used to characterize the chemical identity of the trapped intermediate.

Establishing the kinetics of carbon dioxide binding, activation and reduction by nitrogenase is another critical aspect of the mechanism. Carbon dioxide is a symmetrically linear molecule but due to the asymmetric C=O stretching and C=O

bending mode, it is active in infrared (IR) spectroscopy.<sup>12</sup> Hence, monitoring the time resolved IR spectrum using Stop-Flow IR instrument, the kinetics of different steps involved in carbon dioxide binding, activation and reduction to either carbon monoxide or formate can be established. In addition, the change in the kinetics with amino acid substitution around the FeMo-cofactor or using different nitrogenase (FeFe or VFe) would further insight into the role of the amino acid or the heterometal on the carbon dioxide reduction by nitrogenase. Finally, the involvement of metal hydride or the proton transfer in any step of carbon dioxide reduction can also be probed by measuring the solvent kinetic isotope effect ( $\text{H}_2\text{O}$  vs.  $\text{D}_2\text{O}$ ) on the formation or the decay of IR active species. All these information are valuable to establish or refine the mechanism proposed in Chapter 3 and 4.

Also, mentioned in Chapter 3 and 4, nitrogenase is the only single enzyme that reduces carbon dioxide to three different products (carbon monoxide, formate and methane). Formate is water soluble, non-toxic, source of energy, and starting material for various synthesis and hence there is a considerable interest in designing a catalyst that reduces carbon dioxide to formate.<sup>13</sup> In literature, several molecular catalysts are reported that are kinetically able to catalyze carbon dioxide to formate but the thermodynamics for these reactions are generally favored in the reverse direction.<sup>14</sup> This prevents efficient conversion of carbon dioxide to formate. Interestingly, the reduction of carbon dioxide to formate by molybdenum nitrogenase is an irreversible process as required for an ideal catalyst but this process suffers from a lower catalytic selectivity. On the other hand, there is no information on vanadium or iron-iron nitrogenase on their efficiency and

catalytic selectivity for carbon dioxide reduction to formate. Hence, as a future direction for this research, the catalytic selectivity of all three nitrogenase toward formate formation should be measured. This information not only translates in designing of an efficient catalyst for carbon dioxide reduction to formate but also helps in understanding the reactivity of metal hydride formed on the cofactor of different nitrogenase.

Finally, applying the established mechanistic knowledge to tune the catalytic selectivity of nitrogenase toward formate would be another future direction for this research area. Nitrogenase reduces carbon dioxide to both formate and carbon monoxide. However, due to high affinity of carbon monoxide for the reduced FeMo-cofactor, it acts as a potent inhibitor for the reduction of carbon dioxide to formate. This is evident by a strong inhibition of formate formation in presence of externally added CO at a relatively low concentration (**Figure 7-3**).

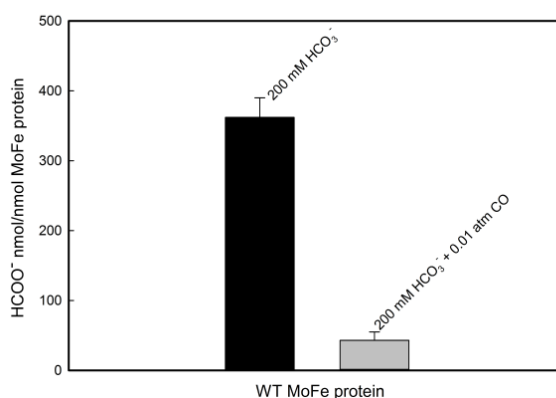


**Figure 7-3: Inhibition of CO<sub>2</sub> reduction to HCOO<sup>-</sup> in presence of CO.** The formation of HCOO<sup>-</sup> is significantly inhibited when the WT MoFe protein is turnover in presence of 200 mM HCO<sub>3</sub><sup>-</sup> with 1% CO atmosphere relative to Argon atmosphere. Condition: 1 mg MoFe protein, 1 mg Fe protein, 200 mM HCO<sub>3</sub><sup>-</sup>, +/- CO, and 60 min. reaction time.

We, therefore, hypothesize that inhibition of carbon monoxide formation during

carbon dioxide reduction should favor formate formation. To gain the preliminary result, we explored one of the critical aspects of CO formation i.e., the electrostatic stabilization of the high energy transition state by  $\alpha$ -96<sup>Arg</sup> residue as explained in Chapter 3. As predicted, the substitution of  $\alpha$ -96<sup>Arg</sup> by His resulted in the MoFe protein that did not catalyze any CO formation and diverted about 50% of total electron flux toward  $\text{HCOO}^-$  formation (Figure 7-4).

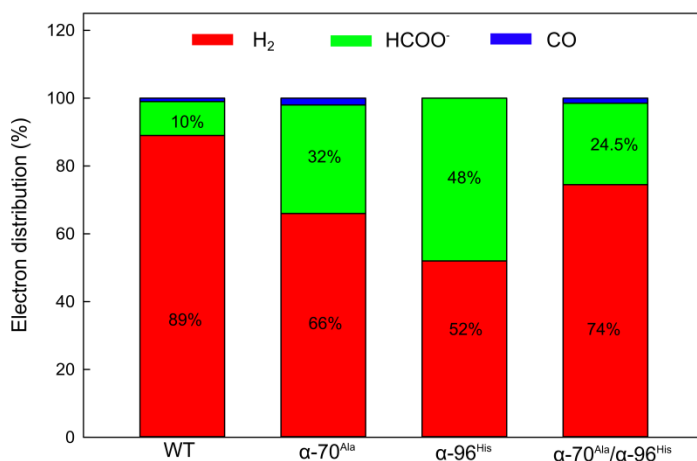


**Figure 7-4: Showing electron distribution during CO<sub>2</sub> reduction by different variants of MoFe protein.** Lack of CO formation in  $\alpha$ -96<sup>His</sup> MoFe protein favors high electron distribution toward HCOO<sup>-</sup>. As controls, data with  $\alpha$ -70<sup>Ala</sup> and  $\alpha$ -70<sup>Ala</sup>/ $\alpha$ -96<sup>His</sup> MoFe proteins are also shown. Similar to  $\alpha$ -96<sup>His</sup> MoFe protein, both these variants increases substrate accessibility to the active site but less electrons are diverted toward HCOO<sup>-</sup> as both variants makes CO. Conditions: 1 mg MoFe protein, 1 mg Fe protein, 200 mM HCO<sub>3</sub><sup>-</sup>, and 60 min. reaction time.

However, the quantum mechanical calculations predict that if the steric hindrance around active site of nitrogenase is relieved, there is no barrier for the formation of formate. This means that it is thermodynamically possible to transfer 100% of electrons toward formate. One of the barriers might be the energy required for the transport of the carbon dioxide from solvent to the FeMo-cofactor. Such barrier have previously been

demonstrated for the transport of  $N_2$  to the FeMo-cofactor.<sup>15</sup> Similar computational studies should be carried out for the transport of carbon dioxide to the active site. Such studies will provide a guide to make appropriate amino acid substitutions around the substrate channel that ultimately enhances the catalytic selectivity of nitrogenase toward formate formation.

### **Mechanism of $N_2$ reduction**

On Chapter 5 and 6, we established that nitrogenase is activated for  $N_2$  activation and reduction through a kinetically and thermodynamically reversible oxidative addition/reductive elimination mechanism.<sup>16</sup> During these studies, we are able to photolyze the trapped dihydride intermediate and thus generate one of the key states of the FeMo-cofactor known as *S* state. Ongoing computational studies have shown that the *S* state is thermodynamically favorable to bind  $N_2$  and promptly hydrogenate it to the diazene level intermediate. Therefore, it is essential to accumulate atomic level information on *S* state to understand nitrogenase catalysis. ENDOR ( $^{57}\text{Fe}/^{95}\text{Mo}$ ) complemented with Mössbauer spectroscopic ( $^{57}\text{Fe}$ ) studies on the *S* state generated on  $^{57}\text{Fe}$  or  $^{95}\text{Mo}$  enriched  $\alpha$ -70<sup>lle</sup> MoFe protein would be ideal to understand the electronic of the FeMo-cofactor. In addition, Mo and Fe EXAFS on the *S* state would further insight if any conformational distortion has occurred within FeMo-cofactor before and after the reductive elimination of dihydride.

ENDOR studies on the trapped dihydride intermediate have suggested that the two dihydride are on bridging geometry. However, ENDOR data were collected at very low temperature (4-12 K). Ongoing computational studies show that there is a very low



energy barrier for the transition of bridging hydride to terminal and therefore it is rational to imagine that the dihydrides might be fluctuating through different conformations at the room temperature. Our preliminary data collected through Nuclear Resonance Vibrational Spectroscopy (NRVS) at 60 K have already hinted two different conformations of dihydride; one being terminal and other bridging. A future direction for this study would be to simulate the vibrational spectrum using quantum mechanical calculations and match with the experimental data followed by complementing it through  $^1\text{H}/^2\text{H}$  ENDOR study on dihydride intermediate at 60 K.

## References

- (1) Davydov, R.; Khadka, N.; Yang, Z.-Y.; Fielding, A. J.; Lukoyanov, D.; Dean, D. R.; Seefeldt, L. C.; Hoffman, B. M. *Isr. J. Chem.* **2016**, *56* (9–10), 841–851.
- (2) Khadka, N.; Dean, D. R.; Smith, D.; Hoffman, B. M.; Raugei, S.; Seefeldt, L. C. *Inorg. Chem.* **2016**, *55* (17), 8321–8330.
- (3) Yang, Z.-Y.; Ledbetter, R.; Shaw, S.; Pence, N.; Tokmina-Lukaszewska, M.; Eilers, B.; Guo, Q.; Pokhrel, N.; Cash, V. L.; Dean, D. R.; Antony, E.; Bothner, B.; Peters, J. W.; Seefeldt, L. C. *Biochemistry* **2016**, *55* (26), 3625–3635.
- (4) Brown, K. A.; Harris, D. F.; Wilker, M. B.; Rasmussen, A.; Khadka, N.; Hamby, H.; Keable, S.; Dukovic, G.; Peters, J. W.; Seefeldt, L. C.; King, P. W. *Science* **2016**, *352* (6284), 448–450.
- (5) Milton, R. D.; Abdellaoui, S.; Khadka, N.; Dean, D. R.; Leech, D.; Seefeldt, L. C.; Minteer, S. D. *Energy Environ. Sci.* **2016**, *9* (8), 2550–2554.
- (6) Paengnakorn, P.; Ash, P. A.; Shaw, S.; Danyal, K.; Chen, T.; Dean, D. R.; Seefeldt,

- L. C.; Vincent, K. A. *Chem. Sci.* **2016**.
- (7) Igarashi, R. Y.; Laryukhin, M.; Dos Santos, P. C.; Lee, H.-I.; Dean, D. R.; Seefeldt, L. C.; Hoffman, B. M. *J. Am. Chem. Soc.* **2005**, *127* (17), 6231–6241.
- (8) Lukoyanov, D.; Barney, B. M.; Dean, D. R.; Seefeldt, L. C.; Hoffman, B. M. *Proc. Natl. Acad. Sci. U.S.A.* **2007**, *104* (5), 1451–1455.
- (9) Lee, C. C.; Hu, Y.; Ribbe, M. W. *Science* **2010**, *329* (5992), 642–642.
- (10) Hu, Y.; Lee, C. C.; Ribbe, M. W. *Science* **2011**, *333* (6043), 753–755.
- (11) Hu, Y.; Lee, C. C.; Ribbe, M. W. *Dalton Trans.* **2012**, *41* (4), 1118–1127.
- (12) Aresta, M.; Dibenedetto, A.; Quaranta, E. In *Reaction Mechanisms in Carbon Dioxide Conversion*; Springer Berlin Heidelberg: Berlin, Heidelberg, 2016; pp 1–34.
- (13) Vo, T.; Purohit, K.; Nguyen, C.; Biggs, B.; Mayoral, S.; Haan, J. L. *ChemSusChem* **2015**, *8* (22), 3853–3858.
- (14) Appel, A. M.; Bercaw, J. E.; Bocarsly, A. B.; Dobbek, H.; DuBois, D. L.; Dupuis, M.; Ferry, J. G.; Fujita, E.; Hille, R.; Kenis, P. J. A.; Kerfeld, C. A.; Morris, R. H.; Peden, C. H. F.; Portis, A. R.; Ragsdale, S. W.; Rauchfuss, T. B.; Reek, J. N. H.; Seefeldt, L. C.; Thauer, R. K.; Waldrop, G. L. *Chem. Rev.* **2013**, *113*, 6621–6658.
- (15) Smith, D.; Danyal, K.; Raugei, S.; Seefeldt, L. C. *Biochemistry* **2014**, *53* (14), 2278–2285.
- (16) Lukoyanov, D.; Yang, Z.-Y.; Khadka, N.; Dean, D. R.; Seefeldt, L. C.; Hoffman, B. M. *J. Am. Chem. Soc.* **2015**, *137* (10), 3610–3615.

**APPENDIX**

**EXPERIMENTAL METHODS**

### Mediated-Electrocatalysis of Nitrogenase

Nitrogenase is O<sub>2</sub> sensitive and hence all the experiments must be performed in an anaerobic environment using Argon filled glove box.

#### **Stocks Preparation**

- Dissolve Poly vinyl amine (PVA) in 250 mM HEPES pH=7.4 to make the stock of 10 mg/mL. Adjust the pH back to 7.4 if there were change in pH.
- Mix ethylene glycol diglycidyl ether (EGDGE) with 250 mM HEPES pH=7.4 to make the stock of 10% (v/v).
- Dilute MoFe protein to 20 mg/mL in 250 mM HEPES pH=7.4.
- Dissolve Bis(cyclopentadienyl) cobalt (II) in 250 mM HEPES pH=7.4 to make final concentration of about 10 mM.

#### **Polishing the Electrode**

- Glassy carbon electrode with 3 mm diameter is used for the experiment.
- The electrode is first rinsed with distilled water then polished using 0.5 micron alumina slurry made in water. Polishing for 30 s to 60 s in “8” fashion is enough. Rinse the electrode again with water to get rid of any adsorbed alumina. At this point, the surface of the glassy carbon should look shinny. If not, repeat the process.

#### **Adsorbing protein on the electrode surface**

- In a 500  $\mu$ L Eppendorf tube add 15  $\mu$ L of PVA (10 mg/mL) followed by 2  $\mu$ L of

EGDGE. Immediately add 15  $\mu\text{L}$  of MoFe Protein (20 mg/mL), mix them well and drop-cast 5  $\mu\text{L}$  of this mixture on each electrode surface. Let the mixture dry on the surface of electrode. Depending on humidity of the glove box, drying process usually takes 1 to 2 hrs.

- EGDGE, a diether, crosslink free amine of PVA and protein while the hydrophobic backbone of PVA adsorbed with glassy carbon surface. Hence, during this process protein is encapsulated in the PVA matrix while the matrix adsorbed physically on the glassy carbon surface.

### **Electrocatalysis**

- Take 3 to 5 mL of 250 mM HEPES pH=7.4 in a 10 mL beaker. HEPES acts as both buffer and electrolyte.
- Dip the Platinum wire or mesh in the buffer and connect it to the counter electrode wire (black wire).
- Also, dip the Saturated Calomel Electrode in the buffer and connect it to the reference electrode (Faint pink wire).
- Dip the electrode in the buffer that has dry protein cast on it and connect it to the working electrode wire (Red wire). Avoid touching of working electrode to the bottom of the beaker. The protein cast swells when dipped in the buffer and slight abrasion can cause the loss of the protein from the PVA matrix. This will decrease the catalytic efficiency.
- Add Bis(cyclopentadienyl) cobalt (II) to an appropriate concentration. Usually, for this system it requires 600  $\mu\text{M}$  of Bis(cyclopentadienyl) cobalt (II) to reach

saturation.

- Add the substrate if needed at this point.
- Turn the potentiostat on.
- Start the Nova 1.1 program. It should now display on bottom left corner that the software is connected with the potentiostat.
- Click on “Setup View” icon. 4<sup>th</sup> on the tool bar.
- Select “cyclic voltammetry (CV) potentiostatic” option. On the right window set the parameter as below:

Set Potential (V) = -0.8

CV Staircase

Start Potential (V) = -0.8

Upper vertex potential (V) = -1.35

Lower Vertex potential (V) = -0.8

Number of stop crossover = 2

Scan rate (V/s) = 0.002

- Click on start bottom (left bottom) to initiate the experiment.
- The data are automatically saved which can be accessed using “Analysis view” icon located on the 7<sup>th</sup> position of the tool bar.

### **Processing data**

- Click on “Analysis view” icon.
- Select the spectrum. The most recent ones are on the bottom of the list.

- Click on “I vs E” option on the middle left box. A plot of Current vs Potential appears on the right window.
- Right click on the spectrum and select “copy data to the clipboard”.
- Open notepad and paste the data. Save the note pad.
- Open Sigma plot. Select “import file” option on left top corner. Select the notepad file to open. Click on open. A new window appears. In this window select “**white spaced**” option and hit enter. The data display in sigma plot with two columns, left being the potential and right being the corresponding current.
- Plot the graph.
- At this point, the current is in its absolute value. However, normally they are represented as current density [ $J / \mu\text{A cm}^{-2}$ ] which can be done by simple mathematical manipulation. The diameter of electrode is 3 mm. Thus, the area of electrode surface is  $.007 \text{ cm}^{-2}$ . Thus factoring out the absolute current by  $.000000704$  changes the absolute current to the current density.

### **Kinetic Isotope effect**

- The CV is taken exactly as described above. First the CV is taken with 2 mL 100% D<sub>2</sub>O with 200 mM HEPES pD=7.4. Then, 100% H<sub>2</sub>O with 200 mM HEPES pH=7.4 is added on successive order to change the mole fraction (n) of D<sub>2</sub>O in the following order, n= 1, .75, .5, .25, and 0. 0 mole fraction of D<sub>2</sub>O means pure H<sub>2</sub>O. During this experiment, the concentration of Bis(cyclopentadienyl) cobalt (II) is kept constant at 667  $\mu\text{M}$ . The ratio of current at -1.25 V in H<sub>2</sub>O vs D<sub>2</sub>O gives the kinetic isotope effect. In addition, the plot of

current at -1.25 V in Y axis with mole fraction of D<sub>2</sub>O in X axis gives a plot that can be fitted to one, two or multiple transfer events. The plot with an appropriate fit is called “proton inventory curve”.

## **Electron Paramagnetic Resonance Spectroscopy**

### **Liquid helium cryostat operation**

1. Two days before the experiment pump the transfer line vacuum (overnight).
2. One day before the experiment pump the cryostat vacuum (overnight).
3. Install the cryostat in the magnet (follow Bruker instruction video).
4. Start nitrogen flow: do not adjust flow – it is already set, just open the main valve – the flow will be minimal. This is just simply to keep the wave guide flushed with nitrogen and to keep it void of moisture (water absorbs microwaves).
5. Fill up the nitrogen Dewar in the back of the magnet for the temperature reference.
6. Turn on the ITC temperature controller.
7. Insert He transfer line into the He transport Dewar.
  - 7.1 Open the black He valve on top of the transfer line. DO NOT CONFUSE IT WITH THE VACUUM VALVE! Put the nut and O-ring onto the transfer line “leg”.
  - 7.2 Open the top valve and start inserting the “leg” Proceed VERY SLOWLY (inserting of the entire length should take about 3-5 minutes).
  - 7.3 Check He flow by inserting of the transfer line tip into the bottle with ethanol



– you should be able to clearly observe bubbles.

8. Carefully insert the transfer line into the cryostat. Do not tighten the screw yet.
9. Connect the white vacuum tube to the transfer line and start the gray membrane (GAST) pump on the floor. It will start pulling helium through cryostat.
10. Helium is now flushing the system. Do not tighten the transfer line connection until the sound of the pump dramatically changes. You should be able now to observe temperature dropping at significant rate.

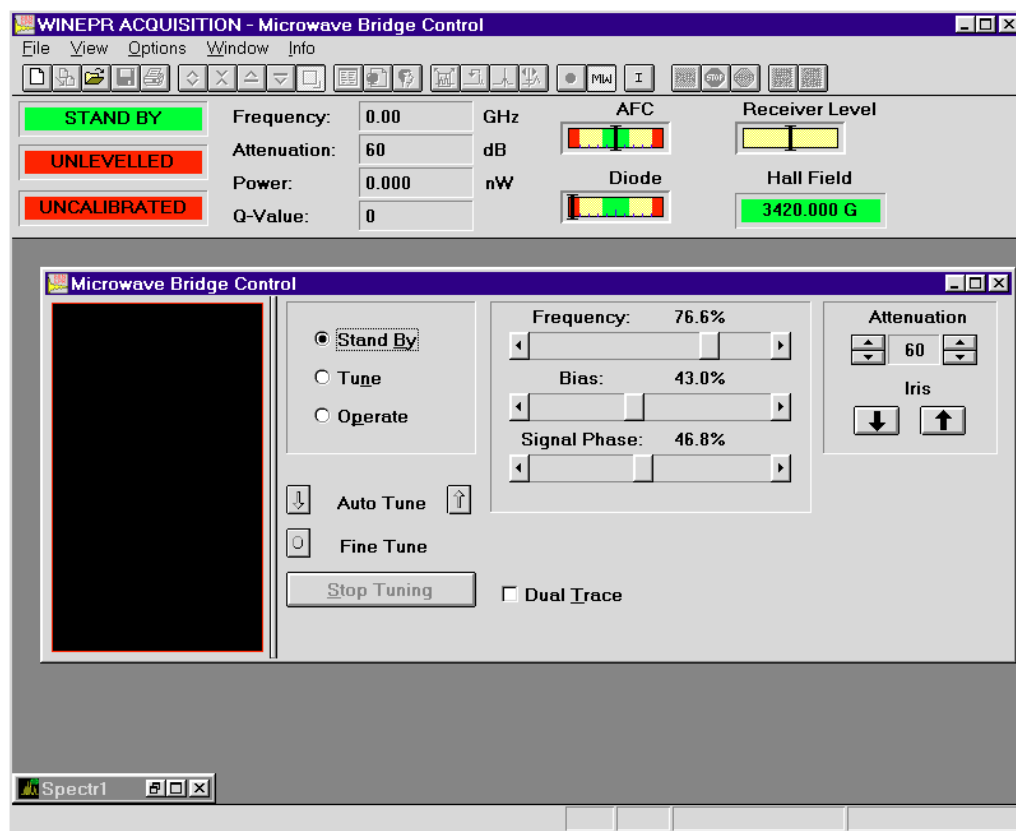
### **Startup and tuning procedure**

1. Turn on water chiller
  - 1.1 Open water valve
  - 1.2 Turn on the chiller pump and make sure that the orange FULL light is lit. If it is not full, open the cover and add distilled water.
2. Turn on the spectrometer
  - 2.1 Turn on the switch on the wall.
  - 2.2 Turn on switches on the back of the spectrometer cabinet and microwave bridge.
  - 2.3 Turn on switches on the front of the cabinet and magnet power supply.
  - 2.4 Start spectrometer control software on the computer. It should be able to communicate with the spectrometer.
3. Open the microwave bridge control dialog box. Click the button labeled MW in the tool bar. The microwave bridge control dialog box will appear (Fig. 1)
4. Switch the microwave bridge to Tune mode. The bridge status indicator shows the

three states for the bridge, Stand By, Tune, and Operate (Fig. 1). The bridge is now in the Stand By mode. Click the Tune button

Figure 1

The Microwave Bridge Control dialog box.



5. Set the microwave attenuator to 25 dB by clicking the arrows on either side of the attenuation display (Fig. 1). The arrows on the left side change the attenuation in 10 dB steps; the arrows on the right side change the attenuation in 1 dB steps.
6. Observe the mode pattern on the display monitor. It should resemble one of the mode tuning patterns in Fig. 2. If the amplitude is too small increase the

microwave power in 1 dB steps by decreasing the attenuation. If it is too large, increase the attenuation in 1 dB steps.

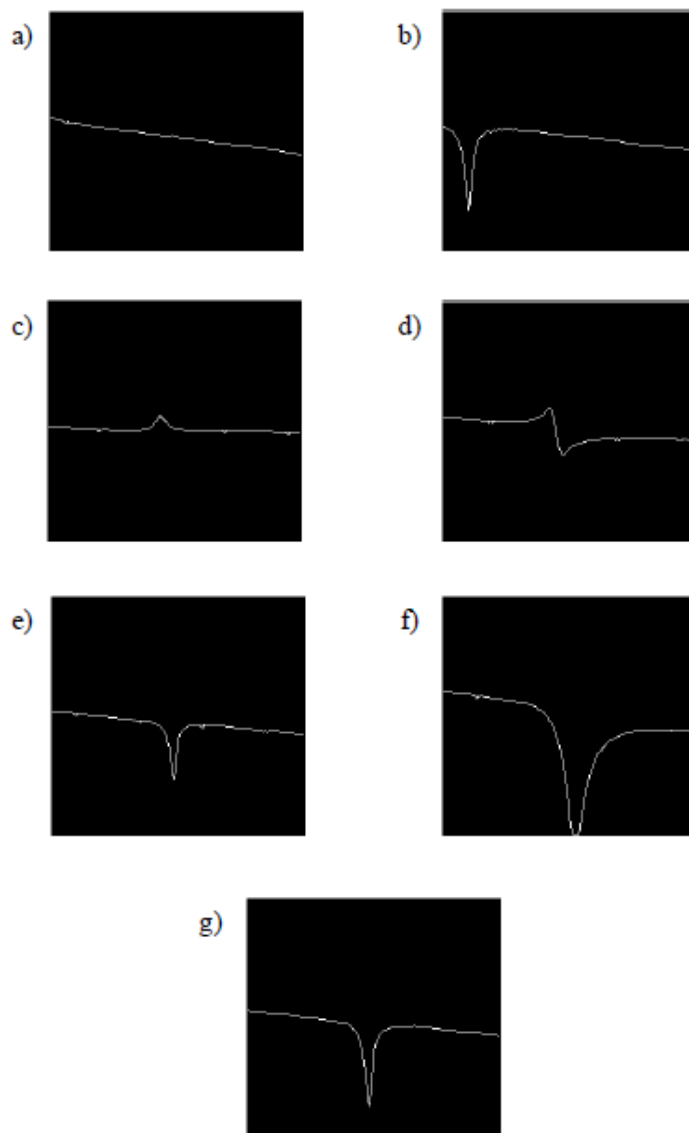


Figure 2

Mode Tuning Patterns for the Microwave Source

- a) off resonance b) slightly off resonance c) on resonance, phase  $180^\circ$  off d) on resonance  $90^\circ$  off e) on resonance, correct phase, undercoupled f) on resonance, correct phase, overcoupled g) on resonance, correct phase, critically coupled.
7. Adjust the Frequency slider bar to locate and center the mode pattern “dip” on the display monitor. By centering the “dip” on the display monitor, the microwave source is set to oscillate at the same frequency as the cavity resonant frequency.
  8. Clean the sample tube to be inserted into the cavity by wiping the outside of the tube with tissue paper. It is vital to avoid contamination of the cavity as paramagnetic contaminants may result in spurious EPR signals or baseline distortions.
  9. Switch to Stand By. Insert the sample tube carefully into the cavity. The tube should be slightly loose before you tighten the collet nut. The bottom of the tube should rest in the indentation on the pedestal or in the sample holder (cryostat operation). Tighten the collet nut to firmly hold the sample tube in place. Switch back to Tune.
  10. Retune the microwave source by repeating the procedure of Step 7. You may notice a shift in the frequency, width, and depth of the cavity “dip” when you insert the sample.
  11. Tune the signal (reference) phase. Adjust the Signal Phase slider bar (Fig. 1) until the depth of the “dip” is maximized and the “dip” looks somewhat symmetric (Fig. 2). The phase will be fine-tuned later.
  12. Click the Operate button in the dialog box. Adjust the Frequency slider bar until

the needle of the AFC meter (Fig. 1) is centered. Sometimes the needle may rush off to the right or left edges of the meter. This happens when the AFC (Automatic Frequency Control) is no longer locked. If this happens, click the Tune button, repeat Step 10, and then try again.

13. Adjust the bias level. Change the microwave attenuation to 50 dB. Adjust the Bias slider bar (Fig. 1), until the Diode meter needle is centered. The center corresponds to 200 microamperes of diode current. Sometimes the AFC meter may rush off either to the right or left and lose lock at 50 dB. In most case, the AFC will lock again at higher power levels. If not, switching between Operate and Tune modes and back again at 30 dB attenuation will lock AFC once more.
14. Match the cavity for maximum sensitivity. If the cavity and waveguide are truly matched (or critically coupled), the reflected microwave power seen by the detector should remain constant (i.e. 0) when we vary the attenuation. This is the criterion we use for critical coupling. The coupling is controlled by adjusting the iris screw. First, increase the microwave power by 10 dB (i.e. attenuator setting 40 dB). Click the ↑ or ↓ iris buttons until the diode current again returns to 200 microamperes. Repeat the procedure (-10 dB steps) until you have reached an attenuator setting of 10 dB. You will notice that as you increase the power, the diode current becomes more sensitive to the position of the iris screw. Another thing you may notice is that the AFC meter also changes with the iris screw position. Simply adjust the frequency slider bar until the needle is centered again. When you have reached 10 dB attenuation, adjust the Signal Phase slider bar until

you achieve a local maximum in the diode current. You should not have to adjust it very much. Verify that you have achieved critical coupling by changing the attenuation from 10 dB to 50 dB with virtually no change in the diode current. Repeat the matching and bias level adjustment procedures if necessary.

**APPENDIX**

## **My Contribution**

### **Chapter 2**

Protein purification, enzyme activity assay, protein solvent exchange (where necessary), EPR and ENDOR samples preparation, and writing manuscript.

All EPR and ENDOR data were collected by Roman Davydov at Northwestern University

### **Chapter 3**

Protein purification, enzyme activity assay, protein solvent exchange (where necessary), designing and executing all experiments, and writing manuscript.

All the computational works were done at Pacific Northwestern National Laboratory (PNNL) by Dayle Smith and Simone Raugei.

### **Chapter 4**

Protein purification, enzyme activity assay, designing and executing all experiments, and writing manuscript.

### **Chapter 5**

Protein purification, enzyme activity assay, protein solvent exchange (where necessary), EPR and ENDOR samples preparation, and writing manuscript.

All EPR and ENDOR data were collected by Dmitriy Lukoyanov at Northwestern University.

### **Chapter 6**

Protein purification, enzyme activity assay, protein solvent exchange (where necessary), EPR and ENDOR samples preparation, and writing manuscript.

All EPR and ENDOR data were collected by Dmitriy Lukoyanov at Northwestern University.



**JOHN WILEY AND SONS LICENSE  
TERMS AND CONDITIONS**

Jan 02, 2017

This Agreement between Nimesh Khadka ("You") and John Wiley and Sons ("John Wiley and Sons") consists of your license details and the terms and conditions provided by John Wiley and Sons and Copyright Clearance Center.

License Number	4020980436679
License date	Jan 02, 2017
Licensed Content Publisher	John Wiley and Sons
Licensed Content Publication	Israel Journal of Chemistry
Licensed Content Title	Exploring Electron/Proton Transfer and Conformational Changes in the Nitrogenase MoFe Protein and FeMo-cofactor Through Cryoreduction/EPR Measurements
Licensed Content Author	Roman Davydov,Nimesh Khadka,Zhi-Yong Yang,Andrew J. Fielding,Dmitriy Lukoyanov,Dennis R. Dean,Lance C. Seefeldt,Brian M. Hoffman
Licensed Content Date	Jul 29, 2016
Licensed Content Pages	11
Type of use	Dissertation/Thesis
Requestor type	Author of this Wiley article
Format	Print and electronic
Portion	Full article
Will you be translating?	No
Title of your thesis / dissertation	Mechanism of substrates reduction by nitrogenase
Expected completion date	Mar 2017
Expected size (number of	250

pages)

Requestor Location Nimesh Khadka  
12 Aggie Village Apt I

LOGAN, UT 84341  
United States  
Attn: Nimesh Khadka

Publisher Tax ID EU826007151

Billing Type Invoice

Billing Address Nimesh Khadka  
12 Aggie Village Apt I

LOGAN, UT 84341  
United States  
Attn: Nimesh Khadka

Total 0.00 USD

Terms and Conditions

#### TERMS AND CONDITIONS

This copyrighted material is owned by or exclusively licensed to John Wiley & Sons, Inc. or one of its group companies (each a "Wiley Company") or handled on behalf of a society with which a Wiley Company has exclusive publishing rights in relation to a particular work (collectively "WILEY"). By clicking "accept" in connection with completing this licensing transaction, you agree that the following terms and conditions apply to this transaction (along with the billing and payment terms and conditions established by the Copyright Clearance Center Inc., ("CCC's Billing and Payment terms and conditions"), at the time that you opened your RightsLink account (these are available at any time at <http://myaccount.copyright.com>).

#### Terms and Conditions

- The materials you have requested permission to reproduce or reuse (the "Wiley Materials") are protected by copyright.
- You are hereby granted a personal, non-exclusive, non-sub licensable (on a stand-alone basis), non-transferable, worldwide, limited license to reproduce the Wiley Materials for the purpose specified in the licensing process. This license, **and any CONTENT (PDF or image file) purchased as part of your order**, is for a one-time use only and limited to any maximum distribution number specified in the license. The first instance of republication or reuse granted by this license must be

completed within two years of the date of the grant of this license (although copies prepared before the end date may be distributed thereafter). The Wiley Materials shall not be used in any other manner or for any other purpose, beyond what is granted in the license. Permission is granted subject to an appropriate acknowledgement given to the author, title of the material/book/journal and the publisher. You shall also duplicate the copyright notice that appears in the Wiley publication in your use of the Wiley Material. Permission is also granted on the understanding that nowhere in the text is a previously published source acknowledged for all or part of this Wiley Material. Any third party content is expressly excluded from this permission.

- With respect to the Wiley Materials, all rights are reserved. Except as expressly granted by the terms of the license, no part of the Wiley Materials may be copied, modified, adapted (except for minor reformatting required by the new Publication), translated, reproduced, transferred or distributed, in any form or by any means, and no derivative works may be made based on the Wiley Materials without the prior permission of the respective copyright owner. **For STM Signatory Publishers clearing permission under the terms of the [STM Permissions Guidelines](#) only, the terms of the license are extended to include subsequent editions and for editions in other languages, provided such editions are for the work as a whole in situ and does not involve the separate exploitation of the permitted figures or extracts**, You may not alter, remove or suppress in any manner any copyright, trademark or other notices displayed by the Wiley Materials. You may not license, rent, sell, loan, lease, pledge, offer as security, transfer or assign the Wiley Materials on a stand-alone basis, or any of the rights granted to you hereunder to any other person.
- The Wiley Materials and all of the intellectual property rights therein shall at all times remain the exclusive property of John Wiley & Sons Inc, the Wiley Companies, or their respective licensors, and your interest therein is only that of having possession of and the right to reproduce the Wiley Materials pursuant to Section 2 herein during the continuance of this Agreement. You agree that you own no right, title or interest in or to the Wiley Materials or any of the intellectual property rights therein. You shall have no rights hereunder other than the license as provided for above in Section 2. No right, license or interest to any trademark, trade name, service mark or other branding ("Marks") of WILEY or its licensors is granted hereunder, and you agree that you shall not assert any such right, license or interest with respect thereto
- NEITHER WILEY NOR ITS LICENSORS MAKES ANY WARRANTY OR REPRESENTATION OF ANY KIND TO YOU OR ANY THIRD PARTY, EXPRESS, IMPLIED OR STATUTORY, WITH RESPECT TO THE MATERIALS OR THE ACCURACY OF ANY INFORMATION CONTAINED IN THE MATERIALS, INCLUDING, WITHOUT LIMITATION, ANY

IMPLIED WARRANTY OF MERCHANTABILITY, ACCURACY, SATISFACTORY QUALITY, FITNESS FOR A PARTICULAR PURPOSE, USABILITY, INTEGRATION OR NON-INFRINGEMENT AND ALL SUCH WARRANTIES ARE HEREBY EXCLUDED BY WILEY AND ITS LICENSORS AND WAIVED BY YOU.

- WILEY shall have the right to terminate this Agreement immediately upon breach of this Agreement by you.
- You shall indemnify, defend and hold harmless WILEY, its Licensors and their respective directors, officers, agents and employees, from and against any actual or threatened claims, demands, causes of action or proceedings arising from any breach of this Agreement by you.
- IN NO EVENT SHALL WILEY OR ITS LICENSORS BE LIABLE TO YOU OR ANY OTHER PARTY OR ANY OTHER PERSON OR ENTITY FOR ANY SPECIAL, CONSEQUENTIAL, INCIDENTAL, INDIRECT, EXEMPLARY OR PUNITIVE DAMAGES, HOWEVER CAUSED, ARISING OUT OF OR IN CONNECTION WITH THE DOWNLOADING, PROVISIONING, VIEWING OR USE OF THE MATERIALS REGARDLESS OF THE FORM OF ACTION, WHETHER FOR BREACH OF CONTRACT, BREACH OF WARRANTY, TORT, NEGLIGENCE, INFRINGEMENT OR OTHERWISE (INCLUDING, WITHOUT LIMITATION, DAMAGES BASED ON LOSS OF PROFITS, DATA, FILES, USE, BUSINESS OPPORTUNITY OR CLAIMS OF THIRD PARTIES), AND WHETHER OR NOT THE PARTY HAS BEEN ADVISED OF THE POSSIBILITY OF SUCH DAMAGES. THIS LIMITATION SHALL APPLY NOTWITHSTANDING ANY FAILURE OF ESSENTIAL PURPOSE OF ANY LIMITED REMEDY PROVIDED HEREIN.
- Should any provision of this Agreement be held by a court of competent jurisdiction to be illegal, invalid, or unenforceable, that provision shall be deemed amended to achieve as nearly as possible the same economic effect as the original provision, and the legality, validity and enforceability of the remaining provisions of this Agreement shall not be affected or impaired thereby.
- The failure of either party to enforce any term or condition of this Agreement shall not constitute a waiver of either party's right to enforce each and every term and condition of this Agreement. No breach under this agreement shall be deemed waived or excused by either party unless such waiver or consent is in writing signed by the party granting such waiver or consent. The waiver by or consent of a party to a breach of any provision of this Agreement shall not operate or be construed as a waiver of or consent to any other or subsequent breach by such other party.
- This Agreement may not be assigned (including by operation of law or otherwise)

by you without WILEY's prior written consent.

- Any fee required for this permission shall be non-refundable after thirty (30) days from receipt by the CCC.
- These terms and conditions together with CCC's Billing and Payment terms and conditions (which are incorporated herein) form the entire agreement between you and WILEY concerning this licensing transaction and (in the absence of fraud) supersedes all prior agreements and representations of the parties, oral or written. This Agreement may not be amended except in writing signed by both parties. This Agreement shall be binding upon and inure to the benefit of the parties' successors, legal representatives, and authorized assigns.
- In the event of any conflict between your obligations established by these terms and conditions and those established by CCC's Billing and Payment terms and conditions, these terms and conditions shall prevail.
- WILEY expressly reserves all rights not specifically granted in the combination of (i) the license details provided by you and accepted in the course of this licensing transaction, (ii) these terms and conditions and (iii) CCC's Billing and Payment terms and conditions.
- This Agreement will be void if the Type of Use, Format, Circulation, or Requestor Type was misrepresented during the licensing process.
- This Agreement shall be governed by and construed in accordance with the laws of the State of New York, USA, without regards to such state's conflict of law rules. Any legal action, suit or proceeding arising out of or relating to these Terms and Conditions or the breach thereof shall be instituted in a court of competent jurisdiction in New York County in the State of New York in the United States of America and each party hereby consents and submits to the personal jurisdiction of such court, waives any objection to venue in such court and consents to service of process by registered or certified mail, return receipt requested, at the last known address of such party.

### **WILEY OPEN ACCESS TERMS AND CONDITIONS**

Wiley Publishes Open Access Articles in fully Open Access Journals and in Subscription journals offering Online Open. Although most of the fully Open Access journals publish open access articles under the terms of the Creative Commons Attribution (CC BY) License only, the subscription journals and a few of the Open Access Journals offer a choice of Creative Commons Licenses. The license type is clearly identified on the article.

#### **The Creative Commons Attribution License**

The [Creative Commons Attribution License \(CC-BY\)](#) allows users to copy, distribute and transmit an article, adapt the article and make commercial use of the article. The CC-BY license permits commercial and non-

**Creative Commons Attribution Non-Commercial License**

The [Creative Commons Attribution Non-Commercial \(CC-BY-NC\)License](#) permits use, distribution and reproduction in any medium, provided the original work is properly cited and is not used for commercial purposes.(see below)

**Creative Commons Attribution-Non-Commercial-NoDerivs License**

The [Creative Commons Attribution Non-Commercial-NoDerivs License](#) (CC-BY-NC-ND) permits use, distribution and reproduction in any medium, provided the original work is properly cited, is not used for commercial purposes and no modifications or adaptations are made. (see below)

**Use by commercial "for-profit" organizations**

Use of Wiley Open Access articles for commercial, promotional, or marketing purposes requires further explicit permission from Wiley and will be subject to a fee.

Further details can be found on Wiley Online

Library <http://olabout.wiley.com/WileyCDA/Section/id-410895.html>

**Other Terms and Conditions:**

**v1.10 Last updated September 2015**

Questions? [customercare@copyright.com](mailto:customercare@copyright.com) or +1-855-239-3415 (toll free in the US) or +1-978-646-2777.

---

---

## American Chemical Society's Policy on Theses and Dissertations

**If your university requires you to obtain permission, you must use the RightsLink permission system. See RightsLink instructions at <http://pubs.acs.org/page/copyright/permissions.html>.**

This is regarding request for permission to include **your** paper(s) or portions of text from **your** paper(s) in your thesis. Permission is now automatically granted; please pay special attention to the **implications** paragraph below. The Copyright Subcommittee of the Joint Board/Council Committees on Publications approved the following:

### Copyright permission for published and submitted material from theses and dissertations

ACS extends blanket permission to students to include in their theses and dissertations their own articles, or portions thereof, that have been published in ACS journals or submitted to ACS journals for publication, provided that the ACS copyright credit line is noted on the appropriate page(s).

### Publishing **implications** of electronic publication of theses and dissertation material

Students and their mentors should be aware that posting of theses and dissertation material on the Web prior to submission of material from that thesis or dissertation to an ACS journal may affect publication in that journal. Whether Web posting is considered prior publication may be evaluated on a case-by-case basis by the journal's editor. If an ACS journal editor considers Web posting to be "prior publication", the paper will not be accepted for publication in that journal. If you intend to submit your unpublished paper to ACS for publication, check with the appropriate editor prior to posting your manuscript electronically.

**Reuse/Republication of the Entire Work in Theses or Collections:** Authors may reuse all or part of the Submitted, Accepted or Published Work in a thesis or dissertation that the author writes and is required to submit to satisfy the criteria of degree-granting institutions. Such reuse is permitted subject to the ACS' "Ethical Guidelines to Publication of Chemical Research" (<http://pubs.acs.org/page/policy/ethics/index.html>); the author should secure written confirmation (via letter or email) from the respective ACS journal editor(s) to avoid potential conflicts with journal prior publication\*/embargo policies. Appropriate citation of the Published Work must be made. If the thesis or dissertation to be published is in electronic format, a direct link to the Published Work must also be included using the ACS Articles on Request author-directed link – see <http://pubs.acs.org/page/policy/articlesonrequest/index.html>

\* Prior publication policies of ACS journals are posted on the ACS website at <http://pubs.acs.org/page/policy/prior/index.html>

If your paper has **not** yet been published by ACS, please print the following credit line on the first page of your article: "Reproduced (or 'Reproduced in part') with permission from [JOURNAL NAME], in press (or 'submitted for publication'). Unpublished work copyright [CURRENT YEAR] American Chemical Society." Include appropriate information.

If your paper has already been published by ACS and you want to include the text or portions of the text in your thesis/dissertation, please print the ACS copyright credit line on the first page of your article: "Reproduced (or 'Reproduced in part') with permission from [FULL REFERENCE CITATION.] Copyright [YEAR] American Chemical Society." Include appropriate information.

**Submission to a Dissertation Distributor:** If you plan to submit your thesis to UMI or to another dissertation distributor, you should not include the unpublished ACS paper in your thesis if the thesis will be disseminated electronically, until ACS has published your paper. After publication of the paper by ACS, you may release the entire thesis (**not the individual ACS article by itself**) for electronic dissemination through the distributor; ACS's copyright credit line should be printed on the first page of the ACS paper.



## CURRICULUM VITAE

**Nimesh Khadka**

Dept. of Chemistry and Biochemistry, Utah State University, 0300 Old Main Hill  
Logan Utah, 84322-0300

Email: nimesh.khadka@aggiemail.usu.edu; Phone: (435) 938-1645

---

**EDUCATION**

**Graduate Student (Biochemistry)** 2011-present  
*Utah State University (Advisor: Prof. Lance C. Seefeldt)*

**B.S., (Biochemistry)** 2004-2008  
*Pokhara University, Kathmandu, Nepal*

**RESEARCH EXPERIENCE**

**Graduate Research** 2012–present  
*Department of Chemistry and Biochemistry, Utah State University, Logan, Utah*  
Advisor: Prof. Lance C. Seefeldt

- Mechanistic Insight into the Substrate Reduction Catalyzed by Nitrogenase

**Undergraduate Research** 2008-2009  
*Department of Biochemistry, Pokhara University, Nepal*  
Advisor: Prof. V. P. Agarawal

- Conformational Variation of Tri-chloroacetate (TCA) Precipitated Bovine Serum Albumin (BSA)

*Department of Life Science and Biotechnology, Yonsei University, S. Korea, 2008*  
Advisors: Prof. JiYong Park

- In-vitro Study of Alginate Microsphere for Oral Delivery of Protein Drugs

**PEER-REVIEWED PUBLICATIONS**

- Lukoyanov D., **Khadka N.**, Dean D. R., Seefeldt L. C., Hoffman B. M. Photo Induced Reductive Elimination of H<sub>2</sub> from the Nitrogenase Dihydride (Janus) State Involves an FeMo-cofactor H<sub>2</sub> Intermediate. *Inorg. Chem.* (2017) Accepted.
- **Khadka N.**, Dean D.R., Smith D, Hoffman B.M., Rauegi S, Seefeldt L.C. CO<sub>2</sub> Reduction Catalyzed by Nitrogenase: Pathways to Formate, Carbon Monoxide and Methane. *Inorg. Chem.* **2016**, 55(17), 8321-8330.
- Milton R. D., Abdellaoui S., **Khadka N.**, Dean D.R., Leech D., Seefeldt L. C., Minter S.D. Nitrogenase Bioelectrocatalysis: Heterogeneous Ammonia and Hydrogen Production by MoFe Protein. *Energy Environ. Sci.* **2016**, 9, 2550-2554.

- Lukoyanov D., **Khadka N.**, Yang Z-Y., Dean D. R., Seefeldt L. C., Hoffman B. M. Reductive Elimination of H<sub>2</sub> Activates Nitrogenase to Reduce the N≡N Triple Bond: Characterization of the E<sub>4</sub>(4H) Janus Intermediate in Wild-Type Enzyme. *J. Am. Chem. Soc.* **2016**, *138* (33), 10674-10683.
- Davydov R., **Khadka N.**, Yang Z-Y., Fielding A.J., Lukoyanov D., Dean D.R., Seefeldt L.C., Hoffman B.M. Exploring Proton-Coupled Electron Transfer and Conformational Changes in the Nitrogenase MoFe Protein and FeMo-cofactor Through Cryoreduction/EPR Measurements. *Isr. J. Chem.* **2016**, *56*, 841-851.
- Brown K.A., Harris D.F., Wilker M.B., Rasmussen A., **Khadka N.**, Hamby H., Keable S., Dukovic G., Peters J.W., Seefeldt L.C., King P.W. Light-driven Dinitrogen Reduction Catalyzed by a CdS:nitrogenase MoFe. *Science* **2016**, *352*(6284), 448-450.
- Lukoyanov D., **Khadka N.**, Yang Z-Y., Dean D. R., Seefeldt L. C., Hoffman B. M. Reversible Photoinduced Reductive Elimination of H<sub>2</sub> from the Nitrogenase Dihydride State, the E<sub>4</sub>(4H) Janus Intermediate. *J. Am. Chem. Soc.* **2016**, *138*(4), 1320-1327.
- Lukoyanov D., Yang Z-Y., **Khadka N.**, Dean D. R., Seefeldt L. C., Hoffman B. M. Identification of a Key Catalytic Intermediate Demonstrate that Nitrogenase is Activated by the Reversible Exchange of N<sub>2</sub> for H<sub>2</sub>. *J. Am. Chem. Soc.* **2015**, *137*(10), 3610-3615.
- Yang Z-Y., **Khadka N.**, Lukoyanov D., Hoffman B. M., Dean D. R., Seefeldt L. C. On Reversible H<sub>2</sub> Loss Upon N<sub>2</sub> Binding to FeMo-cofactor of Nitrogenase. *Proc. Natl. Acad. Sci. USA*, **2013**, *110* (41), 16327-32.

## RESEARCH TECHNIQUES/SKILLS

- **Spectroscopic and Analytical methods:** Electron Paramagnetic Resonance, 1D and 2D Nuclear Magnetic Resonance, Gas Chromatography-Mass Spectrometer, Liquid Chromatography-Mass Spectrometer, Infrared Spectroscopy, UV-Vis Spectroscopy, Fluorescence Spectroscopy, Gas Chromatography-Flame Ionization Detector, Gas Chromatography-Thermal conduction Detector, High Performance Liquid Chromatography, Column Chromatography.
- **Biochemical methods:** Protein expression, Anaerobic/Aerobic Protein Purification, Protein labelling, Mechanistic Enzymology, Steady-state and Pre Steady State Kinetics, Protein dynamics, Kinetic Isotope Effect, Basic Molecular Biology.
- **Electrochemistry and photochemistry:** Covalent and Non-covalent Adsorption of Protein on Electrode, Direct and Mediated Bioelectrocatalysis, Cyclic Voltammetry, Chronoamperometry, Bulk electrolysis, Mechanistic study of redox enzyme, Coupling of Biological Redox Chemistry with photo-excited electrons.
- **Other Skills:** Statistical analysis of data, Kinetic Fitting, Literature Search, Designing Experiments, Analyzing Data, Making high Publication Quality Figures.

## TEACHING EXPERIENCE

### Teaching Assistant

*Department of Biochemistry, Pokhara University, Nepal*

2009-2010

- Undergraduate lab. course

*Department of Chemistry and Biochemistry, Utah State University, Logan, Utah*  
2011-2015

- Lab instructor for general chemistry CHEM 1210, 1215, and 1022
- Lab instructor for general biochemistry CHEM 3710

## POSTER PRESENTATIONS

- **Khadka N.**, Milton R. D., Dean D.R., Minter S.D., Seefeldt L.C. Probing How Amino Acid Substitution Alters Hydride Reactivity in Nitrogenase. 6<sup>th</sup> Hansen Life Science Retreat, Utah State University, Logan, Utah. September 2016.
- **Khadka N.**, Dean D.R., Smith D., Hoffman B.M., Raugei S., Seefeldt L.C. Mechanistic Insight into CO<sub>2</sub> Reduction Catalyzed by Nitrogenase. 19<sup>th</sup> International Congress on Nitrogen Fixation, Pacific Grove, California. October 2015.
- **Khadka N.**, Dean D.R., Smith D., Hoffman B.M., Raugei S., Seefeldt L.C. Mechanistic Insight into CO<sub>2</sub> Reduction Catalyzed by Nitrogenase. 5<sup>th</sup> Hansen Life Science Retreat, Utah State University, Logan, Utah. September 2015.
- **Khadka N.**, Yang Z-Y., Dean D. R., Seefeldt L. C. Understanding the mechanism of CO<sub>2</sub> reduction by nitrogenase. 4<sup>th</sup> Hansen Life Science Retreat, Utah State University, Logan, Utah. September 2014.
- **Khadka N.**, Yang Z-Y., Lukoyanov D., Hoffman B. M., Dean D. R., Seefeldt L. C. Insight into obligatory H<sub>2</sub> evolution upon N<sub>2</sub> binding to FeMo-cofactor of nitrogenase. 3<sup>rd</sup> Hansen Life Science Retreat, Utah State University, Logan, Utah. September 2013.
- **Khadka N.**, Yang Z-Y., Lukoyanov D., Hoffman B. M., Dean D. R., Seefeldt L. C. Understanding N<sub>2</sub> dependent HD exchange mechanism catalyzed by nitrogenase. 2<sup>nd</sup> Hansen Life Science Retreat, Utah State University, Logan, Utah. September 2012.

## PROFESSIONAL AFFILIATION

- American Chemical Society

## CERTIFICATION

- Lab Safety, Utah State University
- Radiation Safety, Utah State University

**AWARDS AND HONORS**

- Undergraduate scholarship (Tuition waiver), Pokhara University, Kathmandu, Nepal (2004-2008)
- Thomas F. Emery Outstanding Graduate Student in Biochemistry (2016)